Liquefaction and Paleo-liquefaction in Christchurch, New Zealand

---

A thesis submitted in partial fulfilment for the
degree of Doctor of Philosophy in Geology

at the
University of Canterbury

by
Sarah H. Bastin

February 2016

Abstract

Liquefaction during the 4th September 2010 M_w 7.1 Darfield earthquake and large aftershocks in 2011 (Canterbury earthquake sequence, CES) caused severe damage to land and infrastructure within Christchurch, New Zealand. Approximately one third of the total CES-induced financial losses were directly attributable to liquefaction and thus highlights the need for local and regional authorities to assess liquefaction hazards for present and future developments. This thesis is the first to conduct paleo-liquefaction studies in eastern Christchurch for the purpose of determining approximate return times of liquefaction-inducing earthquakes within the region. The research uncovered evidence for pre-CES liquefaction dated by radiocarbon and cross-cutting relationships as post-1660 to pre-1905. Additional paleo-liquefaction investigations within the eastern Christchurch suburb of Avondale, and the northern township of Kaiapoi, revealed further evidence for pre-CES liquefaction. Pre-CES liquefaction in Avondale is dated as post-1321 and pre-1901, while the Kaiapoi features likely formed during three distinct episodes: post-1458 and possibly during the 1901 Cheviot earthquake, post-1297 to pre-1901, and pre-1458. Evaluation of the liquefaction potential of active faults within the Canterbury region indicates that many faults have the potential to cause widespread liquefaction within Avondale and Kaiapoi. The identification of pre-CES liquefaction confirms that these areas have previously liquefied, and indicates that residential development in eastern Christchurch between 1860 and 2005 occurred in areas containing geologic evidence for pre-CES liquefaction. Additionally, on the basis of detailed field and GIS-based mapping and geospatial-statistical analysis, the distribution and severity of liquefaction and lateral spreading within the eastern Christchurch suburb of Avonside is shown in this study to be strongly influenced by geomorphic and topographic variability. This variability is not currently accounted for in site-specific liquefaction assessments nor the simplified horizontal displacement models, and accounts for some of the variability between the predicted horizontal displacements and those observed during the CES. This thesis highlights the potential applications of paleo-liquefaction investigations and geomorphic mapping to seismic and liquefaction hazard assessments and may aid future land-use planning decisions.

UNIVERSITY OF CANTERBURY
Te Whare Wānanga o Waitaha
CHRISTCHURCH NEW ZEALAND

Deputy Vice-Chancellor's Office
Postgraduate Office

Co-Authorship Form

This form is to accompany the submission of any thesis that contains research reported in co-authored work that has been published, accepted for publication, or submitted for publication. A copy of this form should be included for each co-authored work that is included in the thesis. Completed forms should be included at the front (after the thesis abstract) of each copy of the thesis submitted for examination and library deposit.

Chapter 2 *– Paleo-liquefaction in Christchurch, New Zealand*

Published in Geological Society of America Bulletin

The manuscript was compiled and written by Sarah Bastin. Dr Kari Bassett and Dr Mark Quigley provided detailed reviews and suggestions to the contents and structure of the manuscript.

Certification by Co-authors:
If there is more than one co-author then a single co-author can sign on behalf of all
The undersigned certifys that:

- The above statement correctly reflects the nature and extent of the PhD candidate's contribution to this co-authored work
- In cases where the candidate was the lead author of the co-authored work he or she wrote the text

Name: *Mark Quigley* Signature: 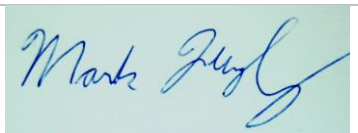 Date: *2/2/16*

UNIVERSITY OF CANTERBURY
Te Whare Wānanga o Waitaha
CHRISTCHURCH NEW ZEALAND

Deputy Vice-Chancellor's Office
Postgraduate Office

Co-Authorship Form

This form is to accompany the submission of any thesis that contains research reported in co-authored work that has been published, accepted for publication, or submitted for publication. A copy of this form should be included for each co-authored work that is included in the thesis. Completed forms should be included at the front (after the thesis abstract) of each copy of the thesis submitted for examination and library deposit.

Chapter 3 *– Late Holocene liquefaction at sites of contemporary liquefaction during the 2010-2011 Canterbury Earthquake Sequence*

Accepted for publication in the Bulletin of the Seismological Society of America

The manuscript was compiled and written by Sarah Bastin. Alterations made to the manuscript included in this thesis were also made by Sarah Bastin. Dr Kari Bassett and Dr Mark Quigley provided revisions of the content and structure of the manuscript. Prof Russell Green and Brett Maurer provided assistance with the back-calculated magnitude bound curves (~5%), while Prof Brendon Bradley provided assistance with the back-calculated ground motions (~3%).

Certification by Co-authors:

If there is more than one co-author then a single co-author can sign on behalf of all

The undersigned certifys that:

- The above statement correctly reflects the nature and extent of the PhD candidate's contribution to this co-authored work
- In cases where the candidate was the lead author of the co-authored work he or she wrote the text

Name: *Mark Quigley* Signature: 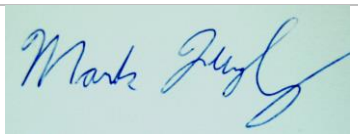 Date: *2/2/16*

UNIVERSITY OF CANTERBURY
Te Whare Wānanga o Waitaha
CHRISTCHURCH NEW ZEALAND

Deputy Vice-Chancellor's Office
Postgraduate Office

Co-Authorship Form

This form is to accompany the submission of any thesis that contains research reported in co-authored work that has been published, accepted for publication, or submitted for publication. A copy of this form should be included for each co-authored work that is included in the thesis. Completed forms should be included at the front (after the thesis abstract) of each copy of the thesis submitted for examination and library deposit.

Chapter 4 *– The subsurface stratigraphy of liquefaction dikes and intrusions: paleo-seismic implications and correlations with epicentral distance*

Intended for submission to Sedimentology or the New Zealand Journal of Geology and Geophysics

The manuscript was written by Sarah Bastin. Dr Kari Bassett and Dr Mark Quigley provided detailed revisions of the content and structure of the manuscript.

Certification by Co-authors:
If there is more than one co-author then a single co-author can sign on behalf of all
The undersigned certifys that:

- The above statement correctly reflects the nature and extent of the PhD candidate's contribution to this co-authored work
- In cases where the candidate was the lead author of the co-authored work he or she wrote the text

Name: *Mark Quigley* Signature: 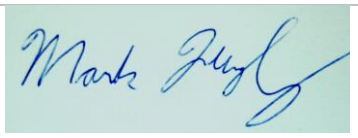 Date: *2/2/16*

UNIVERSITY OF CANTERBURY
Te Whare Wānanga o Waitaha
CHRISTCHURCH NEW ZEALAND

Deputy Vice-Chancellor's Office
Postgraduate Office

Co-Authorship Form

This form is to accompany the submission of any thesis that contains research reported in co-authored work that has been published, accepted for publication, or submitted for publication. A copy of this form should be included for each co-authored work that is included in the thesis. Completed forms should be included at the front (after the thesis abstract) of each copy of the thesis submitted for examination and library deposit.

Chapter 5 – Geomorphic, geologic, and topographic influences on the distribution and severity of liquefaction during the 2010 – 2011 Canterbury EarthquakeSequence

Intended for submission to Engineering Geology

The manuscript was written by Sarah Bastin. Additions and alterations made to the manuscript included in the thesis were also made by Sarah Bastin. Dr Sjoerd van Ballegooy contributed to the content of the manuscript and checked the scientific context (~7%), while Dr Kari Bassett and Dr Mark Quigley provided revisions of the structure of the manuscript.

Certification by Co-authors:
If there is more than one co-author then a single co-author can sign on behalf of all
The undersigned certifys that:

- The above statement correctly reflects the nature and extent of the PhD candidate's contribution to this co-authored work
- In cases where the candidate was the lead author of the co-authored work he or she wrote the text

Name: *Mark Quigley* Signature: 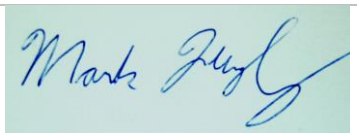 Date: *2/2/16*

UNIVERSITY OF CANTERBURY
Te Whare Wānanga o Waitaha
CHRISTCHURCH NEW ZEALAND

Deputy Vice-Chancellor's Office
Postgraduate Office

Co-Authorship Form

This form is to accompany the submission of any thesis that contains research reported in co-authored work that has been published, accepted for publication, or submitted for publication. A copy of this form should be included for each co-authored work that is included in the thesis. Completed forms should be included at the front (after the thesis abstract) of each copy of the thesis submitted for examination and library deposit.

Chapter 2 & 5 *– Characterization of modern and paleo-liquefaction features in eastern Christchurch, NZ following the 2010-2011 Canterbury Earthquake Sequence*

Published in peer-reviewed conference proceedings of the 19th NZGS Geotechnical Symposium

The manuscript was written by Sarah Bastin. Dr Kari Bassett and Dr Mark Quigley provided revisions of the structure and content of the manuscript (~10%).

Certification by Co-authors:
If there is more than one co-author then a single co-author can sign on behalf of all
The undersigned certifys that:

- The above statement correctly reflects the nature and extent of the PhD candidate's contribution to this co-authored work
- In cases where the candidate was the lead author of the co-authored work he or she wrote the text

Name: *Mark Quigley* Signature: 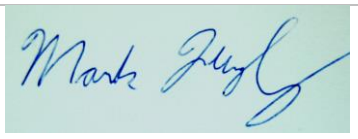 Date: *2/2/16*

UNIVERSITY OF CANTERBURY
Te Whare Wānanga o Waitaha
CHRISTCHURCH NEW ZEALAND

Deputy Vice-Chancellor's Office
Postgraduate Office

Co-Authorship Form

This form is to accompany the submission of any thesis that contains research reported in co-authored work that has been published, accepted for publication, or submitted for publication. A copy of this form should be included for each co-authored work that is included in the thesis. Completed forms should be included at the front (after the thesis abstract) of each copy of the thesis submitted for examination and library deposit.

Chapter 5 *– Comparison of liquefaction-induced land damage and geomorphic variability in Avonside*

Published in peer-reviewed conference proceedings of the 6th International Conference on Earthquake Geotechnical Engineering

The paper was written by Sarah Bastin. Dr Kari Bassett and Dr Mark Quigley provided revisions relating the content and structure of the paper (~10%)..

Certification by Co-authors:
If there is more than one co-author then a single co-author can sign on behalf of all
The undersigned certifys that:

- The above statement correctly reflects the nature and extent of the PhD candidate's contribution to this co-authored work
- In cases where the candidate was the lead author of the co-authored work he or she wrote the text

Name: *Mark Quigley* Signature: 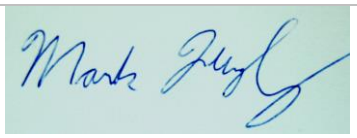 Date: *2/2/16*

Acknowledgements

This thesis is the culmination of four years of research, funded by an EQC capability fund, with additional support from MBIE and the Department of Geological Sciences at the University of Canterbury Mason Trust Fund, all of whom are gratefully thanked for their funding.

Firstly, I want to thank my supervisors Associate Professor Mark Quigley and Dr Kari Bassett for their constant support and guidance throughout this thesis. Mark, your high expectations and constant challenging of my work has encouraged me to develop and back my own research ideas. Thank you for everything. Also, thank you to Kari for your constant help, support, and encouragement.

I would also like to thank Dr Martitia Tuttle for inspiring me to undertake this project; without your initial guidance this work wouldn't have eventuated. I would also like to thank Professor Russell Green and Brett Maurer from Virginia Tech, Dr Brendon Bradley from the University of Canterbury, and Dr Sjoerd van Ballegooy from Tonkin + Taylor for their help with the engineering side of this thesis, and to Dr Matthew Hughes for his help with GIS. Thank you also to Sjoerd for promoting my work to other engineers and industry professionals. I also need to thank David Jacobson and all the other field assistants that have put up with the challenging field conditions that arise when you trench in disaster zones with high water-tables and potential asbestos and sewage contamination.

Thanks also to all of the friends that I have made in the department over the years that have helped me in some way throughout this thesis. There are too many of you to name, but thanks for all the laughs and beers. I must also thank you to my office mates Louise, Hamish, and Heather it was nice to be on the PhD roller-coaster with other like-minded people. Also, thank you to Toni Cox for your friendship and support throughout our degree and post-graduate studies.

I also need to thank my partner Karl for constantly challenging me to learn how to do things properly and for encouraging me to produce the best work I am capable of. Your encouragement and quirky sense of humour when it all seemed too stressful is really appreciated. Lastly, I need to thank my parents for their constant support and help which has allowed me to keep my life some-what balanced and keep horse riding. Thank you for always being willing to help in any way possible.

Contents

List of Figures

List of Tables

Chapter 1

Introduction

1.1 Scientific background

Cyclic shearing of unconsolidated and fluid-saturated granular sediments during earthquake-induced ground motion may cause pore-water pressures to increase and reduce shear strength within the affected sediment. Liquefaction occurs as pore-water pressures increase and exceed the static confining pressure causing the sediment to deform and resulting in the breakdown of the grain arrangement (Seed and Idriss, 1982; Youd and Hoose, 1977; Youd et al., 2001; Idriss and Boulanger, 2008). Liquefied sediment and associated pore-water may be ejected to the ground surface via feeder dikes which commonly utilize fractures in the overlying sedimentary cover. Ejected sediment commonly manifests at the surface as sand blows and/ or blistering of the surface by near-surface sediment injection, while ejected pore water commonly causes surface flooding (Seed and Idriss, 1982; Sims, 1975; Obermeier, 1996; Idriss and Boulanger, 2008; Cubrinovski and Green, 2010; Quigley et al., 2013). Liquefaction may also result in vertical (subsidence) and/or lateral (lateral spreading) ground deformation (Seed and Idriss, 1982; Idriss and Boulanger, 2008; Cubrinovski and Green, 2010). Lateral spreading typically occurs in sloping ground or gently-sloping ground proximal to a free-face (e.g. river bank) where liquefaction is triggered. Sediment is transported down-slope and towards the free-face via basal glide and stretching within the liquefied layer, and typically results in fissuring of the overlying strata and the associated ejection of liquefied sediment (Seed and Idriss, 1982; Idriss and Boulanger, 2008; Youd et al., 2001). The surficial liquefaction features may be rapidly reworked into forms

that are challenging to distinguish from the surrounding sediment deposits and may not be well preserved in the geologic record (Sims, 1975; Reid et al., 2012; Quigley et al., 2013). The subsurface liquefaction features including liquefaction dikes and sills may be preserved in the geologic record where host sediments are preserved. Pre-historic liquefaction features preserved in the geologic record are termed paleo-liquefaction (Obermeier, 1996; Tuttle, 2001).

Sediments considered highly susceptible to liquefaction are unconsolidated and saturated fine grained sand to silt with a clay content <15% that are within 10 m of the surface and in settings a hosting a shallow water table (Youd and Hoose, 1977; Youd et al., 2001; Idriss and Boulanger, 2008). Holocene fine to very fine sands deposited within fluvial, deltaic, or aeolian environments are generally considered to be highly susceptible to liquefaction (Youd and Hoose, 1977). Geomorphic variability within these deposits has not been systematically compared to variations in liquefaction severity nor surficial manifestation of liquefaction. Secondary factors influencing the resistance to liquefaction include the degree of sorting which affects the porosity, permeability and cohesion of the sediment (Youd and Hoose, 1977; Seed and Idriss, 1982). Liquefaction susceptibility generally decreases with increasing sediment age due to the precipitation of cements and the increasing depth of burial which increases the overlying confining pressures (Youd and Hoose, 1977; Seed and Idriss, 1982).

Non-uniform ground surface subsidence and lateral spreading induced by liquefaction poses a significant hazard to the built environment (Seed and Idriss, 1982; Idriss and Boulanger, 2008; Cubrinovski and Green, 2010; Cubrinovski et al., 2012) Severe liquefaction-induced damage has been reported following many recent and historic large earthquakes including the 1906 San Francisco (Youd and Hoose, 1977), 1964 Japan (Idriss and Boulanger, 2008), 1989 Loma Prieta, California (Sims, 1975), 1990 Luzon, Philippines (Orense, 2011), 1999 Kocaeli, Turkey (Sonmez et al., 2008), 2010 Haiti (Madabhushi et al., 2013), and the 2010 - 2011 Canterbury Earthquakes (Cubrinovski and Green, 2010; Quigley et al., 2013; van Ballegooy et al., 2014a). Liquefaction-induced damage during these events significantly increased the financial losses, and in some cases, resulted in increased loss of life. Liquefaction-induced subsidence has also been shown to increase flood and marine inundation, and decrease liquefaction triggering thresholds following the 2010-2011 Canterbury Earthquakes, thus resulting in secondary hazards and

financial losses (Hughes et al., 2015; Tonkin and Taylor, 2015, 2013b). The direct and secondary hazards posed by liquefaction during the recent and historic earthquakes highlights the need for local and regional authorities to assess liquefaction hazards for present and future land-use development and for seismic hazard assessments.

1.1.1 Application of paleo-liquefaction studies for assessing seismic and liquefaction hazards

Paleo-liquefaction features preserved within the geologic record provide evidence for pre-historic earthquakes with shaking intensities and durations exceeding the threshold value for liquefaction (Obermeier, 1996; Green et al., 2005; Tuttle and Barstow, 1996). Paleo-liquefaction studies have been employed to determine seismic hazards within areas known to experience infrequent large earthquakes and/or contain blind faults where the timing and magnitude of previous earthquakes is unknown (Obermeier, 1996; Obermeier et al., 2001; Obermeier, 1998; Obermeier et al., 2005; Tuttle and Barstow, 1996; Tuttle, 2001; Tuttle et al., 2002, 2006). Investigations rely on accurate identification and dating of paleo-liquefaction features across a large geographic area to determine the size of the liquefaction field associated with historic and/ or pre-historic earthquakes. The magnitude of the historic/ pre-historic earthquake may be evaluated from the magnitude-bound method, which uses the farthest distance of paleo-liquefaction from the inferred tectonic source, or from the cyclic stress method, which assumes that the paleo-earthquake must have exceeded the minimum threshold value for liquefaction at the site. Minimum thresholds may be combined with regional attenuation models to estimate the magnitude of the paleo-earthquake (Obermeier et al., 2001).

Paleo-liquefaction studies have successfully been applied within the New Madrid seismic zone to constrain the timing of pre-historic earthquakes triggering liquefaction. Studies have also constrained that liquefaction in the New Madrid seismic zone during the great 1811-12 earthquakes occurred during a couple of very large earthquakes rather than a series smaller earthquakes (Tuttle and Barstow, 1996; Tuttle, 2001; Tuttle et al., 2002, 2006). These studies within the New Madrid Seismic zone highlight the potential applications of paleo-liquefaction features in assessing seismic hazards within areas where traditional fault specific paleo-seismic studies may not be employed.

1.1.2 Methods for evaluating liquefaction susceptibility

The potential for liquefaction at a given site or region may be evaluated from in-situ or laboratory testing. Laboratory based methods typically apply horizontal cyclic loads to sediment samples to estimate the shear stresses developing in the soil due to the vertical propagation of shear waves during an earthquake. The generated cyclic stresses are then compared with the cyclic resistance of the soil to calculate a threshold value for liquefaction triggering (Seed and Idriss, 1982; Idriss and Boulanger, 2008).This methodology requires the in-situ stresses to be replicated within the laboratory which often proves problematic (Seed and Idriss, 1982; Idriss and Boulanger, 2008).

In-situ testing methods are commonly applied for simple site-specific liquefaction analysis as they provide a lower cost alternative that enables many tests to be conducted across a site, including repeated tests before and after seismic events. The Standard Penetration Test (SPT), Cone Penetration Test (CPT), and/or Shear Wave Velocity measurements are commonly employed within sandy sediments, while the Becker Penetration Test (BPT) is commonly used in gravels. The CPT and SPT are widely applied as the industry standard for evaluating the resistance of subsurface sediments to liquefaction (Youd and Hoose, 1977; Idriss and Boulanger, 2008; Boulanger and Idriss, 2014). The SPT and CPT measure the resistance of the subsurface sediments to a steel-rod being pushed vertically under a constant load; recorded as an N-value for SPT and q_c for CPT. The recorded values act as a proxy for grain size, porosity, and density of the subsurface sediments which is a direct function of their resistance to liquefaction (Seed and Idriss, 1982; Idriss and Boulanger, 2008; Youd and Hoose, 1977).

The resistance of the subsurface deposit to liquefaction is commonly evaluated from the in-situ testing using the stress-based approach derived by Seed and Idriss (1982) and later updated by Idriss and Boulanger (2008) and Boulanger and Idriss (2014). The methodology compares the earthquake-induced cyclic stress ratios (CSR) with the cyclic resistance ratios (CRR) of the soil to derive a Factor of Safety (FS) against liquefaction triggering. The FS is defined from the ratio of CRR to CSR with liquefaction predicted to trigger when FS <1. The CSR is calculated for a given depth within the subsurface sediment profile based on the seismic demand on the given unit (Seed and Idriss, 1982; Idriss and Boulanger,

2008; Youd and Hoose, 1977). The Seed-Idriss simplified liquefaction procedure incorporates corrections to account for the overburden and the effective overburden pressures exerted on the sediment at depth, and the maximum horizontal acceleration as a fraction of gravity. A stress reduction coefficient that accounts for the dynamic response of the soil profile is also included (Seed and Idriss, 1982; Idriss and Boulanger, 2008; Boulanger and Idriss, 2014). The CRR is derived from the q_c or N-value derived from the SPT or CPT and requires corrections for the overburden stress and atmospheric pressure. The q_c must additionally be corrected for unequal area effects on the cone tip including the area ratio and pore pressure. Corrections must also be made for the fines content of the subsurface sediment. The CRR of the subsurface sediments is dependent on the duration of shaking which is expressed through an earthquake magnitude scaling factor (MSF). Field observations from historic liquefaction-triggering earthquakes have been collated to constrain the CRR. These observations were corrected to a common reference condition of a moment magnitude 7.5 earthquake, effective vertical stress of 1 atmosphere, and level ground conditions. The MSF must therefore be applied to account for earthquakes and sites outside of these reference conditions (Idriss and Boulanger, 2008; Boulanger and Idriss, 2014).

Additional parameters for assessing liquefaction resistance include the Liquefaction Potential Index (LPI), and the Liquefaction Severity Number (LSN). The LPI utilises the simplified procedure derived by Seed and Idriss (1982) to estimate the potential for liquefaction at a given site from the factors of safety derived for the upper 20 m of the soil profile (Iwasaki et al., 1978). The method assumes that the severity of liquefaction is proportional to the thickness of the liquefied layer, proximity of the liquefied layer to the surface, and the amount by which the factor of safety (FS) is less than 1. LPI values can range from 0 at a site with no potential for liquefaction to 100 in which the entire 20 m profile has a factor of safety of 0. The LSN was derived by Tonkin and Taylor (2013a) to assess land performance following the 2010-2011 Canterbury earthquake sequence. The parameter is calculated for the top 10 m of the sediment profile and accounts for volumetric strains at given depths below the surface. Weighting is given so that deeper units have less influence than the upper units.

The resistance to liquefaction triggering of the subsurface sediments may be incorporated into empirical and/ or semi-empirical models to predict total lateral spreading-induced horizontal ground displacements for a given site. These models

have been derived from field observations made following recent earthquakes and incorporate the cumulative thickness of liquefiable sediment (FS <1), with seismological (e.g. earthquake moment magnitude, source distance), and topographic parameters (e.g. distance to the closest free-face and height of the free-face). The empirical model derived by Zhang et al. (2004) and the multi-linear regression equations proposed by Bartlett and Youd (1995) and updated in Youd et al. (2002) are typically employed in simple geotechnical assessments.

1.1.3 Liquefaction research within New Zealand

New Zealand is situated astride the interface of the Australian and Pacific tectonic plates. The New Zealand Seismic Hazard Model (NZSHM) predicts that >80% of New Zealand has a 475-year return time of peak ground accelerations (PGA) >0.1 g, and >60% of New Zealand's South Island has a 475-year return time of peak ground accelerations (PGA) >0.2 g (Stirling et al., 2012). Many of the main cities and large townships within New Zealand are located proximal to the coastline and are partially underlain by unconsolidated and saturated sediments considered to have a low resistance to liquefaction (Brown and Weeber, 1992; Stirling et al., 2008; Christensen, 1994). Liquefaction triggering is predicted at PGA >0.09 g indicating that many of these areas are predicted to liquefy under the 475-year return PGA (Santucci de Magistris et al., 2013).

Previous studies have documented the distribution of potentially liquefiable sediments within the cities of Christchurch and Wellington, and across the wider Hawkes Bay region (Elder et al., 1991; Berrill et al., 1994; Beca, 2000; Christensen, 1994; Christchurch Engineering Lifelines Group, 1997; Clough, 2005). Cases of historic liquefaction within New Zealand between 1848 and 1984 have been collated by Fairless and Berrill (1984) and are summarized in Table 1.1. The 1987 Edgecombe earthquake also caused localized areas of severe liquefaction and lateral spreading within the townships of Napier and Whakatane which was documented in detail by Christensen (1994). It is possible that liquefaction occurred during earthquakes prior to 1848 and went unrecorded as liquefaction was not originally recognised as an earthquake-induced phenomenon, and as much of New Zealand is sparsely populated. Recent cases of liquefaction within New Zealand include the recurrent liquefaction recorded within the wider Christchurch area during the

2010-2011 Canterbury earthquake sequence (Cubrinovski and Green, 2010; Cubrinovski et al., 2011; Quigley et al., 2013), and localized liquefaction within township of Blenheim following the 2013 M_w 6.6 Cook Strait and M_w 6.6 Lake Grassmere earthquakes (van Dissen et al., 2013).

TABLE 1.1: Historic Cases of Liquefaction in New Zealand

Year	Location	MMI	Description
1848	Lower Wairau Valley Marlborough	X	Sand blows, subsidence, and surface fissuring
1855	Wairarapa	XI+	Sand blows, subsidence, surface fissures
1888	Amuri/ Hope Fault	XIII	Sand blows and subsidence
1895	Taupo	VIII+	Surface fissuring, pumice ejection
1901	Cheviot, North Canterbury	IX	Surface flooding, sand blows, Lateral spreading
1913	Westport	VIII	Lateral spreading
1929	Arthurs Pass	IX	Sand blows
1931	Hawkes Bay	XI	Surface flooding, sand blows differential settlement, lateral spreading
1942	Southern Wairarapa	VIII	Surface flooding, sand blows lateral spreading
1968	Inangahua	X	Surface flooding, sand blows

1.1.4 Liquefaction during the Canterbury Earthquake Sequence and previous work

The 2010-2011 Canterbury earthquake sequence (CES) caused at least 10 distinct episodes of observed liquefaction in parts of eastern Christchurch, New Zealand (Quigley et al., 2013). Severe liquefaction-induced damage was reported following the September 2010 M_w 7.1 Darfield main shock, and the February 2011 M_w 6.2 (i.e., 2011 Christchurch earthquake), June 2011 M_w 6.0, and December 2011 M_w 5.9 aftershock earthquakes (Cubrinovski and Green, 2010; Cubrinovski et al., 2011; Quigley et al., 2013). Differential ground subsidence and lateral spreading induced by liquefaction caused severe damage and disruption to civil infrastructure and lifelines within the city, requiring a large financial input for remediation and resulting in the central government purchase of more than 6000 residential properties in eastern Christchurch. Reconnaissance mapping following the September 2010 and February 2011 earthquakes indicated severe liquefaction occurred to the

east of the Central Business District in Christchurch, specifically along the inner meander loops of the Avon River and proximal to the Avon-Heathcote estuary (Cubrinovski and Green, 2010; Cubrinovski et al., 2011; Green et al., 2005; Cubrinovski and Robinson, 2015).

Research commissioned by both the Waimakariri and Christchurch District Councils had determined the high liquefaction potential of the sediments underlying the region prior to the Canterbury earthquake sequence (Elder et al., 1991; Brown and Weeber, 1992; Christchurch Engineering Lifelines Group, 1997; Clough, 2005). Maps illustrating the anticipated distribution of liquefaction following a large liquefaction-triggering earthquake were made publicly available on the Environment Canterbury website, with two scenarios depicted; a standard event, and an event during a high water table. The trigger for liquefaction was anticipated to be either an Alpine Fault or an event on one of the many active faults along the rangefront of the Southern Alps (Beca, 2000).

Pre-CES liquefaction had been reported in the northern township of Kaiapoi following the $\sim M_w$ 6.9 Cheviot earthquake, while no pre-CES liquefaction had been reported within Christchurch (Berrill et al., 1994). The historic record of earthquakes in the region is limited to post-1843, following European settlement. The timing and approximate return times of liquefaction triggering earthquakes within the wider Christchurch area are therefore unknown.

Of the >10 liquefaction triggering earthquakes during the CES, only the rupture of the Greendale fault during the 4 September 2010 earthquake caused a surface rupture, and this was rapidly re-worked into the surrounding deposits by local land-owners (Hornblow et al., 2014). No surficial evidence of the faults that ruptured during the CES is likely to be preserved. The CES therefore highlights the limitations of fault-specific paleo-seismic studies utilizing surface rupture traces to identify fault locations and estimate seismic hazards. The widespread liquefaction triggered within eastern Canterbury during the CES is likely to be preserved within the geologic record, and therefore provides an additional landscape record of earthquakes triggering strong ground motions.

1.2 Thesis Structure

This thesis is presented in four main chapters written and presented as a suite of Ph.D. chapters, however a modified form of each chapter has also been published (Chapter 2), accepted for publication (Chapter 3), or will be submitted for publication in international peer reviewed journals (Chapters 4 and 5).

Chapter 2 presents detailed descriptions of the surface distribution and subsurface morphology of Canterbury earthquake sequence (CES) liquefaction features and the results from the first paleo-liquefaction investigation to be conducted within eastern Christchurch. Trenching at two sites within the eastern Christchurch suburb of Avonside revealed multiple generations of CES dikes that crosscut Holocene-to-recent fluvial and anthropogenic stratigraphy, and aligned with pre-CES liquefaction features. The potential of known historic earthquakes triggering liquefaction at the study sites is also evaluated from a New Zealand specific ground motion prediction equation and compared with local and global liquefaction triggering thresholds.

Chapter 3 further investigates evidence of paleo-liquefaction at three sites within the eastern Christchurch suburb of Avondale, and two sites within the northern township of Kaiapoi. Pre-CES features cross-cut the fluvial stratigraphy and align with CES liquefaction features at the study sites. The liquefaction potential of known active faults within the wider Canterbury region are evaluated from back-calculated magnitude bound curves and peak ground accelerations (PGA) approximated from the New Zealand specific ground motion prediction equation and compared with a global liquefaction triggering threshold.

Chapter 4 compares the morphology of the subsurface CES liquefaction features exposed at six of the study sites with site-specific PGA and the epicentral distances of the main liquefaction triggering CES earthquakes. The widths of the liquefaction dikes do not scale with the epicentral distances, nor site-specific PGA and the number of liquefaction episodes preserved in the subsurface significantly under-represents the number of liquefaction episodes that occurred during the CES. Lateral-spreading induced extensional strains, predominant subsurface sediment type, and the liquefaction susceptibility of the subsurface sediments appear to exert primary influences on dike width and the number of distinct liquefaction episodes preserved.

Chapter 5 provides an in depth study on the influence of geomorphic and geologic variability on the distribution and severity of liquefaction and associated horizontal and vertical ground displacements within the eastern Christchurch suburb of Avonside following the September 2010 and February 2011 earthquakes. The horizontal displacements recorded within the suburb vary significantly from those predicted by the Zhang et al. (2004) empirical model. Geomorphic and topographic variability is shown to significantly influence the distribution and severity of liquefaction and the horizontal ground displacements and accounts for some of the variability between the predicted and observed horizontal displacements during the CES.

Chapter 6 summarizes the key findings of this thesis and briefly discusses directions for future research.

1.2.1 Justification of thesis structure and content

The work presented within this thesis was conducted within post-disaster Christchurch, and commenced while the earthquakes were still ongoing. As a result gaining access to residential properties and obtaining permission for trenching was often difficult due to the numerous health and safety hazards. Dr Mark Quigley, a primary supervisor of this thesis, formerly owned the property at 11 Bracken Street (Site 2 within the thesis) and allowed investigations to be conducted within his backyard. In addition, Dr. Quigley collected an abundance of observational data at his property throughout the CES which lead to the in-depth studies on the geomorphic influences on the distribution of liquefaction within Avonside (Chapter 5) and the paleo-liquefaction investigation (Chapter 2). Additionally, access was granted to Sullivan Park by CERA (Christchurch Earthquake Recovery Authority) (Site 1 in this thesis). This resulted in three separate trenching investigations conducted over three summers, which is reflected by the excavation of five trenches at the site. Trenches were initially excavated for this thesis, followed by educational trenches opened for the 2013 Geosciences post-conference field trip, and for the 2014 Frontiers abroad students.

The paleo-liquefaction investigation within Avondale was invited as part of the ground improvement trials funded by EQC and led by Tonkin and Taylor. The observations made in these trenches and associated results were collated as part of the site-selection rationale for the report.

The results of the grain size analysis are presented in Appendix H. Analysis of the sediment samples was limited by earthquake damage to the laser sizer which resulted in it being out of commission for over a year, and has since resulted in machine errors within the very fine sand to silt grain sizes. As a result the grain size distributions of the samples collected within Avonside have not been analyzed in detail within this thesis.

1.3 Scientific contributions arising from the thesis

At the time of thesis submission, Chapter 2 has been published in the Geological Society of America Bulletin (GSA Bulletin; Bastin et al. (2015b)), and parts of the content included within Chapters 2 and 5 have been published in peer-reviewed, article-length conference proceedings (Bastin et al., 2013a, 2015a). The conference paper Bastin et al. (2013a) won best paper and presentation at the 2013 New Zealand Geotechnical Society conference and was subsequently published in NZ Geomechanics News (Bastin et al., 2013b). Chapter 3 has recently been accepted for publication in the Bulletin of the Seismological Society of America (BSSA) (Bastin et al. 2016). The site and trench numbering in Chapter 3 have been altered slightly from the manuscript submitted to BSSA to ensure that it fits with Chapter 2, and the site numbering outlined in Chapter 4. Chapters 4 and 5 will be submitted for review in the near future.

The content presented within this thesis has been widely presented in conference abstracts and as conference talks and/ or posters (see Section 1.3.2). In addition, the candidate has co-authored papers published in *Geology* and *Engineering Geology* (Quigley et al., 2013; Maurer et al., 2014), and is co-author on manuscripts in review at the Bulletin of the Seismological Society of America (Villamor et al (in review)) and Seismological Research Letters (Tuttle et al (in review)). The candidate is also co-author on a consultancy report (Villamor et al., 2016).

1.3.1 Refereed publications

Bastin, S., Bassett, K., Quigley, M., Maurer, B., Green, R.A., Bradley, B., Jacobson, D., Late Holocene liquefaction at sites of contemporary liquefaction during

the 2010-2011 Canterbury Earthquake Sequence, New Zealand, Accepted for publication in the Bulletin Seismological Society of America.

Bastin S., MC Quigley, & KN Bassett (2015). Paleo-liquefaction in Christchurch, New Zealand. The Geological Society of America Bulletin, 127(9-10) 1348-1365.

Bastin, S., Quigley, M.C., Bassett, K. (2015). Comparison of liquefaction-induced land damage and geomorphic variability in Avonside, New Zealand, 6th International Conference on Earthquake Geotechnical Engineering, 1-4 November 2015, Christchurch, New Zealand.

Bastin, S., Quigley, M., Bassett, K., (2013). Characterization of modern and paleo-liquefaction features in eastern Christchurch, NZ following the 2010-12 Canterbury earthquake sequence, Geomechanics News 86: 38-46.

Bastin, S., Quigley, M., Bassett, K., (2013). Characterization of modern and paleo-liquefaction features in eastern Christchurch, NZ following the 2010-12 Canterbury earthquake sequence, Proc. 19th NZGS Geotechnical Symposium, 8 p.

Quigley, M., **Bastin, S.,** & Bradley, B. (2013). Recurrent liquefaction in Christchurch, New Zealand, during the Canterbury earthquake sequence, Geology, 41: 419-422.

Maurer, B., Green, R.A., Quigley, M., **Bastin, S**. (2015). Development of Magnitude Bound Relations for Paleoliquefaction Analyses: New Zealand Case Study, Engineering Geology, 197: 253-266.

Villmor, P., Giona-Bucci, M., Almond. P., Tuttle, M., Langridge, R., Clark, K., Ries, W., Vandergoes, M., Barker, P., Martin, F., **Bastin. S.,** Watson, M., Howarth, J., Quigley, M., (2014). Exploring methods to assess paleo-liquefaction in the Canterbury area, GNS Science Consultancy Report 2014/183.

1.3.2 Refereed publications in review

Villamor, P., Almond, P., Tuttle, M. P., Giona-Bucci, M., Langridge, R.M., Clark, K., Ries, W., **Bastin, S.H.,** Eger, A., Vandergoes, M., Quigley, M.C., Barker, P., Martin, F., and J. Howarth. Liquefaction features produced by the 2010-2011 Canterbury earthquake sequence in southwest Christchurch, New Zealand

and preliminary assessment of paleoliquefaction features, Bulletin Seismological Society of America (in review).

Tuttle. M., Villamor, P., Almond, P., **Bastin, S.H.,** Giona-Bucci, M., Langdridge, R. and K. Clark. Paleoliquefaction Studies: Lessons from the 2010-2011 Canterbury, New Zealand, Earthquake Sequence. Seismological Research Letters (in review).

1.3.3 Conference abstracts

Bastin, S., Bassett, K., Quigley, M., 2015, Exploring methods of assessing liquefaction hazards, Geosciences New Zealand Program with Abstracts, Wellington, New Zealand.

Bastin, S., Quigley, M., Bassett, K., 2014, Paleo-liquefaction in Christchurch, New Zealand, Geological Society of America Annual Conference, Vancouver, Oct 22.

Bastin, S., Quigley, M., Bassett, K., 2014, Using geomorphology to predict the distribution of liquefaction, Geosciences New Zealand Program with Abstracts, New Plymouth, New Zealand.

Bastin, S., Bassett, K., Quigley, M., 2013, The paleoseismic history of Kaiapoi, North Canterbury from paleoliquefaction investigation, Geosciences New Zealand Program with Abstracts, Christchurch, New Zealand.

Bastin, S., Bassett, K., Quigley, M., Wilson, T., 2012, Liquefaction in Christchurch during the 2010-2011 Canterbury earthquake sequence and evidence for paleoliquefaction, In: Parsons, V. (editor), 2012. From warnings to effective response and recovery: Proceedings of the 6th Australasian Natural Hazards Management Conference. GNS Science Miscellaneous Series 45: 67.

Bastin, S., Quigley, M., Bassett, K., 2012, Characterisation of modern and paleoliquefaction features in Christchurch, New Zealand following the 2010-2011 Canterbury earthquake sequence, Abstract NH11A-1546, presented at 2012 Fall meeting, AGU, San Fransisco, Calif., 3-7 Dec.

Bastin, S., Quigley, M., Bassett, K., 2012, Liquefaction in Christchurch during the 2010 - 2011 Canterbury earthquake sequence and evidence for Paleoliquefaction, Geosciences New Zealand Program with Abstracts, Hamilton, New Zealand.

Chapter 2

Paleo-liquefaction in Christchurch, New Zealand

Abstract

Liquefaction during the 2010 moment magnitude (M_w) 7.1 Darfield earthquake and large aftershocks (known as the Canterbury earthquake sequence) caused severe damage to land and infrastructure in Christchurch, New Zealand. Liquefaction occurred at M_w-weighted peak ground accelerations ($PGA_{7.5}$) as low as 0.06g at highly susceptible sites. Trenching investigations conducted at two sites in eastern Christchurch enabled documentation of the geologic expressions of recurrent liquefaction and determination of whether evidence of pre-Canterbury earthquake sequence liquefaction is present. Excavation to water table depths (1-2 m below surface) across sand blow vents and fissures revealed multiple generations of Canterbury earthquake sequence liquefaction feeder dikes that crosscut Holocene-to-recent fluvial and anthropogenic stratigraphy. Canterbury earthquake sequence dikes crosscut and intrude oxidized and weathered dikes and sills at both sites that are interpreted as evidence of pre-Canterbury earthquake sequence liquefaction. Crosscutting relationships combined with ^{14}C dating constrain the timing of the pre-Canterbury earthquake sequence liquefaction to post-A.D. 1660 to pre-ca. A.D. 1905 at one site, and post-A.D. 1415 to pre-ca. A.D. 1910 at another site. The $PGA_{7.5}$ of five well-documented historical earthquakes that caused regional damage between 1869 and 1922 are approximated for the study sites using a New Zealand specific ground motion equation. Only the June 1869 M_w ~4.8

Christchurch earthquake produces a median modelled $PGA_{7.5}$ that exceeds the $PGA_{7.5}$ 0.06g threshold for liquefaction. Pre-historic earthquakes sourced from regional faults, including the 1717 Alpine fault M_w ~7.9 ± 0.3 and ca. 500-600 yr B.P. M_w 7.1 Porters Pass fault earthquakes, provide additional potential paleo-seismic sources for pre-Canterbury earthquake sequence liquefaction. The recognition of pre-Canterbury earthquake sequence liquefaction in late Holocene sediments is consistent with hazard model based predicted return times of PGAs exceeding the liquefaction triggering threshold in Christchurch. Residential development in eastern Christchurch from ca. 1860 to 2005 occurred in areas where geologic evidence for pre-Canterbury earthquake sequence liquefaction was present, highlighting the potential of paleo-liquefaction studies to predict locations of future liquefaction and to contribute to seismic hazard assessments and land-use planning.

2.1 Introduction

Cyclic shearing of loosely compacted and fluid-saturated sediments during earthquake induced ground motion results in excess pore-water pressures and reduced shear strength in the affected media. Sediment transitions to a liquefied state as excess pore-water pressures exceed the static confining pressure, causing large strains and flowage of the sediment, and breakdown of the grain arrangement (Seed and Idriss, 1982; Idriss and Boulanger, 2008). Liquefied sediment may be ejected to the ground surface via feeder dikes that commonly utilize fractures in the sedimentary cover overlying the liquefied stratum. Surface ejecta commonly manifests as sand blows, blistering of the surface by near-surface sediment injection, and vertical (subsidence) and/or lateral (lateral spreading) ground deformation (Seed and Idriss, 1982; Sims and Garvin, 1995; Tuttle and Barstow, 1996; Obermeier, 1996; Galli, 2000; Idriss and Boulanger, 2008; Cubrinovski and Green, 2010; Tuttle and Hartleb, 2012; Quigley et al., 2013). Surface liquefaction features may be rapidly (i.e., within hours to months) reworked into forms that are difficult to distinguish from aeolian, fluvial, or estuarine deposits (Sims and Garvin, 1995; Reid et al., 2012; Quigley et al., 2013) complicating the geologic identification of pre-historic features. However, sub-surface liquefaction features such as dikes, laterally injected sills, and other injection features are commonly present in the

geologic record where host sediments are preserved, enabling the detection of historic or pre-historic (i.e., paleo-liquefaction) events (Obermeier, 1996; Obermeier et al., 2005; Tuttle et al., 2006). Paleo-liquefaction features ranging in age from 10^2 yr (Sims and Garvin, 1995) to several 10^8 yr (Loope et al., 2013) have been identified from geologic investigations.

Paleo-liquefaction provides evidence for paleo-earthquakes with site-specific strong ground motions and shaking durations that exceeded threshold values for liquefaction (Green et al., 2005). Analysis of paleo-liquefaction features preserved in the geologic record may enable recurrence intervals, ground motions, and magnitudes of the paleo-earthquakes to be estimated (Obermeier et al., 1991; Obermeier, 1996; Tuttle et al., 2002; Green et al., 2005; Tuttle and Atkinson, 2010). Paleo-liquefaction investigations rely on the accurate identification of features, interpretation of their relative ages, and constraints on the shaking intensities under which liquefaction was triggered (Obermeier et al., 1991; Sims and Garvin, 1995; Obermeier, 1996; Tuttle, 2001; Tuttle et al., 2002). The minimum peak ground acceleration (PGA) required to trigger liquefaction is typically determined for a site using site-specific geotechnical tests (i.e., Cone Penetration Tests [CPT], Standard Penetrations Tests [SPT], and Swedish Weight Sounding [SWS]) (Seed and Idriss, 1982; Idriss and Boulanger, 2008). Seismic triggering thresholds for initiating liquefaction are typically characterized using moment magnitude-weighted $PGA_{7.5}$ (Green et al., 2005; Quigley et al., 2013). A $PGA_{7.5}$ value represents the equivalent PGA for a M_w 7.5 event. This is calculated from a magnitude scaling factor (MSF) that accounts for the shaking duration and frequency content of the ground motion ($PGA_{7.5}$ = PGA x 1/MSF; Idriss and Boulanger (2008)). Recent compilations of earthquake and liquefaction data suggest a liquefaction-inducing threshold of $PGA_{7.5}$ = 0.09g (Santucci de Magistris et al., 2013), although minor liquefaction has been reported in highly susceptible sediments under $PGA_{7.5}$ as low as ∼0.06g (Quigley et al., 2013). Sedimentary (e.g., grain size, clay content)and hydrologic characteristics (e.g., water table depth) of the source sediment influence liquefaction susceptibility.

The 2010 - 2011 Canterbury earthquake sequence caused at least 10 distinct episodes of observed liquefaction in parts of eastern Christchurch, New Zealand (Quigley et al., 2013; Cubrinovski et al., 2011). The most severe liquefaction-induced damage was reported following the September 2010 M_w 7.1 Darfield main shock, and the February 2011 M_w 6.2 (i.e., 2011 Christchurch earthquake), June

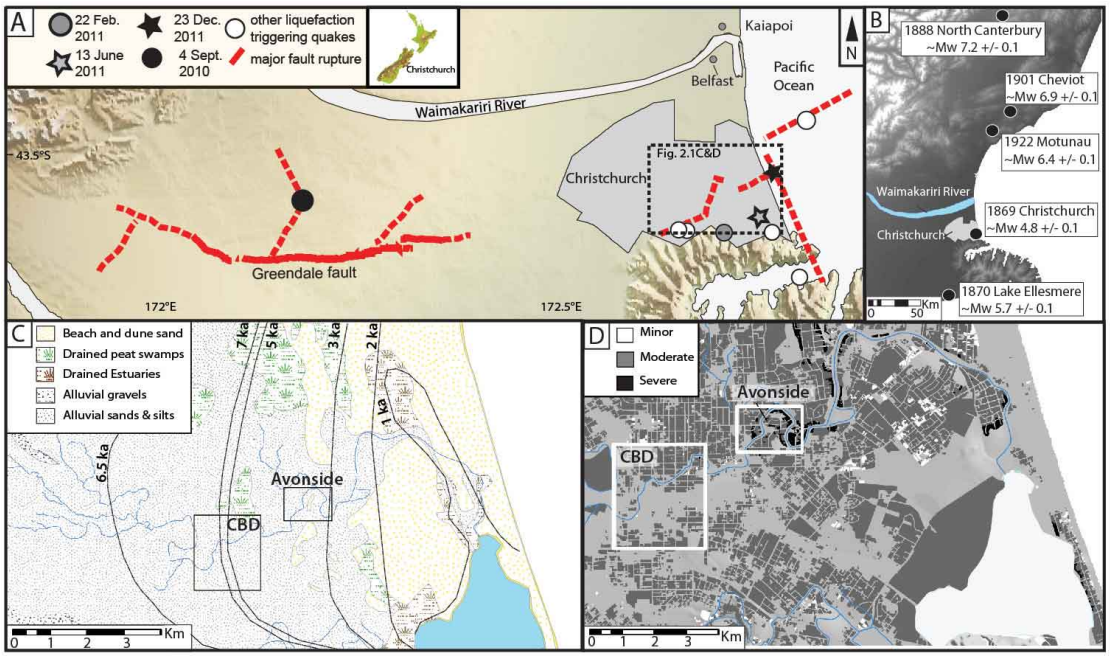

FIGURE 2.1: A) Epicentral locations of the 2010-2011 CES earthquakes that generated liquefaction within Avonside. The rupture of the Greendale fault (bold line) and projected locations of the sub-surface faults (dashed lines) that ruptured in the February, June and December 2011 aftershocks are indicated (Modified from Quigley et al. (2013)). B) The approximate epicentral locations of the five historic earthquakes causing damage within the wider Christchurch area from 1869-1922. Pre-CES liquefaction was reported in Kaiapoi and Belfast (indicated) following the 1901 Cheviot earthquake. C) Simplified geological map of the Christchurch area with the approximate locations of the 7- 1 ka b.p. shorelines indicated with respect to Avonside and the CBD (modified from Brown and Weeber (1992)). D) The aerial extent and severity of liquefaction as mapped following the 22 February 2011 earthquake.

2011 M_w 6.0, and December 2011 M_w 5.9 aftershock earthquakes (Fig. 2.1) (Cubrinovski and Green, 2010; Cubrinovski et al., 2011; Quigley et al., 2013). As a result of extensive land and infrastructure damage, more than 6000 residential properties in eastern Christchurch were purchased by the central government (http://cera.govt.nz/residential-red-zone). Recent estimates of post-insurance pay out losses exceed NZ 1 billion dollars (U.S.D 800 million; http://www/stuff/co.nz /national/christchurch-earthquake/865545/Govt-faces-1billion-redzone shortfall). Understanding the timing, location, magnitude, and frequency of liquefaction inducing earthquakes in Christchurch thus has the potential to inform land-use planning decisions and make contributions to seismic hazard modeling (e.g., Stirling et al. (2012)).

Pre-Canterbury earthquake sequence liquefaction was reported in Kaiapoi and

Belfast (Fig. 2.1B) following the 1901 M_w 6.8 Cheviot earthquake (Berrill et al., 1994). No pre-Canterbury earthquake sequence liquefaction had been recorded in Christchurch. In this chapter, the sub-surface morphology of Canterbury earthquake sequence liquefaction features are described for two study sites, with the goals of (1) documenting how this earthquake sequence is manifested in the geologic record, and (2) characterizing the source layer of contemporary liquefaction. New stratigraphic and chronologic evidence for previously undocumented pre-Canterbury earthquake sequence liquefaction in eastern Christchurch is also presented.

2.2 Geologic setting

2.2.1 Christchurch Area

The city of Christchurch (population ∼360,000) is primarily situated upon a low-relief and low-elevation alluvial landscape (0-20 m above sea level) on the east coast of New Zealands South Island (Fig. 2.1). The city and eastern suburbs are predominantly underlain by drained peat swamps, fluvial sands and silts, and estuarine, dune, and foreshore sands (Fig. 2.1C) (Brown and Weeber, 1992). Channelized gravels in the uppermost several meters are typically attributed to deposition by the braided Waimakariri River that intermittently avulsed through the city prior to European settlement (Fig. 2.1) (Cowie, 1957; Brown and Weeber, 1992). To the west of the central city, fluvial sands and gravels predominate (Fig. 2.1C).

The sediments in eastern Christchurch were deposited by shoreline progradation and marine regression following the mid-Holocene highstand with shorelines recorded ∼3 km west of the present central city at ∼6500 yr B.P. (Fig. 2.1C) (Brown and Weeber, 1992). The fluvial sands and silts reflect deposition by the meandering Avon and Heathcote Rivers within the city (Fig. 2.1C). The youthful, unconsolidated nature of the fine sands to silt underlying eastern Christchurch combined with high water tables (1-2 m depth) and localized artesian water pressures pose a long-recognized high liquefaction hazard (Elder et al., 1991). This was confirmed during the Canterbury earthquake sequence (Cubrinovski and Green,

2010). Liquefaction may also have been exacerbated in parts of the eastern suburbs by leakage of underlying artesian aquifers through breached aquitards (Cox et al., 2012).

2.2.2 Avonside Study Area

The study area of Avonside, eastern Christchurch experienced severe liquefaction-induced damage during the Canterbury earthquake sequence (Fig. 2.1D). Avonside is encompassed within an inner meander bend of the Avon River, which undergoes tidally influenced flow inversions (Fig. 2.1C). The suburb is underlain by fine sand and silt of point bar and over bank deposits of the Avon River, along with coastal swamp and sand dune deposits (Fig. 2.1C) (Silby, 1856; Brown and Weeber, 1992). Localized channelized gravels that are present at ∼2 m depth may be related to historic floods of the Waimakariri River through this area prior to European settlement (Silby, 1856; Brown and Weeber, 1992). The position of the ∼5000 yr. B.P. coastline was ∼3 km to the west, and the ∼3000 yr. B.P. coastline was ∼0.5-1 km east of the study sites (Fig. 2.1C) (Brown and Weeber, 1992). The modern coastline is located ∼5 km to the east (Fig. 2.1C). The water table is located between 1 and 2 m depth; however, it can rise to ∼0.5 m depth during wet periods (Brown and Weeber, 1992).

Two sites were chosen for trenching to investigate the morphology and stratigraphic relationships of the Canterbury earthquake sequence and pre-Canterbury earthquake sequence liquefaction features in the sub-surface (Fig. 2.2A): Sullivan Park (Site 1; Fig. 2.2B), and the former site of a residential property at 11 Bracken Street (Site 2; Fig. 2.2D). Site 1 was selected based on the intensity of lateral spreading cracks and lack of near-surface anthropogenic influence on the spatial distribution of liquefaction (Fig. 2.2C). Site 2 was selected as it was continuously monitored by Quigley et al. (2013) during the Canterbury earthquake sequence (Fig. 2.2E). Calibration of the observations for the occurrence and non-occurrence of liquefaction with nearby accelerometer measurements of PGA enabled a $PGA_{7.5}$ liquefaction triggering threshold to be established for the susceptible sediments at Site 2 of $PGA_{7.5}$ ∼0.06g (minor liquefaction) to $PGA_{7.5}$ 0.12g (major to severe liquefaction; for a full description of $PGA_{7.5}$ derivation methodology for this study site, see Quigley et al. (2013).

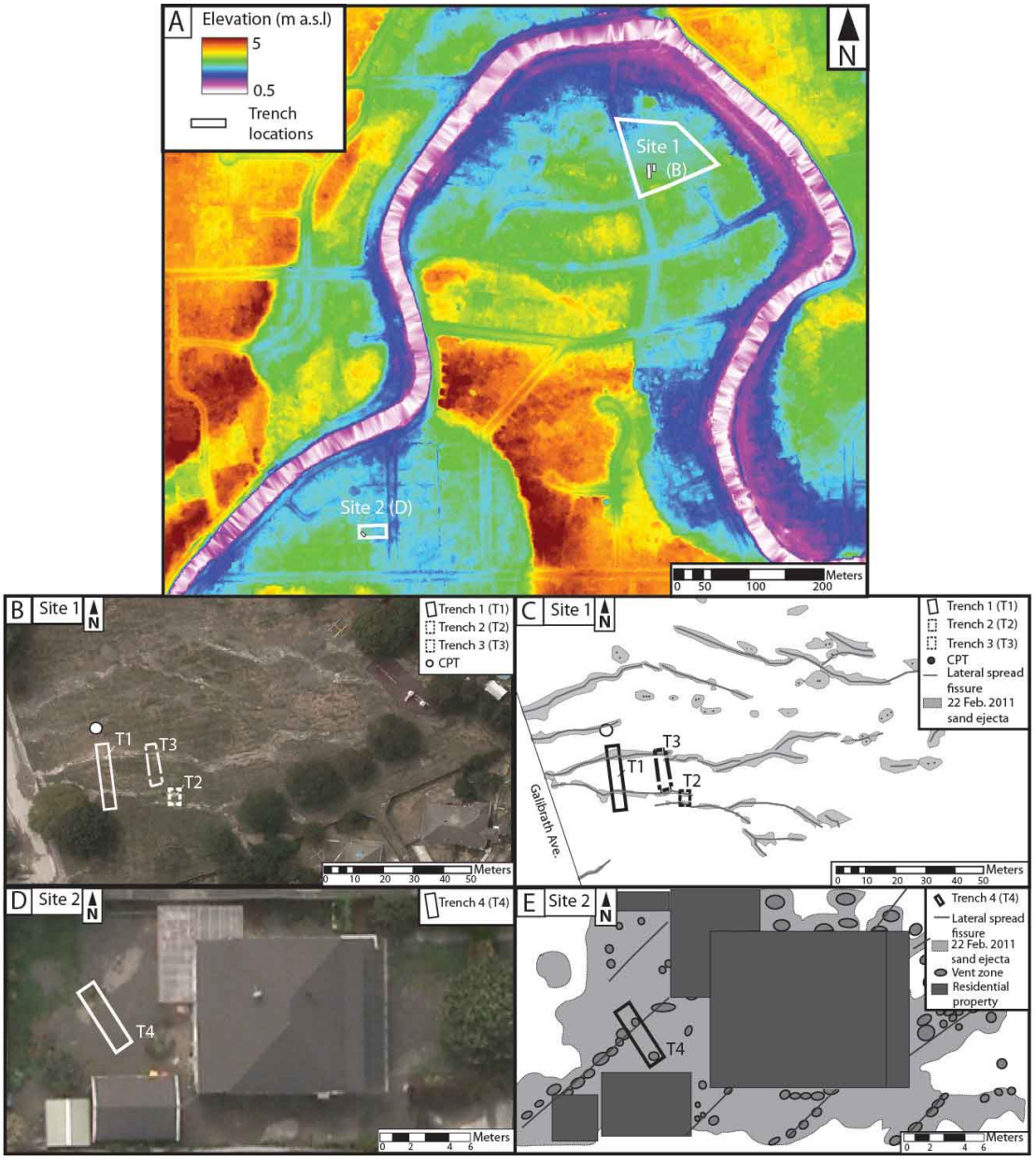

FIGURE 2.2: A) 0.5 m DEM of Avonside with the location of the two study sites indicated. B) Uninterrupted aerial photograph of Site 1 following the February 2011 earthquake with the location of the trenches and CPT indicated. C) The mapped distribution of liquefaction features, trenches and CPT at Site 1. C) Uninterrupted aerial photograph of Site 2 following the February 2011 earthquake with the trench location indicated. D) The mapped distribution of liquefaction ejecta following the February 2011 earthquake with the location of the trench and residential dwelling indicated (modified from Quigley et al. (2013)).

2.3 Methods

2.3.1 Trenching

The sub-surface morphology of the Canterbury earthquake sequence and prior liquefaction features were documented using well-established criteria for identifying earthquake-induced liquefaction features, including analysis of aerial photography, trenching, and dating of sub-surface deposits (Sims, 1975; Obermeier et al., 1991; Obermeier, 1996; Tuttle, 2001). Documentation of the sub-surface features that fed known Canterbury earthquake sequence surface vents, and comparison with published photographs of sub-surface liquefaction features aided the identification and interpretation of other liquefaction features that pinched out beneath the surface (Obermeier et al., 2005; Tuttle, 2001; Counts and Obermeier, 2012). High resolution aerial photographs flown on 24 February 2011 by NZ Aerial Mapping for the Christchurch Response Centre were examined to identify the distribution of features at each site (Fig. 2.2). Trenches were excavated perpendicular to aligned sand blow vents and lateral spreading fissures at both sites (Fig. 2.2). Trench walls were cleaned using handheld scrapers and then photographed and logged at centimeter scale to document small-scale changes in the morphology of the liquefaction features and the surrounding stratigraphy. The trench floor was also logged at several locations of interest at Site 1 (Fig. 2.3A). The documentation of Canterbury earthquake sequence liquefaction features and their relationship with the surrounding sediment enabled prior liquefaction features to be identified within the stratigraphy. The liquefaction features and the surrounding stratigraphy were described in terms of their grain size, sorting, color, and degree of sediment mottling. Full sediment descriptions of each unit are presented in Appendix A. Two hand-augered holes at Site 1 were excavated to 2.5 m depth, where the sediment became cohesionless and failed to be retained within the auger head.

2.3.2 Radiocarbon Dating

The ages of the pre-Canterbury earthquake sequence liquefaction features and trench stratigraphy were constrained from radiocarbon dating of detrital wood fragments obtained from key stratigraphic horizons. Samples were dried at 40 °C

for 1 week and then sorted to separate the organic material from the host sediment. Between 10 and 20 mg samples of organic material were submitted to the Rafter Radiocarbon Laboratory in Wellington, New Zealand, for accelerator mass spectrometry (AMS) radiocarbon analysis. Samples were prepared for analysis by sub-sampling, picking, and grinding of the wood fragments, and repeated acid and alkali treatment, after which they were combusted and converted to graphite by reduction with hydrogen over iron catalyst. Ages were calibrated using the Southern Hemisphere calibration curve (SHCAL04) (McCormac et al., 2004). The radiocarbon ages referred to in the text are reported as 2 sigma calendar calibrated age ranges. The uncalibrated conventional radiocarbon ages and detailed age range distributions of the calendar calibrated ages are presented in Table 2.1. Detailed descriptions of the calibrated age ranges are presented in Appendix C.

2.3.3 Optically Stimulated Luminescence Dating

Two sediment samples were collected from Site 1 for optically stimulated luminescence (OSL) dating to further constrain the likely depositional ages of the trench stratigraphy. Sampling was conducted by pushing 5-cm-diameter stainless-steel tubes into cleaned sections of the trench wall. Samples were dated by infrared stimulated luminescence (IRSL) of the polymineral fine grain fraction (4-11 mm) using a Riso TL-DA-15 with an infrared diode array at the OSL facility at the University of Victoria, Wellington, New Zealand. The equivalent dose was determined in the blue spectral band (filters BG39+Kopp 5-58) by the single aliquot additive dose method with late light subtraction (SAR method) (Aitken, 1998). The multiple aliquot additive dose method (MAAD) was applied to determine the dose rate. Radionuclide contents of ^{238}U, ^{232}Th, and ^{40}K, a values, and water content were measured from a sample aliquot. Samples were stored for 3 weeks after irradiation, a 5 minute preheat was then applied to isolate the stable signal component. After 6 months of storage, samples were subjected to a fading test. All measurements were conducted at room temperature (Aitken, 1998). Optical ages are presented in Table 2.2. The OSL technical report is presented in Appendix D.

2.3.4 Geotechnical Testing

A CPT (Cone Penetration Test) was conducted ∼20 m north of trench 1 at Site 1 to a depth of 20 m (Fig. 2.2B). The CPT measures the resistance of the sub-surface sediments to an instrumented cone being pushed at a constant rate (Idriss and Boulanger, 2008). The relative resistance of the sub-surface sediments acts as a proxy for the sub-surface properties and for delineating stratigraphy. The CPT is commonly applied to determine the liquefaction susceptibility of a given area due to its rapid testing times, continuous recording, high accuracy, and the repeatability of the test (Idriss and Boulanger, 2008).

The liquefaction potential of the sub-surface strata was evaluated from the CPT using the Idriss and Boulanger (2008) method. This method establishes the liquefaction potential by comparing the cyclic stress ratio (CSR), which evaluates loading induced at different depths by an earthquake, with the cyclic resistance ratio (CRR), which represents the ability of the soil to resist liquefaction. The likelihood that a soil will liquefy is expressed as a factor of safety against liquefaction (FS), where FS <1 is considered potentially liquefiable. The results of the CPT sounding were correlated with the stratigraphy to 2.5 m depth, as determined from the trench and hand auger. This enabled the possible depth of the liquefied source sediment to be constrained. The Boulanger and Idriss (2014) methodology was not employed as this analysis was conducted prior to its publication.

2.4 Site 1: Sullivan Park

Sullivan Park is located centrally within Avonside and within 50 m of the Avon River (Fig. 2.2). The park has almost flat topography with elevations of 1.5 - 2 m above sea level across the site (Fig. 2.2). Analysis of the post-February 2011 aerial photography indicates that lateral spreading-induced fissuring and associated sand blows formed across the site during the Canterbury earthquake sequence (Fig. 2.2C). Three trenches (T1-T3) were excavated perpendicular to the axis of two lateral spreading fissures to lengths of ∼18 m (T1), ∼6 m (T2), and ∼8 m (T3) and a depth of ∼1.5 m (Fig. 2.2B). The trench excavation depth was limited to ∼1.6 m by the depth of the water table. Two hand-augered holes were excavated in T1 and T2 (A1 and A2, respectively) to a depth of 2.5 m. The trench and auger

logs are presented in Figures 2.3, 2.4, 2.5, and 2.7, and selected field photographs are presented in Figures 2.6 and 2.8. The CPT data is presented in Figure 2.9.

2.4.1 Trench Fluvial Stratigraphy

The three trenches (T1-T3; Figs. 2.3, 2.4, and 2.5) exposed stratigraphy composed of a plastic silt (unit III) with interbedded lenses of fine to medium sand (unit IV), overlain by normally graded beds of fine sand to silt (unit IIa-e). The stratigraphy is capped by ∼20 to 50 cm of topsoil (unit I; Appendix 1). The two hand augers (A1-A2) indicate that the plastic silt (unit III) is underlain by medium sand (unit V), and a granule to pebble horizon (unit VI) at ∼2 to 2.5 m depth (Figs. 2.3D and 2.4D; Appendix 1).

Interpretation of Depositional History

The medium sand (unit V) and granule to pebble bed (unit VI) are coarser than the overlying stratigraphy and are consistent with deposits within the active floodplain of the Waimakariri River (Fig. 2.3D). Units V and VI are therefore interpreted to most likely represent crevasse splay deposits from a pre-European flood event of the Waimakariri River (Brown and Weeber, 1992). The overlying plastic silt (unit III) was likely deposited in a marsh or oxbow lake adjacent to the meandering Avon River that periodically received sediment during flood events, as indicated by the interbedded lenses of fine to medium sand (unit IV). The normally graded beds of fine sand to silt (unit IIa-e) exposed in T1-T3 (Figs. 2.3, 2.4, and 2.5) are interpreted as over bank flood deposits from the nearby Avon River. The stratigraphy is consistent with the pre-European (i.e., pre-mid-nineteenth century) avulsion of the Avon River across the site and the historical reports of periodic flooding of the Avon River during periods of heavy rain between 1865 and 1953 (Cowie, 1957). Unit I is interpreted as a topsoil horizon. There are no well documented rates of soil formation for the Christchurch region due to the varied land uses throughout the development of the city, and so no surface age may be inferred from the topsoil thickness.

Radiocarbon dating of two sub-rounded wood fragments obtained from unit II in T3 at depths of 0.8 m (S1) and 0.9 m (S2) yielded ages of 2858-2493 B.C. (S1) and A.D. 1660-1803 (S2), respectively (Fig. 2.5; Table 2.1). Two small, sub-rounded wood fragments were also obtained from unit III in T1 from depths of

1.4 m (S3) and 1.55 m (S4). The samples yielded predominant ages of A.D. 1229-1276 (S3) and A.D. 665-765 (S4) respectively (Fig. 2.3B; Table 2.1). S1 yielded a complicated age spectra (Table 2.1) with a mean age significantly older than the bounding strata suggesting that the dated material may be reworked detritus;

it is therefore excluded from further discussions. S2, S3, and S4 all were small, sub-rounded wood fragments that lacked root-like geometries or lateral continuity. These ages are interpreted to approximate the depositional age of the sediment due to the consistency between the reported ages of S2-4. Therefore, the ages indicate that the trench stratigraphy was most likely deposited over a maximum period from ca. A.D. 665 to present.

OSL dating of two samples obtained from the unit II in T1 from depths of 0.86 m (O1) and 1.05 m (O2) yielded ages of 838 B.C. (±210 yr) and 818 B.C. (±210 yr), respectively (Fig. 2.3B; Table 2.2). During testing, it was observed from experimental data that these samples were composed of bleached and partially bleached sand and therefore were not sufficiently exposed to light prior to re-deposition (N. Wang, 2013, personal commun.). These ages are interpreted to reflect maximum ages, with the depositional ages of the host sediment possibly much younger.

2.4.2 Trench Anthropogenic Stratigraphy

The fluvial stratigraphy exposed in T1-T3 is crosscut by anthropogenic pits, ∼20-100 cm wide and ∼20-90 cm deep, with sub-vertical walls (Figs. 2.3, 2.4, and 2.5). The pits contain silt (unit PF, for pit fill) with irregular lenses of carbonaceous silt (5-10%), oxidized whole and fragmented lamb fetlock bones, fern mats, and fragments of ground-up and burnt bone (Fig. 2.6A; Appendix A). The lenses of burnt bone are surrounded by an oxidation front in unit III (Fig. 2.6D).

T1 (Fig. 2.3A) is crosscut by multiple anthropogenic pits (P1-P4, and P8). P1-P3 exhibit internal lensoidal stratigraphy and crosscut the fluvial stratigraphy from ∼20 to ∼70 cm depth to the trench floor. P4 (Fig. 2.3A) underlies and is separated from P3 by ∼20 cm of unit II; it is composed of unit PF with rare fragments of oxidized bone and fern mat. A fifth pit (P8) was exposed as the west wall of T1 was cut back by ∼50 cm; it contains unit PF with no internal lenses (Fig. 2.3C). Excavation of P3, P4, and P8 in plan view indicates that these pits comprise a

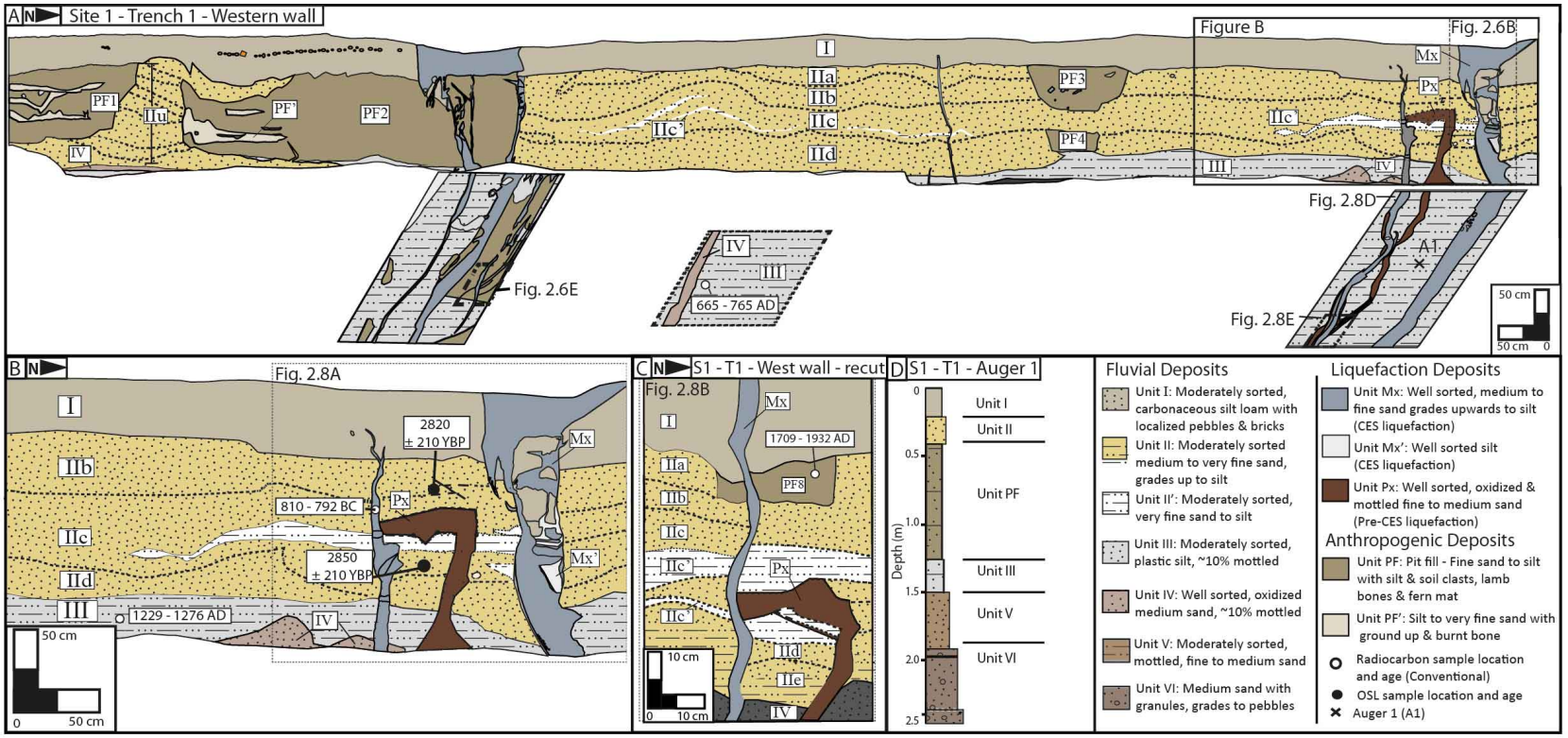
A N Site 1 - Trench 1 - Western wall
Figure B
Fig. 2.6B
PF1
IIu
PF
PF2
IV
I
IIa
IIb
IIc
IIc'
IIc'
IIc'

TABLE 2.1: Radiocarbon data and age estimates

Sample No.	Depth (m)	Locality	Description	δ13C and Source of measurement	Radiocarbon Age (years BP)	Calendar calibrated age	
						2σ	1σ
S1	0.8	Trench 3 Site 1	Wood fragment from fluvial sand (Unit IIc)	-26.4±0.2	4126±25	2858 - 2807 BC (17.1% of area) 2752 - 2719 BC (5.8% of area) 2701 - 2562 BC (64.1% of area) 2531 - 2493 BC (7.8% of area)	2834 - 2814 BC (10.6% of area) 2670 - 2571 BC (55.7% of area) 2509 - 2504 BC (1.7% of area)
S2	0.9	Trench 3 Site 1	Wood fragment from fluvial sand (Unit IId)	-27.1±0.2	220±9	1660 - 1684 AD (17.3% of area) 1730 - 1803 AD (77.4% of area)	1669 - 1675 AD (6.9% of area) 1739 - 1787 AD (56.2% of area) 1793 - 1798 AD (5.9% of area)
S3	1.4	Trench 1 Site 1	Wood fragment from basal silt (Unit III)	-32.3 ± 2.0	813±8	1229 - 1276 AD	1203 - 1295 AD
S4	1.55	Trench 1 Site 1	Wood fragment from basal silt (Unit III)	-24.9±0.2	1364±15	665 - 694 AD (46.6% of area) 705 - 706 AD (0.9% of area) 749 - 765 AD (20.2% of area)	660 - 721 AD (68.1% of area) 742 - 770 AD (26.7% of area)
S5	0.2	Trench 1 Site 1	Fern sample from pit	-22.3±0.2	111±4	1709 - 1721 AD (4.7% of area) 1811 - 1838 AD (29.9% of area) 1847 - 1859 AD (2.9% of area) 1863 - 1866 AD (0.6% of area) 1880 - 1932 AD (56.5% of area)	1817 - 1830 AD (22.2% of area) 1894 - 1921 AD (46.2% of area)
S6	1.8	Pit 9 Site 1	Charcoal sample from Pit 9	-26.4±0.2	815±20	1223 - 1279 AD	1230 - 1252 AD (41.9% of area) 1261 - 1275 AD (27.7% of area)
S7	1.15	Trench 1 Site 1	Wood fragment from in CES dike	-26.5±0.2	2683±16	810 - 792 BC	828 - 779 BC
S8	0.5	Trench 4 Site 2	Wood fragment from silt loam	-26.3±0.1	545±18	1415 - 1435 AD	1408 - 1442 AD
S9	1.1	Trench 4 Site 2	Wood fragment from silt loam	-23.7 ±0.1	606±18	1330 - 1331 AD (1.3% of area) 1392 - 1412 AD (65.8% of area)	1324 - 1346 AD (21.6% of area) 1389 - 1418 AD (73.1% of area)

corner of a larger pit (P9) that extends from ∼20 cm to 1.8 m depth and is capped by an iron lid (Fig. 2.7). The intervening bed of unit II between P3 and 4 (Fig. 2.3A) was not observed during excavation of P9. It is possible that the relationship observed on the wall of T1 reflects an irregularly dug wall or collapse of the corners of the larger pit into the surrounding fluvial sediment. T2 is crosscut by two pits (P5 and P6; Figs. 2.4 and 2.6A), and T3 is crosscut by one pit (P7; Fig. 2.5), all of which are composed of unit PF and exhibit internal lensoidal stratigraphy.

Interpretation of Anthropogenic History

A wool scouring factory operated adjacent to Site 1, and historical photographs place the park within the property boundaries of the factory (Bremer, 1985). The history of the wool scouring industry within Avonside is poorly documented; however, it is known that the Avonside scouring factory opened shortly after the Woolston scoury was established in A.D. 1864, with activity continuing at the site until ca. 1905 (Bremer, 1985). Cesspits are reported as being in use during production in an attempt to reduce pollution in the Avon River (Bremer, 1985). The anthropogenic pits identified in T1-T3 (Figs. 2.3, 2.4, 2.5, and 2.6A) are interpreted as cesspits due to the irregular pit walls and internal stratigraphy consistent with intermittent shovelling of waste (Fig. 2.7). The presence of only fetlock bones further supports that these are cesspits, as fetlock bones were not removed during skinning and therefore would have been disposed of on site (Bremer, 1985). It is likely that the pits in T2 (P5-P6; Figs. 2.4 and 2.6A), T3 (P7; Fig. 2.5), and P1-P2 in T1 (Fig. 2.3A) also comprise sections of other large cesspits; however, this cannot be confirmed, as these pits were not excavated in plan view.

The anthropogenic pits crosscut the fluvial stratigraphy from ∼20 cm depth, indicating that excavation of these pits post-dated deposition of the fluvial stratigraphy beneath 20 cm. The recorded timing of production at the factory is consistent with a radiocarbon age of A.D. 1709-1932 obtained from a fern mat exposed in P8 (S5; Fig. 2.3C; Table 2.1). A charcoal fragment obtained within P9 at 1.8 m depth (S6) yielded a radiocarbon age of A.D. 1223-1279 (Fig. 2.7; Table 2.1). The reported age is inconsistent with the reported timing of production at the factory suggesting that it may be derived from reworked detritus.

TABLE 2.2: Optically Stimulated Luminescence data and age Estimates

Sample No.	Depth (m)	Locality	Water[a] (%)	Radionuclide concentrations					α-value	Cosmic Dose Rate (Gy/ka)	De (Gy/)	Dose Rate (Gy/ka)	Optical age (Y.B.P)
				K (%)	Th[b] (ppm)	U[c] (ppm)	U[d] (ppm)	U[e] (ppm)					
O1	1.05	Trench 1	21.2	2.22	10.88	3.00	3.02	3.66	0.13	0.1797	13.21	4.64	2850
		Site1		±0.05	±0.18	±0.37	±0.22	±0.32	±0.01	±0.0090	±0.57	±0.28	±210
O2	0.86	Trench 1	21.2	2.24	10.54	3.42	2.99	3.32	0.09	0.1845	11.95	4.24	2820
		Site 1		±0.05	±0.14	±0.26	±0.15	±0.23	±0.01	±0.009	±0.62	±0.23	±210

[a]estimated time-averaged moisture contetns, based on measured field water vales (% dry weight)
[b]From ^{208}Tl, ^{212} Pb , ^{228} Ac
[c]From ^{234}Th
[d]From ^{226}Ra, ^{214}Pb, ^{214}Bi
[e]From ^{210}Pb

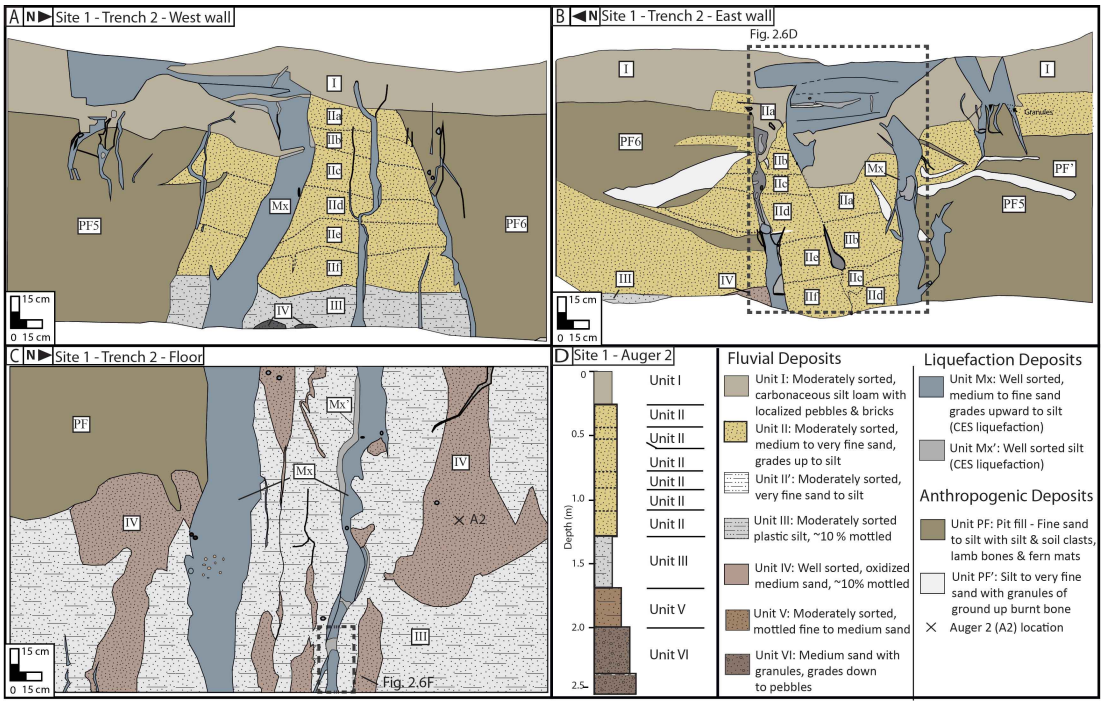

FIGURE 2.4: Detailed trench log of the west (A) and east (B) walls, and floor (C) of T2 (Site 1). The location of auger 2 (A2) is also indicated. The Canterbury earthquake sequence (CES) liquefaction dikes (Mx) crosscut the fluvial stratigraphy (IIII) and anthropogenic cesspits (PF5-PF6) from the trench floor to surface. Small CES dikes (∼10 cm long; Mx) are observed to originate within PF5 (A). D) Auger 2 (1.5-2.5 m) indicates that the stratigraphy is underlain by moderately sorted fine to medium sand (unit V) that contains granules to pebbles (unit VI) from 2.3 to 2.5 m depth.

2.4.3 Canterbury Earthquake Sequence Liquefaction Features

Canterbury earthquake sequence liquefaction features were recognized in the subsurface by (1) their alignment with and traceable continuity into the observed surface Canterbury earthquake sequence sand blows and fissures and (2) their crosscutting relationship with the fluvial and anthropogenic stratigraphy. These liquefaction features were documented in detail in order to record the morphologies of sub-surface liquefaction and assist with the identification and interpretation of pre-Canterbury earthquake sequence liquefaction features. The Canterbury earthquake sequence liquefaction features all consist of gray, well-sorted, fine to medium sand, unless otherwise stated, and lack the oxidation and mottling developed in the surrounding stratigraphy.

Canterbury Earthquake Sequence Lateral Spreading Fissures

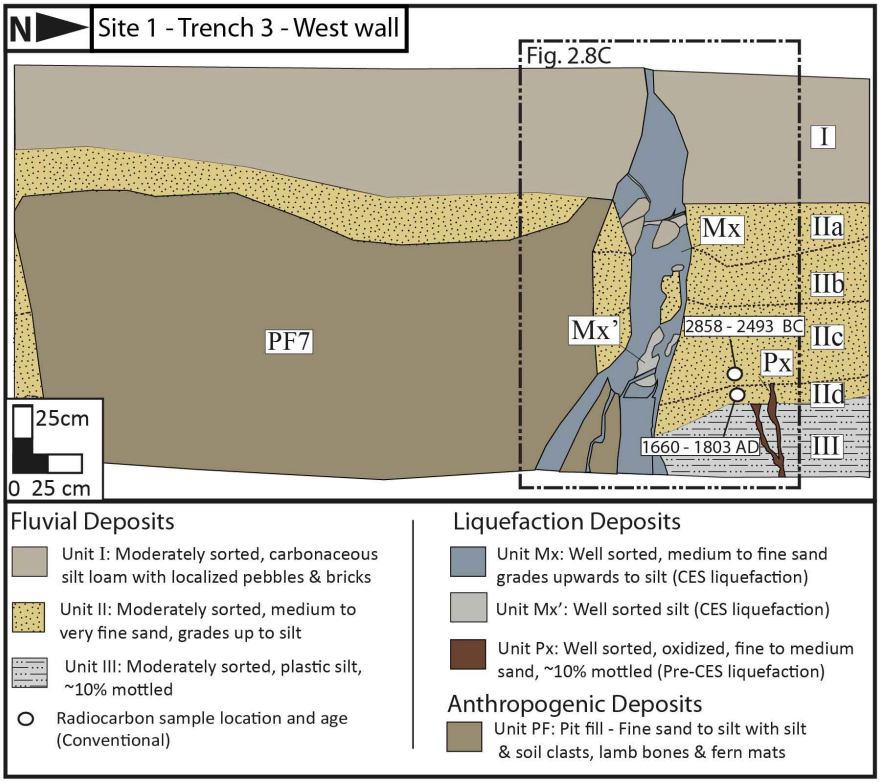

FIGURE 2.5: Detailed trench log of the west wall of T3. The CES liquefaction dike (Mx) crosscuts the fluvial (I-III) and anthropogenic (P7) stratigraphy from the trench floor to the surface. The pre-Canterbury earthquake sequence dike (Px) crosscuts the fluvial stratigraphy (I-III) from the trench floor to ~90-95 cm depth. The location and results of the ^{14}C samples are also indicated.

The large (>50 cm in width) lateral spreading fissure intersected in T1 and T2 (Fig. 2.2B) is bounded by inward-dipping fractures in the sub-surface, forming a graben (Figs. 2.3A and 2.6C). The grabens in T1 (Fig. 2.3A) and on the east wall of T2 (Figs. 2.4B and 2.6D) are bounded by two sub-vertical, planar dikes, ~2-35 cm wide, that down-drop the stratigraphy by ~30-40 cm. The fissure can be traced across the floor of T2 where the bounding dikes are composed of medium sand with granules to pebbles (5-10%) of oxidized sandstone (Fig. 2.4C). The fissure aligns with a ~20-cm wide, sub-vertical, planar dike on the west wall of T2 (Fig. 2.4A).

Canterbury Earthquake Sequence Liquefaction Dikes

The smaller lateral spreading fissure (<50 cm in width) intersected in T1 and T3 (Fig. 2.2B) corresponds with ~25-cm wide, sub-vertical, planar dikes in the sub-surface that crosscut the fluvial and anthropogenic stratigraphy and feed into the surface fissure. The dikes decrease in width and fine upward (Figs. 2.3A, 2.6B,

and 2.6C). The dike in T1 contains down-dropped clasts of topsoil ∼5-15 cm in diameter (Figs. 2.3A and 2.6B), while the dike in T3 contains incorporated clasts of topsoil and unit PF ∼5-10 cm in diameter (Fig. 2.6C).

Smaller sub-vertical, planar dikes, ∼5-10 cm wide in T1-T3, crosscut the stratigraphy from the trench floor to 10 cm depth, where they pinch out; they are composed of fine sand to silt (Figs. 2.3A, 2.4A, 2.5, and 2.6A). Silt layers, ∼1-2 mm thick, are observed along the dike margins (Fig. 2.6B) and internally within the dikes, where they separate two units of fine sand (Fig. 2.6F). Lateral grading from fine sand to silt is also observed within the ∼5-10 cm wide dike on the floor of T2 (Figs. 2.4C and 2.6F). Dikes ∼1-2 cm wide and 10-40 cm long were observed to originate within the pit fill (unit PF) on the west wall of T2 (Figs. 2.4A and 2.6A). These small dikes terminate beneath the surface, are composed of silt, and increase in width with depth.

The dikes identified in T1-T3 crosscut the fluvial and anthropogenic stratigraphy from the trench floor to between 0-10 cm depth (Figs. 2.3, 2.4, and 2.5). This indicates that formation of these dikes post-dated deposition of the lower (beneath 10 cm) stratigraphy. The dikes that reach the surface feed into the Canterbury earthquake sequence liquefaction fissures and sand blows (Figs. 2.3, 2.4, 2.5, and 2.6), confirming that they formed during the Canterbury earthquake sequence. The similar morphology, composition, and lack of mottling and oxidation of the dikes that pinch out beneath the surface indicate that they are also of Canterbury earthquake sequence age. A detrital wood fragment obtained from within a ∼5-cm wide dike at ∼1.15 m depth in T1 yielded a radiocarbon age of 810-792 B.C. (S7; Fig. 2.3B; Table 2.1). This is interpreted to reflect the maximum depositional age of the liquefied sediment source.

Interpretation of Canterbury Earthquake Sequence Liquefaction Features

The alignment of the sub-surface grabens and dikes with the surface fissures indicates that these features represent lateral spreading fissures in-filled by liquefied sediment. The increasing width of the dikes with depth suggests that these features formed by the upward injection of sediment, as opposed to downward-propagating surface cracking, in which features would be expected to decrease in width with depth (Figs. 2.3, 2.4A, 2.4B, and 2.5) (Counts and Obermeier, 2012). Individual dikes range in width from ∼2 to 50 cm (Fig. 2.3, 2.4, 2.5, and 2.6A). These varied widths likely reflect complexities in the three-dimensional dike geometries

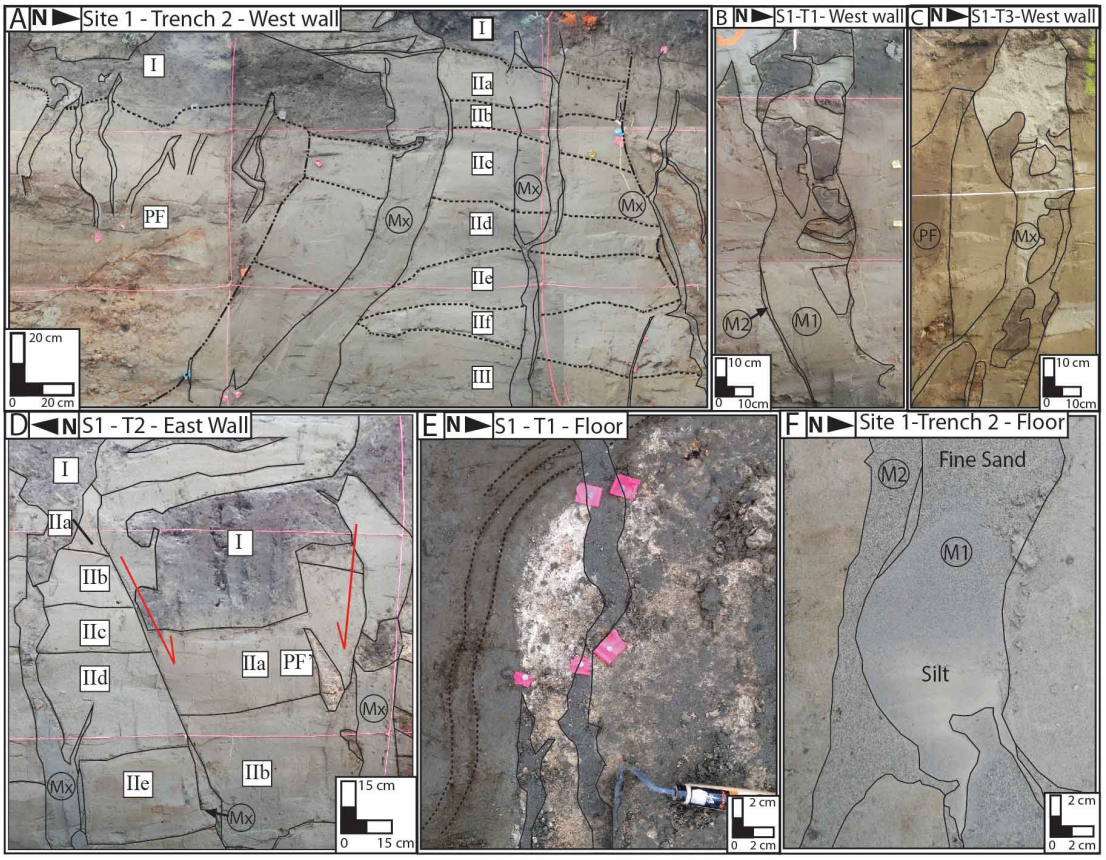

FIGURE 2.6: A) Interpreted field photograph of the west wall of T2 (Site 1). The fluvial stratigraphy (III and outlined in black dotted line) and anthropogenic cesspits (PF and outlined in black lines and dots) are crosscut by Canterbury earthquake sequence liquefaction features (Mx and outlined in black solid lines). (B) The ~25-cm wide lateral spreading fissure at the north end of T1 contains down-dropped topsoil clasts and a dike-parallel silt lining that separates two Canterbury earthquake sequence events (M1 and M2). (C) The ~25-cm wide lateral spreading fissure at the north end of T3 contains down-dropped clasts of topsoil and unit PF. (D) The ~50-cm wide lateral spreading fissure on the east wall of T2 forms a graben that down-drops the fluvial stratigraphy (I-III) by ~40 cm and is bounded by liquefaction dikes (Mx). (E) The lens of white bone fragments on the floor of T1 is surrounded by an oxidation front (dotted black line) and is crosscut by Canterbury earthquake sequence dikes (outlined in black). (F) The ~7-cm wide dike on the floor of T2 exhibits 12-mm-thick, dike-parallel silt lining and internal silt lining (outlined in black), suggesting that two Canterbury earthquake sequence events are preserved within the one dike (M1 and M2). M1 also exhibits intra-dike sorting fining from fine sand to silt.

resulting from interactions with host sediment, variations in lateral spreading, and differing source depths.

The predominately gray, well-sorted, fine to medium sand comprising the <50-cm wide Canterbury earthquake sequence dikes is consistent with the fine to medium

sand of unit V identified in A1, suggesting that it may be sourced from this unit (Fig. 2.3D). The medium sand with localized granules of oxidized sandstone comprising the >50-cm wide Canterbury earthquake sequence dike on the floor of T2 (Fig. 2.4C) is consistent with unit VI identified in A1 at 2.2-2.8 m depth (Figs. 2.3D and 2.4D). The CPT sounding (Figs. 2.2B and 2.9) indicates that the stratum from 1.5 to 2.2 m depth (unit V in A1; Fig. 2.3D) was potentially liquefiable under the ground accelerations generated in the 2010 Darfield earthquake, and the February 22_{nd} 2011 Christchurch earthquake (FS <1). The underlying stratum from 2.2 to 2.8 m (unit VI) was not liquefiable during the Canterbury earthquake sequence; however, the unit at 2.8-3 m was potentially liquefiable in the February 2011 earthquake (Fig. 2.9). Therefore, the CPT supports the interpretation that the smaller Canterbury earthquake sequence dikes were likely sourced from unit V, while the >50-cm wide dike was likely sourced from the unit at 2.8-3 m depth, and likely entrained granules from unit VI during ejection. As the unit at 2.8-3 m was only liquefiable during the February event, the larger dike likely formed during this event. This indicates that the higher shaking intensities that occurred during the February 2011 event triggered liquefaction at greater depths than the other Canterbury earthquake sequence events.

The well-sorted and fining-upward nature of the medium to fine sand to silt within the dikes indicates that sediment sorting occurred during ejection/injection. The sediment sorting is consistent with the Hjulstrm curve, in which very fine sand has the lowest critical velocity required to entrain particles and thus is mobilized first (Hjulstrm, 1939). The fining-upward trend may reflect decreasing flow velocity of the escaping fluids, possibly due to the formation of wide conduits (i.e., the lateral spreading cracks), enabling fluid pressure dissipation and resulting in a decreased grain size entrained in the flow. The intra-dike lateral grading from fine sand to silt (Fig. 2.6F) indicates that flow rates varied laterally within the dike during ejection. This sorting may reflect obstruction of flow around an object (e.g., topsoil clast), resulting in the deposition of silt in voids as the flow waned. The intra-dike clasts of topsoil and unit PF (Figs. 2.3A, 2.5, 2.6B, and 2.6C) likely formed by fragmentation of the host sediment during sediment ejection, with the clasts settling through the liquefied sediment as the flow waned or as a result of their higher density compared to the surrounding liquefied sediment.

The dike-parallel silt linings on the dike margins (Figs. 2.6B and 2.6F) suggest

that flow velocities were lower on the dike margins, resulting in silt being deposited out of suspension. The preservation of dike-parallel silt linings within a dike (Figs. 2.6B and 2.6F) suggests that multiple liquefaction episodes may be preserved within one dike. This may reflect either pulsed ejection of sediment during one earthquake, or that conduit reactivation occurred in successive Canterbury earthquake sequence events.

2.4.4 Pre-Canterbury Earthquake Sequence Liquefaction Features

Pre-Canterbury earthquake sequence liquefaction was identified in the trenches based on their structural similarities to/and crosscutting relationships with the Canterbury earthquake sequence liquefaction features and the surrounding stratigraphy.

Pre-Canterbury Earthquake Sequence Liquefaction Dike

The lateral spreading fissure intersected in T1 (Figs. 2.3A and 2.3B) and T3 (Fig. 2.5) crosscuts oxidized dikes on the trench wall and floor (Fig. 2.8). The oxidized dikes consist of well sorted, oxidized, and mottled (∼1-7 mm wide), medium sand with granules of oxidized sandstone (Fig. 2.8).

In T1, the ∼7-cm wide oxidized dike crosscuts unit III and unit IId to ∼70 cm depth, where it appears to dissipate and become indistinguishable from unit IIc (Figs. 2.3B and 2.8A). No deformation or evidence for the oxidized dike was observed in the overlying stratigraphy (Figs. 2.3B and 2.8A). The west wall of T1 was cut back by ∼50 cm to further analyze this relationship (Fig. 2.3C). The oxidized dike continued to be traceable to ∼70 cm depth, where it dissipates into the fluvial sand to silt of unit IIc (Figs. 2.3C and 2.8B). In T3, the oxidized dike crosscuts units III and IId to ∼90-95 cm depth (Figs. 2.5 and 2.8C), and is comparatively narrower (∼2-3 cm wide) than in T1. Excavation of P9 in plan view revealed an oxidized dike that is crosscut by the pit at 1.8 m depth (Figs. 2.7B and 2.8B). The oxidized dike emerges from the northwest side of P9, where it varies from ∼2 to 4 cm in width.

Interpretation of Feature

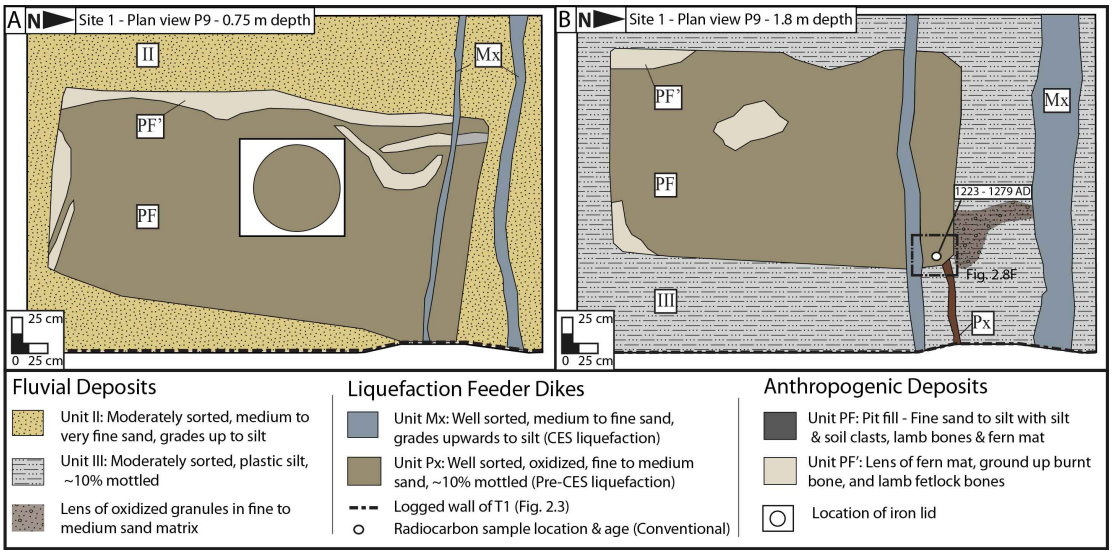

FIGURE 2.7: A) Detailed log of the large pit (P9) as exposed in plan view at 0.75 m depth. The pit (PF) crosscuts the fluvial sand (unit II), is crosscut by a Canterbury earthquake sequence (CES) dike (Mx), and is capped by an iron lid (indicated). The location of the logged section of T1 (Fig. 2.3A) is also indicated. (B) Detailed log of the large pit (P9) as exposed in plan view at 1.8 m depth. The pit crosscuts the fluvial silt (unit III) and the pre-Canterbury earthquake sequence dike (Px), and is crosscut by a Canterbury earthquake sequence dike.

The oxidized dikes identified in T1 (Figs. 2.3A and 2.3B) and T3 (Fig. 2.5) approximately align with the Canterbury earthquake sequence lateral spreading feature and exhibit similar sub-vertical and planar morphologies to the Canterbury earthquake sequence dikes, thus suggesting that the dikes were seismically triggered. The mottling within the oxidized dikes (Fig. 2.8) formed through precipitation of reduced iron in pore spaces during water-table lowering (van Breemen and Buurman, 2002). The well-developed mottles in the oxidized dikes suggest long residence in fluctuating water tables, therefore indicating that the dikes were emplaced in an event predating the Canterbury earthquake sequence. To the best of our knowledge, there is no empirical data constraining the rate of mottle formation in a sub-surface deposit under fluctuating water tables, so no absolute age for dike emplacement can be determined from the degree of mottling alone.

The pre-Canterbury earthquake sequence dike in T1 crosscuts units III and IId and is overlain by unit IIc (Fig. 2.3B), indicating that it most likely post-dates deposition of units III and IId, and the A.D. 665-765 radiocarbon age for unit III (S4; Table 2.1). The pre-Canterbury earthquake sequence dike in T3 crosscuts units III and IId (Fig. 2.5), indicating that it post-dates the radiocarbon age

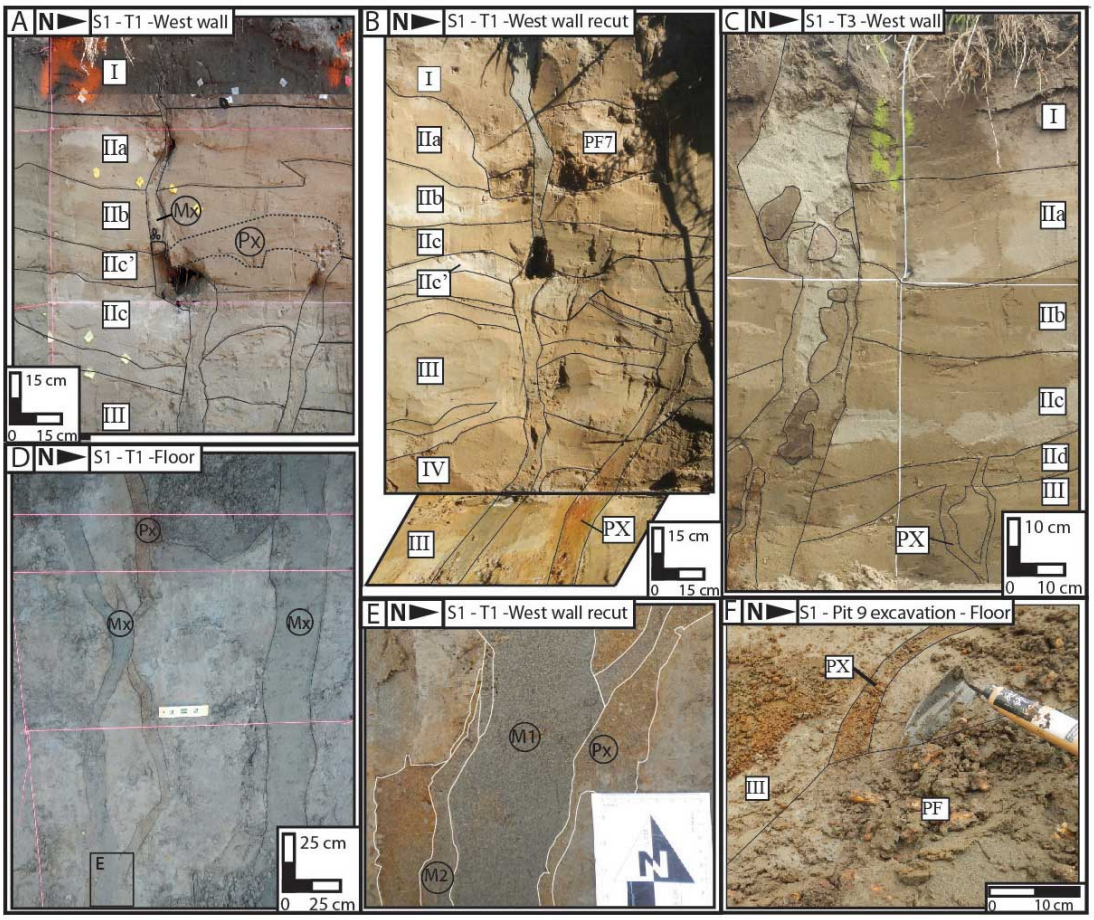
A N S1 - T1 -West wall
I
IIa
IIb
Mx
Px
IIc'
IIc
III
15 cm
0 15 cm
B N S1 - T1 -West wall recut
I
IIa
PF7
IIb
IIc
IIc'
III
IV
III
PX
15 cm
0 15 cm
C N S1 - T3 -West wall
I
IIa
IIb
IIc
IIc
IIc

of A.D. 1660-1803 (S2; Table 2.1) derived from a charcoal sample in unit IId. These ages are considered to reflect maximum depositional ages, and the actual age of the pre-Canterbury earthquake sequence dikes may in fact be younger. The pre-Canterbury earthquake sequence dike crosscut by the cesspit (P9; Fig. 2.7B) indicates that dike injection must pre-date excavation of the cesspit. The exact age of the pit cannot be determined from historical records; however, it most likely pre-dates closure of the factory at ca. 1905.

The oxidized dikes can be traced between T1, T3, and adjacent to P9, where they continuously align with the ∼25-cm wide lateral spreading fissure. The traceability of these oxidized dikes suggests that they may comprise a prior lateral spreading fissure formed during a pre-Canterbury earthquake sequence earthquake event. The oxidized dikes decrease in width from ∼7 cm in T1 (Fig. 2.3) to ∼2-3 cm in T3 (Fig. 2.5) and adjacent to P9 (Fig. 2.7). This may reflect either varied widths along the length of the feature and/or pinching out at the terminus of the fissure. The oxidized dikes in T1 and T3 exhibit similar morphologies to the ∼25-cm wide Canterbury earthquake sequence lateral spreading fissure, and they appear to dissipate into the fluvial sand to silt (unit II) with no obvious evidence for surface ejecta (Figs. 2.3B, 2.3C, and 2.5). It is possible that either the oxidized dikes reached the surface, with the ejecta being re-worked during deposition of unit II (Figs. 2.3B and 2.8B), or the pre-Canterbury earthquake sequence dikes dissipated within a low-strength layer at depth. Non-seismic methods for triggering liquefaction that are outlined in Owen et al. (2011), including gravity acting on slopes, unequal loading due to topography, density contrasts, fluid shear, and biological action, do not fit the depositional and hydrological setting of Avonside. The dike morphologies also do not correspond with the non-seismic soft-sediment deformation features outlined in Montenat et al. (2007) and Counts and Obermeier (2012), further supporting the interpretation that the oxidized dikes were seismically triggered.

The medium sand with localized granules of oxidized sandstone composition of the pre-Canterbury earthquake sequence dikes (Figs. 2.3, 2.5, and 2.8) is consistent with the Canterbury earthquake sequence dike on the floor of T2 (Fig. 2.4C) and unit VI at 2-2.6 m depth (Figs. 2.3D and 2.4D). The consistent composition suggests that both the pre-Canterbury earthquake sequence and Canterbury earthquake sequence dikes entrained material from this unit and may have been sourced

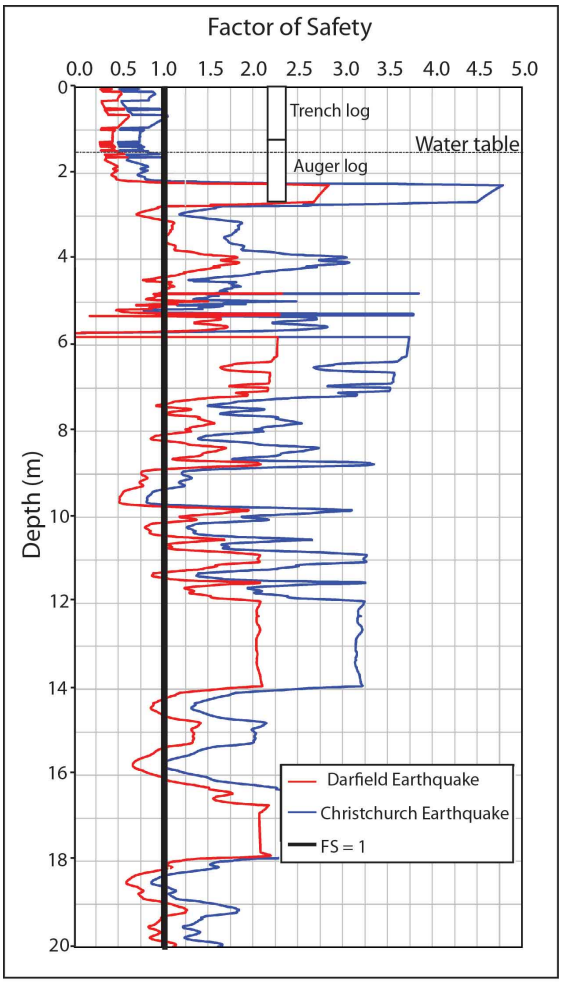

FIGURE 2.9: The CPT conducted at Site 1 indicates that the sediment from 1.6 to 2.5 m depth was potentially liquefiable (FS <1) under the peak ground accelerations (PGAs) generated in the September 2010 and February 2011 earthquakes. The sediment from 2.8 to 3 m depth was also potentially liquefiable (FS <1) under the PGAs of the February 2011 earthquake.

from the underlying unit at 2.8-3 m depth, which was potentially liquefiable (FS <1) in the February 2011 earthquake (Fig. 9).

2.5 Site 2: Bracken Street

The Bracken Street site has flat topography with elevations of 0.6-0.8 m above sea level across the site (Fig. 2.2). The dwelling on the site was erected in ca. A.D. 1910. A trench (T4) was excavated perpendicular to the aligned sand blow vents (Fig. 2.2C), to a length of ∼10 m and a depth of ∼1.4 m. The depth of the

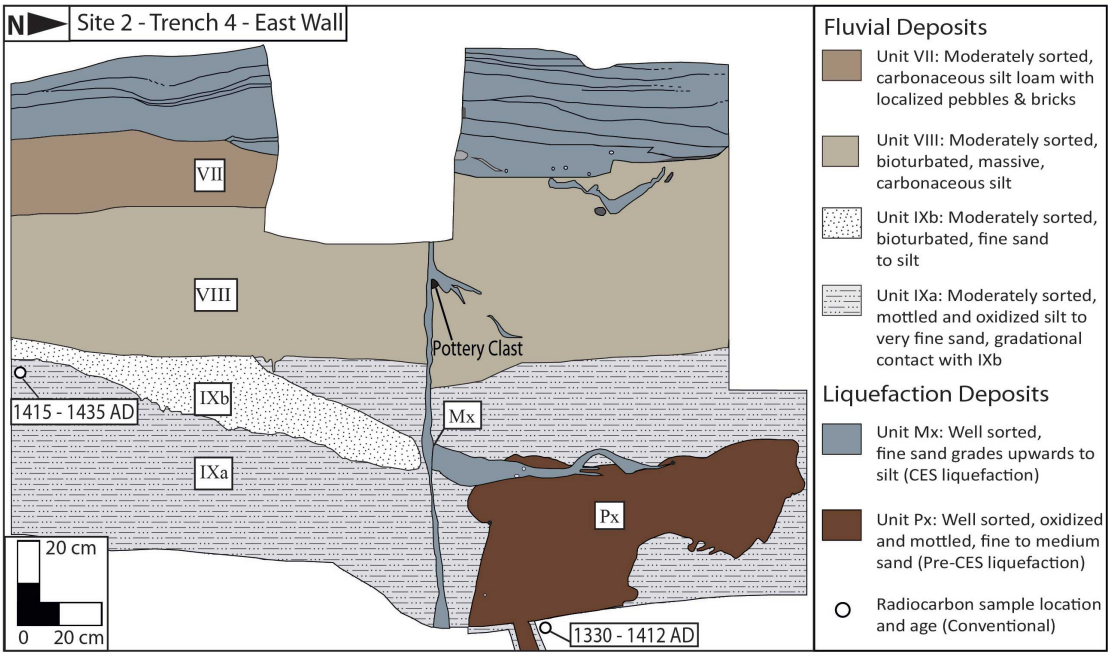

FIGURE 2.10: Detailed log of the south end of the east wall in T4 (Site 2). The Canterbury earthquake sequence (CES) dike (Mx) crosscuts the fluvial stratigraphy (VII-IXa) and the dike-fed pre-Canterbury earthquake sequence injection feature (Px) and feeds into the surface ejecta. The stratigraphy within the surface ejecta and the location and ^{14}C ages of the samples are also indicated.

trench was limited by the depth to the water table, which was ∼1.3-1.4 m during excavation.

2.5.1 Trench Fluvial Stratigraphy

T4 exposed stratigraphy composed of non-plastic silts (unit IXa) with interbedded, lenticular, very fine sand (unit IXb), capped by ∼50 cm of topsoil (unit VIII; Fig. 10; Appendix 1). The upper ∼25 cm section of topsoil contains a discontinuous anthropogenic layer of pottery, glass, and pebbles (unit VII; Fig. 2.10).

Interpretation of Depositional History of the Site

The non-plastic silts (unit IXa) exposed in T4 (Fig. 2.10) are interpreted as overbank flood deposits from the Avon River in a low-energy depositional setting such as that of a marsh or oxbow lake. The inter-bedded lenses of very fine sand (unit IXb) indicate that the area was periodically flooded by higher-energy events. The lenticular morphology of these fine sand lenses (unit IXb) indicates that the flood events sometimes formed small channels. The exposed stratigraphy reflects the

present depositional setting of the site within the low-elevation (1-1.5 m above sea level) floodplain of the Avon River (Fig. 2.2) and is consistent with historical reports of periodic flooding of the Avon River during periods of heavy rain (Cowie, 1957).

Radiocarbon dating of two detrital wood fragments obtained from unit IXa at depths of 0.5 m (S8) and 1.1 m (S9) yielded ages of AD. 1415-1435 (S8) and A.D. 1330-1412 (S9), respectively (Fig. 2.10; Table 2.1). These ^{14}C ages indicate that the stratigraphy was deposited over a maximum period from A.D. 1330 to present.

2.5.2 Canterbury Earthquake Sequence Liquefaction Features

Canterbury earthquake sequence liquefaction features were recognized in T4 (Fig. 2.10) by their traceable continuity into the observed surface sand blows. The Canterbury earthquake sequence features were documented in detail to determine whether the morphologies of liquefaction features were consistent between the two sites, and to aid identification of pre-Canterbury earthquake sequence liquefaction features. The Canterbury earthquake sequence liquefaction features are all composed of gray, well-sorted, fine sand to silt unless otherwise stated.

Canterbury Earthquake Sequence Liquefaction Dikes

The linear array of surface sand blows intersected at the southern end of T4 (Fig. 2.2D) aligns with a ∼4 cm wide, sub-vertical, planar dike in the sub-surface that crosscuts the fluvial stratigraphy from the trench floor to the surface (Fig. 2.10). A small, ∼0.5-2 cm wide sub-vertical and planar dike crosscuts the stratigraphy from the trench floor to ∼10 cm depth at the northern end of the trench.

The dikes all increase in width with depth and lack the oxidation and mottling developed in the surrounding stratigraphy (Fig. 2.10). No evidence for vertical grading is observed within these dikes. Contact-parallel silt linings, ∼1 mm thick, are observed on the margins of the ∼4 cm wide dike (Fig. 2.10), while no silt lining is observed on the margins of the ∼0.5-2-cm wide dike.

Canterbury Earthquake Sequence Sub-surface Liquefaction Sill

The ∼4 cm wide dike crosscuts a ∼1-2 cm wide sill at ∼50 cm depth (Fig. 2.10). The sill exhibits a composition consistent with that of the Canterbury earthquake

sequence dike and is separated from the dike by the ∼1-2-mm-thick dike-parallel silt lining (Fig. 2.10).

Interpretation of Canterbury Earthquake Sequence Liquefaction Features

The ∼4 cm wide dike crosscuts the fluvial stratigraphy from the trench floor to the surface (Fig. 2.10), indicating that it post-dates deposition of the fluvial stratigraphy. The alignment of the sub-surface dike with the surface sand blow (Fig. 2.10) confirms that it formed during the Canterbury earthquake sequence, which is further supported by its lack of oxidation and mottling. The sill and the ∼0.5-2 cm wide dike are of similar composition to the Canterbury earthquake sequence dikes that unequivocally reach the surface and also lack oxidation and mottling. The similar composition indicates that the smaller dikes and sill also formed during the Canterbury earthquake sequence. The increasing width of the dikes with depth (Fig. 2.10) supports the interpretation of these dikes as having formed by the upward injection of sediment (Counts and Obermeier, 2012). The sub-vertical and planar morphology of the dikes at Site 2 is consistent with the morphologies of the dikes documented at Site 1. The consistent morphology indicates that dike geometries, as well as the well-sorted grain-size distributions, may be used to identify liquefaction features in the sub-surface and in the absence of surface ejecta.

The dike-parallel silt linings along the margin of the ∼4 cm wide dike (Fig. 2.10) indicate that flow velocities were lower adjacent to the dike wall. The presence of the silt lining separating the sill from the dike suggests that the sill formed prior to the last liquefaction event ejected through the dike. This indicates that at least two generations of Canterbury earthquake sequence liquefaction are preserved within the sub-surface.

The dikes at Site 2 (Fig. 2.10) are comparatively narrower than those identified at Site 1 (∼4 cm at Site 2 and up to 25 cm at Site 1; Figs. 2.3, 2.4, 2.5, and 2.10). The varied widths may be attributed to the varied distance of each site from the river, as it was observed that the width and spatial density of surface features decrease away from the river (Bastin et al., 2015b). The varied widths of the dikes may also reflect variations in the stratigraphy overlying the liquefied layers, which are predominantly composed of fluvial silts at Site 2 and fluvial sands at Site 1. It is possible that the predominately silt stratigraphy at Site 2 may inhibit fracturing, thus possibly resulting in the formation of comparatively narrower dikes.

2.5.3 Pre-Canterbury Earthquake Sequence Liquefaction Features

Pre-Canterbury earthquake sequence liquefaction features were identified in T4 based on their structural similarities and crosscutting relationships with the Canterbury earthquake sequence liquefaction features and the surrounding stratigraphy, and from comparison with the pre-Canterbury earthquake sequence features identified at Site 1.

The Canterbury earthquake sequence dike at the southeast end of T4 crosscuts a bulbous shaped lens of oxidized and mottled, well-sorted, fine to very fine sand (Fig. 2.10). This lens crosscuts the fluvial stratigraphy from the trench floor to ∼80 cm depth and exhibits irregular and bioturbated contacts (Fig. 2.10). Excavation around this feature revealed a dike at ∼1.5-1.7 m depth that merges with the bulbous lens and is of consistent grain size and sorting (Fig. 2.10). The dike ranges from 5 to 7 cm in width and exhibits a similar sub-vertical, planar geometry to the Canterbury earthquake sequence dike at Site 2 (Fig. 2.10), and the oxidized dikes at Site 1 (Fig. 2.8). Excavation beyond this point was limited by the height of the water table.

Interpretation of Pre-Canterbury Earthquake Sequence Liquefaction Features

The dike beneath the oxidized lens (Fig. 2.10) indicates that it formed by the upward injection of liquefied sediment. The similar sub-vertical, planar geometry of the oxidized dike and the adjacent Canterbury earthquake sequence dike indicates that the oxidized feature was seismically triggered. The oxidation and mottling within this feature indicate that it has been subjected to prolonged fluctuations in the height of the water table, indicating that it pre-dates the Canterbury earthquake sequence. The bulbous shape of the oxidized lens, combined with its irregular contacts (Fig. 2.10) and lack of evidence for surface ejecta, suggests that this feature formed by the sub-surface injection of liquefied sediment. The bulbous morphology of this feature is inconsistent with the Canterbury earthquake sequence injection sills observed at both sites 1 and 2. This feature may therefore reflect injection into and subsequent deformation of a lens of fine sand, possibly being the paleo-channel comprising unit IXb (Fig. 2.10). Liquefaction dikes are likely to preferentially form within loosely consolidated sands such as that within a paleo-channel, as the sand provides a path of lower resistance compared to the surrounding silt. The site-specific depositional and hydrological conditions and the

bulbous morphology of the oxidized feature are inconsistent with the liquefaction-triggering mechanisms and morphologies of non-seismic liquefaction features described in Montenat et al. (2007); Owen et al. (2011); Counts and Obermeier (2012). This supports the interpretation that this oxidized lens and associated dike formed during a pre-Canterbury earthquake sequence earthquake.

The pre-Canterbury earthquake sequence liquefaction injection feature crosscuts the fluvial silt (unit IXa) from the trench floor to ∼80 cm depth. This indicates that this liquefaction feature likely formed in an event that post-dated deposition of the fluvial silt (unit IXa), and the ^{14}C ages of A.D. 1415-1435 (S8; Fig. 2.10; Table 2.1). The lack of surface ejecta associated with this feature indicates that the causative earthquake triggered liquefaction at depth; however, it did not generate the shaking intensities required to fracture the overlying soil cap and eject liquefied sediment to the surface at this location. It is possible that localized ejecta did form at other locations across this site and were not intersected within this trench. The lack of surface ejecta means that the ground surface at the time of injection cannot be determined, and no additional constraints can be placed on the timing of the paleo-earthquake. The depth of the liquefied source stratum for the Canterbury earthquake sequence dikes and pre-Canterbury earthquake sequence liquefaction feature cannot be determined for this site as excavation was limited by the shallow water table.

2.6 Possible timing and seismic source for paleo-liquefaction

2.6.1 Timing and origin of paleo-earthquake(s)

The approximate timing of the earthquake(s) forming the pre-Canterbury earthquake sequence liquefaction features at sites 1 and 2 can be approximated by combining crosscutting relationships with ^{14}C ages of the host sediments. The pre-Canterbury earthquake sequence dikes at Site 1 crosscut the strata to ∼70 cm depth in T1 (Fig. 2.3) and ∼90-95 cm depth in T3 (Fig. 2.5) and are crosscut by P9 (Figs. 2.7 and 2.8B). This indicates that the pre-Canterbury earthquake sequence dikes post-date the depositional age of A.D. 1660-1803 for unit IIc (S2;

Fig. 2.5; Table 2.1) and pre-date the closure of the wool scouring factory in ca. 1905.

The OSL ages (Fig. 2.3B; Table 2.2) are within error of the ^{14}C age of 810-792 B.C. for the liquefied source strata (Table 2.1). It is possible that the OSL ages are dominated by reworked sediment sourced from the liquefied unit or its age equivalent elsewhere via redeposition of liquefied material ejected from depth, bioturbation causing mixing of the surface ejecta with the surrounding fluvial deposits, or via erosion and redeposition of ca. 2.6-2.8 ka sediment from elsewhere without bleaching.

The pre-Canterbury earthquake sequence liquefaction feature at Site 2 crosscuts the fluvial stratigraphy to ∼80 cm depth (Fig. 2.10), indicating that it post-dates the depositional age of A.D. 1415-1435 for unit IXa. No additional constraints on the timing of the earthquake can be concluded from crosscutting relationships; therefore, it cannot be concluded whether the pre-Canterbury earthquake sequence liquefaction features at both sites formed during the same earthquake event.

The historic record of earthquakes within the wider Christchurch area is limited to post-1843, following European settlement. Historic reports indicate that five damaging earthquakes occurred within ∼150 km of Christchurch between 1869 and 1922 (Fig. 1B) (Pettinga et al., 2001; Downes and Yetton, 2012)). The magnitudes and inferred Modified Mercalli Indices (MMI) in Christchurch for each of these events are presented in Table 2.3 (Downes and Yetton, 2012). The 1869 M_w ∼4.8 Christchurch earthquake occurred on 5 June 1869 at NZST 8.30 a.m. and was felt throughout the city (Elder et al., 1991; Stirling et al., 1999; Pettinga et al., 2001; Downes and Yetton, 2012). The highest shaking intensity was recorded within the Central Business District (CBD) causing the collapse of chimneys, the Christchurch cathedral spire, and a brick wall of a house (Stirling et al., 1999). Damage within Avonside and northeast Christchurch included extensive damage to the contents of residential properties, and many damaged or fallen chimneys. The reported damage corresponds with the effects of a MMI 7 earthquake (Downes and Yetton, 2012). Downes and Yetton (2012) assigned a macroseismic epicenter of 43.55°S, 172.60°E and upper-crustal hypocentral depth of 5 km, which is located at the center of the isoseismal pattern based on the accounts from residents and the distribution of damage (Stirling et al., 1999). Following the earthquake, it was observed by a local resident that the tide runs higher up the Heathcote River than

formerly, suggesting that settlement, potentially induced by liquefaction, may have occurred (Downes and Yetton, 2012).

Damage during the 1870 $\sim M_w$ 5.7 Lake Ellesmere earthquake was less widespread, with only damage to the contents of residential properties and chimneys reported within Avonside. The 1888 $\sim M_w$ 7.2 North Canterbury and 1901 $\sim M_w$ 6.9 Cheviot earthquakes caused widespread damage within the wider Christchurch area, including toppling of the Cathedral spire during both events (Cowan, 1991; Downes and Yetton, 2012). Damage was also reported in Christchurch following the 1922 $\sim M_w$ 6.4 Motunau, North Canterbury, earthquake (Downes and Yetton, 2012). No surface manifestation of liquefaction was reported in Avonside following any of these events; however, it is possible that localized surface ejecta formed and went unreported due to the sparsely populated, rural and industrial nature of much of this area at this time. Large known pre-historic earthquakes prior to the settlement of Christchurch during the time interval encompassing the pre-Canterbury earthquake sequence liquefaction features include the 1717 Alpine fault M_w 8.1 (Sutherland et al., 2007) and ca. 500-600 yr B.P. $M_w \sim 7.2$ Porters Pass fault earthquakes (Howard et al., 2005). The approximate epicentral locations and shaking intensities generated in Christchurch for these events are poorly constrained given the broad constraints on earthquake M_w and the lack of historical accounts. Additional large earthquakes in the Canterbury region are not considered due to the limited historical record.

2.6.2 Triggering of Liquefaction

The $PGA_{7.5}$ 0.06g liquefaction-initiation threshold at Site 2 (Quigley et al., 2013) was established based on the observation of localized, small sand blows ($\sim$20 cm in diameter) that formed in the M_w 5.0 April 2011 earthquake. Widespread liquefaction ejecta were reported at the site at $PGA_{7.5}$ >0.1g (Fig. 2.11) (Quigley et al., 2013). No empirically derived liquefaction triggering threshold was established for Site 1; however, a similar threshold is likely given their geographic proximity, the similar geomorphic and geologic settings, and the similar water-table depths.

Site-specific $PGA_{7.5}$ estimates were derived for Site 1 for the five well-documented historical events using the ground motion prediction equation (GMPE) outlined by Bradley (2013; Table 2.3). Site class E (very soft soil) characteristics were

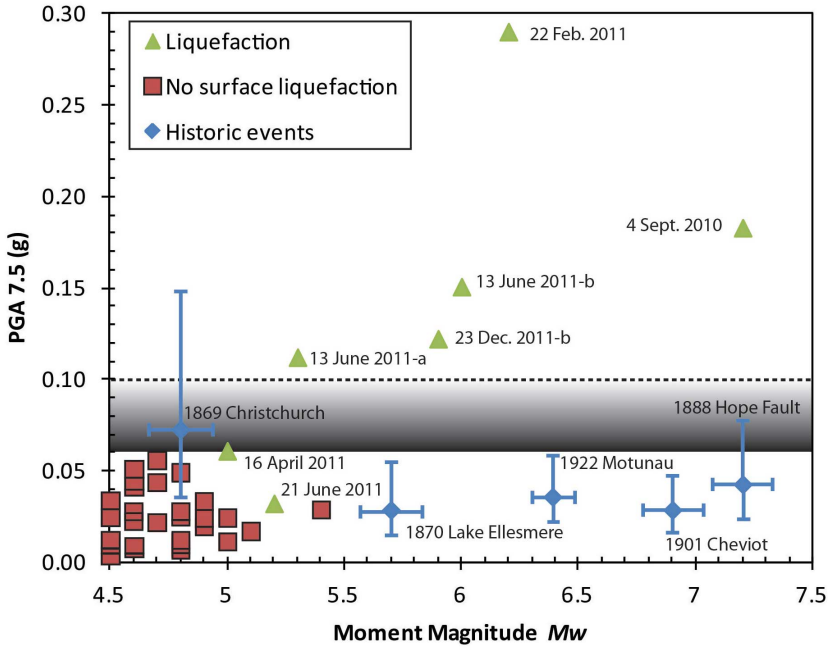

FIGURE 2.11: The calculated $PGA_{7.5}$ (peak ground acceleration equivalent for a M_w 7.5 event) for the Canterbury earthquake sequence events that did and did not cause liquefaction at Site 2 compared with earthquake magnitude (M_w). The calculated median $PGA_{7.5}$ (box) and associated 16th and 84th percentiles (error bars), and inferred magnitudes for the paleo-events are also plotted. The plotted $PGA_{7.5}$ values are compared to the liquefaction triggering thresholds for minor to severe liquefaction during the Canterbury earthquake sequence as constrained for Site 2 by Quigley et al. (2013).

assumed for the study site. This GMPE is a New Zealand-specific model derived from comparison of four different pre-existing models and calibrated against recorded ground motions in New Zealand (Bradley, 2013). The model utilizes the inferred magnitude, distance from epicenter, predominant rock type, and fault type (i.e., normal, reverse, or strike slip) to calculate the approximate PGA experienced at the site (Table 2.3). Directionality was not considered due to the lack of constraints on the rupture directivity. The results provide a distribution with both the median and standard deviation PGAs. The 16th and 84th percentiles of this distribution were derived from the 50th percentile median PGA (Table 2.3). The PGA values were $M_{w\ 7.5}$-weighted ($PGA_{7.5}$) using the methodology outlined in Idriss and Boulanger (2008). The $PGA_{7.5}$ value enables direct comparison of ground accelerations generated by events with different M_w and epicentral distances. The median $PGA_{7.5}$ is plotted with the error bars representing the 16th and 84th percentiles (Fig. 2.11). The plotted $PGA_{7.5}$ is compared with the liquefaction triggering thresholds of $PGA_{7.5}$ ~0.06g for minor liquefaction and $PGA_{7.5}$ 0.1g for severe liquefaction at Site 2 (Fig. 2.11). Of the five historical events, only

the 1869 Christchurch earthquake produces a modelled median (50th percentile) $PGA_{7.5}$ that exceeds the threshold for minor liquefaction (Table 2.3). The 1869 earthquake pre-dates closure of the wool scouring factory; therefore, it is possible that the pre-Canterbury earthquake sequence dikes at Site 1 formed during this event, and the pit (P9) was excavated following this event.

Liquefaction during the Canterbury earthquake sequence was reported at distances of ∼8 km from the epicenter following the 19 October 2010 M_w 5.0 aftershock (Cubrinovski and Green, 2010) and ∼14 km from the epicenter of the 16 April 2011 M_w 5.0 aftershock (Quigley et al., 2013). This indicates that moderate-to-large (M_w 5-7.9) events can trigger liquefaction at distances greater than that predicted from empirical global compilations of M_w versus distance to most distal liquefaction feature (Ambraseys, 1988; Galli, 2000; Cubrinovski and Green, 2010), particularly in highly susceptible sediments or in areas prone to seismic amplification. Therefore, it is possible that the 1869 earthquake triggered minor liquefaction at an approximate epicentral distance of 6 km in highly susceptible sediments. The termination of the pre-Canterbury earthquake sequence dikes at ∼70 and ∼90 cm depth indicates that either ∼90 cm of sedimentation occurred at the site following the event, or that the dikes terminated beneath the surface. It is considered unlikely that ∼90 cm of sediment accumulated at the site post-1869 and during production at the wool scouring factory. The similar geometries of the pre-Canterbury earthquake sequence dikes and Canterbury earthquake sequence lateral spreading fissure suggest that the pre-Canterbury earthquake sequence dikes may comprise a lateral spreading fissure. The geometry of the dikes, combined with the inferred sedimentation at the site, suggests that the pre-Canterbury earthquake sequence features formed in an event prior to the 1869 event. It is possible that these features formed during a large, far-field earthquake such as the ∼M_w 7.9 $\pm$ 0.3 1717 Alpine fault event, which post-dates the depositional age of A.D. 1660-1803 for unit IIc (S2; Fig. 2.5; Table 2.1). The GMPE indicates that this event likely generated $PGA_{7.5}$, exceeding the liquefaction triggering threshold at the site (Bradley, 2013).

The New Zealand Seismic Hazard Model (NZSHM) predicts approximate return times of ∼50 yr for PGAs of 0.11g (MMI 6-7) and ∼200 yr for PGAs of 0.22g (MMI 7-8) for class C material (shallow soils) in the Christchurch area (Stirling et al., 2008). This suggests a high likelihood of earthquake-induced strong ground motions exceeding the liquefaction triggering threshold within the last ∼220 yr,

TABLE 2.3: Inferred magnitudes and MMIs for the five historic earthquakes and calculated $PGA_{7.5}$ for Site 1

Event	**M_w**	**MMI**	**Distance from epicentre (Km)**	**PGA 50th prc.**	**$PGA_{7.5}$ 16th prc.**	**$PGA_{7.5}$ 50th prc.**	**$PGA_{7.5}$ 84th prc.**	**Calculated MMI**
1869 Christchurch	4.8± 0.1	7	4	0.148±.013	0.040±.005	0.074±.009	0.124±.005	7
1870 Lake Ellesemere	5.7± 0.1	6	37	0.049±.004	0.017±.002	0.031±.003	0.055±.005	5.5
1888 Hope Fault	7.2± 0.1	2	102	0.046±.0035	0.026±.002	0.043±.004	0.071±.0017	5
1901 Cheviot	6.8± 0.1	6-7	105	0.034±.001	0.017±.001	0.028±.001	0.047±.001	4.5
1922 Motunau	6.4± 0.1	6-7	58	0.042±.001	0.021±.001	0.036±.001	0.062±.001	5

particularly in sediments that are highly susceptible to liquefaction (e.g., site class E, very soft soils; NZS.1170.5 (2004)). The approximate return times exclude the occurrence of earthquake clustering and are therefore considered to reflect average return times.

2.6.3 Liquefaction Susceptibility of Avonside

The liquefaction potential of the two sites in Avonside is governed by their hydrologic, geologic, and geomorphic setting. The liquefaction potential of the sub-surface sediments generally decreases over time due to sedimentation, compaction, and the formation of secondary cements (Seed and Idriss, 1982; Idriss and Boulanger, 2008). The water table within Avonside is tidally influenced and controlled by the height of the Avon River, which remains approximately at sea level. Therefore, sub-surface sediments at 1-2 m depth are likely to have remained in the saturation zone following initial deposition, which, combined with their relatively young age (810-792 B.C.; S7; Table 2.1), suggests that limited cementation or aging is likely to have occurred. Quigley et al. (2013) showed a power-law relationship between the spatial extent and maximum stratigraphic thicknesses of sediment ejecta during the Canterbury earthquake sequence with $PGA_{7.5}$. This implies that any changes to the liquefaction source sediment during the Canterbury earthquake sequence (e.g., densification) did not have a discernible influence on the liquefaction susceptibility of the site in subsequent earthquakes. The liquefaction susceptibility of the study sites during pre-CES liquefaction is therefore unlikely to have been modified significantly by sediment densification.

The surface at Site 1 has aggraded by ∼20 cm since excavation of the pits (Figs. 2.3, 2.4, and 2.5), suggesting that the site was still actively aggrading following the pre-Canterbury earthquake sequence event. The geometry of the pre-Canterbury earthquake sequence dikes at Site 1 suggests ∼70 to 90 cm of sedimentation may be inferred at the site since the paleo-earthquake. This inferred sedimentation may have increased the overburden pressure on the liquefiable strata, increasing the cyclic stress threshold required to initiate liquefaction and therefore decreasing the liquefaction susceptibility of the site. The sediment accumulation at Site 2 cannot be directly calculated; however, historical records of periodic flooding (Cowie, 1957) suggest that sedimentation has most likely occurred at the site

since the paleo-earthquake. Any compaction of sub-surface strata during the previous episodes of liquefaction is unlikely to have had a major effect on liquefaction susceptibility. The inferred sedimentation, limited compaction and limited cementation suggest the liquefaction triggering threshold during the earthquake(s) forming the pre-Canterbury earthquake sequence liquefaction features in Avonside is likely to have been consistent or lower than that during the Canterbury earthquake sequence.

2.7 Implications for paleoseismic studies and future land use

The identification of pre-Canterbury earthquake sequence liquefaction at both sites in Avonside indicates that residential development within eastern Christchurch (ca. 1860-2005) took place on top of sediments where geologic evidence for liquefaction was present in the shallow sub-surface. The identification of the pre-Canterbury earthquake sequence at both sites in Avonside highlights the potential of paleo-liquefaction investigations, in addition to geotechnical data, to contribute to land-use planning. Future residential and commercial developments could therefore utilize paleo-liquefaction observations to assist with making informed decisions on land zonation and building design criteria.

The approximate alignment of the pre-Canterbury earthquake sequence features with the ∼25-cm wide lateral spreading fissure at Site 1 and the ∼5-cm wide dike at Site 2 indicates that some zones of weakness were reoccupied during the subsequent earthquake events (Figs. 2.3, 2.5, and 2.10). The identification of two generations of Canterbury earthquake sequence liquefaction within the sub-surface at both sites (Figs. 2.8 and 2.10), despite the 10 Canterbury earthquake sequence liquefaction events recorded at Site 2 (Quigley et al., 2013), suggests that geologic evidence for paleo-liquefaction may significantly under-represent the number of distinct liquefaction events at the site. Feeder dike generations identified in paleo-liquefaction studies should therefore be generally treated as proxies for the minimum number of liquefaction inducing earthquakes.

The CPT and hand auger data indicate that the Canterbury earthquake sequence dikes are comparably wider than the pre-Canterbury earthquake sequence dikes (<7 cm). This implies that the shaking intensity and severity of liquefaction

experienced during the Canterbury earthquake sequence is likely to have been the most severe since initial deposition of the fluvial sediment ca. A.D. 665. The width of liquefaction dikes preserved within the sub-surface may act as proxies for the intensity of shaking and associated severity of liquefaction experienced during historic earthquakes in certain instances.

2.8 Conclusions

Canterbury earthquake sequence liquefaction features at sites 1 and 2 consist of liquefaction dikes and sills that exhibit sub-vertical, planar morphology and increase in width with depth. The dikes and sills are composed of gray, well-sorted, fine to medium sand that lacks the oxidation and mottling developed in the surrounding sediment. Pre-Canterbury earthquake sequence liquefaction features were also identified at both sites, including dikes at Site 1 and an injection feature at Site 2. These pre-Canterbury earthquake sequence features were distinguished from the Canterbury earthquake sequence features by their oxidized and mottled appearance and bioturbated contacts.

The presence of pre-Canterbury earthquake sequence liquefaction confirms that earthquake-induced strong ground motions exceeding the threshold value for liquefaction occurred within eastern Christchurch prior to the 2010 Darfield earthquake. Crosscutting relationships combined with ^{14}C dating at Site 1 indicate that this event most likely occurred between A.D. 1660-1803 (S2) and ca. 1905.

The $PGA_{7.5}$ values calculated for Site 1 for the five historic events indicate that only the 1869 Christchurch earthquake generated ground motions in excess of the local liquefaction triggering threshold of $PGA_{7.5}$ ~0.06g (Quigley et al., 2013). The recorded damage within Avonside during the event (MMI 7) and reports of the tide running up the Heathcote River support the inference that liquefaction may have been triggered during this event. The calculated $PGA_{7.5}$ for this event corresponds with minor liquefaction in the Canterbury earthquake sequence. This supports the interpretation that minor liquefaction in highly susceptible sediments may have formed during this event.

The documentation of liquefaction in moderate-to-large (M_w ~5-7.9) earthquakes at distances exceeding that predicted by Ambraseys (1988) (i.e., ~8 km from epicenter for the October 2011 M_w 5.0 earthquake, ~14 km from epicenter for

the April 2011 M_w 5.0 earthquake, and ~6 km from the inferred epicenter for the 1869 Christchurch M_w 4.8 0.1 earthquake) indicates that even moderate M_w earthquakes on blind faults can trigger liquefaction in highly susceptible sediments or in areas prone to seismic amplification at distances greater than predicted. More data documenting the spatial distribution of liquefaction associated with moderate M_w earthquakes will help to better refine the liquefaction hazard posed by earthquakes of this nature.

Chapter 3

Late Holocene liquefaction at sites of contemporary liquefaction during the 2010-2011 Canterbury Earthquake Sequence

Abstract

The 2010-2011 Canterbury earthquake sequence (CES) caused up to ten episodes of liquefaction at highly susceptible sites in eastern Canterbury resulting in severe damage to land and infrastructure. Subsurface investigations at five sites over two study areas revealed CES dikes and sills that align with and crosscut pre-CES liquefaction features including dikes, a lateral sill, a sand blister, and a buried compound sand-blow. Crosscutting relationships combined with ^{14}C dating constrain the timing of the pre-CES liquefaction features to likely post-AD 1321 and pre-1901 in one study area. Pre-CES features in the second study area likely formed in three distinct episodes: Post-AD 1458 and possibly during the 1901 Cheviot earthquake, between AD 1297 and 1901, and Pre-AD 1458. The liquefaction potential of known active faults within the wider Canterbury region are evaluated from back-calculated magnitude bound curves and peak ground accelerations (PGA) approximated using a New Zealand specific ground motion prediction equation and compared with global liquefaction triggering thresholds. Analysis indicates that many active faults within North Canterbury and offshore that are within 50

km of the study sites and capable of triggering M_w >6.5 earthquakes have the potential to cause widespread liquefaction. Ruptures of these faults may have formed the pre-CES liquefaction features. Combining the back-calculation approach with the modelled peak ground accelerations proves effective in determining the active faults capable of triggering liquefaction at the study sites, and are therefore capable of triggering liquefaction in the future.

3.1 Introduction

Earthquake-induced cyclic shearing may trigger deformation in loosely consolidated and saturated sediment causing pore-water pressures to increase in the affected media. Liquefaction may occur as pore-water pressures exceed the initial vertical confining stresses causing the breakdown of the grain arrangement (Seed and Idriss, 1982; Idriss and Boulanger, 2008). Pore-water and liquefied sediment may be ejected to the ground surface through subsurface dikes or it may be injected into the near surface as lateral sills, stalled dikes, and/ or injection features (Sims, 1975; Tuttle and Barstow, 1996; Obermeier, 1996; Tuttle and Hartleb, 2012; Quigley et al., 2013). Liquefaction ejecta typically manifests at the surface as sand blows, fissures, surface flooding, and localized vertical (i.e. subsidence) and/ or horizontal (i.e. lateral spreading) ground movement (Seed and Idriss, 1982; Tuttle and Barstow, 1996; Obermeier, 1996; Cubrinovski and Green, 2010; Tuttle and Hartleb, 2012; Quigley et al., 2013). The surficial features are susceptible to erosion or reworking into surrounding sediments by aeolian and/ or fluvial action and therefore may be removed from or obscured in the geologic record (Sims, 1975; Reid et al., 2012; Quigley et al., 2013). Subsurface liquefaction features are commonly preserved in the geologic record where host sediments are preserved and are termed paleo-liquefaction (Obermeier, 1996; Tuttle, 2001; Obermeier et al., 2005).

Paleo-liquefaction provides evidence for paleo-earthquake shaking that exceeded the threshold value for liquefaction (Green et al., 2005). Analysis of paleo liquefaction features enables recurrence intervals, ground motions, and magnitudes of paleo-earthquakes to be estimated (Obermeier, 1996; Tuttle et al., 2002; Green et al., 2005; Tuttle and Atkinson, 2010). Site-specific peak ground accelerations (PGA) may be back-calculated for historic earthquakes and/or ruptures of known active faults using ground motion prediction equations (GMPE). Comparison of modelled PGA with liquefaction-triggering thresholds enables faults capable of

triggering liquefaction to be identified. Recent compilations of earthquake and liquefaction data suggest a liquefaction-inducing threshold of $PGA_{7.5} = 0.09g$ (Santucci de Magistris et al., 2013), although minor liquefaction has been reported in highly susceptible sediments under $PGA_{7.5}$ as low as ∼0.06g (Quigley et al., 2013). Magnitude-bound curves, which correlate earthquake magnitude to the maximum site-to-source distance of observed liquefaction, are also widely applied in paleo-liquefaction studies. The curves constrain the distribution of rupture locations and magnitudes that have the potential for inducing liquefaction at a given site (Obermeier, 1998; Olson et al., 2005; Papathanassiou et al., 2005; Tuttle, 2001; Pirrotta et al., 2007). A methodology for back-calculating magnitude-bound curves has been proposed by Maurer et al. (2015). This methodology identifies the range of possible earthquake sources capable of triggering liquefaction at a site with paleo-liquefaction.

The 2010-2011 Canterbury Earthquake Sequence (CES) caused repeated episodes of liquefaction in parts of eastern Christchurch and in the northern township of Kaiapoi, New Zealand (Fig. 3.1) (Cubrinovski and Green, 2010; Wotherspoon et al., 2011; Quigley et al., 2013). Severe liquefaction-induced damage to land and infrastructure recurred during the September 2010 M_w 7.1 Darfield, February 2011 M_w 6.2, June 2011 M_w 6.0, and December 2011 M_w 5.9 earthquakes and resulted in the central government purchase of upwards of 6000 residential properties (Cubrinovski and Green, 2010; Cubrinovski et al., 2011; Quigley et al., 2013; Parker and Steenkamp, 2012). The historic earthquake record in the wider Christchurch area is limited to post European settlement of the area in 1843. Historic reports indicate that five damaging earthquakes occurred within the Canterbury region prior to the CES and between 1869 and 1922 (Pettinga et al., 2001; Downes and Yetton, 2012). The 1922 Motunau, North Canterbury M_w 6.4 earthquake caused localized damage within Christchurch. The 1901 ∼M_w 6.9 Cheviot caused widespread damage within the Canterbury area and triggered liquefaction in Kaiapoi (Fig. 3.1) (Berrill et al., 1994). The 1888 ∼M_w 7.2 Hope Fault, 1870 ∼M_w 5.7 Lake Ellesmere, and 1869 ∼M_w 4.8 Christchurch earthquakes also caused widespread damage in the wider Christchurch region (Elder et al., 1991; Stirling et al., 1999; Pettinga et al., 2001; Downes and Yetton, 2012). Pre-historic earthquakes known to have affected the Canterbury region include the 1717 ∼M_w 8.1 Alpine Fault (Sutherland et al., 2007) and ca. 1400 - 1500 M_w. ∼7.2 Porters Pass earthquakes (Howard et al., 2005). No liquefaction was reported nor has been identified in Christchurch following any of these events or in Kaiapoi following events other than the 1901

earthquake (Berrill et al., 1994; Downes and Yetton, 2012). Understanding the approximate timing, location, and magnitude of liquefaction-inducing pre-historic earthquakes within the Canterbury region is therefore important in informing future land-use planning decisions and may contribute to seismic hazard modelling (Stirling et al., 2012).

In this chapter, new stratigraphic and chronologic evidence is presented for pre-CES liquefaction at three sites in eastern Christchurch and two sites in Kaiapoi, with the goal of further constraining the timing of previous liquefaction-inducing earthquakes within the Canterbury region. The potential that ruptures on known active faults will trigger liquefaction at the study sites is also evaluated from peak ground accelerations approximated using a New Zealand specific ground motion prediction equation and compared with liquefaction triggering thresholds, and from back-calculated magnitude bound curves.

3.2 Geologic Setting

The eastern Canterbury region is situated upon a low relief and low elevation alluvial landscape (0 to 20 m above sea level) along the eastern margin of the Canterbury Plains (Fig. 3.1). The region is predominantly underlain by drained peat swamps, fluvial sands and silts, and estuarine, dune, and foreshore sands (Fig. 3.1) (Brown and Weeber, 1992; Forsyth et al., 2008). The western Canterbury region is primarily underlain by fluvial gravel, sand, and silt deposited by the Waimakariri River during its avulsion across the Canterbury Plains and subsequent overbank flow (Cowie, 1957; Brown and Weeber, 1992).

The sediments in eastern Canterbury were deposited during shoreline progradation and marine regression following the mid-Holocene high-stand with shorelines recorded up to 8 km inland from the location of the modern shoreline at ~6,500 yr before present (Brown and Weeber, 1992). Fluvial sands and silts comprise re-worked deposits of the braided Waimakariri River and transported by the meandering rivers (i.e. Avon and Kaiapoi Rivers; Fig. 3.1) which regularly avulsed across the region prior to European settlement (Cowie, 1957; Brown and Weeber, 1992). The youthful and unconsolidated nature of the fine sands to silts combined with high water tables (1 to 2 m depth) and localized artesian water pressures

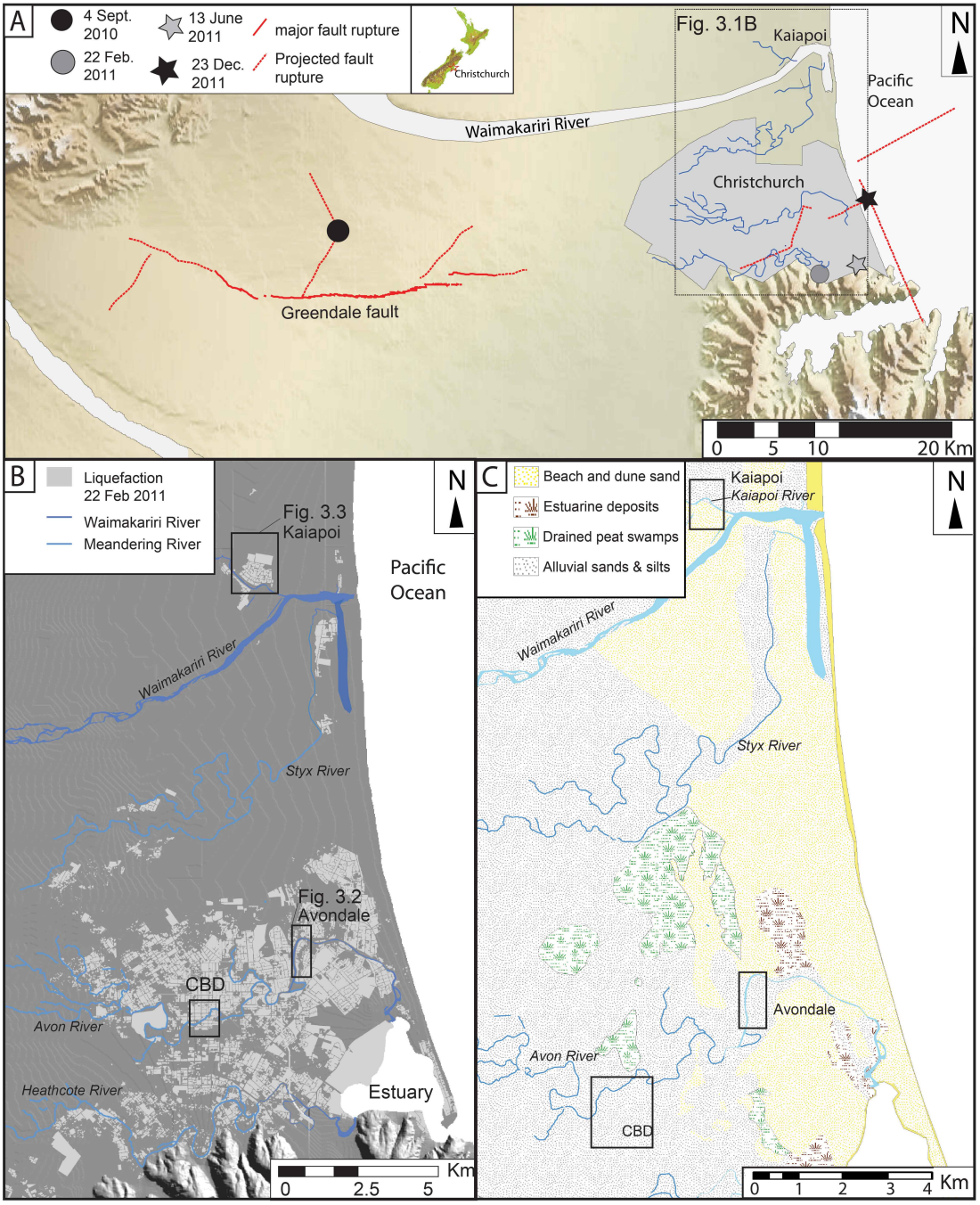

FIGURE 3.1: A) Epicentral locations of the 2010-2011 CES earthquakes that triggered liquefaction within Avondale and Kaiapoi. The rupture of the Greendale fault (bold line) and projected locations of the subsurface faults (dotted lines) that ruptured during the February, June, and December 2011 earthquakes are also indicated (Modified from Quigley et al. (2013)). B) Aerial extent of liquefaction within the wider Christchurch area as mapped following the 22 February 2011 earthquake. C) Simplified map of the surficial sediments in the wider Christchurch area (modified from Brown and Weeber (1992) and Forsyth et al. (2008)) with the locations of the Avondale (Fig. 3.2) and Kaiapoi (Fig. 3.3) study areas indicated with respect to the Christchurch CBD.

pose a long recognized high liquefaction hazard (Elder et al., 1991; Brown and Weeber, 1992; Christchurch Engineering Lifelines Group, 1997; Clough, 2005).

3.2.1 Avondale Study Area

The study area of Avondale, eastern Christchurch experienced severe liquefaction induced damage during the CES (Fig. 3.1). The southern extent of the suburb is situated adjacent to an anthropogenically straightened section of the meandering Avon River which undergoes tidally influenced flow inversions. Straightening of the river was completed in 1950 to allow for improved rowing on the river. The northern extent of the suburb is encompassed by an inner depositional bank of the Avon River (Fig. 3.2A). The area is underlain by fine sand and silt of point bar, over-bank, and adjacent swamp deposits of the Avon River (Fig. 3.1) (Silby, 1856; Brown and Weeber, 1992). Areas of low elevation (>1 m a.s.l) adjacent to the river were in-filled by ∼1 m of river dredging comprising sand and silt prior to the subdivision of the area in the early 1960s (Wilson, 1989). The approximate position of the ∼3000 yr B.P. coastline is ∼1.5 km west of the study sites; the ∼2000 yr B.P. coastline was ∼0.5 km to the east (Brown and Weeber, 1992). The water table is at ∼ 1 m depth however this may rise to ≤0.5 m depth during wet periods (Brown and Weeber, 1992).

Three former residential properties were chosen for trenching (Fig. 3.2A); the site at 31 Ardrossan Street (henceforth Site 3; Fig. 3.2B), 45 Cardrona Street (henceforth Site 4; Fig. 3.2C), and the driveway of 53 Cardrona Street (henceforth Site 5; Fig. 3.2D). The three sites were selected based on the intensity and alignment of liquefaction ejecta across the sites. Low elevation sites directly adjacent to the river were avoided due to the inferred presence of fill and height of the water table (∼1 m).

3.2.2 Kaiapoi Study Area

The second study area comprises the township of Kaiapoi (population 10,200), located ∼20 km north of Christchurch city and within ∼4 km of the present Pegasus Bay coastline (Fig. 3.1). The township is situated adjacent to the banks of the Kaiapoi River on a low relief and low elevation alluvial landscape (0 to 2 m above sea level). The Kaiapoi River represents the former north branch of

FIGURE 3.2: A) Aerial photograph of the Avondale study area with the locations of Sites 3-5 and the proximal CPTs indicated. B-D) Interpreted aerial photographs of Site 3 (B), Site 4 (C), and Site 5 (D) with trench locations and the distribution of liquefaction ejecta following the February 2011 earthquake indicated.

the Waimakariri River; flow was diverted to the south branch through a canal constructed in 1868 and followed by levees in 1930 (Griffiths, 1979). The north branch became confined to a single channel within Kaiapoi, re-named the Kaiapoi River in 1969 (Wood, 1993). The area north of the Kaiapoi River is primarily underlain by fine sand of beach and dune deposits, and fine sand to silt of overbank flood deposits of the Kaiapoi River and former north branch (Hawkins, 1957). The water table is at ~1-0.8 m depth however this may rise to ≤0.2 m depth during wet periods (Brown and Weeber, 1992).

Two sites were chosen for trenching (Fig. 3.3A); the former residential property at 125 Sewell Street (henceforth Site 6; Fig. 3.3B) and Kirk Street Reserve (henceforth Site 7; Fig. 3.3C). Site 6 was selected as it was identified by Berrill et al. (1994) as likely to have liquefied during the 1901 Cheviot earthquake. Site 7 was

FIGURE 3.3: A) Aerial photograph of the Kaiapoi study area with the location of study sites 6-7 and proximal CPT indicated. B) Interpreted aerial photograph of Site 6 following the February 2011 earthquake with the location of the trench and liquefaction ejecta indicated. C) Aerial photograph of Site 7 with the trench location and liquefaction ejecta indicated.

selected as it is proximal to the area identified as liquefying during the 1901 earthquake (Berrill et al., 1994), exhibited CES surface ejecta, and lacked near-surface anthropogenic influences on the spatial distribution of CES liquefaction ejecta.

3.3 Methods

3.3.1 Trenching

The distribution of surficial CES liquefaction features were determined at each site from high resolution aerial photographs flown on 24 February 2011 by NZ Aerial Mapping for the Christchurch Response Centre were examined to determine (Fig. 3.2 & 3.3). Trenches were excavated perpendicular to aligned sand blow vents at each site (Fig. 3.2 & 3.3). Trench walls and selected sections of the trench floor were cleaned using hand-held scrapers then logged at centimetre scale to document the morphology and stratigraphic relationships of the CES and pre-CES liquefaction features. Liquefaction features and stratigraphy were described in terms of their grain size, sorting, colour, and degree of sediment mottling. Full sediment descriptions of each unit are presented in Table A2; Appendix A. Munsell soil colours are not included as these were not documented during trenching.

3.3.2 Radiocarbon dating

Ages of the pre-CES liquefaction features and trench stratigraphy were approximated from radiocarbon dating of detrital wood and shell fragments. Dating was limited by the availability of organic material within the trenches. Samples of detrital wood were dried at 40°C for one week then sorted to separate the organic material from the host sediment. Between 10 - 20 mg of the organic material (charcoal or shell) was submitted to the Rafter Radiocarbon Laboratory in Wellington, New Zealand for Accelerator Mass Spectrometry (AMS) Radiocarbon analysis. Samples were prepared for analysis by sub-sampling, picking and grinding of the fragments, repeated acid and alkali treatment, then combusted and converted to graphite by reduction with hydrogen over iron catalyst. Ages were calibrated using Southern Hemisphere calibration curve (SHCAL04) (McCormac et al., 2004). Radiocarbon ages are reported in the text as 2-sigma calendar calibrated age ranges. Sample descriptions, un-calibrated conventional radiocarbon ages, and detailed age range distributions of the calendar calibrated ages are presented in Table 3.1. Detailed descriptions of the calibrated age ranges are presented in Appendix C.

3.3.3 Cone Penetration Tests

CPT (Cone Penetration Test) soundings conducted adjacent to Sites 3-7 during the CES were collated to analyze the liquefaction potential of the subsurface sediments (Fig. 3.2 & 3.3). The liquefaction potential of the subsurface sediment was evaluated using the Idriss and Boulanger (2008) method, which compares the cyclic stress ratio (CSR), which evaluates loading induced at different depths by an earthquake, with the cyclic resistance ratio (CRR) that represents the ability of the soil to resist liquefaction. The likelihood that a soil will liquefy is expressed as a factor of safety against liquefaction (FS), which is the ratio of CRR and CSR; liquefaction is predicted to trigger when FS >1. The Boulanger and Idriss (2014) method was not employed as this analysis was conducted prior to publication of this methodology.

3.4 Study Area: Avondale

The three Avondale sites (Sites 3-5; Fig. 3.2A) are located within 110 m of the Avon River. Site 3 is located at the apex of the meander bend and exhibits flat topography at 1.9 to 2 m a.s.l across the site (Fig. 3.2B). Sites 4 and 5 are located along the relatively straight section of the Avon River and exhibit elevations of 2.3 - 2.8 m a.s.l. across the sites (Fig. 3.2). The post-February 2011 aerial photography indicates that lateral spreading induced fissuring and associated sand blows formed across the three sites (Fig. 3.2).

Trenches were excavated at each of the three sites; the trench at Site 3 was excavated to a length of ∼8 m and a depth of ∼1.5 m, the trench at Site 4 was excavated to ∼5 m and a depth of ∼0.9 m, while the trench at Site 5 was excavated to a length of ∼3 m and depth of ∼1.1 m (Fig. 3.2). Trench depths were limited by the depths to the water table which was at ≤1.5 m during excavation. Trench logs are presented in Figure 3.4, and selected field photographs are presented in Figures 3.5 and 3.7. The CPT data is presented in Figure 3.6.

3.4.1 Trench stratigraphy

The trench at Site 3 exposed stratigraphy comprising a basal non-plastic silt to fine sand (unit II) with an interbedded lens of fine to very fine sand (unit III) and overlain by carbonaceous silt to very fine sand (unit I; Fig. 3.4). The stratigraphy is capped by silt to fine sand with granules (unit A3), silt to very fine sand (unit A2), and granules (unit A1; Fig. 3.4A).

The trench at Site 4 exposed a basal non-plastic silt with interbedded very fine sand (unit VI) which is overlain by carbonaceous, very fine sand to silt (unit IV) that contains a lens of fine to very fine sand (unit V; Fig. 3.4B & C). The stratigraphy is capped by granules (unit A1; Fig. 3.4B & C).

The trench at Site 5 exposed a basal fine to very fine sand (unit X) with an interbedded lens of carbonaceous very fine sand to silt (unit XI; Fig. 3.4D). This is overlain by carbonaceous very fine sand (unit VIII) with interbedded lenses of fine to very fine sand (unit IX) and capped by carbonaceous, very fine sand to silt (unit VII; Fig. 3.4D). The stratigraphy exposed in the three trenches is mottled and oxidized below ∼0.5 m depth. Full sedimentological descriptions of each unit are presented in Table A2; Appendix A.

The non-plastic silts to very fine sands exposed in the trenches at Sites 3-5 (units II, VI, & XI) are interpreted as low energy over-bank flood deposits of the Avon River (Fig. 3.4). The fine to very fine sands exposed in the three trenches (unit III, V, VIII, IX & X) suggest that the flood plain periodically received sediment during flood events (Fig. 3.4). The fluvial stratigraphy is consistent with the inferred pre-European migration of the Avon River across the site and historical reports of periodic flooding of the Avon River during periods of heavy rain between 1865 and 1953 (Cowie, 1957).

Unit IV in the trench at Site 4 and unit VII in the trench at Site 5 (Fig. 3.4D) are interpreted as topsoil horizons. There are no well-documented rates of soil formation for the Canterbury urban area due to the varied land uses throughout the development of the region, thus no surface age may be inferred from soil thickness. Unit I exposed in the trench at Site 3 (Fig. 3.4A) is interpreted as a buried soil horizon based on the similar appearance to Unit IV and VII and presence of modern rootlets. It is likely that Unit I is associated with the infilling of the area prior to subdivision (Wilson, 1989). Unit A3, which overlies unit I, is interpreted as

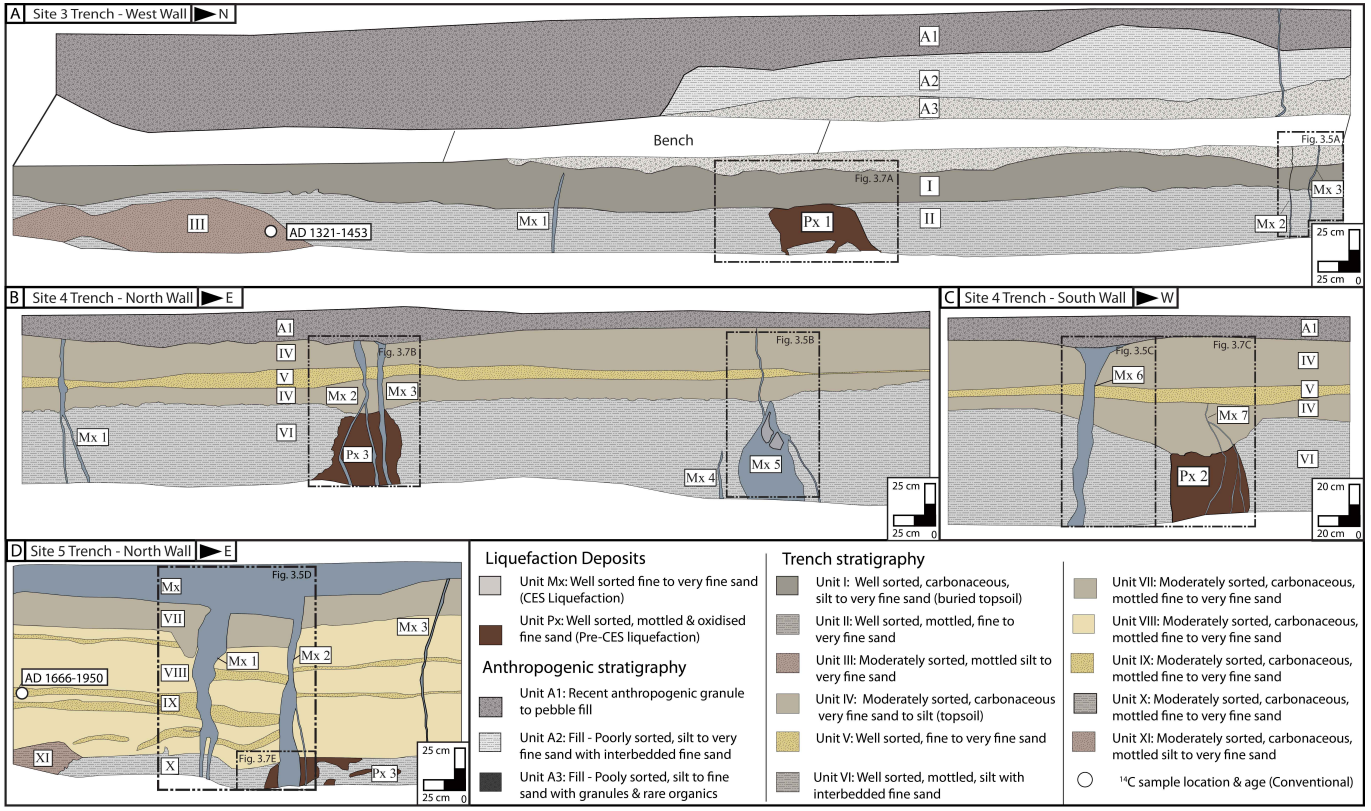

FIGURE 3.4: A) Detailed log of the west wall of the trench at Site 3. The Canterbury earthquake sequence (CES) dikes (Mx1-3) crosscut the fluvial stratigraphy. A pre-CES dike (Px 1) crosscuts unit II and is overlain by buried topsoil (I). Locations and results of the ^{14}C samples are indicated. B) Detailed log of the north wall of the trench at Site 4. The CES dikes (Mx1-5) crosscut the fluvial stratigraphy and are truncated by post-CES fill (A1). The CES dike Mx 5 extends upwards from a bulbous injection feature. A pre-CES dike (Px 2) crosscuts unit VI and is truncated by unit IV which thickens in the area overlying the dike. C) Detailed log of the south wall of the trench at Site 4. The pre-CES dike (Px 2) crosscuts unit VI and is overlain by unit IV which thickens above the dike. D) Detailed log of the north wall of the trench at Site 5. The CES dikes (Mx1-3) crosscut the fluvial stratigraphy and dissipates into the surface ejecta (Mx). A possible pre-CES injection feature (Px 3) crosscuts unit X. The locations and results of the ^{14}C samples are also indicated.

the river dredging used to infill the site and mixed with granules likely deposited during construction at the site (Fig. 4A). Unit A2 was likely deposited during occupation at the site post-1860. The surficial granules exposed in the trenches at Site 3 and 4 (unit A1; Fig. 3.4) are interpreted as post-CES deposits associated with the demolition of the former residential dwellings, subsequent waste removal, and levelling of the site.

Radiocarbon dating of sub-rounded wood fragments obtained from unit III at 1.5 m depth in the trench at Site 3 (R1; Fig. 3.4A) and from unit IX in the trench at Site 5 at 0.6 m depth (R2, Fig. 3.4D) yielded ages of AD 1321 - 1453 (R1) and AD 1666 - 1950 (R2) respectively (Table 3.1). Both R1 and R2 lacked root-like geometries suggesting that they were of detrital origin, thus the reported ages are interpreted to approximate the maximum depositional ages of the sediment.

3.4.2 CES liquefaction features

CES liquefaction features were recognised in the subsurface by (a) their alignment with and traceable continuity into the observed surface CES features, and (b) their crosscutting relationships with the trench fluvial stratigraphy. The morphologies of the subsurface CES liquefaction features are documented in detail to assist with the identification and interpretation of pre-CES liquefaction features.

The surface sand blows intersected in the three trenches (Fig. 3.2) correspond with sub-vertical and planar dikes in the subsurface (Fig. 3.4). The dikes vary in width from 1-3 cm in the trench at Site 3, 3-9 cm at Site 4, and 2-15 cm at Site 5. The <2 cm wide dikes in the trench at Site 3 (Fig. 3.4A & 3.5A) are composed of well-sorted silt to very fine sand, while the >2 cm wide dikes in the three trenches are all coarser and composed of well-sorted fine to very fine sand (unit Mx). The dikes all increase in width with depth and lack the oxidation and mottling developed in the surrounding stratigraphy (Fig. 3.4 & 3.5). Dikes in the trenches at Site 3 and 4 crosscut the fluvial stratigraphy from the trench floor and are truncated by the post-CES fill (unit A1) thus indicating that they formed during the CES (Fig. 3.4 & 3.5). The dikes in the trench at Site 5 crosscut the stratigraphy from the trench floor to the surface where they dissipate into the surficial fine to very fine sand with internal silt drapes that is interpreted as CES liquefaction ejecta (unit Mx; Fig. 3.4D & 3.5D). No evidence for vertical grading is observed within these dikes.

TABLE 3.1: Radiocarbon data and age estimates

Sample No.	Locality	Depth (m)	Description	δ13C and source of measurement	Radiocarbon Age (years BP)	Calendar calibrated age	
						2σ	1σ
R1	Site 3	1.5	Wood fragment from Unit III	-33.6 ± -33.6	563 ± 45	1321 - 1350 AD (10.7% of area) 1387 - 1453 AD (84.4% of area)	1398 - 1439 AD (69.0% of area)
R2	Site 5	0.6	Wood fragment from Unit IX	-26.6 ± 0.2	195 ± 20	1666 - 1709 AD (25.7% of area) 1721 - 1812 AD (57.4% of area) 1837 - 1847 AD (2.4% of area) 1858 - 1880 AD (5.0% of area) 1929 - 1950 AD (4.5% of area)	1671 - 1696 AD (21.6% of area) 1726 - 1747 AD (18.0% of area) 1756 - 1782 AD (18.5% of area) 1796 - 1807 AD (9.9% of area)
R3	Site 6	0.4	Wood fragment from Unit XIII	-27.6 ± 0.2	14807 ± 60	16548 - 16306 BC (32.6% of area) 16160 - 15747 BC (62.5% of area)	16496 - 16376 BC (22.4% of area) 16114 - 15919 BC (45.5% of area)
R4	Site 6	0.6	Wood fragment from Unit XIII	-26.1 ± 0.2	420 ± 16	1458 - 1497 AD (69.2% of area)	1454 - 1504 AD (76.9% of area) 1591 - 1615 AD (18.4% of area)
R5	Site 6	0.8	Wood fragment from Unit XIII	-36.9 ± 0.2	16452 ± 72	17922 - 17722 BC (32.9% of area) 17664 - 17466 BC (62.2% of area)	17825 - 17774 BC (12.9% of area) 17631 - 17491 (54.9% of area)
R6	Site 7	0.3	Shell fragment from Unit XVIII	0.7 ± 0.2	777 ± 22	1452 - 1644 AD (95.3% of area)	1468 -1576 AD (67.7% of area)
R7	Site 7	0.7	Wood fragment from Unit XXII	-23.8 ± 0.2	703 ± 16	1297 - 1314 AD (29.7% of area) 1359 - 1381 AD (39.8% of area)	

Dikes that crosscut the fluvial stratigraphy from the trench floor to between 0.5 to 0.7 m depth where they pinch out and terminate were also observed in the trench at Sites 3 (Mx 1 & 3) and 4 (Mx 4 & 7; Fig. 3.4 & 3.5). The similar morphologies, textures, and lack of oxidation and mottling in these dikes indicate that they are also of CES age (Fig. 3.4 & 3.5). A dike (Mx 5) on the north wall of the trench at Site 4 extends upwards from a bulbous shaped feature that exhibits sharp contacts with the surrounding fluvial sediment and is composed of fine sand with silt clasts (Fig. 3.4B & 3.5B). The morphology of this feature combined with its lack of mottling and oxidation indicates that it comprises a CES subsurface injection feature (Fig. 3.4B & 3.5B).

The increasing width of the dikes with depth supports that these dikes formed by the upwards injection of liquefied sediment as opposed to surface cracking in which features typically decrease in width with depth (Fig. 3.4 & 5) (Counts and Obermeier, 2012). The varied widths of the dikes identified in the three trenches may reflect variations in the three-dimensional geometries of the dikes. The sub-vertical planar morphology and well sorted grain-size distributions of these CES dikes and injection feature are consistent with the morphology and texture of dikes previously described in detail in Chapter 2. The consistent morphologies of the liquefaction features indicate that liquefaction is likely to manifest in the geologic record as sub-vertical planar dikes that increase in width with depth, are composed of well sorted sediment, and are of varying widths.

The CPT soundings indicate that the sediment profile from 2.6 to 5 m depth and beneath 7.5 m at Site 1 likely liquefied (FS <1) during the September 2010 earthquake, while the sediment beneath 2 m depth likely liquefied (FS <1) during the February 2011 earthquake (Fig. 3.6). The subsurface sediment at Sites 4 and 5 contains thin layers beneath 2 m depth that was potentially liquefiable (FS <1) during the September 2010 earthquake (Fig. 3.6). The sediment from 1.8 to 3.2 m depth and beneath 5 m depth likely liquefied (FS <1) during the February 2011 earthquake. The exact source depth cannot be determined directly as excavation was limited by the depth to the water table. The predominately gray, well sorted, silt to fine sand texture of the CES dikes identified in the three trenches suggests that a liquefiable unit or units containing fine sand to silt exists at depth beneath the three sites.

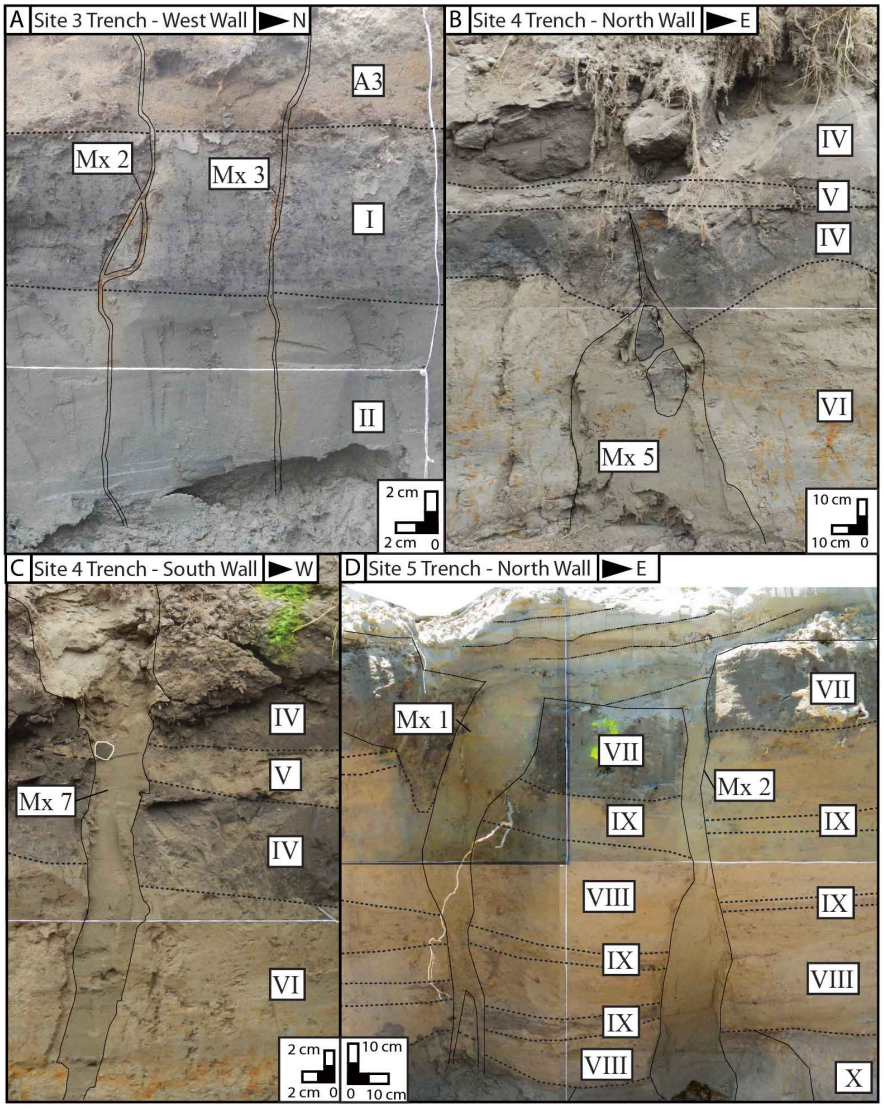

FIGURE 3.5: A) Interpreted field photograph of the west wall of the trench at Site 3. The Canterbury earthquake sequence (CES) dikes (Mx 2 & 3 and outlined in black solid line) crosscut the fluvial (I-II) and anthropogenic stratigraphy (A3) (outlined by black dotted lines). B) The fluvial stratigraphy (IV-VI and outlined by dotted black lines) on the north wall of the trench at Site 4 is crosscut by a CES injection feature (Mx 5 and outlined in solid black line) that extends upwards into a CES dike. C) The fluvial stratigraphy (unit IV-IV; outlined in dotted black lines) on the south wall of the trench at Site 4 is crosscut by a sub-vertical and planar CES dike (Mx 7; outlined in black solid line). D) The fluvial stratigraphy (VII-X; outlined by dotted black lines) on the north wall of the trench at Site 5 is crosscut by two sub-vertical and planar CES dikes (Mx 1 & 2) that feed the CES surface ejecta. Silt drapes preserved within the surface ejecta are indicated by black dashed lines.

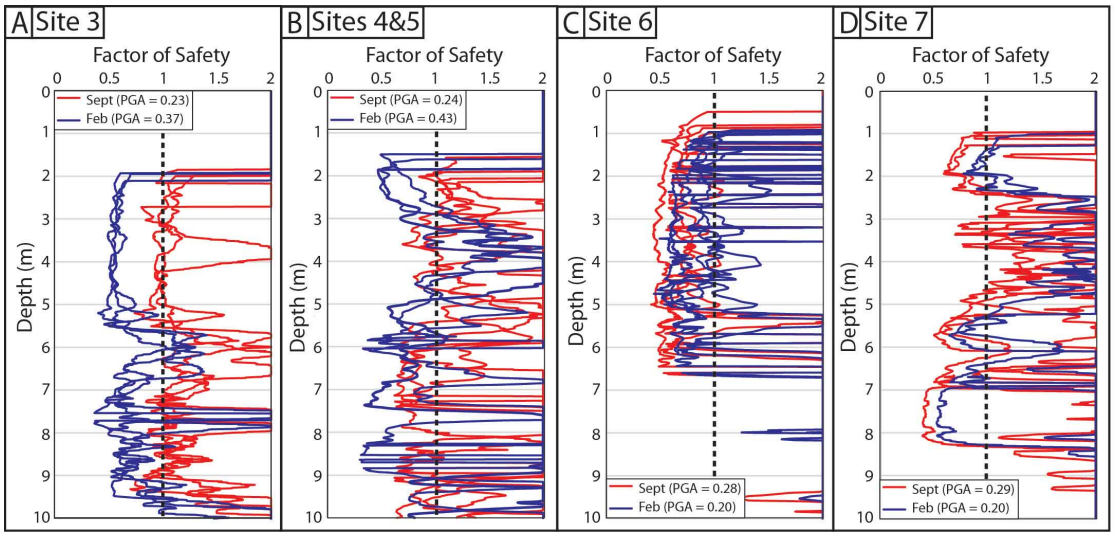

FIGURE 3.6: A) The CPT soundings indicate that the sediment profile from 2.6 to 5 m depth and beneath 7.5 m at Site 1 likely liquefied (FS <1) during the September 2010 earthquake; the sediment beneath 2 m depth likely liquefied (FS <1) during the February 2011 earthquake. B) The subsurface sediment at Sites 4 and 5 contains thin layers beneath 2 m depth that were potentially liquefiable (FS <1) during the September 2010 earthquake, while the sediment from 1.8 to 3.2 m depth and beneath 5 m depth likely liquefied (FS <1) during the February 2011 earthquake. C) At Site 6, the sediment profile beneath 0.5 m at likely liquefied (FS <1) under the PGAs of the September 2010 earthquake, and beneath 0.5 m likely liquefied during the February 2011 earthquake. D) Lenses within the sediment profile beneath 1 m depth at Site 7 likely liquefied during the September earthquake, while lenses within the sediment beneath 1.2 m depth likely liquefied during the February 2011 earthquake.

3.4.3 Pre-CES liquefaction features

Pre-CES liquefaction features were identified in the trenches (Fig. 3.4) based on their mottling and oxidation, morphology, and crosscutting relationships with the CES liquefaction features and surrounding stratigraphy.

Sub-vertical and planar dikes ~20-40 cm wide and composed of mottled and oxidised well sorted fine sand to silt (unit Px) crosscut unit II in the trench at Site 3 and unit VI in the trench at Site 4 (Fig. 3.4 & 3.7). The sub-vertical and planar morphology and the well-sorted texture of these dikes is consistent with the CES dikes identified within the trenches. The dike (Px 1) exposed at Site 3 is truncated by unit I and exhibits no evidence for surface ejecta. It could not be determined whether the dike continued across the trench floor due to flooding of the trench, however, the dike was not observed on the opposite trench wall. The oxidised dike (Px 2) exposed in the trench at Site 4 is overlain by unit IV which thickens from

∼35 cm to ∼60 cm in the area above Px 2 (Fig. 3.4B, 3.4C, and 3.7B). The dike (Px 2) could be traced across the trench floor where it corresponds with a dike (Px 2) on the south wall that is also overlain by unit IV (Fig. 3.7C & D). At Site 5, a CES dike (Mx 2) crosscuts an irregular, bulbous shaped feature that is ∼10 cm wide and composed of mottled and oxidised fine sand to silt with silt clasts (Px 3). Px 3 crosscuts unit X and is crosscut by unit VII (Fig. 3.4D & 3.7E). It could not be determined whether the feature was dike fed as excavation was limited by the depth to the water table. The feature could not be traced across the trench floor due to flooding, and could not be identified on the opposite trench wall.

The sub-vertical and planar morphology of the oxidised and mottled dikes exposed in the trenches at Sites 3 and 4 suggests that they comprise pre-CES dikes or lateral spreading fissures (Fig. 3.4A). The lateral traceability and morphology of Px 2 at Site 4 combined with the thickening of the unit IV in the area overlying the dike suggests that the feature comprises a lateral-spreading fissure that was infilled by flood deposits while exposed at the surface (Fig. 3.4b, 3.7b, c & d). The sharp contacts and morphology of Px 3 are similar to the bulbous CES feature (Mx 5) identified at Site 4 and the pre-CES feature identified at Site 2 in Chapter 2. This suggests that Px 3 may have formed through the subsurface injection of liquefied sediment (Fig. 3.4D). This cannot be confirmed as no dike feeding the feature was observed. However, the silt clasts within Px 3 are consistent with inclusions observed within the CES features and attributed to the fragmentation and entrainment of host sediment during ejection of liquefied sediment, and thus supporting the interpretation that Px 3 comprises a pre-CES injection feature.

The mottling and oxidation of the sediment within Px 1-3 forms through the precipitation of reduced iron in pore spaces during lowering of the water table (van Breemen and Buurman, 2002). The presence of well-developed mottles and oxidation in Px 1-3 suggests long residence within fluctuating water tables, and thus indicates pre-CES emplacement. Px 1 in the trench at Site 3 crosscuts unit II indicating that it post-dates deposition of this unit dated at 1321 - 1453 AD by radiocarbon (R1; Fig. 3.4A). No evidence for surface ejecta or a buried surface was observed suggesting that the top contact was likely truncated prior to or during deposition and formation of the buried soil (unit I). Px 2 at Site 4 crosscuts unit VI and is overlain by unit IV (Fig. 3.4b). No samples suitable for dating were identified in the trench at Site 4 however, it may be inferred that the radiocarbon age of 1321 - 1453 AD for unit II may approximate the depositional age of unit VI

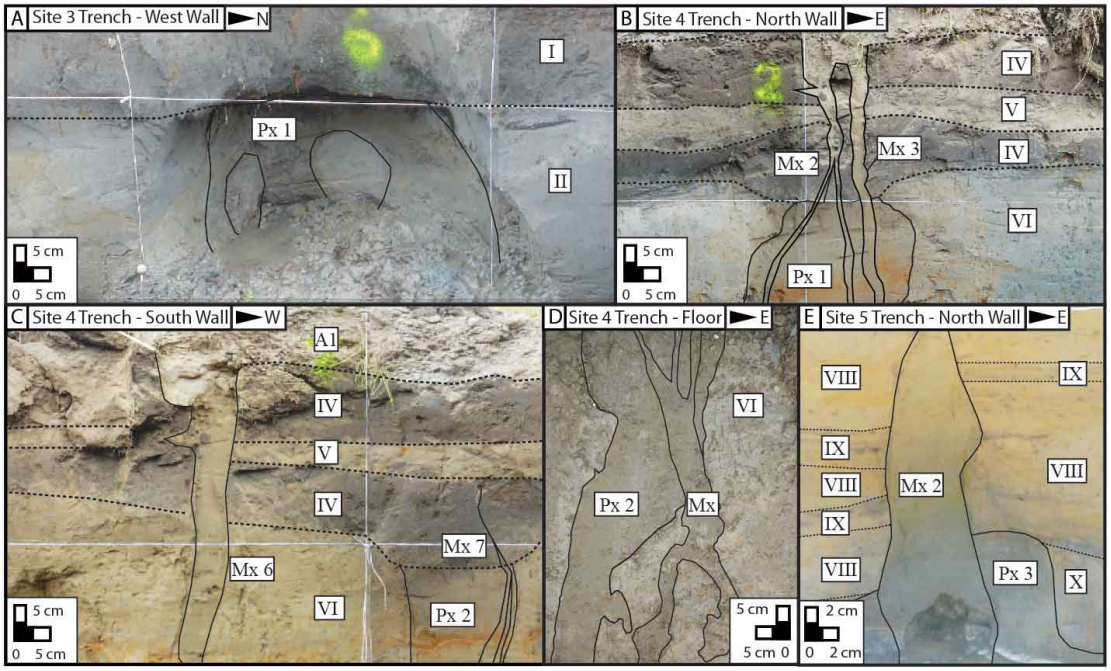

FIGURE 3.7: A) Interpreted field photograph of the west wall of the trench at Site 3. The pre-CES dike (Px 1; outlined in black) crosscuts unit II (outlined by black dotted line) and is truncated by unit I. B) Interpreted field photograph of the north wall of the trench at Site 4 indicating the alignment of the CES (Mx 2 & 3; outlined in black) and pre-CES dikes (Px 2). The pre-CES dike (Px 2) at Site 4 crosscuts unit VI and is overlain by units IV and V. (C) Interpreted field photograph of the south wall of the trench at Site 4. The pre-CES dike (Px 2) crosscuts unit VI which thickens in the area directly overlying the dike, and is cross-cut by small CES dikes (Mx 7). The well-developed oxidation line cross-cuts Px2 and is cross-cut by Mx 6. D) The CES dike (Mx) crosscuts the pre-CES dike (Px 2) on the trench floor. E) Interpreted field photograph of the north wall of the trench at Site 5. The possible pre-CES liquefaction injection feature (Px 3; outlined in black) crosscuts unit X and is overlain by unit VIII and cross-cut by the CES dike (Mx 2)

in the trench at Site 4 based on the proximity of the sites and similar stratigraphies. Px 2 may therefore post-date the radiocarbon ages of 1321 - 1453 AD. Px 3 at Site 5 is crosscut by unit VIII indicating that injection may pre-date the radiocarbon age of AD 1666 - 1950 derived for unit IX (Table 3.1; Fig. 3.4C).

The CES and pre-CES features identified in the three trenches are all composed of well sorted silt to fine sand which indicates that there are liquefiable units at depth containing fine sand to silt. The liquefiable source unit(s) was not observed within these trenches therefore it could not be determined whether the CES and pre-CES features were sourced from the same unit at depth.

3.5 Study Area: Kaiapoi

The two Kaiapoi sites (Sites 6-7; Fig. 3.3A) are located adjacent to an outer meander bend of the Kaiapoi River. The post-February 2011 aerial photography indicates that localized and aliened sand blows formed across both sites (Fig. 3.3). Trenching revealed stratigraphy that could not be correlated between the two sites, thus the two sites are discussed separately.

3.5.1 Site 6: Sewell Street

Site 6 is located within 75 m of the Kaiapoi River at 125 Sewell Street (Fig. 3.3b). The site exhibits relatively flat topography at 2.4 to 2.6 m a.s.l.. A trench was excavated to a length of ∼2.5 m and a depth of ∼0.9 m following the demolition of the former residential dwelling (Fig. 3.3b). The depth of the trench was limited by the depth to the water table which was at ≤0.9 m during excavation. The trench log is presented in Figure 3.8, and selected field photographs are presented in Figure 3.9. The CPT data is presented in Figure 3.6.

3.5.1.1 Trench stratigraphy

The trench exposed stratigraphy comprising a basal silt to very fine sand (unit XIII) with interbedded lenses of silt to very fine sand with cross-laminations (unit XIV), fine to very fine sand (unit XV), and fine to very fine sand with silt laminations (unit XVI; Fig. 3.8). Unit XIII is overlain by silt to very fine sand on the northern wall (unit XII; Fig. 3.8) and granules on the eastern wall (unit A1; Fig. 3.8). The stratigraphy is mottled from ∼0.3 m depth. Full sedimentological descriptions of each unit are presented in Table A2 in Appendix A.

Unit XIII is interpreted as low energy floodplain deposits, while the interbedded silts with cross-laminations and fine to very fine sands (units XIV, XV, XVI) indicate that the site was periodically flooded (Fig. 8). The fluvial stratigraphy is consistent with the present depositional setting within the low elevation (∼2 m a.s.l) floodplain of the Kaiapoi River and historical reports of flooding of the Kaiapoi River and former north branch of the Waimakariri River (Hawkins, 1957;

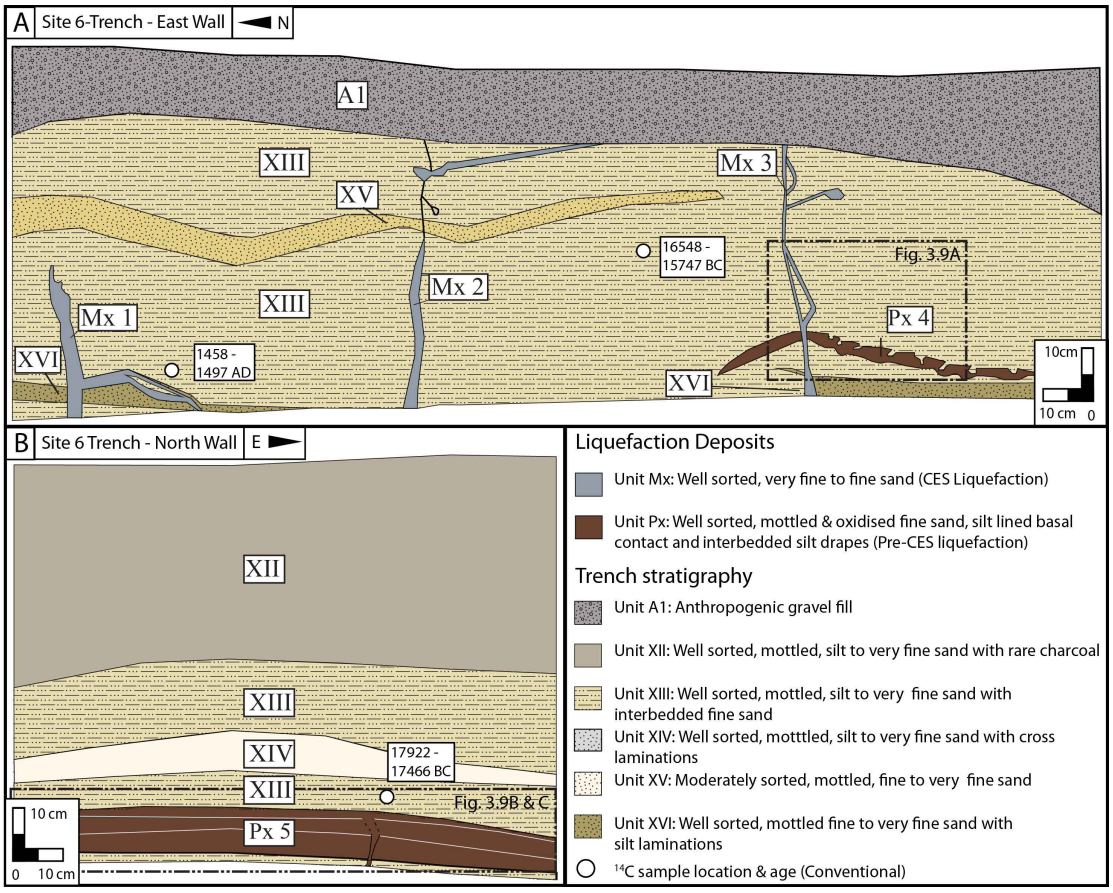

FIGURE 3.8: A) Detailed trench log of the east wall of the trench at Site 6. The CES liquefaction dikes (Mx1-3) crosscut the fluvial stratigraphy (XII-XVI) and are truncated by the post-CES anthropogenic fill (A1). The CES dike Mx 3 crosscuts an irregular sill with bioturbated contacts that is interpreted as a pre-CES sill (Px 4). (B) On the north wall of T4 (Site 4) a dike-fed pre-CES sand blow (Px 5) that contains two internal silt drapes is buried at ∼95 cm depth. The locations and results of the ^{14}C samples are also indicated.

log). The poorly sorted granules on the east wall (unit A1; Fig. 3.8A) are interpreted as post-CES fill. Unit XII on the north wall is interpreted as a topsoil horizon (Fig. 3.8).

Radiocarbon dating of three detrital wood fragments obtained from unit XIII at depths of 0.4 m (R3), 0.6 m (R4), and 0.8 m (R5) yielded ages of 16548-15747 BC (R3), AD 1458-1497 (R4), and BC 17922-17466 BC (R5) respectively (Table 3.1; Fig. 3.8). R3 and R5 provided age spectra inconsistent with R4 and the geologic evolution of the Canterbury coastline, indicating that they likely comprised older, re-worked detritus (Brown and Weeber, 1992; Forsyth et al., 2008). Samples R3 and R5 are therefore excluded from further discussions. R4 was composed of a small, sub-rounded wood fragment that lacked root-like geometries

or lateral continuity, thus suggesting that it was of detrital origin. The AD 1458-1497 age range of R4 is consistent with the geologic evolution of the Canterbury coastline (Brown and Weeber, 1992). The age is therefore interpreted as the maximum depositional age of unit XIII with the actual depositional age possibly much younger.

3.5.1.2 CES liquefaction features

The CES features were documented in detail to determine whether the morphologies of liquefaction features are consistent in the fluvial deposits of both the Avon and Kaiapoi Rivers and to aid identification of pre-CES features. The CES features are all composed of well-sorted fine to very fine sand and lack the oxidation and mottling developed in the surrounding stratigraphy (unit Mx; Fig. 3.8).

The trench exposed two sub-vertical and planar dikes in the subsurface (Mx 2 & 3) that vary in width from ∼2 to 5 cm and exhibit a complex branching pattern (Fig. 3.8 & 3.9A). Dikes Mx 2 and Mx 3 crosscut the fluvial stratigraphy and are truncated by unit A1 indicating that they pre-date deposition of Unit A1 (Fig. 8). Dike Mx 1 crosscuts the stratigraphy from the trench floor to ∼0.5 m depth where it pinches out and branches into a ∼20-30 cm long laterally injected sill (Fig. 3.8A & 3.9B). The lack of oxidation and mottling within Mx 1-3 indicates their recent emplacement, and thus suggests that they formed during the CES. The dikes all increase in width with depth and contain no evidence for vertical and/or lateral grading.

The CPT soundings indicate that the sediment profile beneath 0.5 m depth likely liquefied (FS <1) during the September 2010 earthquake, while the sediment beneath 0.9 m depth likely liquefied (FS <1) during the February 2011 earthquake (Fig. 3.6C). The exact source depth for the dikes cannot be determined directly as excavation was limited by the depth to the water table.

3.5.1.3 Pre-CES liquefaction features

The CES dike (Mx 3) on the east wall crosscuts an irregular sill with bioturbated contacts and comprised of well sorted, oxidised and mottled fine to very fine sand with internal silt drapes and silt clasts (Px 4; Fig. 3.8A & 3.9A). Px 4 crosscuts unit XIII from ∼60 - 65 cm depth and exhibits a morphology consistent with the

adjacent CES sill, and a texture consistent with the pre-CES dikes identified in the trenches at Site 3 and 4.

No dike feeding Px 4 was observed during excavation. Unit XIII on the north wall is interbedded with a mound-shaped feature at ∼85 to 95 cm depth that is composed of well sorted, oxidised and mottled fine sand (Px 5; Fig. 3.8B, 3.9B & C). The feature (Px 5) contains a silt lined basal contact, two internal horizontal silt drapes, and decreases in thickness towards the eastern and western walls of the trench (Fig. 3.8B, 3.9C & D). A ∼2 cm wide sub-vertical and planar dike extends from the trench floor and into the base of Px 5 at its thickest point. The dike exhibits a grain-size distribution and texture consistent with the feature and can be traced through the feature where it crosscuts the internal silt drapes and appears to dissipate into the upper unit of fine sand (Fig. 3.9B & C).

The mottling and oxidation formed within the sill (Px 4) and mound-shaped feature (Px 5) indicates their prolonged residence within fluctuating water tables, and thus indicates pre-CES emplacement (Fig. 3.8 & 3.9). The morphology, texture, and presence of silt clasts within Px 4 indicates that it comprises a pre-CES laterally injected sill, while its bioturbated contacts suggests emplacement occurred very near the surface. No dike feeding the sill was observed, however it is possible that it was re-activated by the CES dike or that the dike was not intersected within the trench. The sill crosscuts unit XIII indicating that injection post-dates the deposition of this unit dated at AD 1458 - 1497 by radiocarbon (R4; Table 3.1).

The dike beneath the oxidised mound-shaped feature (Px 5) indicates that it formed by the upwards ejection of liquefied sediment (Fig. 3.8B & 3.9C). The morphology and texture of Px 5 is consistent with a CES compound sand blow observed at another site by Quigley et al. (2013) which contained four episodes of liquefaction composed of oxidised fine sand grading to gray fine sand and overlain by a silt drape that could not be traced through the vent zone (Fig. 3.9). Px 5 is therefore interpreted as a pre-CES sand-blow, while the presence of two internal silt drapes suggests that three distinct episodes of liquefaction are preserved within the sand blow (Fig. 3.9B). No upper silt lined upper-contact was observed, indicating that the upper surface was likely re-worked. This should therefore be treated as the minimum number of liquefaction events. The pre-CES compound sand blow would have formed at the ground surface at the time of the pre-CES earthquake indicating that ∼0.95 m of sedimentation has since occurred at the site. The higher

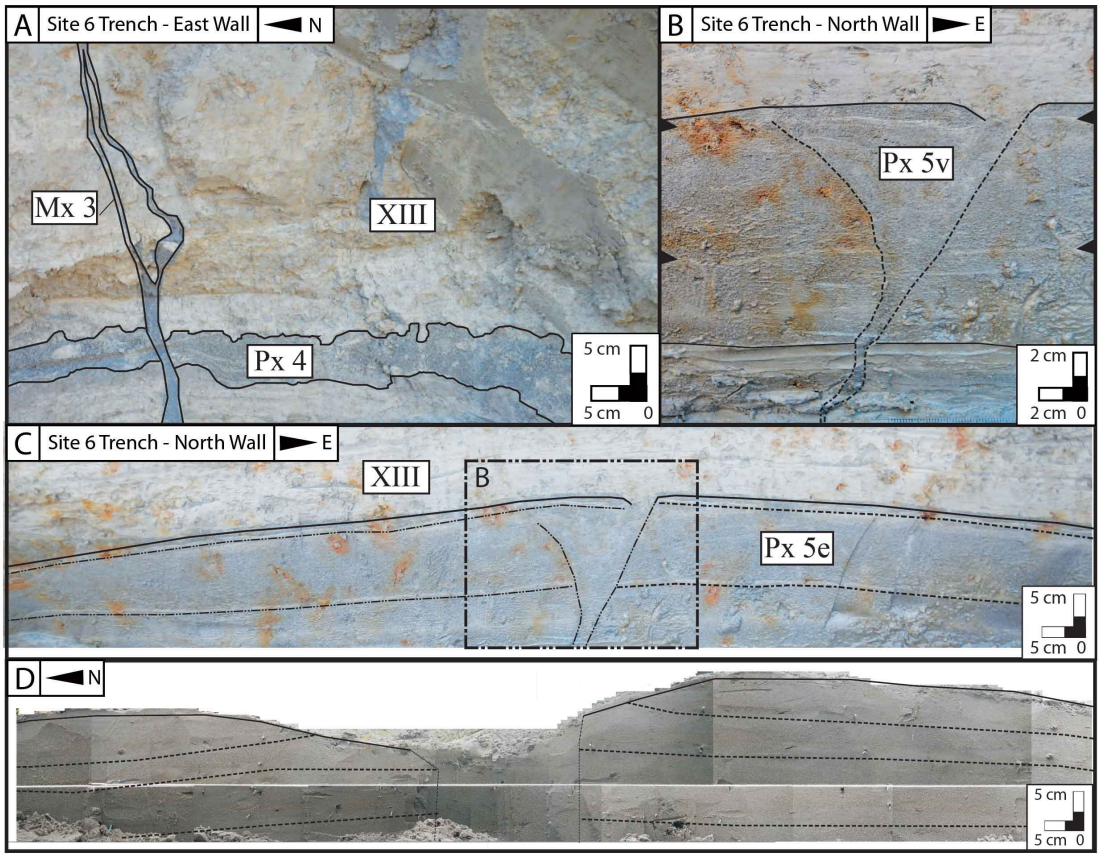

FIGURE 3.9: A) Interpreted field photograph of the east wall of the trench at Site 6. The CES dike Mx 3 crosscuts the fluvial stratigraphy (unit XIII) and the pre-CES lateral sill (Px 4). (B and C) Close-up interpreted field photographs of the north wall of the trench. The fluvial stratigraphy (unit XIII) is interbedded with a dike-fed pre-CES sand blow (Px 5 and outlined in black) that contains two internal silt drapes (arrows in B and dotted black lines in C) that cannot be traced through the vent zone. Px 5v in B identifies the vent zone while Px 5e in C identifies the surface ejecta. D) Interpreted field photograph of a CES sand blow (outlined in black) that contains internal silt drapes (black dotted lines) that cannot be traced across the vent zone (Modified from Quigley et al. (2013))

stratigraphic position of Px 4 (∼60-65 cm depth) indicates that two separate events are preserved within the stratigraphy exposed at the site.

3.5.2 Site 7: Kirk Street Reserve

Site 7 is located within 200 m of the Kaiapoi River and comprises relatively flat topography at 2.3 - 2.8 m a.s.l. across the site. A trench was excavated to a length of ∼6 m and a depth of ∼1.2 m (Fig. 3.3C). The depth of the trench was limited by the depth to the water table which was at ∼1.3 m during excavation.

The trench logs are presented in Figure 3.10 and selected field photographs are presented in Figure 3.11. The CPT data is presented in Figure 3.6.

3.5.2.1 Trench stratigraphy

The north wall of the trench exposed stratigraphy comprising a basal silt to very fine sand (unit XXIV; Fig. 3.10A) overlain by fine to very fine sand with granules and silt clasts (unit XXIII). Unit XXIII contains irregular and deformed lenses composed of fine to very fine sand with rare granules and carbonaceous silt clasts (unit XX), fine sand with cross-laminations and rare silt clasts (unit XXI), and a clast of unit XXIV. The lenses of unit XX and XXI warp around fragmented clasts comprised of silt to very fine sand with rare granules (unit XXII; Fig. 3.10A & 3.11A). The lenses of units XX and XXI all appear deformed, are poorly sorted, and exhibit no evidence for vertical grading or internal structure. Unit XVIII is overlain by normally graded, fine to very fine sand with granules and silt clasts interbedded with fine sand with cross-laminations (unit XVIII) and silt with rare granules and silt clasts (unit XVII).

The south wall exhibits similar stratigraphy of unit XXIV overlain by unit XXIII and lenses of XXI which contains fragments of XXII. These are overlain by unit XIX that is composed of normally graded, fine to very fine sand with cross-laminations, and a granule lined basal contact (Fig. 3.10B). The stratigraphy is capped by unit XVIII and a granule to pebble rich horizon (unit XVIII') which are crosscut by unit XVII (Fig. 3.10B). The stratigraphy is mottled from ∼60 cm depth. Full sedimentological descriptions of each unit are presented in Table A2 in Appendix A.

Unit XXIV is interpreted as a low energy over-bank deposit of the Kaiapoi River or former north branch of the Waimakariri River (Fig. 3.10). The normally graded sands (unit XIX and XVIII) and granule horizon (XVIII') on the south wall are interpreted as over-bank flood deposits. Unit XVII is interpreted as a topsoil horizon (Fig. 3.10). The deformation within unit XXIII and lenses of units XX and XXI are inconsistent with the inferred fluvial flood-plain deposition of the stratigraphy due to their poorly sorted grain-size distributions and irregular and deformed morphologies (Fig. 3.10A & 3.11A). It is possible that units XX and XXI comprised normally graded fluvial deposits, similar to unit XIX, prior to their deformation. The fragments of XXII exhibit a morphology inconsistent with the

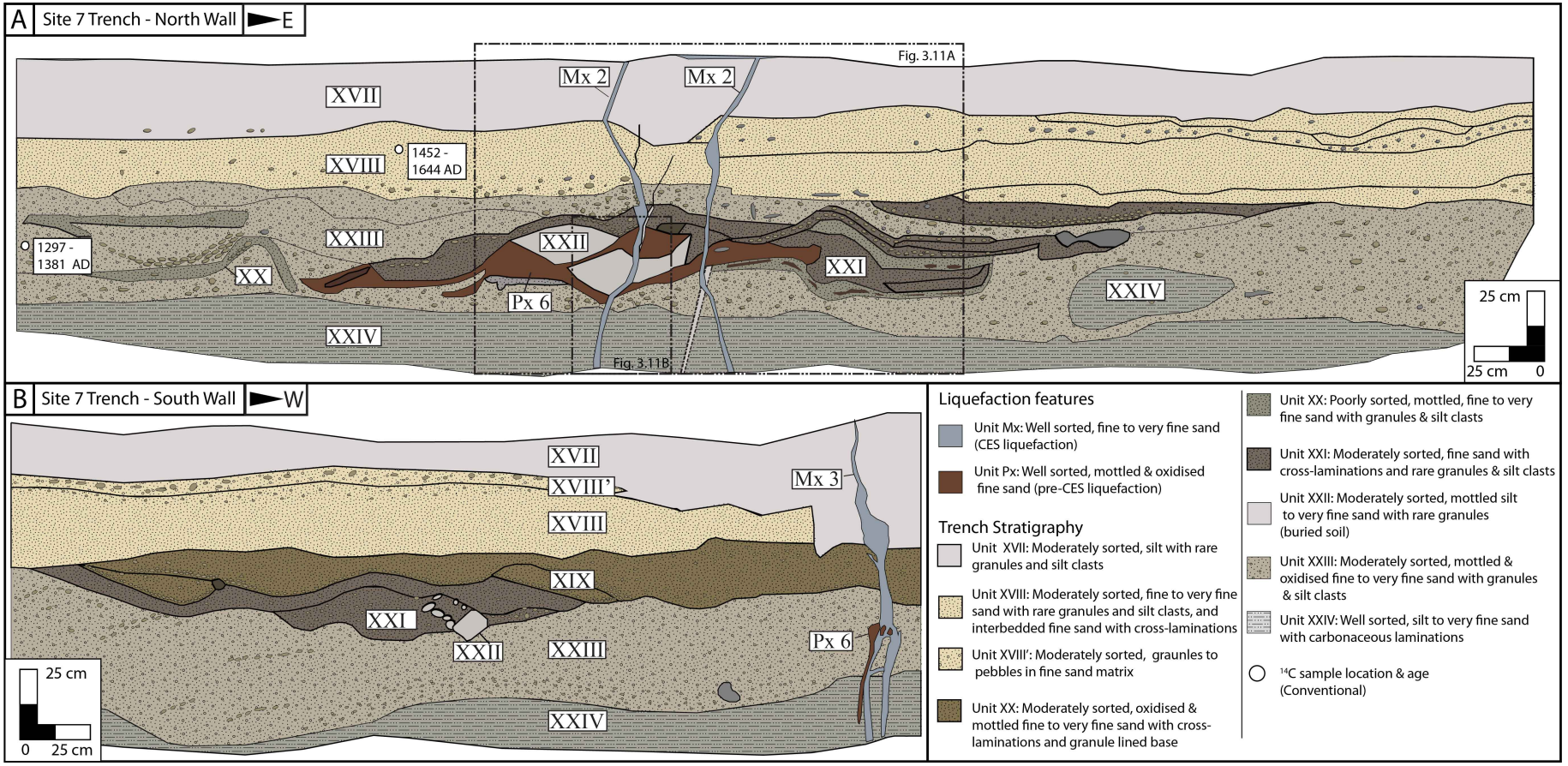

FIGURE 3.10: Detailed trench log of the north (A) and south (B) walls of the trench at Site 7. The CES dikes (Mx1-2) crosscut the stratigraphy (XVII-XXIV) from the trench floor to the surface. (A) The stratigraphy on the north wall contains lenses that exhibit soft sediment deformation (XX-XXI) and are inter-fingered by an irregular and discontinuous sill interpreted as pre-CES buried sand-blister (unit Px 6). The locations and results of the ^{14}C samples are indicated.

surrounding lenses, and a composition that is similar to unit XVII. Unit XXII is therefore interpreted as a fragmented buried soil horizon.

Radiocarbon dating of a shell obtained from unit XVIII at 0.3 m depth (R6) yielded an age of AD 1452-1644, while a wood fragment obtained from unit XXIII at 0.7 m depth (R7) yielded a radiocarbon age of AD 1297-1381 (R7; Table 3.1). The reported radiocarbon age of the shell (R6) is inconsistent with the timing of the historical shorelines that are well documented through the area, thus suggesting that it may have been deposited by anthropogenic activity (Brown and Weeber, 1992). Sample R7 was composed of a small, sub-rounded wood fragment that lacked root-like geometries or lateral continuity suggesting that it comprised detritus; it is therefore interpreted to reflect the maximum depositional age of the sediment.

3.5.2.2 CES liquefaction features

The surface sand-blows correspond with ∼2 to 4 cm wide, sub-vertical and planar dikes in the subsurface (Mx 1 & 3; Fig. 3.10). The dikes crosscut the stratigraphy from the trench floor to the surface indicating that they were emplaced during the CES (Fig. 3.10 and 3.11). The margins of Mx 1-3 are surrounded by an oxidised lining and pockets of oxidised fine sand from the trench floor to ∼75 cm depth. The oxidation suggests that the lining and pockets of fine sand pre-date the CES (Fig. 3.10 & 3.11B). Above 75 cm depth, the dikes lack the oxidation and mottling developed in the surrounding stratigraphy (Figs. 3.10 & 3.11A & B). The dikes are all composed of well-sorted fine to very fine sand, increase in width with depth, and contain no evidence for vertical grading.

The CPT soundings conducted adjacent to Site 7 indicate that the sediment profile beneath 1.0 m depth contains layers that likely liquefied (FS <1) during the September 2010 earthquake, whereas the sediment beneath 1.2 m depth contains layers that likely liquefied (FS <1) during the February 2011 earthquake (Fig. 3.6D). The exact source depth cannot be determined directly as excavation to this depth was limited by the depth to the water table.

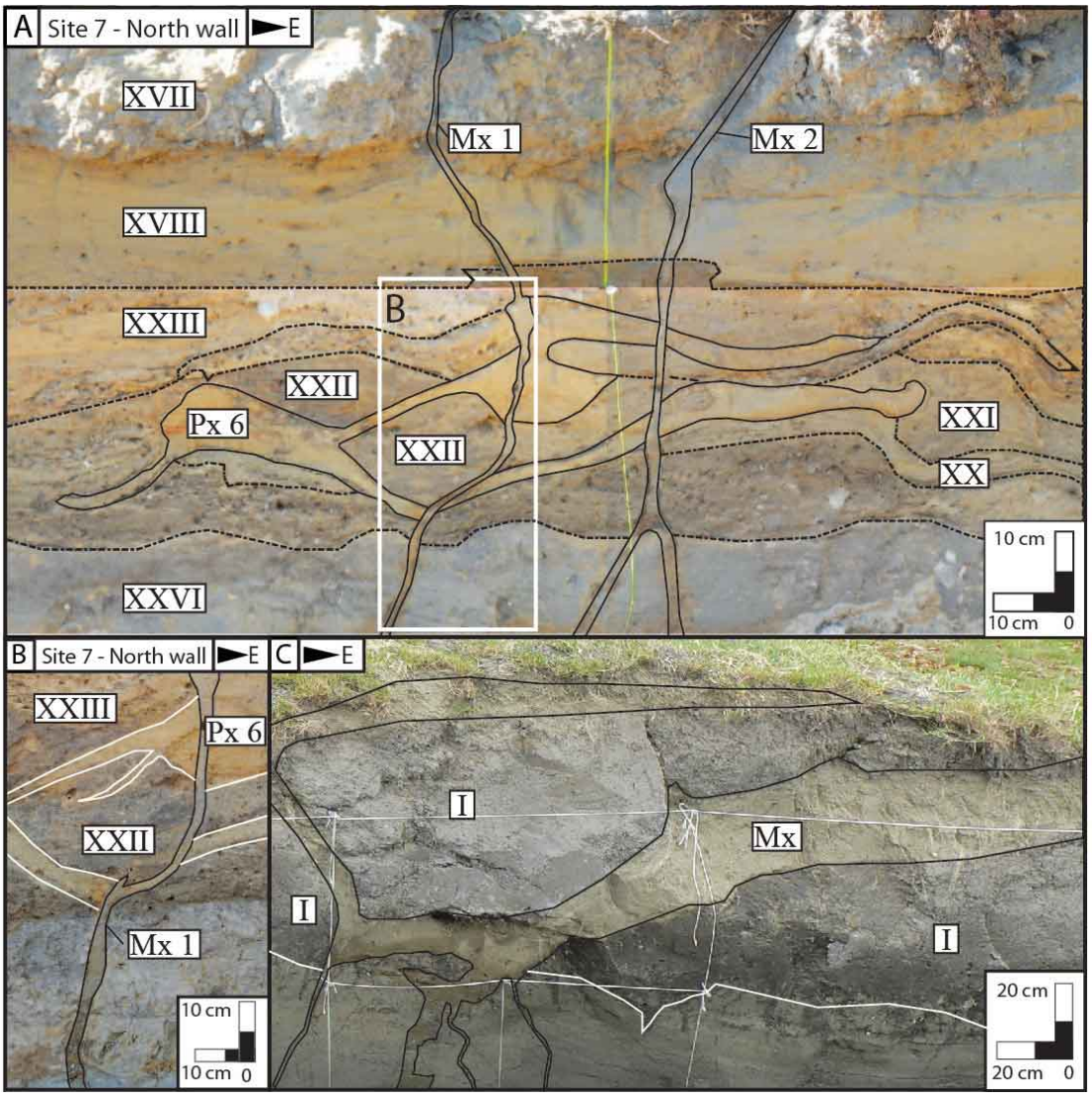

FIGURE 3.11: A) Interpreted field photograph of the north wall of the trench at Site 7. The CES dikes (Mx 1-2) crosscut the deformed stratigraphy (outlined in black dotted lines) from the trench floor to the surface. Units XX-XXI exhibit soft sediment deformation and are inter-fingered by Px 6 which is interpreted as a pre-CES sand blister. Unit XVIII is un-deformed indicating that it post-dates the deformation event. B) Close up and interpreted field photograph of the north wall of the trench at Site 7. The CES dike (Mx 1 and outlined in black) exhibits an oxidised margin from the trench floor to the base of Px 6 (outlined in white) suggesting that the CES dike re-activated the pre-CES sequence dike. C) Interpreted field photograph of a CES surface blister (Modified from Villamor et al. (2016)). The injected liquefied sediment (Mx) crosscuts and fragments the topsoil horizon (unit I).

3.5.2.3 Pre-CES features

A pre-CES liquefaction feature was identified based on its oxidation and mottling, well-sorted grain size distribution, and its crosscutting relationships with the CES features and surrounding stratigraphy.

The irregular and deformed lenses of units XX and XXI within unit XXIII are inter-fingered with an irregular and complex branching feature (Px 6) composed of oxidised and mottled well sorted fine sand (unit Px; Fig. 3.10A & 3.11A). The feature (Px 6) inter-fingers with the deformed units XX and XXI from ∼75 to 60 cm depth and appears to intrude around the contacts of the fragmented topsoil (unit XXII; Fig. 3.10A). The feature could not be identified on the south wall. The deformation and poorly sorted grain-size distributions within units XX and XXI are consistent with convolute bedding depicted in the study of soft-sediment deformation by Owen et al. (2011). The non-seismic methods for triggering deformation do not fit the depositional or hydrological setting of the study site, suggesting that deformation was likely earthquake induced (Owen et al., 2011).

The inter-fingering of Px 6 with units XX and XXI combined with its well sorted grain-size distribution and irregular morphology indicates that the feature was injected into the stratigraphy during the pre-CES earthquake that triggered the soft-sediment deformation. The intrusion of Px 6 around the margins of unit XXII suggests that Px 6 was injected in the near surface causing the former topsoil horizon (XXII) to fragment. This relationship is consistent with the subsurface morphology of a near-surface CES liquefaction injection feature that formed a surface blister and is described by (Villamor et al., 2016). The CES surface blister described by (Villamor et al., 2016) formed through the near-surface injection of liquefied sediment which caused the topsoil to fragment and warp upwards (Fig. 3.11C). Due to the similar morphology, Px 6 is interpreted as a pre-CES surface blister. No dike feeding Px 6 was observed during excavation, however the oxidised margins and fine sand surrounding the CES dike extends from the trench floor to the base of the oxidised feature at ∼75 cm depth and cannot be traced further. This suggests that the pre-CES dike may have been re-activated by the CES dike (Fig. 3.11B). Alternatively, an isolated dike that was not intersected within the trench may have fed Px 6. Px 6 inter-fingers with unit XXIII indicating that the pre-CES event most likely post-dates deposition of this unit and the radiocarbon age of AD 1297-1381 (R7; Table 3.1).

The stratigraphy of the south wall appears to exhibit lateral continuity and is un-deformed compared to the north wall. This suggests that the deformation was localised and further supports that Px 6 comprises a localised sand-blister (Fig. 3.10B). No evidence for a buried soil horizon overlying the deformed stratigraphy was observed, suggesting that the unit that the clasts of unit XXI were derived from may have been eroded prior to deposition of units XVII and XVIII (Fig. 3.10). Units XVII and XVIII do not exhibit deformation, indicating they were likely deposited following the pre-CES earthquake.

3.6 Possible timing of pre-CES earthquakes

The approximate timing of the earthquakes forming the pre-CES liquefaction features in Avondale and Kaiapoi may be constrained from crosscutting relationships combined with relative and ^{14}C ages of the host sediments. It cannot be directly determined whether the pre-CES liquefaction features in Avondale and Kaiapoi formed during the same pre-CES earthquake due to the large age ranges assigned to each feature.

The pre-CES dike identified in the trench at Site 3 (Px 1; Fig. 3.4A) crosscuts the fluvial sediment to ∼105 cm depth, or to ∼40 cm if the thickness of the post-CES fill (unit A1) is removed, Px 1 is overlain by unit I. The pre-CES dike, Px 2, in the trench at Site 4 (Px 2; Fig. 3.4B) crosscuts unit VI to ∼65 cm, or ∼40 cm without unit A1, and is overlain by unit IV. The proximity of the sites combined with the consistent morphology and similar depths of the pre-CES dikes suggests that these dikes likely formed during the same pre-CES earthquake. The dikes therefore most likely post-date the AD 1321-1453 radiocarbon age derived for unit III at Site 3 (R1) and pre-date subdivision of the area in 1960. It cannot be determined whether Px 2 at Site 4 also formed during this event due to the lack of age constraint (Fig. 3.4D).

The pre-CES lateral injection sill (Px 4) identified in the trench at Site 6 (Fig. 3.8A) most likely post-dates the radiocarbon age of AD 1458-1497 (R4; Table 3.1) for unit XIII, and possibly formed during the 1901 Cheviot earthquake, which is known to have caused liquefaction at the site (Berrill et al., 1994). The pre-CES sand blow (Px 5) identified at Site 6 formed at the then ground surface, and thus pre-dates the radiocarbon age of AD 1458-1497 for unit XIII (R4; Table 1).

No evidence for foreshore sediments were observed in the trench indicating that the feature post-dates the mid-Holocene high-stand at ∼6,500 yr before present. The preservation of three episodes of liquefaction within the compound sand blow provides evidence for recurrent liquefaction, and possible earthquake clustering of sufficient magnitude to trigger repeated liquefaction while the sand blow was exposed at the surface.

Quigley et al. (2013) derived a power-law equation for estimating relative $PGA_{7.5}$ based on the variations in relative stratigraphic thickness of units preserved within compound sand-blows. The three units identified within the paleo-sand blow at Site 6 (Px 5) have maximum stratigraphic thicknesses of 3.6 cm, 5 cm and 0.7 cm respectively (normalized to 0.72, 1.0, and 0.14 respectively). The thicknesses yield crude normalized $PGA_{7.5}$ estimates of the first and third units being ∼70% and ∼10% of the $PGA_{7.5}$ of the second event. As no silt upper-contact was observed on the third unit the thickness and relative $PGA_{7.5}$ estimates are considered to be minimums for this event.

The presence and stratigraphic relationships of the CES dikes, pre-CES sill, and pre-CES sand blow at Site 6 indicate that three separate episodes of liquefaction are preserved within the subsurface. This indicates that the area has been subjected to recurrent liquefaction.

The pre-CES surface blister at Site 7 in Kaiapoi (Px 6) deforms unit XXIII indicating that the deformation event likely post-dates the AD 1297-1381 radiocarbon age derived from 0.7 m depth within this unit (R7; Table 3.1). The earthquake-deformed stratigraphy is overlain by ∼0.5 m of fluvial sediment (units XVII and XVIII). It is considered unlikely that ∼0.5 m of accumulated at the site since the 1901 Cheviot earthquake which is known to have caused liquefaction in the area. The surface blister is therefore considered likely to pre-date the 1901 Cheviot earthquake. It cannot be determined whether the pre-CES surface sand blister at Site 7 formed during the same event as the pre-CES sill or sand blow at Site 6 due to the large age ranges assigned to the features and inability to correlate these units stratigraphically.

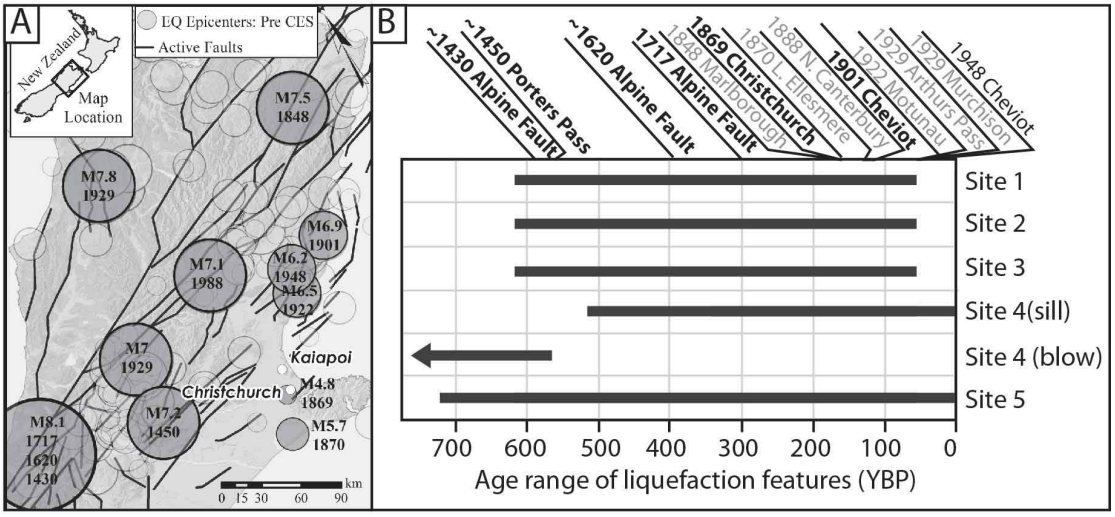

FIGURE 3.12: A) Locations of historic earthquakes and known active fault sources that are included in the PGA and back-calculation analysis (Fault data from Stirling et al. (2012) and Litchfield et al. (2014), and outlined in Table 4.3). B) Constrained ages of the pre-CES liquefaction features identified in Avondale and Kaiapoi compared with the chronology of known historic earthquakes (Pre-CES) that may have triggered liquefaction in the Canterbury region. Earthquakes considered likely to trigger liquefaction at the site (PL >15%) are indicated in black text.

3.7 The liquefaction potential of active faults

The limited historic record of earthquakes within the wider Canterbury region means that the distribution of active faults capable of triggering liquefaction is poorly constrained and thus the return times of earthquakes triggering liquefaction is largely unknown. Comparison of the timing of the historic and known paleo-seismic earthquakes with the age ranges of the pre-CES liquefaction features proves inconclusive in determining the likely causative event due to the large age ranges assigned to each feature (Fig. 3.12). The large age ranges assigned to the paleo-liquefaction features and high number of active faults within the wider Canterbury region causes a significant challenge in determining which earthquake sources might have triggered paleo-liquefaction at the five sites. For this reason the potential for known active faults to induce liquefaction at the study sites is assessed from peak ground accelerations (PGA) predicted at each site and compared with a global liquefaction triggering threshold, and from the back-calculated magnitude-bound curves derived by Maurer et al. (2015).

The liquefaction susceptibility of the five sites in eastern Canterbury is governed by their hydrologic, geologic and geomorphic settings. The liquefaction potential

of the subsurface sediments generally decreases over time due to aging including compaction, burial by continued sedimentation, and the precipitation of cements (Seed and Idriss, 1982; Idriss and Boulanger, 2008; Hayati and Andrus, 2009; Maurer et al., 2014). The subsurface sediments at the study sites are likely to have remained saturated since their initial deposition due to the high water tables within Avondale and Kaiapoi. This saturation combined with shallow burial depth and inferred young Holocene age suggests that limited aging has likely occurred. The liquefaction susceptibility of the five sites is therefore likely to have remained relatively unchanged or may have decreased slightly since the pre-CES liquefaction events. The presence of two episodes of liquefaction at Sites 3-4, and 7, and preservation of 3 episodes of liquefaction at Site 6 indicates that these areas have remained highly susceptible to liquefaction and any changes to the liquefaction source sediment during the pre-CES liquefaction events (e.g. compaction) has not had a discernible influence on the liquefaction susceptibility of the sites. The liquefaction-triggering threshold during the paleo-earthquakes is therefore likely to be consistent with or slightly lower than that during CES.

3.7.1 Site-specific peak ground accelerations for ruptures on active faults

Site-specific peak ground accelerations (PGA) are derived for Avondale and Kaiapoi from rupture scenarios on the known active faults within the wider Canterbury region using the New Zealand-specific ground motion prediction equation (GMPE) proposed by Bradley (2013) (Fig. 3.13). The Bradley GMPE considered four pre-existing global models and was derived from modification of the best-fit Chiou and Youngs (2008) model and calibrated against recorded ground motions in New Zealand. The model computes the median and standard deviation PGAs for a given site using the maximum moment magnitude ($M_{w\ max}$), distance of the fault trace to the site (R_{Rup}), predominant rock or soil type, and fault type (i.e. normal, reverse, or strike slip). Estimates of maximum moment magnitude ($M_{w\ max}$) and distances to fault rupture planes (R_{Rup}) were compiled for the wider Canterbury region using Stirling et al. (2012) and Litchfield et al. (2014) (Table 3.2). Data on offshore faults was derived from Barnes et al. (2011). Site Class E soil characteristics (Very soft soil) were assumed for both study sites (NZS.1170.5, 2004). Rupture directionality was not considered due to the lack of fault-specific

rupture data and as rupture directivity was not explicitly considered during the development of the GMPE.

The median (50th percentile) PGA is plotted for Avondale (Fig. 3.13A) and Kaiapoi (Fig. 3.13C) for each rupture scenario. Median PGA values were magnitude-weighted ($PGA_{7.5}$) using the magnitude scaling factor proposed by Idriss and Boulanger (2008). The $PGA_{7.5}$ represents the equivalent PGA for an M_w 7.5 event and enables direct comparison of ground accelerations irrespective of the earthquake magnitude and distance to epicentre. $PGA_{7.5}$ are plotted for each rupture scenario and compared with the liquefaction triggering threshold of $PGA_{7.5}$ 0.09 g derived by Santucci de Magistris et al. (2013) (Fig. 3.13). The PGA and $PGA_{7.5}$ of the September 2010 and February 2011 earthquakes are also plotted (Fig. 3.13). The corresponding fault name, M_w, PGA, and $PGA_{7.5}$ of the faults labelled in Figure 3.13 are summarised in Table 3.2. The PGA and $PGA_{7.5}$ calculated for all the active faults are summarized in Table B1 in Appendix B.

Active faults within 50 km of Avondale that are considered capable of generating M_w >6.5 earthquakes generally plot above the liquefaction triggering threshold of $PGA_{7.5}$ 0.09 g, indicating that they are likely to trigger widespread liquefaction (Fig. 3.13B). The predicted $PGA_{7.5}$ generated in Avondale from ruptures on the offshore Kaiapoi faults (13), total Kaiapoi faults (15), and the combined Kaiapoi and Pegasus faults (16) are similar to that of the September 2010 earthquake suggesting that ruptures on these faults may trigger moderate-to-severe liquefaction (Fig. 3.13B). The Alpine Fault between Fiordland and Kaniere (121) plots beneath the $PGA_{7.5}$ 0.09 g threshold for liquefaction, however plots above the threshold value for minor liquefaction in highly susceptible sediments during the CES of $PGA_{7.5}$ ~0.06 g (Quigley et al., 2013). This indicates that the 1717 Alpine Fault rupture remains a potentially culpable source for triggering liquefaction in the highly susceptible sediments within Avondale.

In Kaiapoi, the North Canterbury and offshore faults within 50 km of the study sites that are capable of generating M_w >5.5 earthquakes generally plot above the $PGA_{7.5}$ 0.09 g threshold (Fig. 3.13D). The higher number of active faults considered capable of triggering reflects the closer proximity of the area to the North Canterbury and offshore fault systems. The $PGA_{7.5}$ calculated for the combined offshore Kaiapoi (15), Kaiapoi and Pegasus combined (16), Kaiapoi offshore (13) and Pegasus (34) faults all exceed the $PGA_{7.5}$ of the September 2010 earthquake suggesting that they are likely to trigger widespread liquefaction in

TABLE 3.2: Active faults with modelled PGAs exceeding the liquefaction triggering threshold in Avondale and Kaiapoi

Fault ID	**Fault Name**	**M_w**	**Avondale**		**Kaiapoi**	
			PGA	**$PGA_{7.5}$**	**PGA**	**$PGA_{7.5}$**
1	Ashley	7.4	0.15	0.14	0.23	0.22
2	Ashley mouth	5.4	0.05	0.03	0.14	0.08
3	Ashley part	6.1	0.07	0.05	0.14	0.09
4	Cust	7.2	0.12	0.11	0.18	0.17
10	Offshore Fault VI	6.4	0.04	0.03	0.06	0.04
12	Hororata	7.4	0.09	0.09	0.10	0.10
13	Kaiapoi offshore	6.4	0.21	0.16	0.34	0.26
14	Kaiapoi offshore2	6.3	0.05	0.04	0.13	0.09
15	Kaipoi total	6.8	0.24	0.20	0.37	0.31
16	Kaipoi total plus Peg 4 + 4km	7	0.26	0.23	0.39	0.34
18	Kaiwara (South)	7.3	0.08	0.07	0.10	0.10
19	Leithfield	6.8	0.09	0.08	0.15	0.12
26	North Canterbury1	7	0.11	0.10	0.17	0.15
27	North Canterbury2	6.9	0.05	0.04	0.06	0.05
30	North Canterbury8	7.3	0.04	0.04	0.04	0.04
33	Omihi	6.7	0.06	0.05	0.09	0.08
34	Pegasus	7.2	0.18	0.17	0.32	0.29
36	Pegasus pup	5.6	0.09	0.06	0.14	0.08
37	Pegasus 3	6.2	0.08	0.06	0.12	0.08
38	Pegasus 4	6.1	0.09	0.06	0.11	0.08
39	Pegasus 5	6.5	0.13	0.10	0.22	0.17
40	Pegasus 6b	6.4	0.14	0.11	0.19	0.14
41	Port Hills	6.5	0.31	0.24	0.18	0.14
42	Porters to Grey	7.7	0.13	0.14	0.19	0.20
43	Springbank	7.2	0.13	0.12	0.21	0.20
44	Springfield	7.1	0.08	0.07	0.10	0.09
45	Waikuku	6.8	0.11	0.09	0.13	0.11
117	Wairarapa-Nicholson	8.3	0.02	0.03	0.03	0.03
121	Alpine (Fiord-Kelly)	8.3	0.06	0.07	0.07	0.09
122	Alpine (Kelly-Tophouse)	7.9	0.01	0.01	0.01	0.01
123	Hikurangi Wellington	9	0.05	0.07	0.05	0.08

Kaiapoi (Fig. 3.13D). The North Canterbury faults including the Ashley (1), Springbank (43), Cust (4), North Canterbury 1 (26), and Porters Pass- Grey (42) all plot between the $PGA_{7.5}$ of the September and February earthquakes indicating that they are also likely to trigger widespread liquefaction (Fig. 3.13D). The Alpine Fault between Fiordland and Kaniere (121) plots at $PGA_{7.5}$ 0.09 g suggesting that a rupture of this fault length or greater could have triggered liquefaction in Kaiapoi.

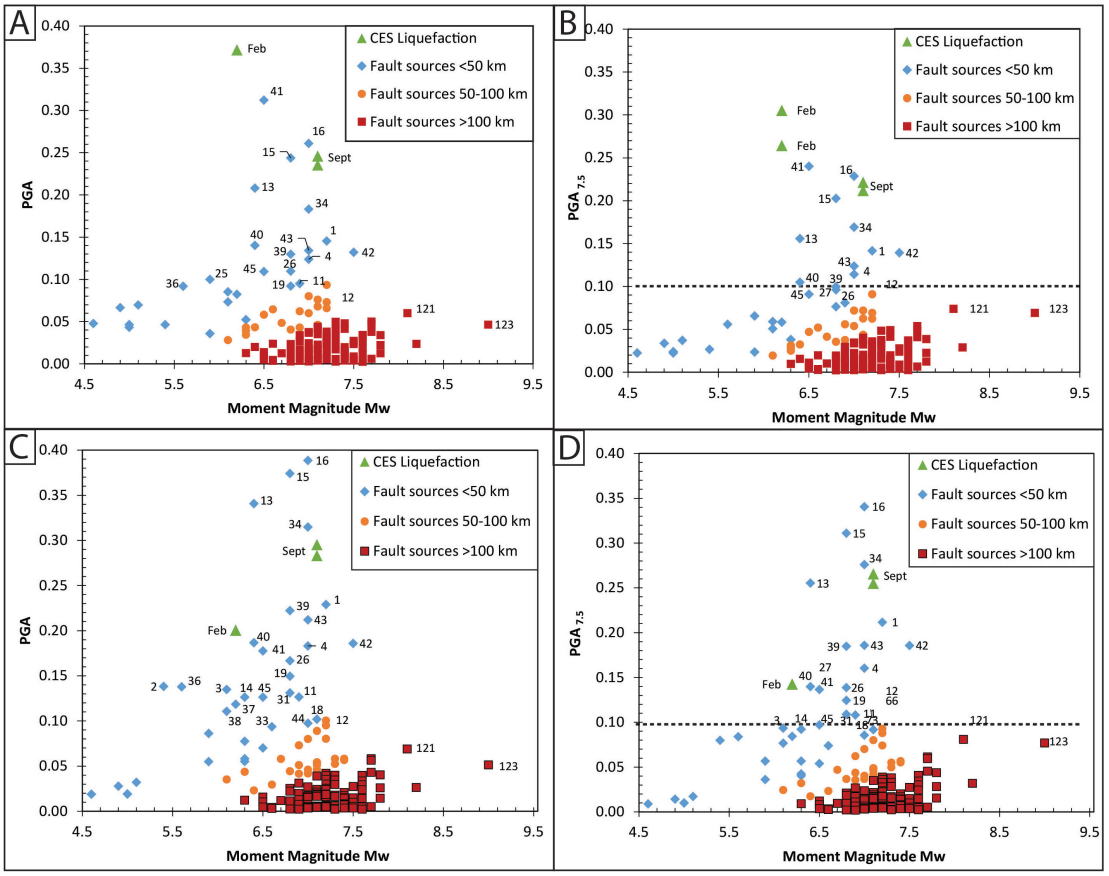

FIGURE 3.13: The calculated median PGA generated in Avondale (A) and Kaiapoi (C) for ruptures on active faults within the wider Canterbury region. The calculated median $PGA_{7.5}$ generated in Avondale (B) and Kaiapoi (D) are compared with the liquefaction triggering threshold of $PGA_{7.5}$ 0.096 g derived by (Santucci de Magistris et al., 2013). Numbers correspond to faults listed in Table 4.2; data on additional faults is presented in Table B1; Appendix B

Comparison of the site-specific PGA with the liquefaction-triggering threshold indicates that faults proximal (within 50 km) to the study sites are likely to trigger liquefaction. It is possible that the paleo-liquefaction features may have formed during pre-historic rupture(s) on these faults. Additionally, many active faults are predicted to generate $PGA_{7.5}$ between the 0.09 and 0.06 g thresholds for liquefaction at both the Avondale and Kaiapoi sites and thus provide additional possible sources for the paleo-liquefaction features (Fig. 3.13; Table B1 in Appendix B).

3.7.2 Probability of liquefaction from magnitude bound curves

The historic earthquakes and active fault sources are plotted in magnitude-bound space with the Maurer et al. (2015) probabilistic curves for Avondale (Fig. 3.14A & B) and Kaiapoi (Fig. 3.14C & D) to evaluate their probability of triggering liquefaction at the study sites. Maurer et al. (2015) derived the back-calculated magnitude bound curves from liquefaction triggering evaluation, site-response analysis, and ground motion prediction (Maurer et al., 2015). Faults with a calculated probability of inducing liquefaction (PL) >15% are considered likely to trigger liquefaction at the study sites (Fig. 3.14). Uncertainties in the probability of liquefaction for each event are quantified by providing minimum and maximum bounds, which approximate 95% confidence bounds (Table 3.3). The study sites are assigned to a single representative location within Avondale or Kaiapoi to simplify the analysis. This results in a minor miscalculation of the site-to-source distance of >0.5 km, which is within the 95% confidence bounds.

Rupture magnitudes and site-to-source distances of the large historic earthquakes were derived from paleo-seismic studies (Howard et al., 2005) and proposed source models (Doser et al., 1999). Empirical site-to-source distance conversions are applied for historic earthquakes with proposed epicentral locations (Scherbaum et al., 2004). Magnitude estimates and site-to-source distances of the active faults are adopted from Stirling et al. (2012) and Barnes et al. (2011) where a maximum rupture scenario is considered. The rupture magnitudes and site-to-source distances of the active-faults are assigned uncertainties of ± 0.36 M_w and ± 4 km, which represent approximate 95% confidence bounds. It is acknowledged that a fully probabilistic model would consider the range of earthquake magnitudes, recurrence interval, and possible segmentation of each fault, however this data is not provided in the NZ seismic hazard model (Stirling et al., 2012) and is considered to be beyond the scope of this study.

In Avondale, the Alpine fault rupture of $\sim M_w$ 8.1 in 1717 and the ca. 1450 $\sim M_w$7.2 Porters Pass earthquake have the highest probabilities of triggering liquefaction for the known historic earthquakes (32% and 19%, respectively) (Fig. 3.14A & B). The 1869 $\sim M_w$ 4.8 Christchurch earthquake has a preferred PL of 7%, however it has an upper-bound estimate of PL = 43% which reflects the large uncertainty in the location of the fault rupture. The upper-bound estimate indicates that

TABLE 3.3: Potential of known historic earthquakes and active faults to induce liquefaction in Avondale and Kaiapoi

Fault Code	**Historic Earthquakes and Active Faults**	**M_w Mean**	**Computed PL: 95% Confidence Bounds**	
			Avondale	**Kaiapoi**
1*	1450 Porter's Pass	7.2	6% - 42% (19%)	10% - 56% (24%)
2*	1717 Alpine	8.1	15% - 50% (32%)	18% - 53% (35%)
3*	1869 Christchurch	4.8	1% - 43% (7%)	1% - 2% (1%)
4*	1901 Cheviot	6.9	2% - 34% (13%)	4% - 50% (23%)
41	Port Hills	6.5	72% - 99% (95%)	23% -87% (62%)
16	Kaiapoi-Pegasus	7	73% - 99% (94%)	93% - 99% (99%)
15	Kaiapoi	6.8	62% - 99% (89%)	88% - 99% (99%)
34	Pegasus	7	51% - 96% (83%)	85% - 99% (98%)
13	Kaiapoi Offshore	6.4	35% - 95% (74%)	71% - 99% (95%)
1	Ashley	7.2	42% - 92% (73%)	70% - 99% (92%)
42	Porters Pass-Grey	7.5	41% - 93% (70%)	63% - 97% (87%)
43	Springbank	7	30% - 87% (64%)	58% - 98% (87%)
4	Cust	7	25% - 83% (56%)	46% - 95% (77%)
45	Waikuku	6.8	20% - 80% (50%)	54% - 98% (86%)
12	Hororata	7.2	18% - 73% (45%)	15% - 69% (40%)
40	Pegasus 6b	6.4	19% - 79% (45%)	28% - 92% (67%)
26	North Canterbury Shelf 1	6.8	14% - 70% (40%)	32% - 90% (69%)
11	Offshore Fault IV	6.9	10% - 61% (30%)	20% - 81% (50%)
39	Pegasus 5	6.4	12% - 66% (30%)	13% - 74% (40%)
19	Leithfield	6.8	7% - 56% (26%)	27% - 87% (60%)
27	North Canterbury Shelf 2	6.7	6% - 52% (23%)	15% - 74% (42%)
121	Alpine: Fiordland to Kaniere	8.1	7% - 46% (23%)	10% - 50% (29%)
18	Kaiwara South	7.1	6% - 51% (22%)	15% - 68% (38%)
44	Springfield	7	6% - 50% (21%)	11% - 65% (33%)
73	Waitohi	7.1	4% - 44% (17%)	10% - 60% (31%)
70	Torlesse	7.2	4% - 42% (16%)	6% - 53% (25%)
30	North Canterbury 8-10	7.1	3% - 40% (15%)	6% - 50% (22%)
110	Clarence Northeast	7.7	2% - 32% (12%)	4% - 40% (16%)
33	Omihi	6.6	2% - 31% (10%)	6% - 54% (24%)
36	Pegasus pup	5.6	1% - 42% (10%)	4% - 71% (27%)
3	Ashley Partial	6.1	1% - 31% (8%)	16% - 73% (35%)
14	Kaiapoi Offshore 2	6.3	1% - 15% (3%)	10% - 71% (35%)
2	Ashley Mouth	5.4	1% - 8% (1%)	3% - 70% (24%)

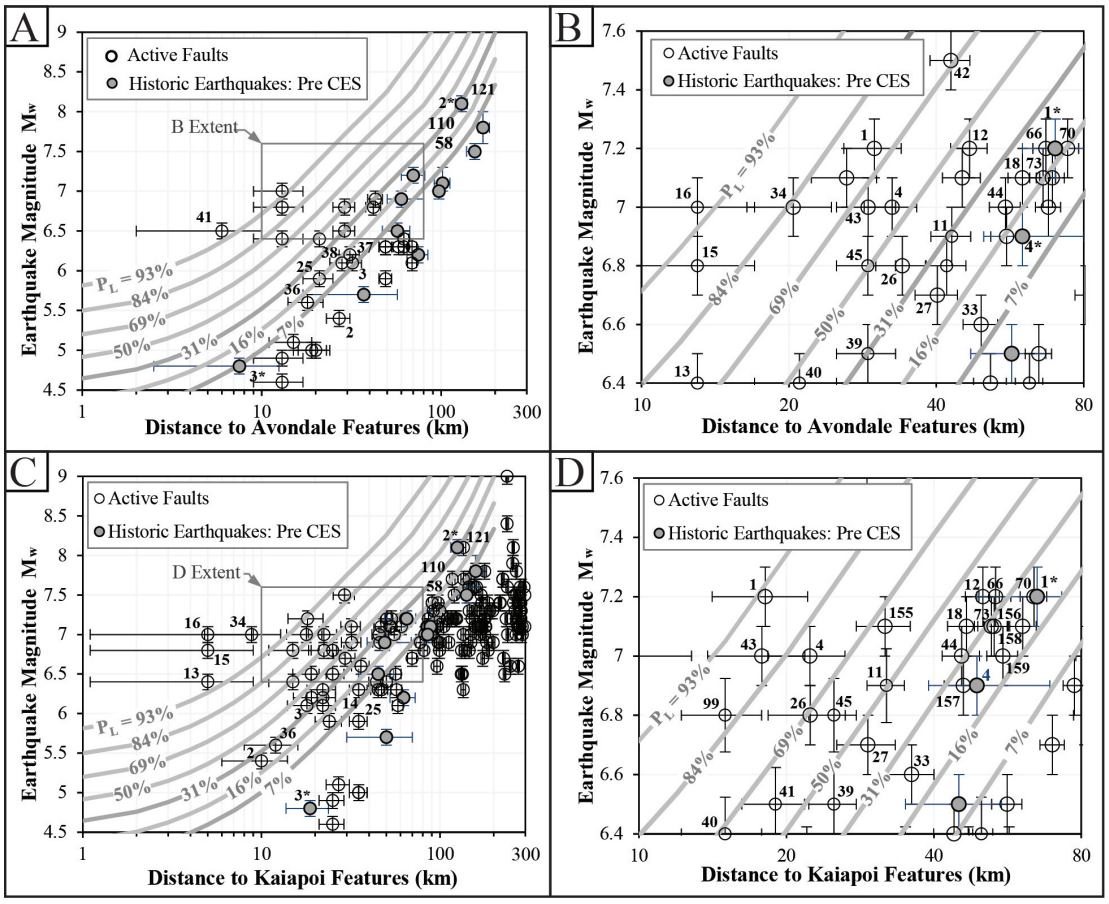

FIGURE 3.14: Magnitude bound curves indicating the probability of known historic earthquakes (pre-CES) and active faults within the wider Canterbury region to induce liquefaction within Avondale (A) and Kaiapoi (C). Subsets of the Avondale (B) and Kaiapoi (D) data are shown in greater detail. Numbers correspond with fault codes listed in Table 4.3.

the earthquake may have triggered liquefaction within Avondale. Of the active fault sources, 23 have maximum rupture scenarios with PL $\geq$ 15% and thus are considered capable of triggering liquefaction. These generally comprise the active faults within 50 km of Avondale and capable of generating M_w >6.5 earthquakes. The Pegasus, Kaiapoi, and Ashley Faults all have PL >70% indicating that earthquakes on these faults have a high probability of triggering liquefaction in Avondale (Table 3.3). The Kaiapoi-Pegasus Fault (16) has a PL similar to the Port Hills Fault (41) which ruptured during the February 2011 earthquake (PL of 94% and 95%) indicating that liquefaction induced during a rupture on the Pegasus Fault is likely to be similar to that observed during the February 2011 earthquake.

In Kaiapoi, the 1717 ~M_w 8.1 Alpine Fault rupture (PL = 35%), ca. 1450 Porters Pass earthquake (PL = 24%), and 1901 Cheviot earthquake (PL = 23%) have

credible potential for inducing liquefaction. The PL estimate for the 1901 Cheviot earthquake is consistent with the observed liquefaction during this event (Berrill et al., 1994). Of the active faults within the region, 29 have maximum rupture scenarios for which PL is greater than 15% and are therefore considered likely to trigger liquefaction. These generally comprise the active faults within 50 km of the study sites that are capable of generating M_w >5.5 earthquakes. The Pegasus, Kaiapoi-Pegasus, Kaiapoi offshore, Springbank, Porters Pass-Grey, Ashley, Cust, and Waikuku Faults have PL >70% indicating that these faults have a high probability of triggering liquefaction. It is likely that liquefaction during a maximum rupture on the Alpine Fault (PL = 35%) would be similar to that observed during the 1901 Cheviot earthquake (PL = 23%).

The back-calculated magnitude bound procedure indicates that historic ruptures on the Alpine Fault and Porters Pass fault, and active faults within the North Canterbury and offshore fault systems, have a high probability of triggering liquefaction. The results are generally in agreement with those identified from comparison of the site-specific PGA and liquefaction triggering threshold. Combining the back-calculation approach with the PGA and $PGA_{7.5}$ derived from the GMPE proves effective in determining the active faults capable of triggering liquefaction at the study sites, and thus may have triggered paleo-liquefaction.

3.8 Implications for paleoseismic studies and future land use

The CES highlights the severe damage and disruption to land, infrastructure, and lifelines that can result from liquefaction (Cubrinovski and Green, 2010; Cubrinovski et al., 2011; Hughes et al., 2015). Due to the limited historic record, the return times of liquefaction-triggering earthquakes within the city are uncertain, and thus the liquefaction hazard posed by future earthquakes is largely unknown. Combining the back-calculation approach with the PGA and $PGA_{7.5}$ derived from the GMPE proves effective in determining the active faults capable of triggering liquefaction at the study sites. The large number of active faults within the wider Canterbury region that are anticipated to trigger liquefaction at the Kaiapoi and Avondale sites highlights the need for local authorities to assess the liquefaction hazard for present and future developments both in Christchurch, and in other

seismically active areas that are underlain by sediments highly susceptible to liquefaction.

The presence of pre-CES liquefaction in Avondale and Kaiapoi indicates that the eastern Canterbury region has liquefied prior to the CES and 1901 Cheviot earthquake. The inferred pre-1901 age of the features in Avondale indicates that residential development took place on top of sediments that contained geologic evidence for liquefaction. The identification of three generations of liquefaction at Site 4 in Kaiapoi (CES, likely 1901, and pre- AD 1497) indicates that the area has been subjected to recurrent liquefaction. Additionally, the preservation of three episodes of liquefaction within the pre-CES compound sand blow provides evidence of possible earthquake clustering prior to the CES clustering. Development in Kaiapoi therefore took place on sediments that had historically liquefied and contained evidence for pre-historic earthquake clustering. The high number of active faults in North Canterbury and offshore that are considered capable of triggering liquefaction in Kaiapoi, combined with the identification of pre-CES liquefaction confirms that the area is highly susceptible to liquefaction.

The presence of both pre-CES and CES liquefaction in the five trenches indicates that the same areas re-liquefy during subsequent earthquake events. The documentation of pre-CES features also highlights the potential of paleo-liquefaction investigations, in addition to geotechnical data, to contribute to land-use planning.

3.9 Conclusions

The CES liquefaction features documented at the five sites consist of liquefaction dikes and sills composed of well sorted fine sand and silt that lacks the oxidation and mottling developed in the surrounding sediment. The dikes all exhibit a similar sub-vertical and planar geometry and increase in width with depth.

Pre-CES liquefaction features identified in the trenches include dikes at Sites 3 and 4, possible pre-CES injection sills at Site 5, a sill and compound sand-blow at Site 6, and a sand blister at Site 7. Crosscutting relationships combined with ^{14}C dating indicate that the Avondale event most likely occurred between 1321 and 1960. The sill identified at Site 6 in Kaiapoi post-dates 1458 and likely formed during the 1901 earthquake, while the sand blow most likely pre-dates 1458. The

sand blister at Site 7 likely formed between 1297 and 1901. The presence of pre-CES liquefaction confirms that moderate-to-large earthquakes occurred in eastern Canterbury prior to the CES and 1901 Cheviot earthquake.

The site-specific PGA indicates that many faults within 50 km of the study sites have the potential to trigger widespread liquefaction and may have formed the pre-CES features. Additionally, many faults have the potential to trigger minor-to-moderate liquefaction in both Avondale and Kaiapoi.

The magnitude-bound back-calculation indicates that the 1717 $\sim M_w$ 8.1 Alpine fault and ca. 1450 $\sim M_w$7.2 Porter's Pass earthquakes are highly likely to have triggered liquefaction in Avondale and Kaiapoi. Additionally, the Pegasus, Kaiapoi, and Ashley Faults are considered highly likely to trigger liquefaction in Avondale (PL >70%) and may have formed the paleo-liquefaction features. In Kaiapoi, the Pegasus, Waikuku, Springbank, Porters Pass, Ashley, and Cust Faults are considered likely to trigger severe liquefaction (PL >70%).

Combining the back-calculation approach with the PGA and $PGA_{7.5}$ derived from the GMPE proves effective in determining active faults capable of triggering liquefaction at the study sites, and are thus capable of triggering liquefaction in the future. The results are generally in agreement as to which faults are likely to have triggered liquefaction in Avondale and/or Kaiapoi.

Chapter 4

The subsurface stratigraphy of liquefaction dikes and intrusions: paleo-seismic implications and correlations with epicentral distance

Abstract

Recurrent liquefaction during the 2010-2011 Canterbury earthquake sequence provides an opportunity to document the surface and subsurface morphology of liquefaction features that formed under different intensities of earthquake shaking (e.g. peak ground acceleration, PGA) and distances from the earthquake source (e.g. epicentral distance). Subsurface investigations at six sites across eastern Canterbury reveal liquefaction dikes that vary in width and morphology. The spatial extent of surficial liquefaction ejecta, sand blow diameters, and dike width at the six sites do not uniquely scale with the distance from the epicentre, nor local PGA at most sites. Furthermore, the subsurface record of liquefaction significantly under-represents the number of liquefaction-triggering earthquakes recorded during the CES. Lateral spreading-induced extensional strains across the study sites, the competency and thickness of the sediment overlying the first potentially liquefiable unit, and the depth and continuity of the first liquefiable unit are shown to

exert primary influences on the surface manifestation of liquefaction, dike width, and number of distinct liquefaction episodes preserved in the subsurface. This chapter highlights some of the limitations of inferring epicentral regions and magnitudes of paleo-earthquakes from paleo-liquefaction due to the influence of variable extensional strains, sediments with heterogeneous liquefaction potential, and variations in shaking intensity on dike widths.

4.1 Introduction

Paleo-seismic studies may utilise paleo-liquefaction features to approximate the timing, magnitudes, and epicentral regions of pre-historic earthquakes (Obermeier, 1996, 1998; Tuttle, 2001; Tuttle et al., 2002; Obermeier et al., 2005, 2001; Cox et al., 2007; Counts and Obermeier, 2012; Tuttle and Hartleb, 2012). The spatial distribution and widths of paleo-liquefaction dikes and the diameter of paleo-sand-blows may also be used to approximate epicentral locations of the pre-historic earthquakes, while dating of subsurface deposits may constrain the approximate timings (Obermeier, 1996; Tuttle, 2001; Castilla and Audemard, 2007; Counts and Obermeier, 2012). The widest dikes are generally thought to form within the source region and decrease in width with increasing distance (Obermeier, 1996; Obermeier et al., 2001; Green et al., 2005). A power-law relationship between decreasing sand-blow diameter with increasing distance from the epicentre has been proposed by Castilla and Audemard (2007). Additional empirical relationships have been derived between the surface-wave magnitude (M_s) and maximum dike width, number of dikes, and the diameter of surficial sand-blows (Lunina and Gladkov, 2015). These empirical relationships are based on the assumption that dike width and sand blow thickness are solely a function of the distance to the epicentre and earthquake magnitude. However, Obermeier (1996) cautioned against using the distribution of liquefaction features as a proxy for epicentral distance, as the density of dikes may be strongly influenced by the thickness of the non-liquefiable sediment overlying the first potentially liquefiable unit (i.e. cap thickness). Empirical curves have also been derived based on the occurrence or non-occurrence of liquefaction at varying epicentral distances and earthquake magnitudes following large historic earthquakes (Ambraseys, 1988; Galli, 2000; Papathanassiou et al., 2005; Pirrotta et al., 2007). These curves may be applied to back-calculate minimum earthquake magnitudes based on the distance to the most distal site of

liquefaction (Obermeier, 1996; Obermeier et al., 2001; Green et al., 2005; Olson et al., 2005; Tuttle and Barstow, 1996). Lower-bound peak ground accelerations may also be estimated at individual sites based on the assumption that the earthquake must have exceeded the minimum threshold value for liquefaction at the site (Obermeier et al., 2001; Green et al., 2005; Olson et al., 2005).

The 2010-2011 Canterbury earthquake sequence (CES) triggered repeated episodes of liquefaction in parts of eastern Christchurch and the northern township of Kaiapoi (Fig. 4.1 & 4.2) (Cubrinovski and Green, 2010; Cubrinovski et al., 2011, 2012; Quigley et al., 2013). At least ten episodes of liquefaction were recorded within highly susceptible sediments in eastern Christchurch (Quigley et al., 2013). Liquefaction-induced differential ground subsidence and lateral spreading caused severe damage to the built environment during the 4th September 2010 M_w 7.1 Darfield earthquake, and the subsequent 22nd February 2011 M_w 6.2 (i.e. Christchurch), 13th June 2011 M_w 6.0, and 23rd December 2011 M_w 5.9 earthquakes (Fig. 4.1) (Cubrinovski and Green, 2010; Cubrinovski et al., 2011; Quigley et al., 2013). Mapping and trenching at sites of recurrent liquefaction during the CES enables direct comparison of the surface manifestation of liquefaction and dike widths with epicentral distances and site-specific PGA.

In this chapter, detailed descriptions of the subsurface morphology of the CES liquefaction features are presented for five sites in eastern Christchurch, and at one site within the northern township of Kaiapoi (Fig. 4.2 & 4.3). Detailed descriptions of the surficial distribution of liquefaction are also presented for two sites within eastern Christchurch. The spatial extent of surficial liquefaction ejecta, diameter of sand-blows, and dike widths are compared with the distance of each site from the epicentre of the main liquefaction triggering CES earthquakes and the maximum PGA experienced at each site. It is shown that dike width, the spatial extent of liquefaction, and the diameter of sand-blows do not correlate strictly with distance from the epicentre, nor PGA in the wider Christchurch area. The subsurface record is also shown to under-estimate the number of CES liquefaction triggering earthquakes at all five sites with the exception of one unique and exceptionally well preserved case. Lateral-spreading induced extensional strains across each site, the competency and thickness of the sediment overlying the first potentially liquefiable unit, and the thickness of the first potentially liquefiable unit appear to exert first order influences on dike width, the spatial extent of surficial liquefaction, and sand blow diameters. Documentation of the surface

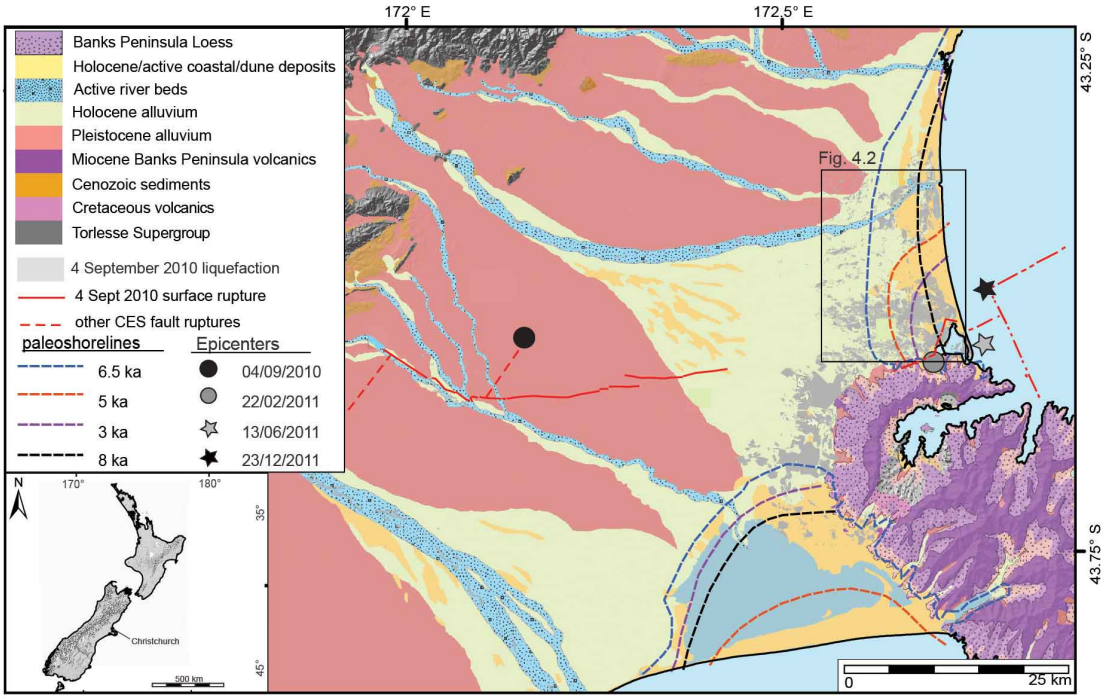

FIGURE 4.1: Simplified geological map of the wider Canterbury area with paleoshorelines indicated. The aerial extent of liquefaction following the 4 September 2010 earthquake, the epicentral locations of the 2010-2011 Canterbury earthquake sequence events that triggered liquefaction at the study sites and the rupture of the Greendale Fault (bold line) and projected locations of the subsurface faults that ruptured in the February, June, and December earthquakes (dotted lines) are also indicated.

manifestation of liquefaction and the subsurface morphology of liquefaction features highlights some of the limitations of inferring epicentral regions from limited paleo-liquefaction data.

4.2 Geologic Setting

The city of Christchurch (population ~350,000) is primarily situated upon the low-relief and low-elevation (0-20 m above sea level) alluvial out-wash plain of the Waimakariri River along the east coast of the South Island of New Zealand (Fig. 4.1). The central city and eastern suburbs are predominantly underlain by alluvial sands, silts, and drained peat swamps interbedded with estuarine, dune, and foreshore sands (Fig. 4.1 & 4.2) (Brown and Weeber, 1992). The area west of the central city is underlain by alluvial sands to silts and gravels (Brown and Weeber, 1992).

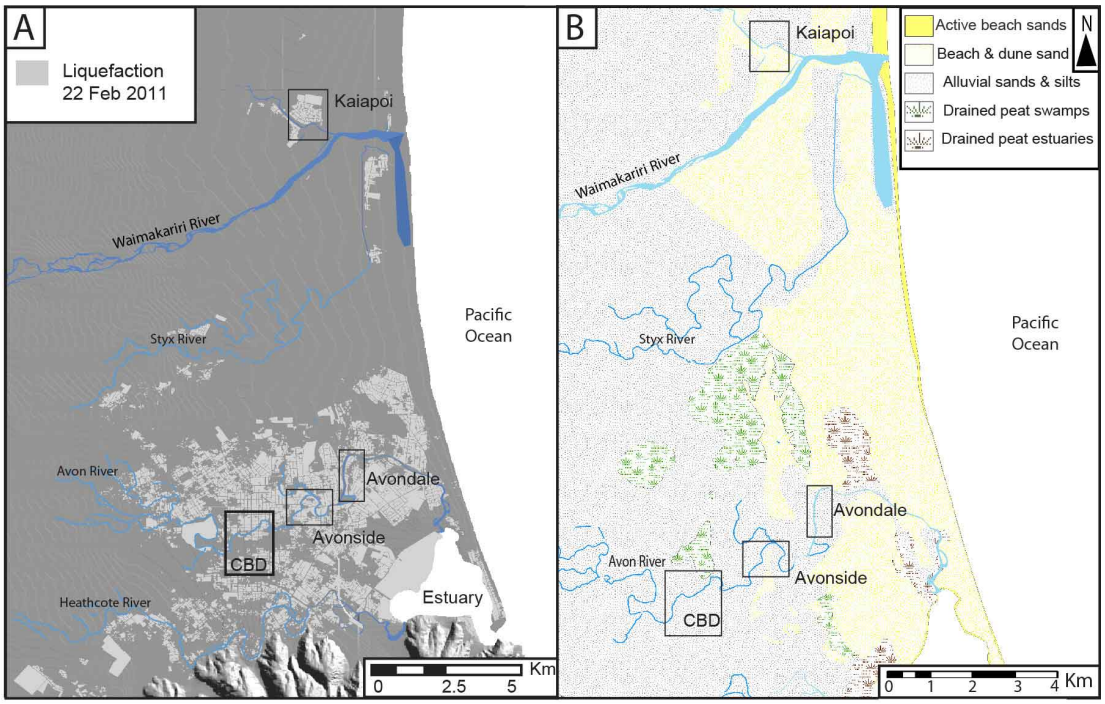

FIGURE 4.2: A) The aerial extent of liquefaction within the wider Christchurch area as mapped following the 22 February 2011 earthquake, with the location of the study areas, Christchurch CBD, the meandering Styx, Avon, and Heathcote Rivers and braided the Waimakariri River indicated. B) Simplified geological map of the wider Christchurch area (modified from Brown and Weeber (1992) and Forsyth et al. (2008)) with the locations of the Avonside, Avondale, Kaiapoi study areas indicated with respect to the Christchurch central business district (CBD).

The alluvial sands and silts underlying eastern Christchurch were initially deposited by the Waimakariri River which regularly avulsed across the region prior to European settlement. The sediments were subsequently re-worked and redeposited by the meandering Avon River which also regularly flooded, and avulsed across the area now comprising the city of Christchurch (Fig. 4.1 & 4.2) (Cowie, 1957; Brown and Weeber, 1992). The peat deposits correspond with peat swamps that formed on the flood-plain adjacent to the meandering rivers. The interbedded estuarine, dune and foreshore sands were deposited by shoreline progradation and marine regression following the mid-Holocene high-stand. Shorelines reached ~3 km west of the present central city and ~10 km inland from the modern coastline at ~6,500 years before present (Fig. 4.1) (Brown and Weeber, 1992). The co-evolution of the floodplain and coastal landscapes within central and eastern Christchurch resulted in significant spatial heterogeneity within the subsurface sediments (Fig. 4.1 & 4.2) (Brown and Weeber, 1992). The youthful, unconsolidated nature of the fine sands to silts underlying eastern Christchurch combined with

high water tables (1-2 m depth) and localized artesian water pressures pose a high liquefaction hazard (Elder et al., 1991; Brown and Weeber, 1992; Christchurch Engineering Lifelines Group, 1997; Clough, 2005).

4.2.1 Study sites

Five study sites were selected within eastern Christchurch, and one site within the northern township of Kaiapoi for comparison of the subsurface morphology of liquefaction features. The eastern Christchurch study sites comprise two sites in the suburb of Avonside, and three sites within the suburb of Avondale. Avonside and Avondale are both situated adjacent to the Avon River and experienced severe liquefaction-induced damage during the CES (Fig. 4.3).

The suburb of Avonside is encompassed within an inner meander bend of the Avon River and is underlain by point bar and over bank fluvial deposits of the Avon River, along with coastal swamp and sand dune deposits (Fig. 4.2B & 4.3A) (Silby, 1856; Brown and Weeber, 1992). The ∼5000 yr. B.P. coastline was ∼3 km to the west, while the ∼3000 yr. B.P. coastline was ∼0.5-1 km east of the study sites (Fig. 4.1) (Brown and Weeber, 1992). The water table is located between 1-2 m depth (Brown and Weeber, 1992). Trenching was conducted at Sullivan Park (Site 1; Fig. 4.3C), and the site of a former residential property at 11 Bracken Street (Site 2; Fig. 4.3D).

The suburb of Avondale is situated adjacent to an anthropogenically straightened section of the Avon River that transitions into an inner meander-bend at the northern extent of the suburb (Fig. 4.2 & 3B). Areas directly adjacent to the river were in-filled by ∼1 m of river dredging prior to the subdivision of the area in the early 1960s (Wilson, 1989). The suburb is predominantly underlain by fine sand and silt of point bar, over-bank, and swamp deposits of the Avon River (Fig. 4.2B) (Silby, 1856; Brown and Weeber, 1992). The ∼3000 yr B.P. coastline was located ∼1.5 km west of the study sites, while the ∼2000 yr B.P. coastline was ∼0.5 km to the east (Fig. 4.1) (Brown and Weeber, 1992). The water table is at ∼1 m depth (Brown and Weeber, 1992). Trenching was conducted at the former residential properties of 31 Ardrossan Street (Site 3; Fig. 4.3E), 45 Cardrona Street (Site 4; Fig. 4.3F), and the driveway of 53 Cardrona Street (Site 5; Fig. 4.3G).

The Kaiapoi study site was selected for comparison with the eastern Christchurch sites. The township of Kaiapoi (population 10,200) is located ∼20 km north-east of Christchurch city and within ∼4 km of the present Pegasus Bay coastline (Fig. 4.1 & 4.2). The area experienced severe liquefaction and lateral spreading during the 4th September 2010 and 22nd February 2011 earthquakes, and minor land damage during the 13th June 2011 earthquake. Kaiapoi is situated adjacent to the banks of the Kaiapoi River which represents the former north branch of the Waimakariri River (Fig. 4.3H). Flow within the Waimakariri River was constrained to the south branch through a canal constructed in 1868 which confined the river to a single channel within Kaiapoi and later re-named the Kaiapoi River (Wood, 1993). The region north of the Kaiapoi River is primarily underlain by dune and foreshore sands, and alluvial fine sand to silt (Fig. 4.1 & 4.2). The water table is at ∼1 - 0.8 m depth (Hawkins, 1957; Brown and Weeber, 1992). Trenching was conducted at the former residential property at 125 Sewell Street (Site 6; Fig. 4.3I).

4.3 Methods

The aerial extent of liquefaction at Sites 1 and 2 was mapped in detail following the 4 September 2010 M_w 7.1 Darfield and 22 February 2011 M_w 6.2 Christchurch earthquakes for comparison with epicentral distances and dike widths (Fig. 4.3). Mapping was conducted in ArcGIS from high-resolution aerial photographs flown on 5 September 2010 and 24 February 2011 by New Zealand Aerial Mapping (NZAM) for the Christchurch Response Centre (available from the Canterbury Geotechnical Database).

Sites 1 and 2 were selected as the distribution of liquefaction ejecta had already been mapped for the September 2010 and February 2011 earthquakes, and is presented in Chapter 5. Additionally, the distribution of liquefaction at Site 2 was well documented by Quigley et al. (2013), while the distribution of ejecta at Site 1 was not obscured or modified by anthropogenic structures or activity and thus could be accurately mapped from the aerial photographs. The sand-blows formed at the two sites during the June and December 2011 earthquakes were not mapped as shadows in the aerial photography reduced confidence in the ability to accurately delineate ejecta coverage. The December ejecta was not mapped as it was deposited on-top of the June ejecta which was not removed from the site following the earthquake, thus the ejecta represents a cumulative aerial extent.

FIGURE 4.3: Aerial photographs of Avonside (A) and Avondale (B) with the location of the study sites and the position of the CPTs proximal to the study sites indicated. C) Aerial photograph of Site 1 with the position of the 5 trenches (outlined in white) and the margins of the paleo-channel indicated (dotted black line). Aerial photographs of the former residential properties comprising Site 2 (D), Site 3 (E), Site 4 (F), and Site 5 (G), with trench locations and the distribution of liquefaction ejecta following the 22 February 2011 earthquake are also indicated. H) Aerial photograph of Kaiapoi with the location of Site 6 and CPT indicated. I) Aerial photograph of Site 6 with the trench location and aerial extent of liquefaction ejecta following 22 February 2011 earthquake indicated (modified from Bastin et al. (2015b) and Bastin et al. (2016).

A trench was excavated at each of the six sites to examine the subsurface morphology of the CES liquefaction features. Trenches were excavated perpendicular to the aligned surficial sand blow vents and fissures at each site as identified from the aerial photographs (Fig. 4.3). Trench walls were cleaned using hand-held scrapers then logged at centimetre scale and photographed to capture small-scale variations in the morphology of the CES liquefaction features.

Peak ground accelerations (PGAs) generated at each of the six sites during the main CES liquefaction triggering earthquakes were derived from the Canterbury Geotechnical database. Strong ground motions were well documented across the city during the CES due to the dense network of seismometers deployed across the region following the 4th September 2010 earthquake (Bradley et al., 2014). The distance of each site to the epicentral location (R_{epi}) of each of the liquefaction triggering CES earthquakes are approximated from the epicentral locations listed by GeoNet (available at: http://www.geonet.org.nz; Table 4.1). The PGAs experienced at each site during the CES along with the epicentral (R_{epi}) distances are presented in Table 4.1.

Horizontal ground displacements are derived for the Avonside and Avondale study sites for the 4th September 2010 and 22nd February 2011 earthquakes, along with the total CES horizontal displacements from the Canterbury Geotechnical database. The horizontal displacements were calculated from comparison of the pre- and post- earthquake digital elevation models (DEM) created from LiDAR point data through a pattern-matching image co-registration process using the methodology outlined by Leprince et al. (2007). The local component of the ground movement (i.e. caused by lateral spreading) was isolated from the absolute ground movement and regional tectonic movements from the fault rupture model by Beavan et al. (2012). The post-February 2011 LiDAR survey did not cover the Kaiapoi area, thus horizontal displacements for Site 6 are estimated from then horizontal displacement vectors available from the Canterbury Geotechnical database. Extensional strains are calculated for the Avonside and Avondale sites from the horizontal displacement data.

The resistance of the subsurface sediments to liquefaction triggering is evaluated for each site from the CPT soundings (Cone Penetration Test) conducted proximal to the sites during the CES (available from the Canterbury Geotechnical Database). The resistance to liquefaction is evaluated using the Idriss and

Boulanger (2008) method which compares the cyclic stress ratio (CSR), that evaluates loading induced at different depths by an earthquake, with the cyclic resistance ratio (CRR), which represents the ability of the soil to resist liquefaction. The likelihood that a soil will liquefy is expressed as a factor of safety against liquefaction (FS) which is the ratio of CSR to CRR; liquefaction is predicted to trigger when FS>1. Analysis was conducted prior to publication of the updated Boulanger and Idriss (2014) methodology.

4.4 CES liquefaction features

The surficial CES liquefaction features including aligned and localized sand blows and surface fissures were identified in the aerial photography from their morphology and gray colouration (Fig 4.4). CES liquefaction features were recognised in the subsurface by their alignment with, and traceable continuity, into the observed CES surficial sand blows and fissures, and their crosscutting relationship with the subsurface stratigraphy. Identification of liquefaction features was aided by comparison with the liquefaction features depicted in Counts and Obermeier (2012) and Owen et al. (2011). Field photographs and logs are presented in Figures 4.4, 4.5, 4.6, 4.7 and dike thickness are summarized in Figure 4.8.

4.4.1 Site 1: Sullivan Park

Sullivan Park is located centrally within the Avonside meander-bend and within 50 m of the Avon River (Fig. 4.3A). Field observations combined with the aerial-photography flown following the 22nd February 2011 earthquake indicates that lateral spreading fissures surrounded by localized liquefaction ejecta formed at the site (Fig. 4.3). The site was selected as it lacked anthropogenic structures, thus the influence of anthropogenic hydrology (e.g. from the rupture of buried pipes) could be discounted as a potential factor influencing the surface and subsurface distribution and morphology of liquefaction features.

Four trenches (T1-T4) were excavated across the lateral spreading fissures at the site, while one trench (T5) was excavated across an area that contained no evidence for surficial liquefaction (Fig. 4.3C). Detailed descriptions of the trench

stratigraphy, CES, and pre-CES liquefaction features are presented in Chapter 2 and Bastin et al. (2015b).

The five trenches (T1-T5) expose fluvial stratigraphy comprising a basal non-plastic silt with interbedded lenses of medium sand and overlain by normally graded beds of fine sand grading to silt. The stratigraphy is capped by ∼20-50 cm of carbonaceous silt forming a topsoil horizon. The beds of normally graded sands in T4 are crosscut by a ∼4.5 m wide paleo-channel composed of cross-bedded fine sand (Fig. 4.4).

The fluvial stratigraphy in T1-3 and T5 is crosscut by anthropogenic waste pits associated with historic activity at a wool scouring factory that operated at the site opposite the park from ∼1865 to ca. 1905 (Fig. 4.5B) (Bremer, 1985). The waste pits range from ∼20 to 100 cm in width and ∼20 to 90 cm in depth and are uniformly comprised of silt, oxidized whole and fragmented lamb fetlock bones, fern mats, ground-up and burnt bone, and lenses of carbonaceous silt (Fig. 4.5). See Chapter 2 and Bastin et al. (2015b) for detailed descriptions of pit stratigraphy.

The fluvial and anthropogenic stratigraphy in T1-5 at Site 1 is crosscut by CES liquefaction dikes (Fig. 4.4 4.5). The dikes are all comprised of gray, well-sorted, fine to medium sand that fines upwards into silt and lacks the oxidation and mottling developed in the surrounding stratigraphy. The margins of the dikes are lined by ∼1 to 2 mm thick silt layers. No liquefaction features are observed within the paleo-channel in T4 (Fig. 4.4). The width the liquefaction dikes exposed in each of the trenches are plotted at 10 centimeter increments in depth in Figure 4.8 (Dikes 1-16).

The surficial lateral spreading fissure intersected at the southern end of T1 (Fig. 4.3) forms a graben in the subsurface that formed along the boundary of one of the anthropogenic pits and down-drops the pit fill by ∼30-40 cm. The graben is bounded by two sub-vertical dikes that vary in width from ∼2 - 35 cm (Fig. 4.5A). The fissure is also intersected at the northern end of T2 where it corresponds with a 4 to 6 cm wide dike that pinches out at ∼30 cm depth and forms along a boundary between the pit fill and fluvial stratigraphy (see Chapter 2). Lateral spreading fissures generally vary in width along their length and taper towards their end points. The variations in the morphology and width of the lateral spreading fissure intersected in T1 and T2 therefore most likely reflects spatial variability along the length of the fissure. T2 is also cross-cut by a lateral spreading fissure which forms

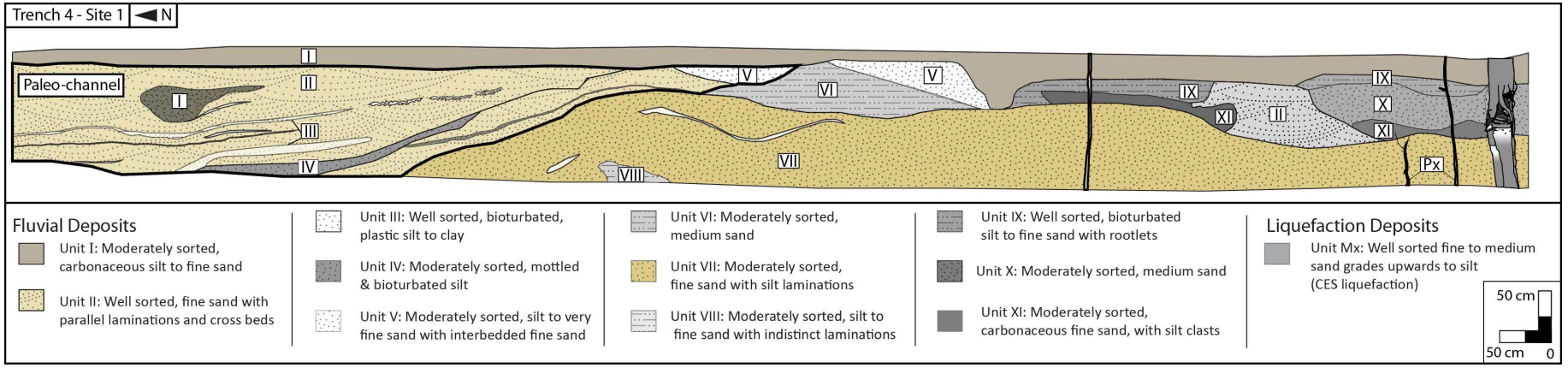

FIGURE 4.4: Detailed trench log of the east wall of Trench 4 at Site 1. The CES dikes (Px) crosscut the fluvial stratigraphy. The CES dike at the southern end of the trench exhibits complex internal stratigraphy indicating 6 episodes of liquefaction are preserved. No liquefaction features were observed within the paleo-channel (indicated).

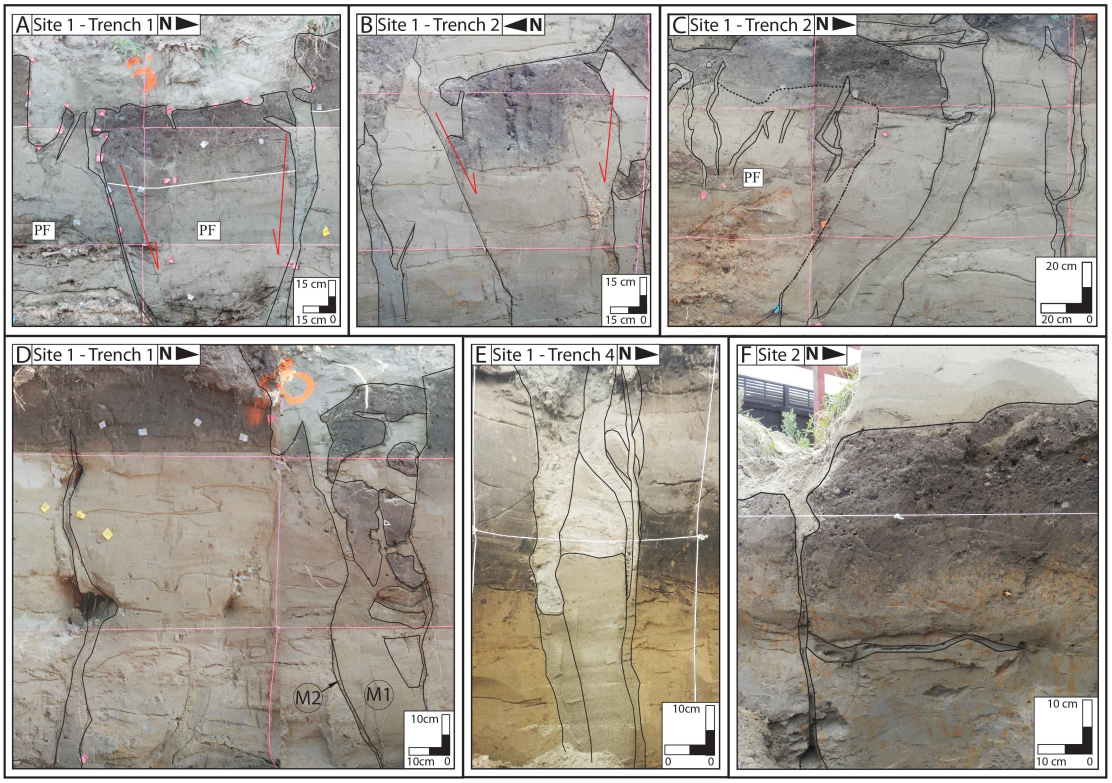

FIGURE 4.5: The surface fissure intersected at the south-end of T1 (Site 1) (A) and on the east wall of T2 (Site 1) (B) form grabens in the subsurface that are bounded by CES dikes (outlined in black). The graben in T1 (A) offsets the anthropogenic pit fill (PF). C) The surface fissure intersected on the west wall of T2 (Site 1) corresponds with a ~25 cm wide dike in the subsurface. Smaller ~5-10 cm wide dikes that pinch out just beneath the surface, and 1-2 cm wide dikes that originate within the pit fill (PF) were also observed. D) The fissure at the north end of T1 (Site 1) corresponds with an ~25 cm wide dike in the subsurface that contains down-dropped topsoil clasts and an internal silt drape that separates two episodes of liquefaction (M1 and M2). A smaller, 2-5 cm wide dike that pinches out beneath the surface was also observed. E) The fissure intersected at the south end of T4 (Site 1) corresponds with a ~25 cm wide dike that contains internal silt linings (outlined in black). Crosscutting relationships of the silt drapes indicate that six episodes of liquefaction are preserved within the dike. F) The surface sand blow intersected in the trench at Site 2 corresponds with a ~4 cm wide CES dike in the subsurface that crosscuts a CES laterally injected sill.

a graben on the east wall, and a ∼20-55 cm wide dike on the west wall (Fig. 4.5B & C).

The lateral spreading fissure intersected at the northern end of T1 (Fig. 4.3C) corresponds with a sub-vertical and planar dike in the subsurface that varies in width from ∼20-50 cm and contains down-dropped clasts of topsoil and anthropogenic pit fill and an internal silt drape separating the fine to very fine sand (Fig. 4.5D). The lateral spreading fissure is also intersected at the northern end of T3 (Fig. 4.3C) where it corresponds with a ∼2-20 cm wide sub-vertical and planar dike in the subsurface. T1 and T3 are located within 20 m of each other, therefore the variations in dike widths between the two trenches further highlights the spatial variability along the length of surface fissures. The internal silt-drape preserved within the dike in T1 indicates two episodes of liquefaction preserved within the dike, and thus provides evidence for conduit re-activation during a later CES event (Fig. 4.5D).

The surface fissure intersected at the southern end of T4 (Fig. 4.3) also corresponds with a sub-vertical and planar dike in the subsurface that varies in width from ∼35-50 cm (Fig. 4.4 & 4.5). The dike contains multiple internal silt drapes separating the fine sand (Fig. 4.4 & 4.5). The morphology and crosscutting relationships of the internal silt drapes suggests that six episodes of liquefaction may be preserved within the one dike (Fig. 4.5D).

The dikes in T5 comprise ∼2-10 cm wide dikes that pinch out beneath the surface and exhibit a complex branching pattern (Fig. 4.8). The dikes in T5 are comparably narrower than those in T1, 2, 3 and T4, which reflects ∼25-50 cm wide lateral spreading fissures intersected in these trenches and the absence of surface features in T5 (Fig. 4.3B & 4.8).

Smaller, ∼0.5 to 10 cm wide, sub-vertical and planar dikes that pinch out and terminate ∼10 cm beneath the surface are also observed in T1-4 (Fig. 4.5C & D). The anthropogenic pit fill in T2 is also cross-cut by small, ∼0.5 to 2 cm wide, and ∼10 to 40 cm long dikes composed of silt, that appear to originate within the anthropogenic pit fill (Fig. 4.5C).

4.4.2 Site 2: Bracken Street

The Bracken Street site is located within 100 m of the Avon River in Avonside (Fig. 4.3A). Detailed monitoring of the site undertaken by Quigley et al. (2013) combined with the strong ground motion data indicates that ≥10 episodes of liquefaction occurred at the site during the CES. The aerial photography and detailed field observations indicate that widespread liquefaction ejecta comprising sand blow lineaments formed across the site during the 4th September 2010 and the 22nd February, 13th June, and 23rd December 2011 earthquakes (Quigley et al., 2013). Minor liquefaction was reported at the site following the 16 April 2011 M_w 5.3 earthquake. A trench was excavated across a linear array of surface sand blows that were re-activated during each liquefaction triggering earthquakes (Fig. 4.3C).

The trench exposes over-bank fluvial stratigraphy comprising a non-plastic alluvial silt with interbedded lenses of very fine sand and overlain by ∼50 cm of topsoil comprised of carbonaceous silt (See Chapter 2 or Bastin et al. (2015b) for full descriptions of the trench stratigraphy).

The surficial sand blow intersected at the southern end of the trench corresponds with a sub-vertical and planar dike in the subsurface that crosscuts the fluvial stratigraphy from the trench floor to the surface. The dike varies in width from ∼0.5 to 4 cm, is composed of gray, well sorted, fine to very fine sand, and contains a ∼1 to 2 mm thick dike-parallel silt lining (Fig. 4.5F). The dike crosscuts a 1 to 2 cm wide sill at ∼50 cm depth that is also composed of gray, well sorted sand (Fig. 4.5F). The sill is separated from the dike by the dike-parallel silt lining suggesting that the sill formed in an event prior to the last liquefaction episode through the dike (Fig. 4.5F). The dike can be traced up both walls of the trench suggesting that it comprises a lateral spreading feature.

A smaller, ∼0.5 to 2 cm wide sub-vertical and planar dike that pinches out at ∼10 cm depth is also present at the northern end of the trench. The dike did not contain evidence for multiple episodes of liquefaction. The widths of the liquefaction dikes are summarised in Figure 4.8 (Dikes 17-18).

4.4.3 Site 3: Ardrossan Street

The Ardrossan Street site is located at the apex of a meander bend and within ∼90 m of the Avon River in Avondale (Fig. 4.3B). The post-February 2011 aerial photography indicates that localised sand blow lineaments formed across the site. A trench was excavated perpendicular to a sand blow lineament (Fig. 4.3E).

The trench exposes stratigraphy comprising over-bank fluvial deposits of a basal non-plastic silt with interbedded lenses of fine to very fine sand, overlain by a buried soil composed of carbonaceous silt to very fine sand. The fluvial stratigraphy is overlain by anthropogenic fill comprising silt to fine sand that is interpreted as river dredging used to infill the site prior to subdivision. The stratigraphy is capped by granules associated with the post-CES demolition of the former residential dwelling and the subsequent waste removal and levelling of the site (See Chapter 3 or Bastin et al. (2016) for full descriptions of the trench stratigraphy).

The fluvial and overlying anthropogenic stratigraphy is crosscut by a ∼0.5 - 1 cm wide CES dike that extend upwards from the trench floor and is truncated by the surficial post-CES granule fill (Fig. 4.6A). The northern end of the trench is cross-cut by two additional CES dikes that vary in width from 2-3 cm and 0.5-1 cm respectively and pinch out at ∼60 cm depth (Fig. 4.6B). The CES dikes in the trench are all composed of gray, well sorted silt to fine sand and do not contain evidence for multiple episodes of liquefaction (Fig. 4.6). Variations in dike widths are outlined at 10 cm increments in depth in Figure 4.8 (Dikes 19-21).

4.4.4 Site 4-5: Cardrona Street

The two Cardrona Street sites (Sites 4-5; Fig. 4.3B) are located ∼110 m from the Avon River and are within 50 m of each other in Avondale. The two sites are discussed together due to their proximity. The post-February 2011 aerial photography indicates that lateral spreading induced fissuring and associated sand blow lineaments formed across the two sites (Fig. 4.3E & F). A trench was excavated perpendicular to the sand blow lineaments at each of the sites (Fig. 4.3E & F).

The trench at Site 4 exposes fluvial stratigraphy comprising a basal non-plastic silt to very fine sand that is overlain by a topsoil horizon composed of carbonaceous silt with an interbedded lens of fine sand. The stratigraphy is capped by granules

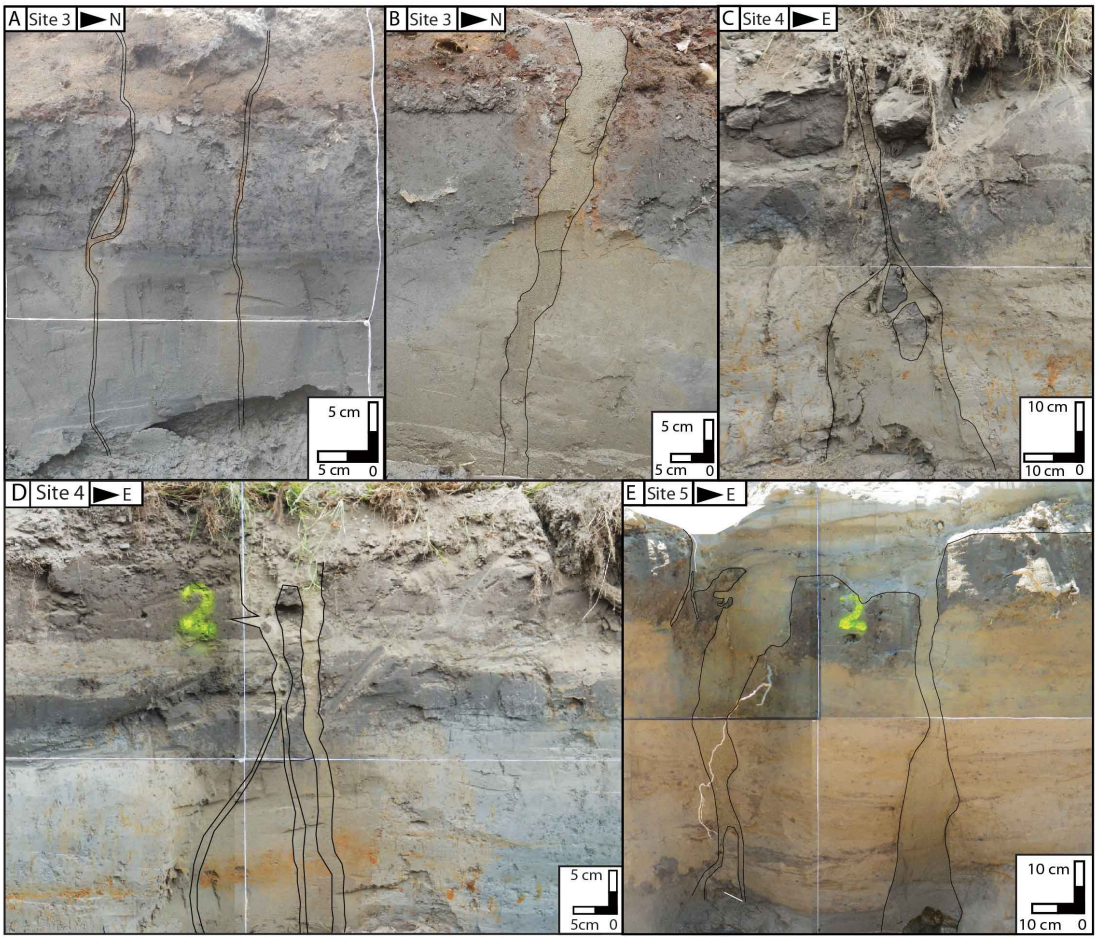

FIGURE 4.6: Interpreted field photograph of the ∼0.5 - 1 cm wide (A) and ∼2-3 cm wide (B) CES dikes observed at Site 3. C) Interpreted field photograph of the CES dike that extends upwards from a bulbous injection feature at Site 4 (outlined in black). D) The trench at Site 4 also exposes ∼1.5-5 cm wide sub-vertical CES dikes. E) The subsurface stratigraphy at Site 5 is crosscut by sub-vertical and planar dikes (outlined in black) that fed the surface liquefaction ejecta.

associated with the post-CES demolition of the former residential property (see Chapter 2 or Bastin et al. (2016) for full descriptions of trench stratigraphy).

The surficial sand blows intersected within the trench at Site 4 correspond with four sub-vertical and planar CES dikes that crosscut the fluvial stratigraphy from the trench floor to beneath the post-CES anthropogenic fill (Fig. 4.6C & D). The dikes range in width from ∼1.5 to 5 cm and are composed of well sorted fine to very fine sand (Fig. 4.6C & D). The central CES dike (Fig. 4.6D) can be traced across the trench floor and up the opposite trench wall where it varies in width from ∼2 to 10 cm. The lateral continuity of the dike indicates that it comprises a lateral spreading fissure. The lateral variability in the width of the feature

highlights the small scale spatial variability that may occur along the length of the liquefaction features. A dike at the eastern end of the trench extends upwards from a bulbous injection feature that ranges in width from 14 to 37 cm (Fig. 4.6C). The bulbous liquefaction injection feature is of consistent composition to the dike and exhibits sharp contacts with the surrounding fluvial sediment indicating that it comprises a CES liquefaction feature (Fig. 4.6C). The dikes do not contain evidence for multiple episodes of liquefaction. The widths of the dikes in the trench are summarised in Figure 4.8 (Dikes 22-24).

The trench at Site 5 exposes fluvial stratigraphy of a basal very fine sand overlain by very fine sand with interbedded lenses of fine sand and capped by a carbonaceous very fine sand topsoil horizon (see Chapter 3 or Bastin et al. (2016) for full descriptions of the trench stratigraphy at the two sites).

The trench at Site 5 exposes three sub-vertical and planar liquefaction dikes that crosscut the fluvial stratigraphy from the trench floor and dissipate within the CES surface ejecta remaining at the site (Fig. 4.6). The individual dikes range in width from 4-13 cm, 1-2 cm, and 3-15 cm and are all composed of well sorted fine to very fine sand (Fig. 4.6E). The dikes did not contain evidence for multiple episodes of liquefaction. Dike widths are summarised in Figure 4.8 (Dikes 25-28).

4.4.5 Site 6: Sewell Street

The Kaiapoi Site at 125 Sewell Street (Site 6) is located within 75 m of the Kaiapoi River (Fig. 4.3H). The aerial photographs indicate that the site experienced severe lateral-spreading induced fissuring and associated ejection of liquefied sediment during the 4th September 2010 and 22nd February 2011 earthquakes (Fig. 4.3I). A trench was excavated perpendicular to a sand blow lineament following the demolition of the former residential property in February 2014 (Fig. 4.3I).

The trench exposes fluvial over-bank stratigraphy comprising a basal silt with interbedded lenses of very fine to fine sand. The stratigraphy is overlain by granules to pebbles associated with the post-CES demolition of the former property and subsequent anthropogenic modification of the ground surface (See Chapter 3 and Bastin et al. (2016) for full descriptions of the trench stratigraphy).

The surface sand blows intersected on the east wall of the trench are fed by two sub-vertical planar dikes composed of gray, well sorted, fine to very fine sand (Fig.

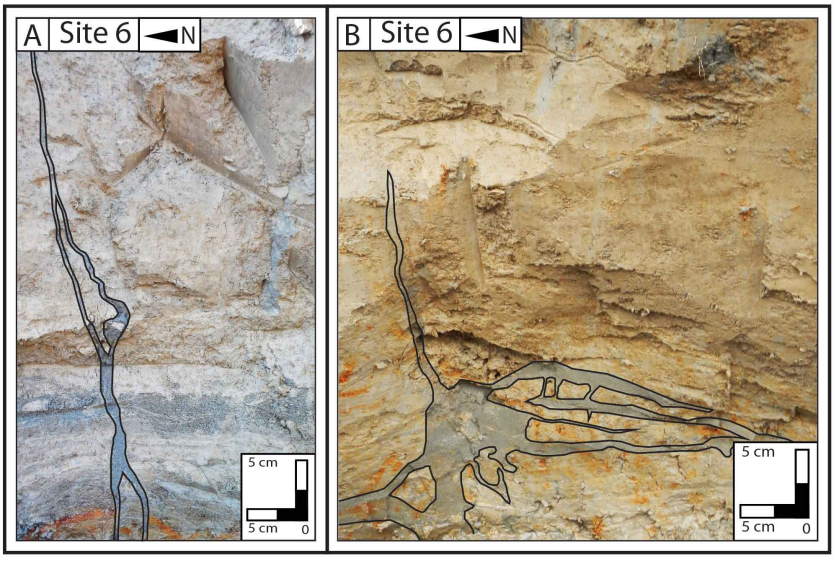

FIGURE 4.7: The subsurface stratigraphy at Site 6 is crosscut by a sub-vertical CES dike in the subsurface (A) and a stalled dike that branches into laterally injected sills (B).

4.7A). The dikes crosscut the fluvial stratigraphy and are cross-cut by the post-CES anthropogenic fill. The dikes vary in width from ∼0.25 - 3.5 cm and 0.5 - 2 cm respectively and exhibit a complex branching pattern in the subsurface (Fig. 4.7A). The stratigraphy at the northern end of the trench is also crosscut by a ∼3-4 cm wide dike that branches into a laterally injected sill at ∼70 cm depth, and pinches out at ∼0.5 m depth (Fig. 4.7B). No clear evidence for multiple episodes of liquefaction was observed in the trench. Dike widths are summarised in Figure 4.8 (Dikes 29-31).

4.5 Variations in dike widths

The widths of the dikes exposed in each of the trenches at the five sites are combined and summarized as box and whisker plots at 0.1 m increments in depth (Fig. 4.8). Dike widths within each of the five trenches at Site 1, and at the study sites within each of the study areas (i.e. within Avonside) are also summarized in Figure 4.8. The epicentral (R_{epi}) distances and maximum PGA are plotted with maximum dike widths for the six sites during the main CES liquefaction triggering earthquakes (Fig. 4.9 and Table 4.1). Maximum widths of the dikes at each of the six sites are also presented in Table 4.1.

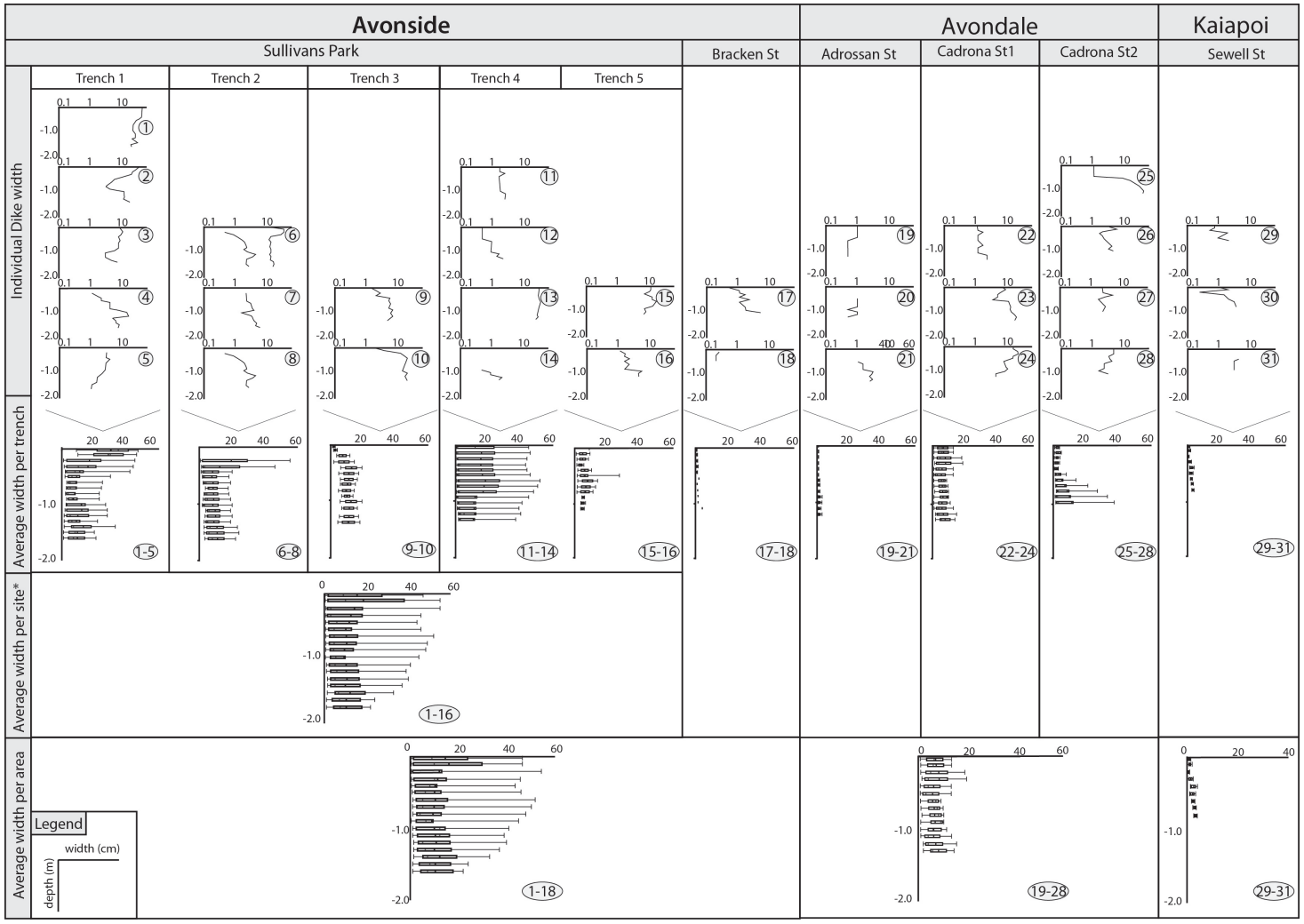

FIGURE 4.8: Summary of individual dike widths exposed in each of the trenches plotted at 0.1 m increments in depth (1-31). Dike widths are summarized for each trench (i.e. 1-5). Boxes represent 25th and 75th percentile widths while whiskers represent minimum and maximum dike widths. The widths of all the dikes encountered in T1-T5 at Site 1 (1-16), within the Avonside (1-18), Avondale (19-28), eastern Christchurch (1-28), and Kaiapoi (29-31) study sites are also summarized.

Maximum dike widths at Site 1 vary from 0.5 to 55 cm (Fig. 4.8). The range in the widths results from the variations between lateral spreading fissures and localised sub-vertical dikes. The spatial variability across the site indicates that factors in addition to distance from the epicentre and PGA influenced dike width at the site.

Site 2 is located within 650 m of Site 1 within Avonside (Fig. 4.3A). Maximum dike widths at Site 2 are 0.5 cm and 4 cm (Table 4.1; Fig. 4.5 & 4.8). The R_{epi} distances for the main liquefaction triggering earthquakes are within 500 m of Site 1, while the PGAs are within 0.05 g (Table 4.1 & Fig. 4.9). The significant variation in dike widths between the two sites supports that factors in addition to epicentral distance and PGA influenced the subsurface morphology of the liquefaction features (Table 4.1; Fig. 4.8).

The three Avondale sites (Sites 3, 4 and 5) are located within 900 m of each other (Fig. 4.3A). The maximum dike widths vary from 3 cm at Site 3, 37 cm at Site 4, and 19 cm at Site 5 (Fig. 4.8; Table 4.1). The comparatively wider dike at Site 4 reflect the bulbous injection feature which extends upwards into the CES dike (Fig. 4.6C). The R_{epi} distances of the three Avondale sites are within 1 km of each other for the main CES liquefaction triggering earthquakes while the PGA is within 0.05 g for each of the events (Fig. 4.9, Table 4.1). The variation in dike widths between the three Avondale sites indicates that dike width does not unequivocally scale with epicentral distances, and that factors in addition to PGA influence dike widths (Table 4.1).

4.5.1 Dike widths across eastern Christchurch

The Avonside study sites are located within 2 km of Sites 4 and 5, and within 3 km of Site 3 in Avondale (Fig. 4.2). Maximum dike widths vary significantly between the five sites (Table 4.1). The R_{epi} distances of the sites are within 2.3 km of each other for the main liquefaction triggering CES earthquakes which further supports that factors other than distance from the epicentre influences dike width (Fig. 4.9, Table 4.1).

The PGAs generated at the Avonside and Avondale sites during the main CES liquefaction triggering earthquakes are within 0.05 g of each other (Table 4.1). The PGAs experienced at the five sites all exceed the liquefaction triggering threshold

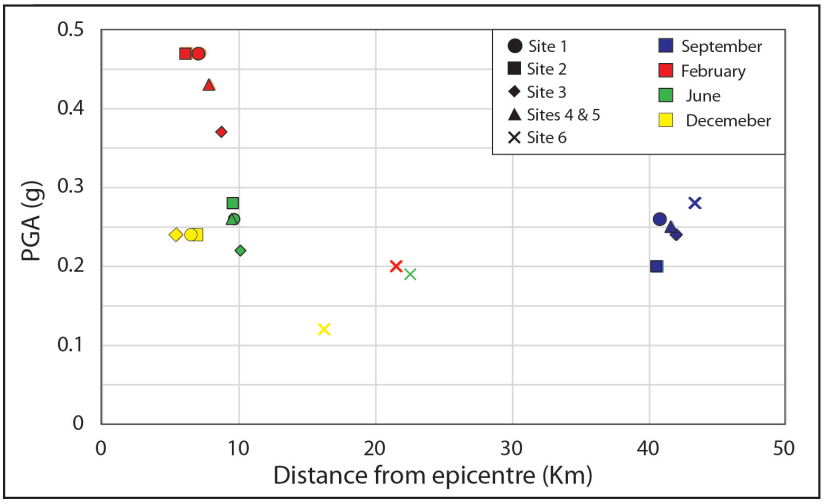

FIGURE 4.9: Peak ground acceleration (PGA) measured at the six study sites during the main CES liquefaction triggering earthquakes compared with the epicentral distances.

of PGA 0.09 g as derived from global liquefaction data (Santucci de Magistris et al., 2013), and exceed the CES liquefaction-triggering threshold of PGA 0.1 g documented by Quigley et al. (2013). The CES threshold was derived from the observation of minor liquefaction ejecta at Site 2 during the April 2011 M_w 5.0 earthquake. It is considered unlikely that the slight variations in PGA would have resulted in the significant spatial variations in dike widths between the sites (Fig. 4.8).

4.5.2 Comparison across eastern Canterbury

The Kaiapoi site (Site 6) is located within 15 km of the five eastern Christchurch sites. The site located at a similar R_{epi} distance as the eastern Christchurch sites from the 4th September 2010 earthquake, and experienced PGAs that are within 0.08 g of that recorded at Sites 1-5 (Fig. 4.9, Table 4.1). The R_{epi} distances for the February, June and December 2011 earthquakes are within 15 km, and the PGA is within 0.2 g of that recorded at Sites 1-5 (Fig. 4.9, Table 4.1). The PGA generated at Site 6 during the June and December 2011 earthquakes (0.19 and 0.12 g respectively) exceeds the global liquefaction triggering threshold derived by Santucci de Magistris et al. (2013) indicating that minor liquefaction may have occurred at the site during these events (Fig. 4.9, Table 4.1).

TABLE 4.1: Epicentral and surface rupture distances for the six study sites and PGA generated at the study sites for the four main CES liquefaction triggering earthquakes compared with maximum and mean dike widths

Site	Max width (cm)	September M_w 7.1 R_{epi} (km)	PGA	February M_w 6.2 R_{epi} (km)	PGA	June M_w 6.0 R_{epi} (km)	PGA	December M_w 5.9 R_{epi} (km)	PGA
Site 1	55.00	40.80	0.26	7.16	0.47	9.64	0.26	6.55	0.24
Site 2	4.00	40.60	0.20	6.17	0.47	9.56	0.28	6.96	0.24
Site 3	3.00	42.00	0.23	8.76	0.37	10.12	0.22	5.50	0.24
Site 4 & 5	35.00	41.64	0.24	7.88	0.43	9.48	0.26	5.43	0.24
Site 6	4.00	43.39	0.28	21.57	0.20	22.52	0.19	16.26	0.12

The maximum dike width at Site 6 (4 cm) is similar to that at Sites 2 and 3 (4 cm and 3 cm respectively) despite the varied R_{epi} distances and PGAs experienced at the sites during the CES. The variations in maximum dike width between the six study sites indicates that the subsurface manifestation of liquefaction was influenced by factors other than epicentral distance, and PGA during the CES.

4.5.3 Comparison of dike width and earthquake moment and surface wave magnitudes

An empirical relationship that correlates maximum dike width to surface-wave magnitude (M_s) has been derived by Lunina and Gladkov (2015). The M_s is calculated from the maximum dike widths at Sites 1 and 2 for comparison with that recorded in the CES.

The maximum dike widths at Site 1 at 2 are 55 and 4 cm respectively which correspond with calculated maximum surface-wave magnitudes of (M_s) of 6.8 and 5.6 (Lunina and Gladkov, 2015). M_s during the CES events are considered to be greater or equal to the M_w7.1 of the September 2010 earthquake on the basis of global empirical M_s to M_w conversions (Yenier et al., 2008; Ristau, 2009). The variation in the computed M_s between the sites, and inconsistencies with that recorded during the CES indicates that factors other than earthquake magnitude influenced the subsurface morphology of the dikes and highlights the potential limitations of the relationship.

4.6 Comparison of sand blow diameters, spatial extent of liquefaction ejecta, and PGA

The surface extent of liquefaction ejecta was mapped for Sites 1 and 2 following the September 2010 and February 2011 earthquakes from the high resolution aerial photography and is presented in Chapter 5. Maximum sand-blow diameters were also derived for the two sites for comparison with dike widths and distance from the epicentre. The surface extent of liquefaction and spatial extent of liquefaction ejecta overlying the area in which T1 at Site 1 was excavated and the location of the trench at Site 2 were also derived from the aerial photography.

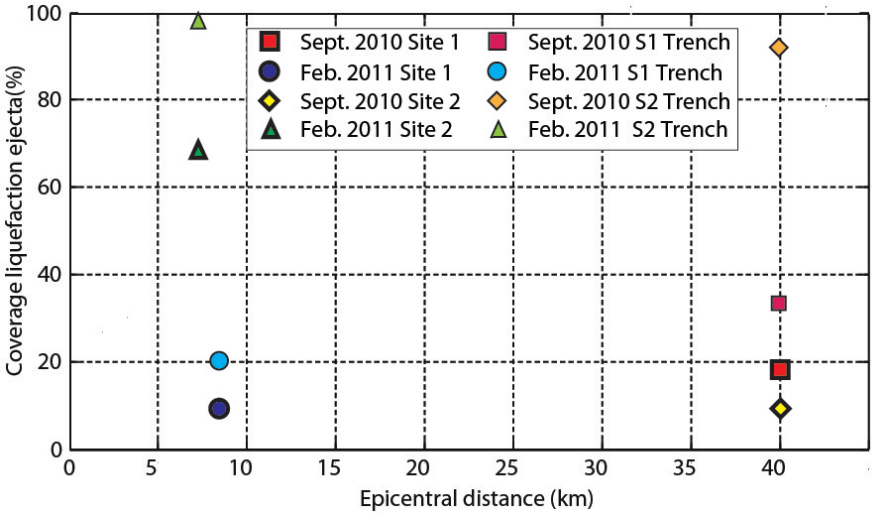

FIGURE 4.10: The percentage of Sites 1 and 2 that were covered by liquefaction ejecta following the September 2010 and February 2011 earthquakes compared with epicentral distances. The coverage of liquefaction ejecta (%) covering the area where T1 at Site 1 and the trench at Site 2 were excavated are also plotted with epicentral distance for the September and February earthquakes.

The surface ejecta at Site 1 predominantly comprised localised liquefaction ejecta surrounding the surface fissures (Fig. 4.3). Mapping indicates that ∼18% of the site was covered by liquefaction following the September 2010 earthquake, while ∼ 9.2% of the site was covered following the February earthquake. The area in which T1 was excavated was ∼34% covered by ejecta for the September earthquake, and ∼21% covered following the February earthquake. In comparison, the surface ejecta at Site 2 comprised aligned sand-blow lineaments. Mapping indicates that ∼12% of the site was covered by ejecta for the September earthquake, while 64% of the site was covered in ejecta following the February 2011 earthquake. The area in which the trench was excavated was 94% covered by ejecta for the September earthquake and 97% covered following the February 2011 earthquake. The coverage of liquefaction ejecta is plotted with epicentral distances in Figure 4.10.

Site 1 exhibited a higher coverage of liquefaction ejecta for the September 2010 earthquake, despite the epicentre being located comparably closer to the site during the February earthquake (Table 4.1). Site 2 exhibited a comparably lower coverage of liquefaction than Site 1 following the September earthquake, and higher coverage for the February 2011 earthquake (Fig. 4.10). The similar R_{epi} distances for Sites 1 and 2 and varied spatial extent of liquefaction ejecta indicates that factors other than epicentral distances influenced the surface manifestation of liquefaction (Fig. 4.10).

The liquefaction ejecta overlying the site of T1 corresponds with 20-50 cm wide dikes in the subsurface that fed the surface fissures. In comparison, the sand-blows intersected in the trench at Site 2 correspond with ∼0.5 to 4 cm wide dikes. The trench at Site 2 exhibits a comparably higher coverage of surficial liquefaction than Site 1 despite being fed by a comparably narrower dike. This indicates that a higher volume of liquefaction was ejected out of the dike at Site 2 compared to Site 1. The variations in dike width and coverage of surficial ejecta at Sites 1 and 2 do not correlate with variations in R_{epi} distances or PGA, indicating that other, site-specific variations influenced the surface and subsurface manifestation of liquefaction at these sites.

4.6.1 Comparison of aerial extent of liquefaction ejecta and epicentral distances

A lower-bound curve between the occurrence and non-occurrence of liquefaction with increasing earthquake M_w and epicentral distance based on historic data was plotted by Ambraseys (1988). These curves have been updated by Galli (2000) and Castilla and Audemard (2007) using additional data from recent earthquakes. The M_w of the main liquefaction triggering CES earthquakes and epicentral distances of the six study sites are plotted on the lower-bound curves presented by Castilla and Audemard (2007) (Fig. 4.11). The CES data is shown to cluster with the global liquefaction data at short epicentral distances (Fig. 4.11). The variability in the data plotted at short epicentral distances further suggests that other, site-specific factors likely influence the liquefaction susceptibility and resultant surface manifestation of liquefaction (Fig. 4.11). The lower-bound curve suggests that the occurrence and non-occurrence of liquefaction scales with earthquake magnitude and epicentral distances. However, the varied surface manifestation and dike widths at varying epicentral distances across eastern Canterbury indicates that the severity of liquefaction does not correlate readily with epicentral distance or earthquake M_w.

An upper-bound curve between sand blow diameter and distance from the epicentre has also been derived by Castilla and Audemard (2007) from global data. The curve is defined by a negative power-law relationship of $Re = (238/D)^{1.11 + 37}$ where Re represents the epicentral distance and D represents the sand blow diameter. The maximum sand-blow diameter at Site 1 was 5.2 m for the September

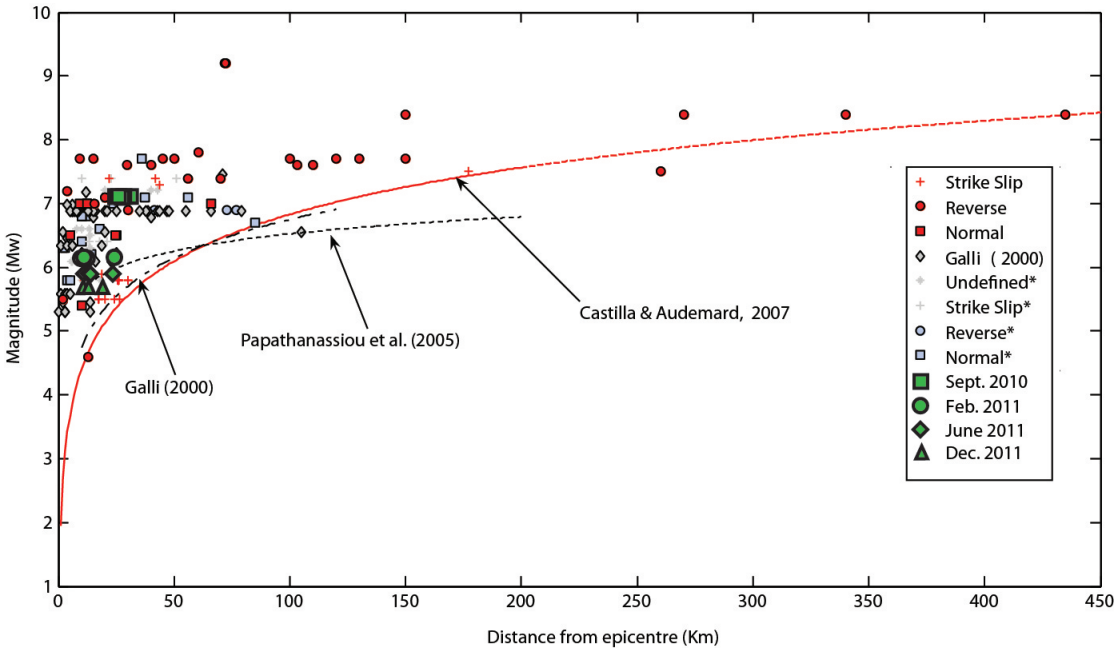

FIGURE 4.11: Lower-bound curve between the occurrence and non-occurrence of liquefaction with increasing earthquake M_w and epicentral distances as derived by Castilla and Audemard (2007). The main liquefaction triggering earthquakes during the CES are plotted with the epicentral distances for the six study sites.

2010 earthquake, and 4.8 m for the February 2011 earthquake. At Site 2, the maximum diameter was 5.5 m for the September 2010 earthquake, and 6 m for the February 2011 earthquake. The sand blow diameter and epicentral distances of the September 2010 and February 2011 earthquakes are plotted for Site 1 and 2 with the bounding curve outlined by Castilla and Audemard (2007) (Fig. 4.12).

The epicentre of the February 2011 earthquake was much closer to the two study sites than the epicentre of the September 2010 earthquake (Table 4.1). The sand-blows that formed at Site 1 during the September 2010 earthquake are comparably larger than those formed during the February earthquake (Fig. 4.12), while the sand-blows that formed at Site 2 during the February 2011 earthquake are only slightly (0.5 m) larger than those formed during the September earthquake (Fig. 4.12). The limited correlation between R_{epi} and sand blow diameter for the two sites suggests that sand-blow diameter does not unequivocally correlate with epicentral distance at these sites. The September 2010 and February 2011 sand blows mapped at Sites 1 and 2 plot below the upper-bound curve outlined by Castilla and Audemard (2007). The global data points constraining the curve are highly variable at short epicentral distances indicating that additional, site-specific factors most likely influence the diameter of sand-blows within the global data.

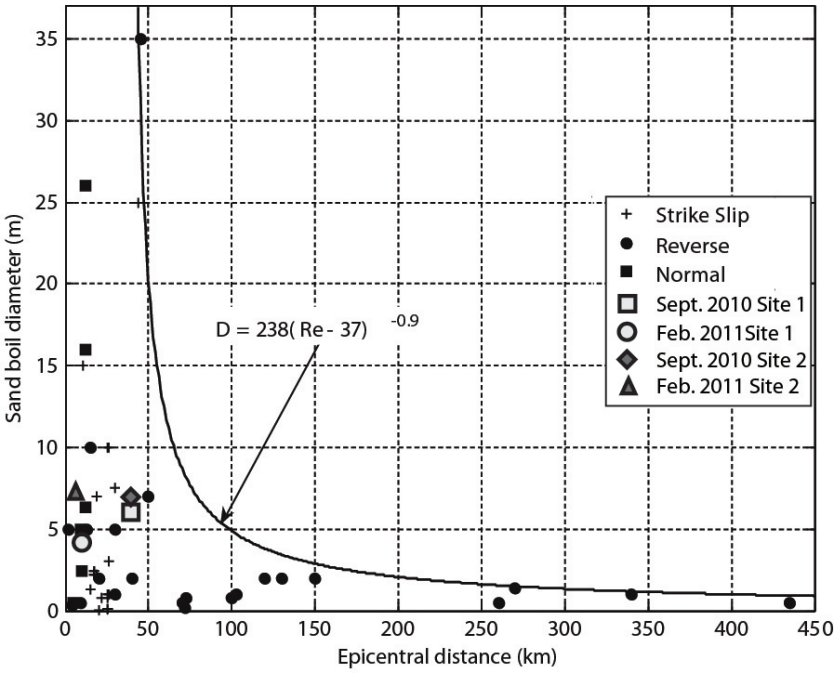

FIGURE 4.12: Upper-bound curve between maximum sand-blow diameter and earthquake magnitude as derived by Castilla and Audemard (2007). The maximum diameter of the sand blows measured at Sites 1 and 2 following the September 2010 and February 2011 earthquakes are also plotted.

Empirical equations between the magnitude-normalized PGA ($PGA_{7.5}$) and the aerial extent and maximum stratigraphic thickness of sand blows for Site 2 has been derived by Quigley et al. (2013). The relationship indicates that the diameter and thickness of the sand-blows at Site 2 was directly related to the $PGA_{7.5}$. The maximum sand-blow diameter at Site 1 occurred during the September earthquake despite the February earthquake generating higher PGA at the site. The variation in sand-blow diameters for these two events suggests that PGA does not unequivocally correlate with PGA and indicates that additional site-specific factors may influence the surface manifestation of liquefaction.

4.7 Comparison of dike widths, spatial extent of liquefaction ejecta, and subsurface stratigraphy

The trenches excavated at the six sites expose fluvial stratigraphy that varies from predominantly alluvial sands to predominantly alluvial silts (Fig. 4.4, 4.5, 4.6, &

4.7). The predominant sediment type in each of the trenches is compared with the mean dike width for each site to determine whether the variations in subsurface sediment type influenced dike width. Smaller-scale variations in the stratigraphy within the trenches (i.e. presence of paleo-channels, anthropogenic pits, and/or anthropogenic fill) are also compared to the dike widths.

4.7.1 Variations across Site 1

The five trenches (T1-T5) excavated at Site 1 expose stratigraphy comprising a basal non-plastic silt overlain by normally graded beds of fine sand to silt and capped by carbonaceous silt. The stratigraphy in the trenches is crosscut by anthropogenic pits comprised of cohesive silts. The stratigraphy in T4 is also crosscut by a paleo-channel (Fig. 4.4 & 4.5).

The CES dikes in T1-5 were observed to be comparably wider in the alluvial sands and silts (maximum width = 50 cm) compared to in the anthropogenic pit fill which is predominantly comprised of cohesive silts (maximum = 15 cm) (Fig. 4.5). It is possible that the comparably narrower dikes observed within the anthropogenic pit fill may result from increased cohesion between the silt particles which, may have inhibited fracturing and dike formation (Fig. 4.5C). The loosely consolidated fine sands likely facilitated the formation of comparably wider dikes. The variations in the widths of the dikes within the alluvial sands and silts compared to the anthropogenic fill suggests that sediment competency influenced dike widths. No clear variations in dike width is observed between the basal cohesive alluvial silt compared to within the overlying alluvial sands.

The paleo-channel intersected in T4 does not contain any subsurface liquefaction features. The margins of the paleo-channel can be traced across the park from subtle variations in topography and grass die-off due to the increased porosity and lack of moisture held within the paleo-channel sand (Fig. 4.3B, 4.4 & 4.13). The surficial lateral spreading fissures appear to dissipate at the margin of the paleo-channel for the September 2010 and June 2011 earthquakes, with minor surface ejecta observed within the paleo-channel. No surficial liquefaction are observed within the paleo-channel following the February 2011 or December 2011 liquefaction-triggering earthquakes (Fig. 4.13). It is likely that the presence of predominantly fine sand at the ground surface in the paleo-channel dissipated pore-water pressures within the liquefiable stratum and thus may have inhibited the

FIGURE 4.13: Aerial photographs of Site 1 flown after the September 2010 (A), February 2011 (B), June 2011 (C), and December 2011 (D) earthquakes. The margins of the paleo-channel (dotted black lines) and position of T1-5 (outlined in white) are also indicated.

surface ejection of liquefied sediment (Seed and Idriss, 1982; Idriss and Boulanger, 2008).

4.7.2 Variations in stratigraphy between the six sites

The trenches excavated at Sites 4 and 5 expose stratigraphy composed of loosely consolidated alluvial sands underlain by cohesive silt, similar to that at Site 1 (Fig. 4.5 & 4.6). The trenches excavated at Site 2 in Avonside, and Site 6 in Kaiapoi expose stratigraphy predominantly composed of non-cohesive alluvial silts (Fig. 4.5, 4.6, & 4.7) while the trench at Site 3 in Avondale exposes stratigraphy containing of alluvial silts overlain by cohesive silt anthropogenic fill comprising river dredgings (Fig. 4.6).

The CES dikes in the alluvial sands at Sites 1, 4, and 5 are comparatively wider (maximum widths of 55, 35, and 19 cm respectively) than those in the cohesive

alluvial silts at Sites 2, 3, and 6 (maximum widths of 4, 3, and 4 cm respectively) (Fig. 4.8). It is possible that cohesion between the alluvial silt grains required comparatively higher pore-water pressures to induce fracturing, and thus form dikes than the loosely consolidated fine to very fine alluvial sands. In addition, the presence of the anthropogenic fill composed of cohesive silt at Site 3 likely increased the over-burden pressures exerted on the subsurface sediment and thus increased the resistance to liquefaction at the site, resulting in the comparably narrow dikes observed at the site (Fig. 4.8).

Comparably fewer liquefaction dikes are observed within the alluvial silts at Sites 2, 3, and 6 (2-3 dikes per trench) compared to the fluvial sands at Sites 1, 4, and 5 (2-5 dikes per trench). Additionally, a higher proportion of liquefaction dikes identified at Sites 2, 3, and 6 terminated beneath the surface compared to Sites 1, 4 and 5 (Fig. 4.5, 4.6, & 4.7). The dikes within Sites 2, 3, and 6 do not contain evidence for multiple episodes of liquefaction, indicating that either fewer dikes formed within the cohesive silts during the CES, or that once a dike had formed the entire width of the dike was continuously re-activated during subsequent liquefaction episodes. The variations in the morphology and number of dikes within the trenches indicates that the subsurface sediment type directly influenced dike morphology.

4.8 Comparison of dike widths, lateral spreading extensional strains, and liquefaction susceptibility of subsurface deposits

The local component of the horizontal ground displacements (i.e. induced by lateral spreading) was compiled for the six sites for the September 2010 and February 2011 earthquakes along with total the CES lateral spreading-induced horizontal displacements. Extensional strains are calculated for each site from the horizontal displacements for comparison with dike widths and surface ejecta.

Lateral spreading typically occurs when liquefaction is triggered at sites with gently sloping ground or located proximal to a free-face (i.e. river bank). The gently sloping ground or free-face provide the gravitational driving force for the downslope transport of liquefied sediment, thus resulting in lateral spreading (Seed and

Idriss, 1982; Idriss and Boulanger, 2008; Cubrinovski and Green, 2010). The geometries of the free-faces, depth to the first potentially liquefiable unit, and the thickness of the first potentially liquefiable unit strongly influences the total horizontal displacements. The depth and thickness of the first potentially liquefiable unit are evaluated for each site from the CPT soundings conducted proximal to the sites during the CES for comparison with the lateral-spreading induced horizontal displacements at each site (Fig. 4.3 & 4.15). Lateral spreading at the study sites was driven by the river-banks which provide free-faces. The slope within the alluvial settings of Sites 1-6 is presumed to be negligible and is therefore considered unlikely to influence lateral spreading (Robinson et al., 2013).

The horizontal displacement vectors are presented in Figure 4.14. The surface liquefaction features at each of the study sites appear to be oriented perpendicular to the extension direction and parallel with the orientation of the closest free-face. The orientation of these features indicates that their formation was directly influenced by lateral spreading at the sites (see Chapter 5 for detailed discussion of factors influencing the surface manifestation of liquefaction).

4.8.1 Site 1: Sullivan Park

Horizontal displacements across Site 1 ranged from ∼0.5 m at the south-west corner to ∼1.7 m in the north-east corner during the 2010 September earthquake. The differential horizontal displacements across the site resulted in high extensional strains with 1.17 m of extension recorded across the site (120 m; Fig. 4.14). Comparably lower horizontal displacements occurred across the site during the 2011 February earthquake with 0.8 m recorded in the north-east corner and 0.4 in the south-west, resulting in 0.35 m of extension over 120 m (Fig. 4.14). The site experienced 1.98 m of extension across the site (120 m) during the CES resulting in overall high extensional strains (Fig. 4.14).

The CPT soundings indicate that the sediment from 1.3 m to 5.5 m depth was potentially liquefiable (FS <1) under the PGAs of the September earthquake (Fig. 4.3C & 4.15). For the February 2001 earthquake, the sediment from 1 m to 8.2 m depth plots well below the FS=1 line indicating that the sediment was potentially liquefiable (Fig. 4.15).

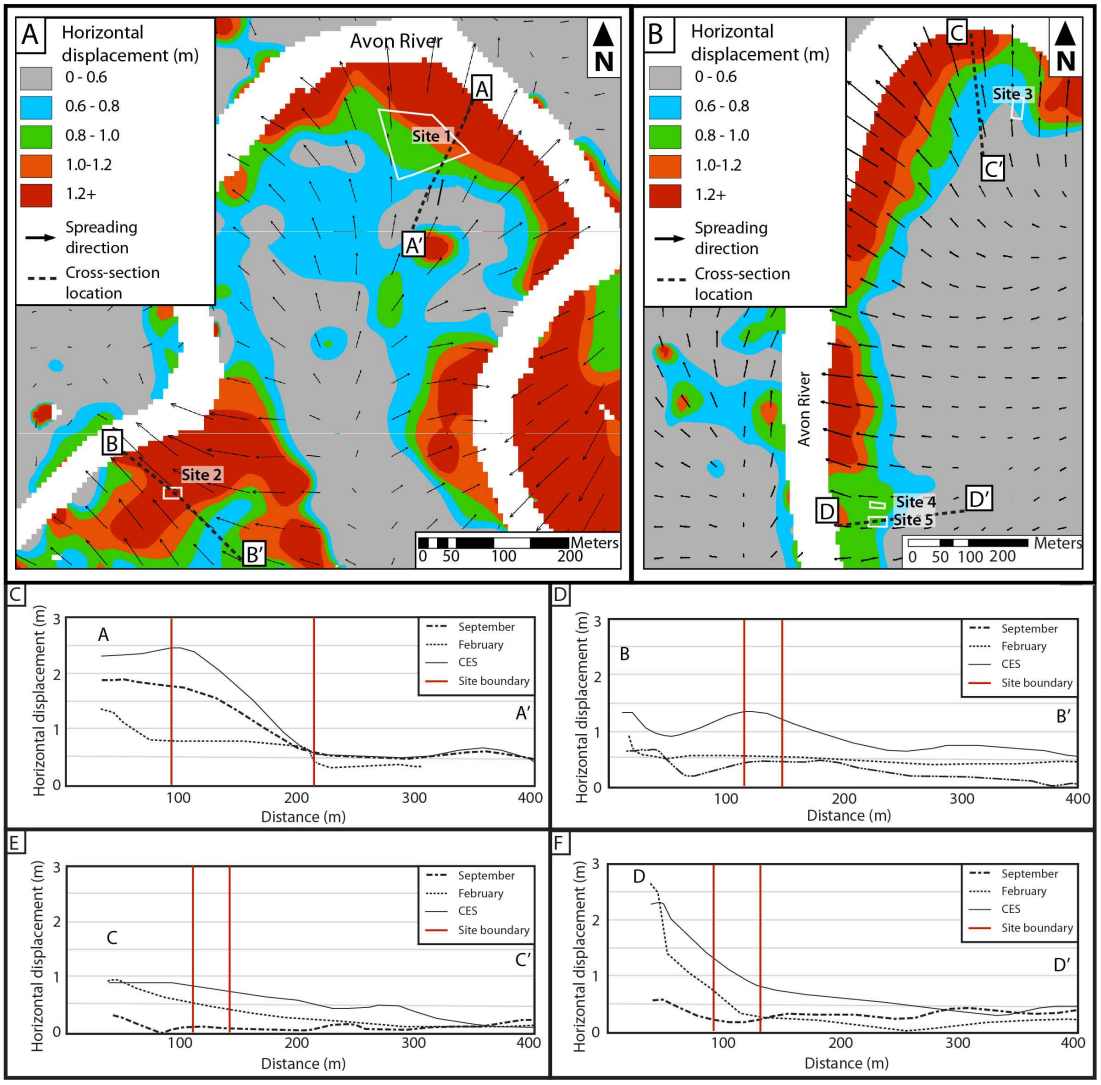

FIGURE 4.14: Total CES horizontal displacements measured within Avonside (A) and Avondale (B). Cross-sectional profiles indicating the displacements measured across the sites following the September 2010 and February 2011 earthquakes, and total CES horizontal displacements.

Site 1 is located proximal to the apex of a meander bend of the Avon River which provides three free-face orientations (Fig. 4.3A). The low-elevations and proximity of the north-east corner to the river likely resulted in the high horizontal displacements in this area (Fig. 4.15 & 4.14). The increased distance from the river in the south-west corner corresponds with the lower horizontal displacements recorded in this area (Fig. 4.14). The high extensional strains recorded across the site during the September 2010 earthquake likely resulted in the formation of the wide CES lateral spreading fissures at the site (Fig. 4.3B & 4.5).

Smaller horizontal displacements and lower extensional strain occurred at the site

during the February earthquake despite the epicentre being more proximal to the site and generating higher PGA at the site. The surficial liquefaction ejecta was also comparably more widespread at Site 1 following the September 2010 earthquake compared to that observed following the February 2011 earthquake which indicates that the higher extensional strains at the site during the September 2010 earthquake directly influenced the surface extent of liquefaction ejecta.

4.8.2 Site 2: Bracken Street

Horizontal displacements of 0.4 m occurred across Site 2 during the 2010 September earthquake, while displacements of 0.5 m occurred across the site during the February 2011 earthquake. The consistency in the displacements recorded across the site indicate that translational movement occurred at the site rather than extensional (Fig. 4.14). Low differential displacements occurred across the site during the CES (0.1 m over 30 m) resulting in very low extensional strain across the site (Fig. 4.14). The predominantly translational to low extensional strains recorded at Site 2 likely resulted in the formation of the comparably narrower dikes observed in the subsurface compared to that observed at Site 1 (Fig. 4.8).

The CPT soundings conducted proximal to the site indicate that the sediment profile from 0.5-0.8 m depth and beneath 1.2 m contains thin units that were potentially liquefiable during the September 2010 earthquake (Fig. 4.15). The sediment profile beneath 0.8 m plots well below the FS=1 line for the PGAs generated in the February 2011 earthquake and thus is considered liquefiable (Fig. 4.15).

Site 2 is situated along a relatively straight section of the river which provides only a single free-face orientation. It is possible that the increased distance from the free-face, presence of a single free-face orientation, and thin liquefying layers may have limited the horizontal displacements at the site during the September 2010 earthquake (Fig. 4.3A). Further information on the influence of the distance from the free-face on lateral spreading is presented in Chapter 5 and Bastin et al. (2015a).

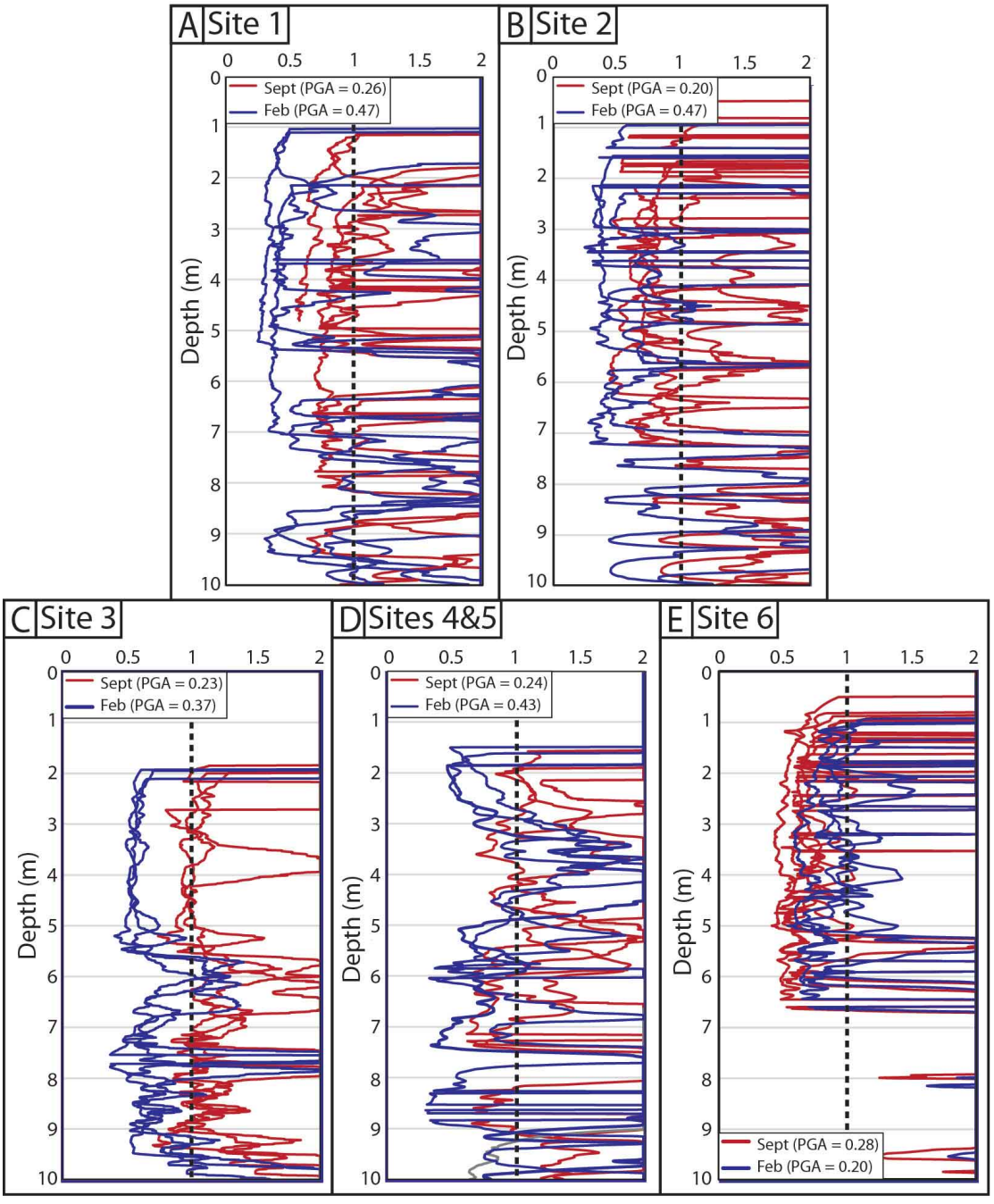

FIGURE 4.15: Summary of the resistance to liquefaction of the subsurface sediments under the PGAs of the September 2010 and February 2011 earthquakes as derived from the CPTs conducted proximal to the study sites. Sediment that plots beneath the FS=1 line is considered potentially liquefiable.

4.8.3 Site 3: Ardrossan Street

Horizontal displacements across Site 3 varied from 0.07 m to 0.09 m during the September earthquake resulting 0.02 m of extension across the site (40 m; Fig. 4.14). The site experienced slightly higher horizontal displacements during the February earthquake (0.45-0.6 m) resulting in moderate extension of 0.17 m across the site (40 m; Fig. 4.14). Total horizontal displacements across the site during the CES ranged from 0.8 to 0.9 m, resulting in moderate extension of 0.1 m over the site (40 m) (Fig. 4.14).

The CPT sounding indicates that thin units within the sediment profile from 2.5 m to 5.5 m depth likely liquefied (FS <1) during the September 2010 earthquake (Fig. 4.15). The sediment beneath 2 m was likely liquefiable (FS <1) during the February 2011 earthquake. The low extensional strains recorded across the site likely resulted in the formation of the comparably narrow dikes.

4.8.4 Sites 4 and 5: Cardrona Street

Horizontal displacements across Sites 4 and 5 range from 0.17 to 0.3 m for the September earthquake resulting in minor extension of 0.1 m across the site (30 m distance) (Fig. 4.14). Displacements range from 0.4 to 0.25 m across the site for the February earthquake thus resulting in low extension of 0.17 m across the site (Fig. 4.14). Total CES displacements range from 0.75- 1.0 m indicating the site experienced moderate-to-high extension of 0.27 m across the site (30 m; Fig. 4.14).

The CPT soundings indicate that thin units within the sediment profile from 2 to 2.2 m depth and beneath 3 m likely liquefied (FS <1) during the September 2010 earthquakes (Fig. 4.15). The sediment profile from 1.5-3.5 m depth likely liquefied (FS<1) during the February 2011 earthquake (Fig. 4.15).

4.8.5 Site 6: Sewell Street

Horizontal displacements for Site 6 were approximated from the displacement vectors available from the Canterbury geotechnical database. The post-February 2011

0.5 m LiDAR survey did not cover the Kaiapoi area, thus resolution of the horizontal displacement data for the site is too coarse for detailed comparisons to be made and for extensional strains to be calculated.

The horizontal displacement vectors indicate that approximately 0.4 m of horizontal displacement occurred at the site during the CES. The CPT soundings indicate that the sediment profile beneath 0.5 m likely liquefied (FS <1) during the September 2010 earthquakes, while the sediment beneath 1.2 m depth likely liquefied (FS<1) during the February 2011 earthquake (Fig. 4.15). This reflects the lower PGAs generated at the site during the February earthquake compared to the September 2010 event.

4.8.6 Variations across the study sites

The high extensional strains that formed across Site 1 during the September 2010 earthquake resulted in formation of wide surface fissures indicating that the area accommodated extension through fragmentation of the surface. The large surface fissures may have enabled dissipation of pore-water pressures within the liquefiable stratum during February 2011 earthquake and thus resulted in the lower horizontal displacements and surface ejecta recorded at the site for this event. The subsurface dikes contain evidence for up to 6 episodes of liquefaction indicating that extensional strains continued to accumulate across the site during the CES, while the preservation of repeated episodes of liquefaction within these dikes indicates that the dikes were re-activated during the CES.

Site 2 incurred translational movement to very low extensional strain during the CES, which likely resulted in the formation of narrow dikes that contained evidence for 1 episode of liquefaction. (Fig. 4.14 & 4.15). The documentation of up to 10 episodes of liquefaction at the site indicates that the dike was re-activated during each liquefaction event at the site (Quigley et al., 2013). The translational movement suggests that the area was rafted towards the river, which likely resulted in the formation of narrow dikes.

The predominance of aligned sand blow vents at Site 2 compared to the predominant surface fissures observed at Site 1 suggests that dike width and the surface manifestation of liquefaction is strongly influenced by the type of ground deformation (i.e. internal extensional strain in a translating block, or translation without

extension) (Fig. 4.3). The area in which the trench was excavated at Site 2 exhibited higher spatial extents of liquefaction ejecta than the area of T1 at Site 1. The lack of large surface fissures at Site 2 may have enabled higher pore-water pressures to be sustained in the liquefaction conduits (feeder dikes) and within the liquefied stratum and thus possibly resulted in comparably higher spatial extents of ejected liquefied sediment at the site.

Site 3 experienced low to moderate extensional strains within the non-liquefying cap during the CES despite being located proximal to an inner meander-bend of the Avon River which provides two free-face orientations (Fig. 4.14). The low extensional strains at the site resulted in the narrow dikes observed within the trench that contained evidence for only one episode of liquefaction (Fig. 4.8). The site is located within a similar depositional setting to Site 1, suggesting it should be highly susceptible to lateral spreading. The depth to the first potentially liquefiable unit under the PGA of the September 2010 and February 2011 earthquakes (2.5 m and 2 m respectively) is comparably deeper than at Site 1 (Fig. 4.15). Additionally, the subsurface comprises thin potentially liquefiable lenses for the September earthquake (Fig. 4.15). It is likely that the comparably deeper liquefying layers and presence of thin liquefying lenses resulted in the lower extensional strains recorded at the site compared to that recorded at Site 1. The higher over-burden pressures generated by the comparably thicker profile of the non-liquefiable sediments at Site 3 may have increased the resistance to liquefaction triggering and thus further limited lateral spreading at the site.

Minor extensional strain within the non-liquefying cap across Sites 4 and 5 during the September 2010 earthquake likely results from the comparably deep depth of the first potentially liquefiable unit (2 m) and the presence of thin lenses of potentially liquefiable sediment from 2-2.2 m and beneath 3 m (Fig. 4.15). Moderate extensional strains across the sites during the February 2011 earthquake likely result from the continuous potentially liquefiable unit from 1.5-3.5 m depth which enabled lateral spreading (Fig. 4.15). Sites 4 and 5 experienced lower horizontal displacements than Site 3, which likely reflects the increased distance of Sites 4 and 5 from the Avon River compared to Site 3. The low extensional strains resulted in the formation of narrow dikes and injection features which preserve evidence for only one episode of liquefaction.

The variations in lateral spreading induced horizontal displacements and extensional strains across the five eastern Christchurch study sites indicates that lateral

spreading is directly influenced by the depth and thickness of the potentially liquefiable sediment. Areas underlain by thick potentially liquefiable units proximal to the surface have comparably higher overall horizontal displacements (i.e. both extensional and translational) than areas underlain by thin lenses of potentially liquefiable sediments that are comparably deeper (Fig. 4.14). Additionally, extensional strain directly influences dike widths and the number of liquefaction episodes preserved within the dikes; areas with high extensional strains have wider dikes and preserve multiple episodes of liquefaction, while narrower dikes that preserve only one generation of liquefaction form in areas of predominantly translational movement to low extensional strain.

4.9 Deriving PGA histories from feeder dikes

The dike preserving six episodes of liquefaction in T4 at Site 1 provides an opportunity to reconstruct dike development during the CES (Fig. 4.4A, 4.5E; 4.16). The preservation of 6 episodes of liquefaction suggests that the lateral spreading fissure continued to widen as a result of continued extensional strain across the site during the CES, and that the extensional strain was localized into pre-existing fractures in the cap (Fig. 4.5D). The chronology of the six episodes preserved within the main dike is derived from cross-cutting relationships of the dike parallel silt linings and from comparison with the horizontal displacements and extensional strains recorded at the site (Fig. 4.16). The dikes preserved within the main dike are attributed to specific liquefaction triggering CES earthquakes. The maximum width of each dike is compared with the PGA of the attributed earthquake to determine whether dike width scales with PGA within a single feature. Dike widths and the likely causative earthquakes are summarized in Table 4.2.

Table 4.2: The earthquake magnitude and corresponding PGA generated at Site 1 during the events forming the conduits within the detailed dike in T4

Event number	Earthquake date & UTC	Earthquake magnitude (M_w)	Earthquake PGA (g)	Dike width (cm)
S1	20100903163500	7.1	0.26	35
S2	20100906114000	5	0.16	35
F1	20110221235100	6.2	0.47	15
F2	20110222000400	5.5	0.15	12
J1 (± J2)	20110613022000	6	0.26	7
D1 (± D2)	20111223021800	5.9	0.25	5

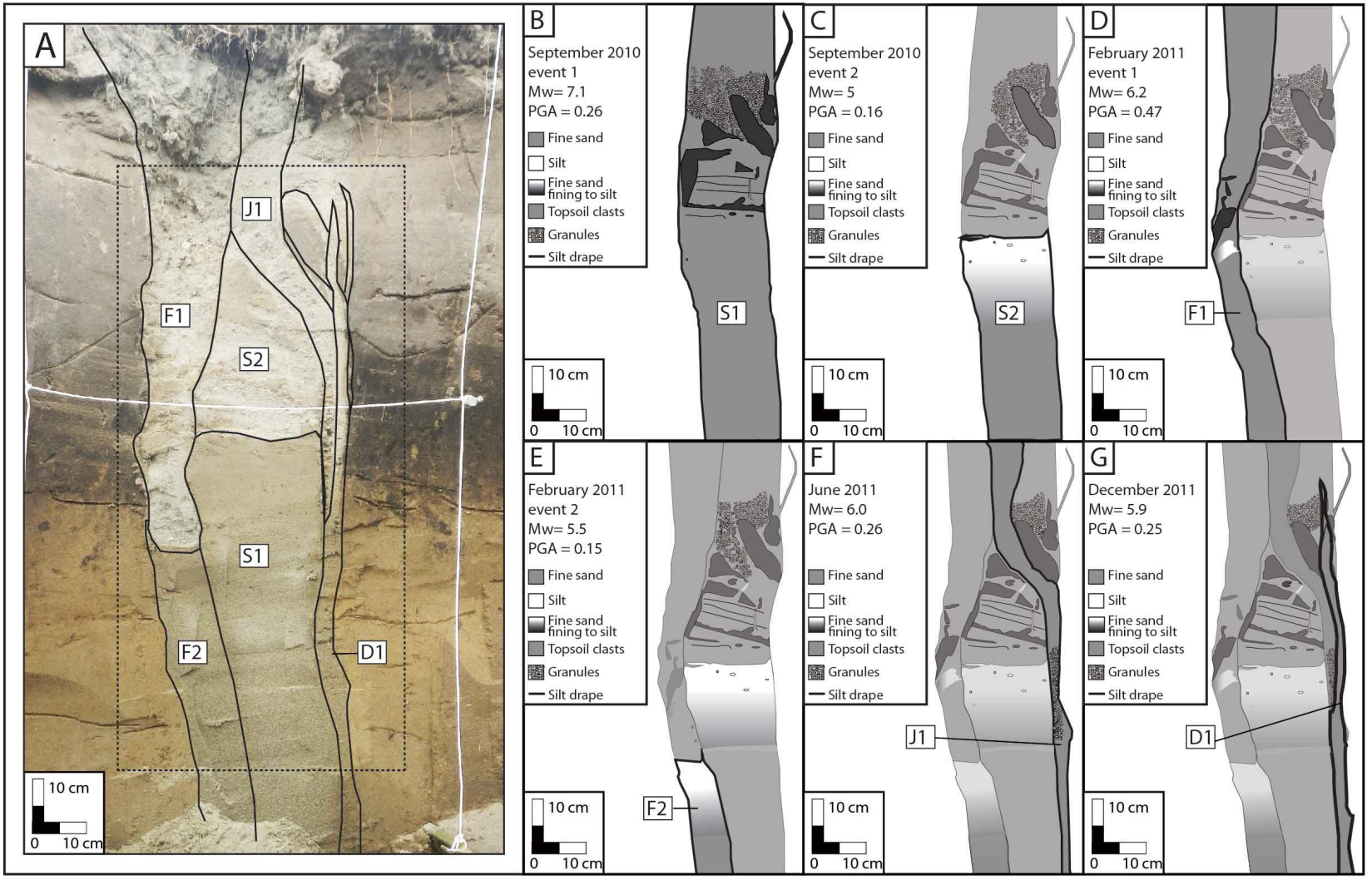

FIGURE 4.16: A) Interpreted photograph of the detailed dike in T4 at Site 1. B-G) Reconstruction of dike development throughout the CES as interpreted from cross-cutting relationships and internal deformation of the units preserved within the dike. The corresponding earthquake magnitude and PGA generated at Site 1 during the respective earthquakes are also indicated.

The widest section of the dike (labelled S1 in Fig. 4.16) is attributed to the September 2010 main-shock as it appears to be crosscut and deformed by all other dikes. The formation of the widest conduit during this event is consistent with the highest extensional strains being recorded at the site during this event (Fig. 4.14). The stalled dike of similar width (S2 in Fig. 4.16) is most likely attributed to an aftershock of the September earthquake due to its similar width and as it appears to deform the horizontal silt drapes formed within the initial dike (Fig. 4.16).

The ∼5-10 cm wide dike (F1 in Fig. 4.16) along the left margin of the September dikes (S1 and S2) is attributed to the February 2011 earthquake. The dike (F1) appears to crosscut and deform the margins of dikes S1 and S2 and appears to be crosscut by later dikes (Fig. 4.16). The comparably narrower width of this dike is consistent with the lower extensional strains recorded across the site during the February earthquake (Fig. 4.16 and 4.14). The stalled dike (F2 in Fig. 4.16) present within dike F1 is considered likely to be attributed to an aftershock of the February earthquake as it occupies the same conduit as the F1 (Fig. 4.16). The stalled dike is attributed to the M_w 5.5 aftershock earthquake on February 22nd 2011 which produced PGA of 0.13 at the study site. The stalling of dike F2 at depth suggests that the magnitude and PGA of the aftershock were not sufficient to cause surface ejection of the liquefied sediment.

The dike along the right margin of S1 is attributed to the M_w 6.0 June 2011 earthquake (J1 in Fig. 4.16). J1 is comparably narrower than the September 2010 and February 2011 earthquakes and is consistent with the lower PGA recoded at the site. It is possible that this dike may have formed, or have been re-activated in the June 2011 M_w 5.3 earthquake that occurred earlier the same day and generated PGA of 0.27 g at the site.

Dike J1 is crosscut by a dike attributed to the M_w 5.9 December 2011 earthquake which appears to stall at ∼20 cm depth (D1 in Fig. 4.16). The aerial photographs suggests that surface ejecta did form in the area overlying the dike suggesting that the dike reached the surface in an area that was not intersected within the trench (Fig. 4.16 & 4.13). The M_w 5.8 earthquake that occurred earlier the same day generated PGA of 0.23 g at the site and provides an additional possible source for the dike. It is possible the subsequent earthquake may have re-activated the dike and removed evidence for the earlier event.

The widest conduit is attributed to the September 2010 earthquake (S1, Fig. 4.16), despite the February 2011 earthquake generating higher PGAs at the site (Table 4.1). The September 2010 earthquake was the first earthquake to fracture the surface at the site, the previously un-fractured cap allowed large pore-fluid pressures to accumulate within the liquefied stratum, which resulted in large extension and formation of the comparably wide dike at the site. The comparably narrower dike formed during the February 2011 earthquake despite the higher PGA generated at the site indicates that dike width does not scale with PGA for these event (Fig. 4.17). Comparison of the widths of the conduits that formed the February, June, and December 2011 earthquakes (F1, J1, and D1) indicates that their width approximately scales with the PGA of these events (Fig. 4.17). The presence of the conduit from the liquefiable unit to the surface for the February, June and December earthquakes likely dissipated pore-water pressures, which resulted less extension at the site and comparably narrower dikes which approximately scale with PGA (Fig. 4.17). The approximate scaling of dike width for F1, J1, and D1, suggests that dike width may be applied to infer relative PGA of the aftershocks preserved within a single dike under consistent hydrologic and sedimentological conditions. However, it should be acknowledged that extensional strains appear to exert a first order influence on dike width, and that additional data is required to further constrain the robustness of this relationship.

4.10 Interpretation of factors influencing spatial extents of surficial liquefaction ejecta and dike widths

Paleo-liquefaction studies typically employ dike widths and sand-blow diameters to infer epicentral regions and magnitudes of paleo-earthquakes. Trenching at six study sites that experienced recurrent liquefaction during the CES revealed liquefaction dikes that varied significantly in width. Individual dike width does not uniquely scale with the PGA across the study sites, nor with epicentral distances of the main CES liquefaction triggering earthquakes. The variations in dike widths between sites indicates that factors in addition to PGA and epicentral distance influenced dike widths at these sites. The exception to this is the recurrent liquefaction preserved within the dike in T4 at Site 1 in which incremental high

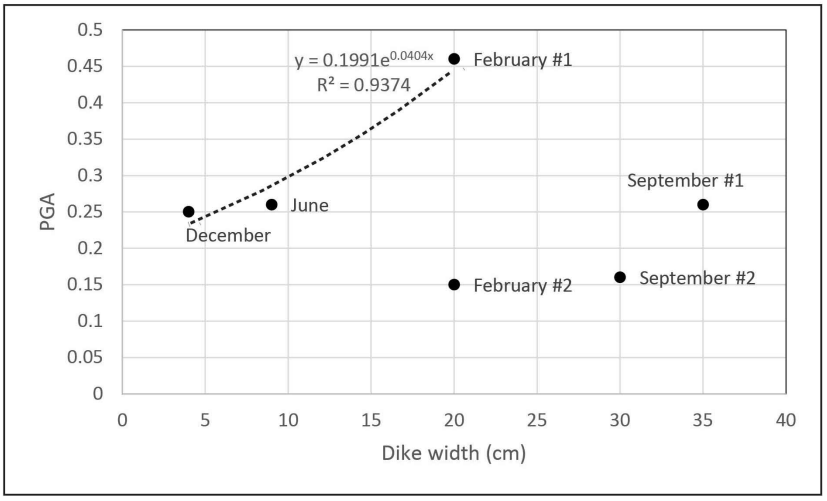

FIGURE 4.17: The width of the conduits formed within the dike in T4 at Site 1 compared with the PGA generated at the site during the respective CES earthquake. The width of the conduits formed in the February, June, and December 2011 earthquakes appear to approximately scale with PGA with the exception of the February 2011 aftershock (February 2). The initial width of the conduit formed during the September 2010 earthquakes does not scale with the PGA of these events.

extensional strains across the site during the CES facilitated the preservation of recurrent liquefaction.

Comparably wider dikes formed at Sites 1, 4, and 5 which are underlain by alluvial sands to silts and experienced high extensional strains. The loosely consolidated alluvial sand to silt likely broke apart or separated to accommodate extensional strains at these sites and thus resulted in the formation of the lateral spreading fissures and comparably wide dikes. Sites 2, 3, and 6 exhibit comparably narrower dikes, are underlain by cohesive alluvial silt, and exhibited translational movement to low extensional strain across the site. The cohesive nature of the silts underlying these sites likely stretched to accommodate the extension across the site thus resulting in the formation of localized narrow dikes. Sites underlain by alluvial silts also exhibited a fewer liquefaction dikes in the subsurface than the sites underlain by alluvial sand, which further supports that the extension of the silts resulted in the formation of localized dikes.

Site 1 exhibited lower spatial extents of surface ejecta than Site 2. The fracturing of the non-liquefying crust in multiple locations within the alluvial sands at Site 1 likely dissipated pore-water pressures and thus possibly resulted in lower volumes of surface ejecta. In comparison, the stretching of the alluvial silts at Site 2 resulted in fewer conduits forming within the non-liquefying crust, which combined with

their narrower widths likely resulted in the higher spatial extents of liquefaction ejecta. The variations in the subsurface morphology and surface manifestation of liquefaction between the two sites highlights the influence of sediment variability and competency on ground failure mechanisms, which is shown to directly influence the subsurface morphology and extent of surface ejecta.

The dikes formed within the anthropogenic fill at Site 1 are generally narrower than the adjacent dikes that formed within the alluvial sands suggesting that localized sedimentologic variability at a site may result in varied morphologies of liquefaction features across a site. In addition, no subsurface liquefaction features are observed within the paleo-channel exposed at Site 1. The variations in the subsurface morphology and spatial extent of liquefaction at Site 1 highlights the influence of small-scale variability in subsurface sediments on the manifestation of liquefaction.

The empirical equations derived by Quigley et al. (2013) indicate that $PGA_{7.5}$ directly correlates with the aerial extent and thickness of sand-blows at Site 2. The correlation suggests that in areas exhibiting predominantly translational movement the surface extent of liquefaction is directly related to $PGA_{7.5}$ which influences liquefaction triggering. These equations do not fit the observed sand-blow diameters mapped at Site 1 following the September 2010 and February 2011 earthquakes, indicating that factors in addition to $PGA_{7.5}$, influenced sand-blow diameters. Additionally, the sand-blows formed at Site 1 during the September 2010 earthquake were comparably larger than that formed during the February 2011 earthquake, which corresponds with the higher extensional strains experienced at the site during the September 2010 earthquake. The variation suggests that extensional strain directly influences the diameter of the surface sand-blows and subsequent surface manifestation of liquefaction.

4.11 Implications for paleo-seismic studies

The surface manifestations of liquefaction, diameters of sand-blows, and the widths of the subsurface dikes feeding the surface ejecta are highly variable amongst the study sites. Sedimentologic variability within the upper non-liquefying layer appears to have strongly influenced the failure mechanisms at the site and the subsequent subsurface morphology of features and surface manifestation of liquefaction.

The spatial extent of surface liquefaction, sand-blow diameters, and dike widths identified at each of the sites do not scale with variations in PGA or epicentral distances between sites. However, sand-blow diameters, and conduits formed within a single dike during subsequent earthquakes are shown to scale with PGA for single sites under constant sedimentolgoic and hyrdrologic conditions. The preservation of multiple episodes of liquefaction within the single CES dike indicates that paleo-liquefaction studies within areas of high extensional strain may be able to identify whether recurrent liquefaction occurred at a site. Although, it is possible that liquefaction during earthquakes on the same day (i.e. June 2011) may not be preserved. The variations in dike widths and surface manifestations between the sites highlights the potential limitations of inferring epicentral locations and PGA from the distribution and morphology of paleo-liquefaction features in areas underlain by heterogeneous sediments.

The February 2011 earthquake triggered liquefaction within more of the subsurface sediment profile at Site 1, although resulted in lower horizontal displacements, extensional strains, and narrower dikes than that observed following the September 2010 earthquake. The variations in dike widths and displacements between these events highlights the influence of a pre-cracked crust in dissipating pore-water pressures on lateral spreading and dike widths.

The study sites fall within the lower bound curve derived by Ambraseys (1988) and updated by Galli (2000) and Castilla and Audemard (2007) for the occurrence of liquefaction with increasing earthquake magnitude and epicentral distances, thus indicating that liquefaction is predicted at the study sites. The varied dike widths and surface manifestations of liquefaction at the study sites, and apparent influence of subsurface sediment variability on the ground failure mechanism suggests that epicentral distances should not be used to infer epicentral locations in areas underlain by sediments exhibiting spatial variability without detailed geologic and geotechnical site investigation. The occurrence and non-occurrence of liquefaction at sites considered susceptible to liquefaction may instead be analysed over a region and combined with bounding curves to approximate earthquake magnitudes and epicentral distances at sites of paleo-liquefaction.

4.12 Conclusions

Trenching investigations conducted at five sites within eastern Christchurch and one site within the northern township of Kaiapoi revealed subsurface CES liquefaction features including sub-vertical and planar dikes, lateral sills, and bulbous injection features. The liquefaction dikes are shown to vary in width within the trenches, between trenches excavated at the same site, and across the six sites. The dikes also exhibit significant spatial variability in their widths along the length of the features (i.e. along lateral spreading fissures). The individual dikes exposed at the study sites do not scale with the site-specific PGAs nor epicentral distances for the liquefaction triggering CES earthquakes.

Subsurface sediment type is shown to directly influence the ground failure mechanism which directly influences dike widths and extents of surface ejecta. Sites underlain by alluvial sands exhibit high extensional strains across the site as the sand tends to fracture to accommodate extension which results in comparably wider dikes, and lower spatial extents of liquefaction ejecta. Sites underlain by alluvial silts exhibit translational movement to low extensional strains as the silts stretch to accommodate movement and thus result in comparably narrower dikes and higher spatial extents of liquefaction ejecta. The preservation of 2-6 episodes of liquefaction within the dikes at Site 1 indicates that extensional strain continued to accumulate across the site throughout the CES and was directed into the already developed dikes.

Small scale variations in the subsurface stratigraphy appear to influence individual dike widths and the surface manifestation of liquefaction. Wider dikes formed within the fluvial sands to silts at Site 1 while narrower dikes formed within the cohesive anthropogenic pit fill. Additionally, no dikes are observed within the sandy paleo-channel at Site 1.

The diameter of the surficial sand-blows at Sites 1 and 2 do not correlate with epicentral distance, however they do plot beneath the upper-bound curve of sand-blow diameter and epicentral distance derived by Castilla and Audemard (2007).

Reconstruction of 6 episodes of CES liquefaction within a single dike at Site 1 enables comparison of PGA and dike width through the CES. A comparably wide conduit formed during the initial liquefaction event, while the widths of conduits formed during subsequent events approximately scale with PGA. The preservation

of recurrent liquefaction within the dike suggests that areas experiencing high extensional strain may host liquefaction dikes that preserve multiple episodes of liquefaction.

The study sites plot within lower bound curve for the occurrence of liquefaction with increasing earthquake magnitude and epicentral distances. The occurrence and non-occurrence of liquefaction at sites susceptible to liquefaction may be used with the bounding curve to approximate earthquake magnitudes and epicentral distances considered capable of triggering liquefaction at sites of paleo-liquefaction. However, the variations in dike widths and surface manifestations of liquefaction between the study sites highlights the limitations of employing dike widths to infer epicentral locations.

Chapter 5

Geomorphic, geologic, and topographic influences on the distribution and severity of liquefaction during the 2010 - 2011 Canterbury Earthquake Sequence

Abstract

Liquefaction during the September 2010 M_w 7.1 Darfield and February 2011 M_w 6.2 Christchurch earthquakes caused severe damage and disruption in parts of Christchurch, New Zealand. Empirical models commonly used to assess liquefaction triggering and lateral spreading displacements inaccurately predicted the severity of liquefaction and lateral spreading observed in parts of Christchurch following the September 2010 Darfield and February 2011 Christchurch earthquakes. In this study, the spatial distribution of 771 surface liquefaction features are mapped in the eastern Christchurch suburb of Avonside following the September 2010 earthquake and 4,872 features are mapped following the February 2011 earthquake. Liquefaction metrics including the density of surface liquefaction features, aerial extent of liquefaction ejecta, and liquefaction-induced horizontal and

vertical ground surface displacements are derived for the study area. The metrics are compared with sediment, geomorphic, and topographic variability across the study area and variations in the thicknesses of the liquefying sediment and overlying non-liquefying layer as determined through Cone Penetration Testing (CPT). Sediment and geomorphic variability within the study area is shown to have significantly influenced the surficial manifestation of liquefaction and horizontal ground surface displacements. Sediment variability and geomorphology is often not incorporated in the empirical models for site-specific liquefaction assessments nor in the simplified lateral spreading models. Implementation of sediment and geomorphic data is shown to improve the fit between predicted and measured horizontal ground displacements within the study area. The density of surface liquefaction features and the liquefaction-related horizontal ground displacements strongly correlate with the distance from the most proximal free-face divided by the height of the free-face (i.e. L/H), and the thickness of the non-liquefying cap divided by the thickness of the liquefying unit (i.e. H_1/H_2). An upper-bound curve between the presence and absence of surficial liquefaction features is produced when H_1/H_2 is multiplied with the L/H, however this does not account for variations in the severity of liquefaction or horizontal displacements. This chapter highlights that geomorphic and topographic variability should be integrated into standard geotechnical approaches for assessing liquefaction and lateral spreading hazards and indicates that a multi-disciplinary area-wide prediction approach should be taken rather than the typically used site-specific assessment methods.

5.1 Introduction

Liquefaction triggered by strong earthquake shaking poses a major hazard to urban environments. Liquefaction-induced lateral displacements, typically referred to as lateral spreading, and differential surface subsidence may cause severe damage to surface and subsurface infrastructure, and result in high financial losses (Cubrinovski and Green, 2010; Cubrinovski et al., 2012; van Ballegooy et al., 2014b; Rogers et al., 2015). The surface ejection of liquefied sediment can cause major disruptions to urban frameworks (Cubrinovski and Green, 2010; Cubrinovski et al., 2012), and require extensive and resource-consuming clean-ups (Villemure, 2013), as well as posing an urban health hazard (Ministry of Health, 2011). Subsidence induced by liquefaction may also increase flood and marine inundation hazards

and increase liquefaction vulnerability leading to secondary hazards and financial losses (Hughes et al., 2015; Russell et al., 2015).

The 2010-2011 Canterbury earthquake sequence (CES) caused at least 10 distinct episodes of observed liquefaction and lateral spreading in parts of eastern Christchurch, New Zealand (Fig. 5.1) (Cubrinovski and Green, 2010; Quigley et al., 2013; van Ballegooy et al., 2014a; Cubrinovski and Robinson, 2015; Quigley et al., 2016). Liquefaction manifested at the ground surface as sand blows and associated surface flooding, lateral-spreading-induced fissuring of the ground surface, and localized differential ground surface subsidence (Cubrinovski and Green, 2010; Cubrinovski et al., 2012; Quigley et al., 2013). Areas severely affected by liquefaction were primarily concentrated around modern and abandoned stream channels and estuarine deposits, indicating that sedimentologic and geomorphic variability influenced liquefaction vulnerability within Christchurch (Wotherspoon et al., 2011; Reid et al., 2012; Cubrinovski and Green, 2010). Liquefaction-induced damage to land and infrastructure comprises approximately one third of the total earthquake-induced losses during the CES, highlighting the significant financial losses that may arise from liquefaction (Rogers et al., 2015). The CES provides an opportunity to determine factors that influence the distribution and severity of the surficial manifestation of liquefaction and lateral spreading.

Sediments considered to have a low resistance to liquefaction are loose, unconsolidated, and saturated fine grained sand to silt generally within 10 meters of the surface (Youd et al., 2001; Idriss and Boulanger, 2008). Historic cases of liquefaction have generally been reported within Holocene fine grained sands to silts deposited in low energy environments including abandoned river channels, point bars, deltas, beach ridges, swamps, estuaries, and reclamation fill (Idriss and Boulanger, 2008). Engineering-based liquefaction assessments typically rely on empirical equations derived from field observations and laboratory testing to predict liquefaction triggering thresholds under given peak ground accelerations (PGA) (i.e. Robertson and Wride (1998); Moss et al. (2006); Idriss and Boulanger (2008); Boulanger and Idriss (2014)). Empirical and semi-empirical models have also been developed to predict lateral spreading-induced horizontal ground displacements from peak ground accelerations, distance from the closest free-face (i.e. riverbank), height of the free-face, and the thickness of the potentially liquefiable sediments (Zhang et al., 2004; Bartlett and Youd, 1995; Youd et al., 2002). The current methods for assessing liquefaction triggering and lateral spreading do not account

for spatial variations in subsurface sediments across a site or area. As a result the predicted liquefaction triggering and calculated horizontal displacements may vary significantly across an area, and from those measured following earthquake events (i.e. Bowen et al. (2012); Robinson et al. (2013); Deterling (2015)). For example, liquefaction assessments from site-specific geotechnical testing suggests that many areas within Christchurch are predicted to exhibit significant small-scale (e.g. 1-10 m) spatial variability in ground performance. However, studies by Russell et al. (2015) indicate that CES liquefaction-induced ground damage was fairly uniform within similar sediment deposits despite the predicted spatial variability. Additionally, the Zhang et al. (2004) and Youd et al. (2002) models for horizontal displacements over-predicted displacements in the upper-reaches of the Avon River and under-predicted displacements within the lower-reaches following the February 2011 Christchurch earthquake (Fig. 5.2) (Robinson et al., 2013; Bowen et al., 2012; Deterling, 2015). The variability between predicted and measured displacements highlights the sensitivity of the lateral spreading models to variations in the input parameters and the potential influence of sedimentologic, geomorphic, and topographic variability (Fig. 5.2).

In this chapter, the distribution of linear liquefaction features and aerial extent of surface liquefaction ejecta are mapped within a study area in eastern Christchurch following the September 2010 and February 2011 earthquakes. The density of linear liquefaction features, coverage of surface ejecta, and the liquefaction-induced horizontal and vertical ground displacements are compared with sedimetologic, geomorphic, and topographic variability within the study area. The mapped liquefaction and ground displacements are also compared with variations in the thickness and depth of the first liquefying layer, and distance from the river, to determine factors influencing the surficial manifestation of liquefaction. Horizontal displacements predicted from the Zhang et al. (2004) model are also compared with those measured within the study area following the September 2010 and February 2011 earthquakes. The input parameters for the model are varied to determine whether the predictive capability of the model may be improved by incorporating geomorphic and sedimentologic variability across the study area

5.2 Geology of Christchurch

5.2.1 Overview of the geology of the Christchurch area

The city of Christchurch (population 360,000) is primarily situated upon a low relief, alluvial landscape (0 to 20 m above sea level) on the east coast of New Zealand's South Island (Fig. 5.1). The Central Business District (CBD) (Fig. 5.1) and eastern suburbs are predominantly underlain by alluvial sands, silts, and drained peat swamps that are interbedded with estuarine, dune, and fore-shore sands (Fig. 5.1) (Brown and Weeber, 1992). The western area of the city is underlain by fluvial sands and gravels (Fig. 5.1).

The alluvial sands and silts underlying central and eastern Christchurch were initially sourced from catchments within the Southern Alps and transported eastwards by the braided Waimakariri River which regularly avulsed across the region prior to European settlement (Fig. 5.1). The sediments were subsequently reworked and re-deposited by meandering rivers (i.e. Avon) that also regularly flooded, and avulsed across the area now comprising Christchurch city (Cowie, 1957; Brown and Weeber, 1992) (Fig. 5.1). Peat deposits reflect swamps that formed in the food-plain adjacent to the meandering rivers (Fig. 5.1). Localized channelized sand to gravel are present at depth and may be related to pre-historic floods of the Waimakariri River across the area (Brown and Weeber, 1992).

The interbedded estuarine, dune and foreshore sands to silts were deposited during regression and coastline progradation following the mid-Holocene highstand. The coastline reached ∼3 km west of the present central city and ∼10 km inland from its current position at ∼6,500 years before present (Fig. 5.1) (Brown and Weeber, 1992). The co-evolution of floodplain and coastal landscapes within central and eastern Christchurch produced significant spatial heterogeneity within the Holocene sediments underlying the city (Fig. 5.1) (Brown and Weeber, 1992).

5.2.2 Meandering River processes and geomorphic development of the Avon River

Severe liquefaction and lateral spreading occurred proximal to the meandering Avon, Heathcote, Styx, and Kaiapoi rivers, the Avon-Heathcote estuary, and

within reclamation fill in eastern Christchurch during the CES (Fig. 5.4) (Cubrinovski and Green, 2010; Reid et al., 2012; Wotherspoon et al., 2011; Cubrinovski et al., 2012; van Ballegooy et al., 2014b; Cubrinovski and Robinson, 2015). The distribution of liquefaction suggests that a basic understanding of fluvial processes and geomorphic landforms may be used to identify areas potentially underlain by sediments susceptible to liquefaction.

Meandering rivers form within low gradient settings and generally comprise a single, sinuous river channel (Fryirs and Brierley, 2012; Ghinassi et al., 2013). During bank-full conditions, the highest flow velocity is concentrated along the outer concave bank of the channel causing erosion and retreat of the river bank (Willis and Tang, 2010). Flow is deflected toward the inner convex bank of the channel where the eroded sediments are transported and deposited as point-bar deposits (Fryirs and Brierley, 2012; Ghinassi et al., 2013). The erosion and subsequent redeposition promotes channel migration across the alluvial plain (Willis and Tang, 2010).

The stratigraphy of the inner-meander bend is typically dominated by point-bar deposits that comprise fining upward sequences of fine sand grading to silt and clay. These deposits are typically inter-bedded with coarser sediments deposited during flood events, and draped by silts deposited as the flow-rates decrease (Willis and Tang, 2010). The alluvial plain proximal to the river is generally comprised of fine-sand to silt deposited as the river over-tops its banks. Back swamps generally form distal to the river where standing water remains following flood-events (Fryirs and Brierley, 2012; Ghinassi et al., 2013).

The river channel may rapidly avulse across the alluvial plain as a sudden shift in the river course promotes the formation of a new channel (Toonen et al., 2012). Avulsion typically occurs as an aggrading river bed cuts through its levees, which may cut-off a meander-bend forming an ox-bow lake (e.g. Hooke (2004)); or it may result from tectonic deformation (e.g. Duffy et al. (2013)). The abandoned river channel may be preserved as paleo-channel that is recognisable as a depression in the landscape (Fryirs and Brierley, 2012; Toonen et al., 2012). Paleo-channels typically comprise sandy deposits accumulated prior to the avulsion event, overlain by finer sediments deposited as flow-rates decreased, and capped by over-bank flood deposits or lake and swamp deposits (Willis and Tang, 2010; Toonen et al., 2012).

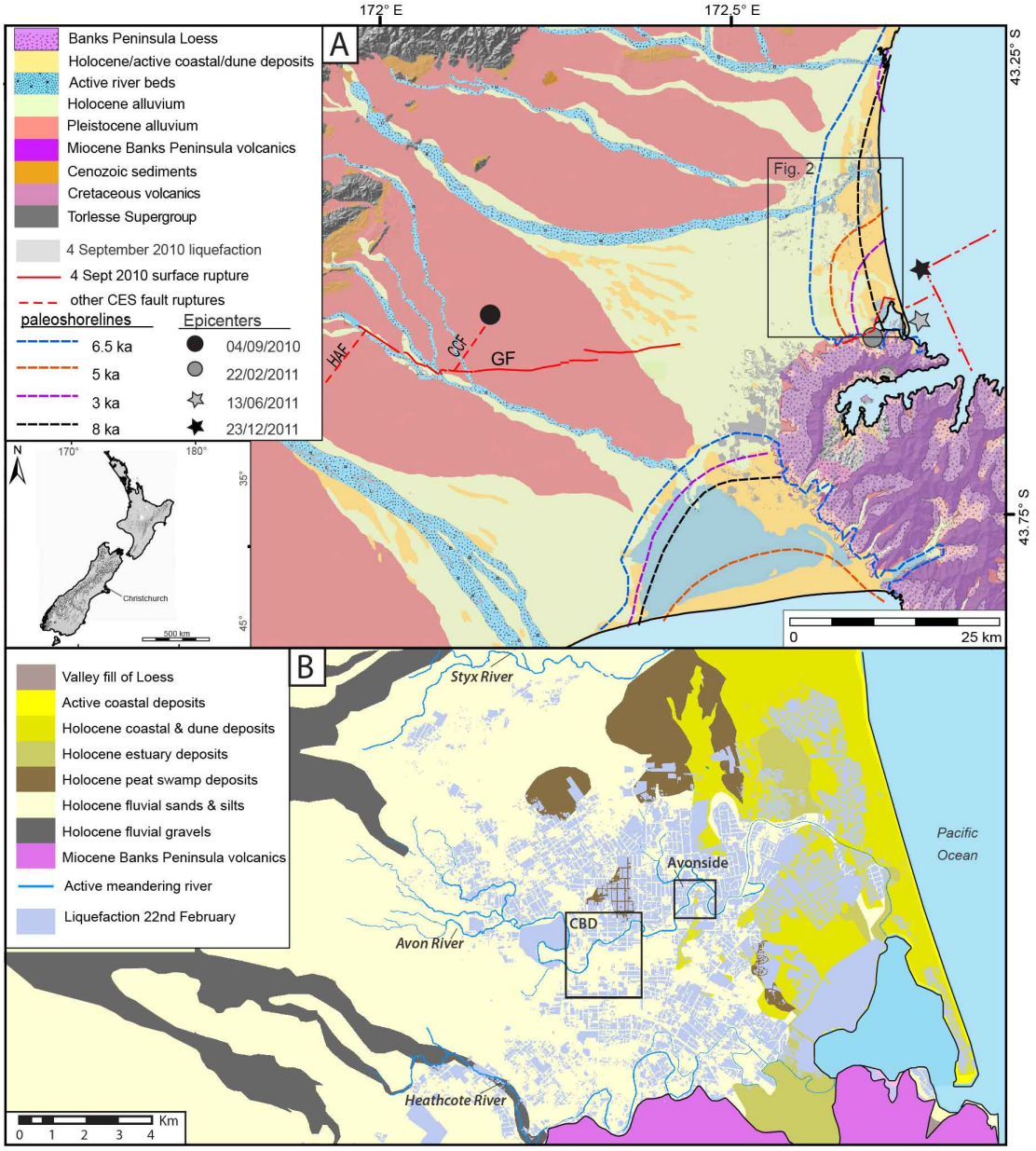

FIGURE 5.1: A) Simplified map of the surficial geology over the wider Christchurch area with the location of the paleo-shorelines indicated. The epicentral locations and the surface rupture trace (bold line) and projected locations of subsurface faults (dotted lines) that triggered liquefaction in eastern Christchurch are also indicated. B) Simplified map of the surficial sediments within the wider Christchurch area (modified from Brown and Weeber (1992) with the location of the Avonside study area with respect to the meandering Heathcote, Avon, and Styx Rivers indicated.

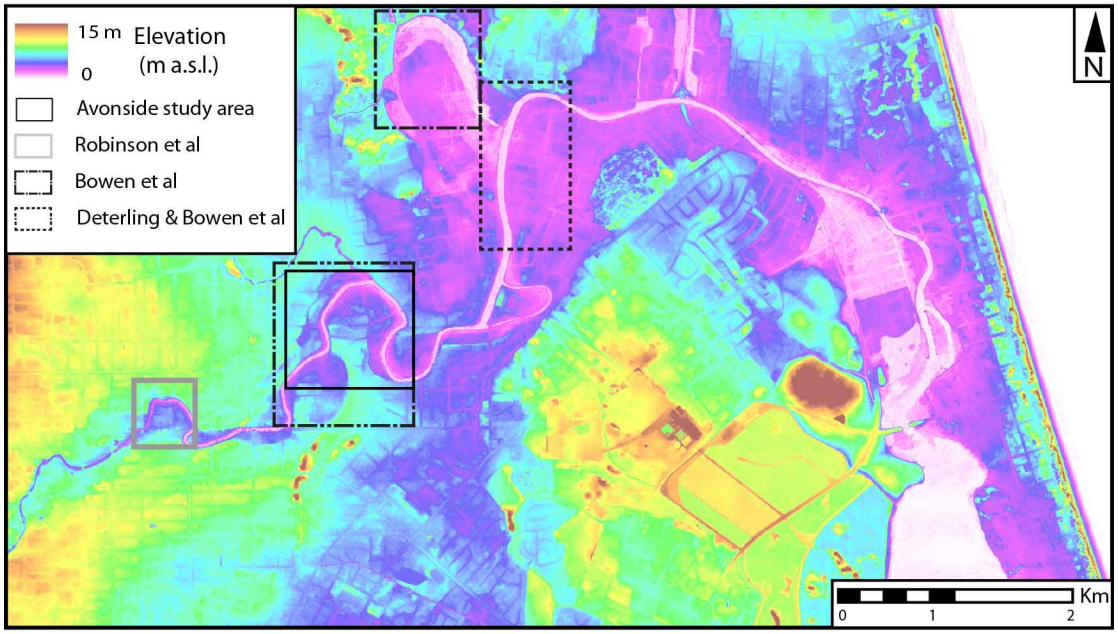

FIGURE 5.2: 0.5 m DEM of the eastern Christchurch area with the locations of the Robinson et al. (2013); Bowen et al. (2012) and Deterling (2015) study areas indicated. The Avonside study area, which corresponds with the Bowen et al. (2012) study area, is also indicated.

The morphology of the Avon River and its surrounding alluvial plain are typical of that formed by meandering rivers (Fig. 5.4 & 5.2). Meander development along the Heathcote River to the south of the city has been constrained by the Port Hills resulting in a unique depositional setting that varies from unconstrained meandering rivers (i.e. Avon River) (Fig. 5.4 & 5.2). The subsurface deposits proximal to the Heathcote River comprise partially saturated silty sediments interbedded with sands. The liquefaction susceptibility of these is not adequately accounted for in current CPT-based methods, thus the results of this study are not considered applicable to the Heathcote River (Stringer et al., 2015). The results of this study are considered to be applicable to other unconstrained meandering rivers (i.e. Styx and Kaiapoi Rivers).

The study area, located within the suburb of Avonside, is encompassed within a low lying inner meander-bend of the Avon River (Fig. 5.1 & 5.2). The area is underlain by fine sand and silt of point bar, over-bank, and channel deposits of the meandering Avon River. Localized channelized gravels that could be related to pre-historic floods of the Waimakariri River are present at depth (Silby, 1856; Brown and Weeber, 1992). The geological map of Christchurch indicates that the central area of higher elevation is underlain by Late Holocene sand dune deposits (Fig. 5.4) (Silby, 1856; Brown and Weeber, 1992).

5.3 Methodology

Multiple methods were employed to assess the spatial distribution of liquefaction and associated ground displacements and determine variations in the liquefaction susceptibility of the subsurface deposits. The distribution of liquefaction and ground dist placements are compared with variations in river morphology and the properties of the subsurface sediments to determine geomorphic and geologic influences on the subsurface manifestation of liquefaction.

5.3.1 Geomorphic mapping

The geomorphology of the study area was mapped from subtle variations in topography and in the shape and morphology of the Avon River as observed within the 0.5 m DEM of the area (Fig. 5.2) (DEM available from the Canterbury Geotechnical Database (http://canterburygeotechnicaldatabase.projectorbit.com)). The topographic and morphological variations across the study area were compared with basic meandering river processes (i.e. channel avulsion and point bar development) to interpret the paleo- and present depositional setting of the area and to further subdivide the area into corresponding geomorphic areas.

5.3.2 Cone Penetration Tests and Boreholes

The Cone Penetration Tests (CPT) and boreholes conducted across the study area during the Canterbury earthquake sequence were collated for the study area from the Canterbury Geotechnical Database (https://canterburygeotechnicaldatabase.projectorbit.com). The CPT measures the resistance of the subsurface sediments to an instrumented cone being pushed vertically downwards at a constant rate which is recorded as q_c (Lunne et al., 2014). The relative resistance of the subsurface sediments are used to infer the sediment behaviour types, and relative densities. Machine boreholes were conducted and logged by companies commissioned by the Earthquake Recovery project. Detailed descriptions of the specific rig capabilities of each company are outlined in Tonkin and Taylor (2011).

The likelihood of liquefaction under the ground accelerations and depth to the ground water table of the September 2010 and February 2011 earthquakes were

calculated for each CPT using the Boulanger and Idriss (2014) methodology. The sediment behaviour-type index (I_c) liquefaction cut-off point of >2.6 was applied, above which sediments are considered too plastic in behaviour to liquefy (Robertson and Wride, 1998). The Fines Content (FC) was estimated from the I_c using the Boulanger and Idriss (2014) correlation with a FC value of 0.1 selected based on the studies by Lees et al. (2015). The event specific water tables were derived for the main CES liquefaction triggering earthquakes by Cox et al. (2012) and are available from the Canterbury Geotechnical Database. The results of the liquefaction assessment of each CPT are presented in the Appendix F in the electronic supplement to this thesis.

The thickness of non-liquefying sediment "cap" layer (H_1) and the thickness of the first liquefying layer (H_2) were measured from the predicted liquefaction profiles for both the September 2010 and February 2011 earthquakes. An example of how the H_1 and H_2 was measured from the liquefaction profiles is outlined in Figure 5.3. In cases where there the liquefying unit contained thin non-liquefying layers, the non-liquefying units were assumed to not have significantly influenced liquefaction at the site and thus are included within H_2 (Fig. 5.3B). Additionally, in cases where thin liquefying units were present within a thicker non-liquefying unit, the thin layer was assumed to not influence the overall liquefaction susceptibility of the site, and thus was included in H_1 (Fig. 5.3C). The ratio of H_1 to H_2 was also derived for each CPT.

5.3.3 Mapping surface liquefaction features and ejecta

I mapped the distribution of the surficial linear liquefaction features that formed in the study area during the September 2010 and February 2011 earthquakes using ArcGIS and the high resolution aerial photographs flown by NZ Aerial Mapping on 5 September 2010 and the 24 February 2011 (available from the Canterbury Geotechnical Database). The length of 771 surface liquefaction features comprising linear arrays of aligned sand-boil vents and lateral spreading fissures were mapped following the September 2010 earthquake while 4,872 surface liquefaction features were mapped in the study area following the February 2011 earthquake (Fig. 5.8). The mapped features were ground-truthed using the surface features still visibly evident between the September 2010 earthquake and September 2012. Some of the lateral spreading fissures mapped following the February 2011 earthquake may

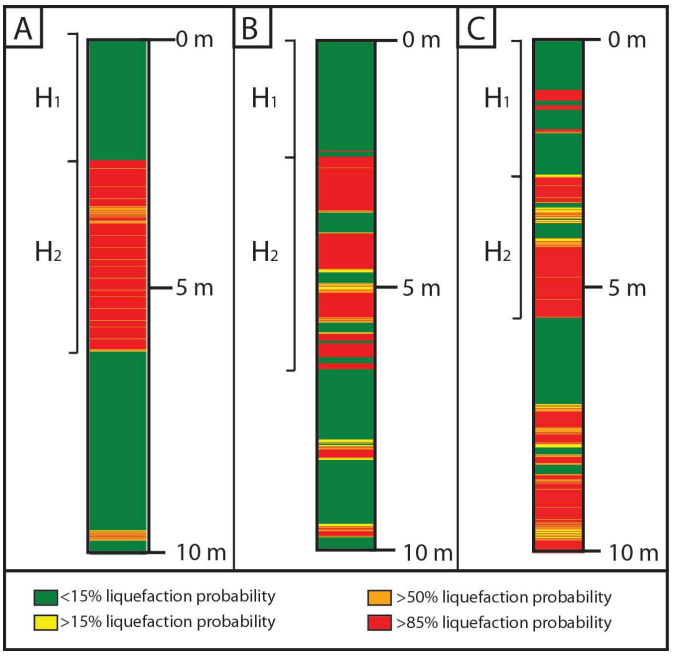

FIGURE 5.3: Indication of how the H_1 and H_2 values were measured from the predicted liquefaction profiles derived from liquefaction analysis of the CPTs.

have been formed during the September 2010 earthquake as the relative timing of the surface fissures could not always be concluded from the aerial photography. The distribution of mapped liquefaction features is presented in Figure 5.8.

The length, azimuth, and minimum distance to the closest down-slope free-face was calculated for each mapped feature within the February 2011 earthquake data set and are plotted in Figure 5.9. Length measurements were locally limited by obstruction from buildings and vegetation, thus it is possible that individual fissures may be longer than that measured. Mapping did not account for the severity of the features as the width of each feature was unable to be accurately estimated from the aerial photographs. Features that formed on roads and driveways were identified but not considered in subsequent data analysis as their orientation and geometry was controlled by weaknesses within engineered surfaces (e.g. roads, etc.) and subsurface infrastructure (e.g. light poles) rather than the subsurface sediments.

The aerial extent of the liquefaction ejecta surrounding the linear arrays of sand blows and surface fissures, along with the ejecta comprising localised surface sand blows and surface flooding, was also mapped in detail in ArcGIS from the post-September 2010 (Darfield) and post-February 2011 (Christchurch) earthquakes high-resolution aerial photographs. The mapped extent of liquefaction ejecta is

presented in Figure 5.11. Mapping did not take into account the thickness of the deposits nor the surface flooding as this could not be accurately determined from the aerial photographs. The surface ejecta was removed from the area following the September 2010 earthquake, thus the ejecta mapped following the February 2011 earthquake represents ejecta caused by that event.

5.3.4 Grain-size analysis of surface liquefaction ejecta

Grain-size analysis was conducted on samples of liquefaction ejecta obtained from selected sites across the study area. Analysis was conducted at the University of Canterbury Sedimentology Lab with a Micrometrics Saturn DigiSizer II 5205. The sample was added to the reservoir until ∼30% beam obscuration was achieved. A laser and charge-coupled device (CCD) was then applied to measure the intensity of light scattered by suspended organic and inorganic particles between 0.06 - 2100 μm at various light angles. The light intensity absorbed by particles is dependent on the size, shape, refractive index, and the wave length of the incident light (Storti and Balsamo, 2010). Two tests were run for each sample to ensure the machine was performing consistently. Results of the grain-size analysis are plotted in Figure 5.12.

5.3.5 X-Ray Fluorescence (XRF) Analysis of surface liquefaction ejecta

The geochemical composition of the liquefaction ejecta was determined by X-Ray Fluorescence analysis. Samples were treated with hydrogen peroxide (∼3-5% solution concentration) to remove any organic matter then rinsed in distilled water and dried at 60°C for one week. Dried samples were milled to a fine powder, with ∼10 gm of the resultant sample submitted for XRF testing. Testing was conducted by the University of Canterbury Geological Sciences Department using a Phillips PW2400 Sequential Wavelength Dispersive X-ray Fluorescence Spectrometer. The rock majors (SiO_2, TiO_2, Al_2O_3, Fe_2O_3T, MnO, MgO, CaO, Na_2O, K_2O, and P_2O_5) were analysed by fused disc and determined on fusion beads using a rhodium tube set at 50KV/55mA. Trace elements (V, Cr, Ni, Zn, Zr, Nb, Ba, La, Ce, Nd, Ga, Pb, Rb, Sr, Th, and Y) were analysed by pressed powder pellets using a

rhodium tube set at 60KV/46mA (Norrish and Hutton, 1969). The results of the analysis are presented in Tables 5.3 and 5.4.

5.3.6 Liquefaction induced ground displacements

Horizontal ground displacements for the September 2010 (Darfield) and February 2011 (Christchurch) earthquakes were obtained from the maps available on the Canterbury geotechnical database. Horizontal ground displacements were derived from comparison of the horizontal position of objects (i.e. buildings) in the LiDAR point cloud created from a pre-CES LiDAR survey, and from the LiDAR surveys flown following the September 2010 and February 2011 earthquakes (Tonkin and Taylor, 2013b). The liquefaction related component of the horizontal ground displacements was derived by subtracting the regional tectonic displacements, derived from the fault rupture model by Beavan et al. (2012), from the absolute ground movements measured from the LiDAR surveys. Horizontal ground displacements are plotted as vectors at the respective LiDAR point cloud in Figure 5.13.

Horizontal ground surface displacements have also been measured from pre- and post- event satellite imagery using an optical imagery correlation process (Martin and Rathje, 2014). The satellite data is considered to yield more accurate estimates than the LiDAR, however, the data only covers part of the study area for the February 2011 earthquake and has not yet been processed for the September 2010 earthquake (Martin and Rathje, 2014). As a result only the LiDAR derived horizontal displacements are considered in this study.

Vertical ground surface subsidence models were derived from the maps available on the Canterbury geotechnical database. Subsidence was calculated from comparison of pre- and post- Digital Elevation Models (DEM) developed from the LiDAR surveys flown prior to the CES, and post-September 2010 and post-February 2011 (Russell et al., 2015). The liquefaction-induced component of the subsidence was derived by subtracting the regional tectonic deformation from the fault rupture model by Beavan et al. (2012); 0.01 m was subtracted for the September 2010 earthquake, and 0.1 m subtracted for the February 2011 earthquake. An additional 0.1 m was subtracted from the subsidence recorded within the study area following the September 2010 earthquake, and 0.1 m was added to the subsidence recorded for the February 2011 earthquake to account for a localised mean error offset in

the post-September 2010 LiDAR survey over the study area, possibly as a result of varied aircraft flight height (Russell et al., 2015).

5.3.7 Deriving quantitative metrics of the distribution of liquefaction and subsurface properties

The study area was divided into a suite of 164 polygons for statistical comparison of the distribution of liquefaction features, ground displacements and the liquefaction susceptibility of the subsurface sediments. Polygons did not cross the mapped geomorphic boundaries. Each polygon was assigned quantitative liquefaction metrics and subsurface properties as derived from the liquefaction analysis of the CPTs. The liquefaction metrics include of the density of linear liquefaction features, coverage of liquefaction ejecta, and mean liquefaction-induced horizontal and vertical ground displacements, while the subsurface properties include the H_1, H_2, and H_1/H_2. The average L/H was also derived for each polygon, which is the distance from the free-face divided by the height of the free-face. The minimum distance to the free-face was measured for each polygon. The distribution of polygons within the study area and the values assigned to each polygon are presented in Appendix G in the electronic supplement to this thesis.

The density of linear liquefaction features was derived by dividing the number of linear liquefaction features mapped within each polygon by the total visible area in the polygon (i.e. not obscured by buildings or vegetation). The density of liquefaction features is referred to herein as ρ_L (Table 5.1). The coverage of liquefaction ejecta (A_L) was derived by combining the aerial extent of all of the mapped liquefaction features within each polygon and dividing the result by the total visible area of the polygon. Horizontal (D_H) and vertical (D_S) ground displacements were assigned to a suite of randomly spaced points within each polygon from the horizontal and vertical ground displacement layers within ArcGIS. The values assigned to each point were exported and the mean ground displacement calculated for each polygon.

The H_1, H_2, and H_1/H_2 values of the most-proximal CPT within the same geomorphic area and at a similar elevation were assigned to the polygons. Assigning values of the proximal CPT ensured that the results were spread across the geomorphic

TABLE 5.1: List of abbreviations used in Chapter 5

Abbreviation	Description
ρ_L	Density of linear liquefaction features
A_L	Coverage of liquefaction ejecta
D_H	Liquefaction-induced horizontal ground displacement
D_S	Liquefaction-induced subsidence
H_1	Thickness of non-liquefying cap
H_2	Thickness of first liquefying layer
H_1/H_2	Ratio of non-liquefying cap to first liquefying layer
L/H	Distance from free-face divided by free-face height

area and not dominated by the higher density of CPTs conducted proximal to the river. Results were not interpolated between the CPTs.

The values assigned to each polygon were collated into the corresponding geomorphic areas. The mean, median, maximum, minimum, and the 25th and 75th quartiles were then derived for each geomorphic area to enable comparison between the geomorphic areas. The results of the analysis of the liquefaction metrics are presented in Figures 5.10 and 5.14, while analysis of the liquefaction profiles and L/H is summarized in Figure 5.16.

5.4 Fluvial geomorphology within the study area

5.4.1 Geomorphic mapping of the study area

The study area is divided into geomorphic areas to reflect variations in the paleodepositional setting of the surficial sediments and river morphology. Two major geomorphic areas are identified, referred to herein as geomorphic areas 1 and 2 (Fig. 5.4). Geomorphic area 1 comprises the central, higher elevation area of remnant high ground underlain by Late Holocene sand dune deposits (Fig. 5.4) (Brown and Weeber, 1992). Geomorphic area 2 comprises the surrounding areas of comparably lower elevation and underlain by Late Holocene fluvial deposits of the Avon River (Fig. 5.4). Geomorphic area 2 is further subdivided into four sub-categories (geomorphic areas 2a-d) reflecting variations in paleo- and present depositional setting and river morphology (Fig. 5.4).

The steep change in elevation along the eastern and western edges of geomorphic area 1 are interpreted as abandoned terrace risers comprising paleo-cut-banks formed by abandoned paleo-channels of the Avon River (Fig. 5.4). The low-elevations, presence of the paleo-cut banks, and morphology of the river indicates that geomorphic area 2a comprises a paleo-channel of the Avon River and associated point-bar deposits (Fig. 5.4). Geomorphic area 2b is situated along the inner-bank of the meander bend. The low-elevations and presence of the paleo-cut bank suggest the area comprises a paleo-channel associated with the avulsion of the river to its present location and point-bar deposits (Fig. 5.4).

The river morphology indicates that geomorphic area 2c is surrounded by the inner-convex bank of the Avon River (Fig. 5.4). The area is interpreted to comprise point-bar deposits associated with the outward migration of the Avon River to its present location (Fig. 5.4). This is further supported by the gradual increase in elevation with increasing distance from the river which reflects accretion of overbank deposits over time (Fig. 5.4). Geomorphic area 2c is further sub-divided into eastern and western sections to account for the change in river orientation (Fig. 5.4).

Geomorphic area 2d consists of the very low elevation areas within 50 m of the Avon River and is separated from the surrounding geomorphic areas by a step-change in elevation (Fig. 5.4). The low elevations and river morphology indicate that geomorphic area 2d comprises the modern levees and proximal active flood plain of the Avon River (Fig. 5.4).

5.4.2 CPT stratigraphy

The tip resistance (q_c) of the CPT soundings and boreholes conducted within the study area are collated for each geomorphic area for comparison of the subsurface sediment properties (Fig. 5.5). The sediment behaviour type index (I_c) derived from the CPT are also plotted with depth for each geomorphic area and presented in Figure 5.5. The I_c parameter defines a sediments behaviour type according to a set of numerical boundaries as derived by (Robertson and Wride, 1998). The numerical boundaries and corresponding I_c are outlined in Table 5.2.

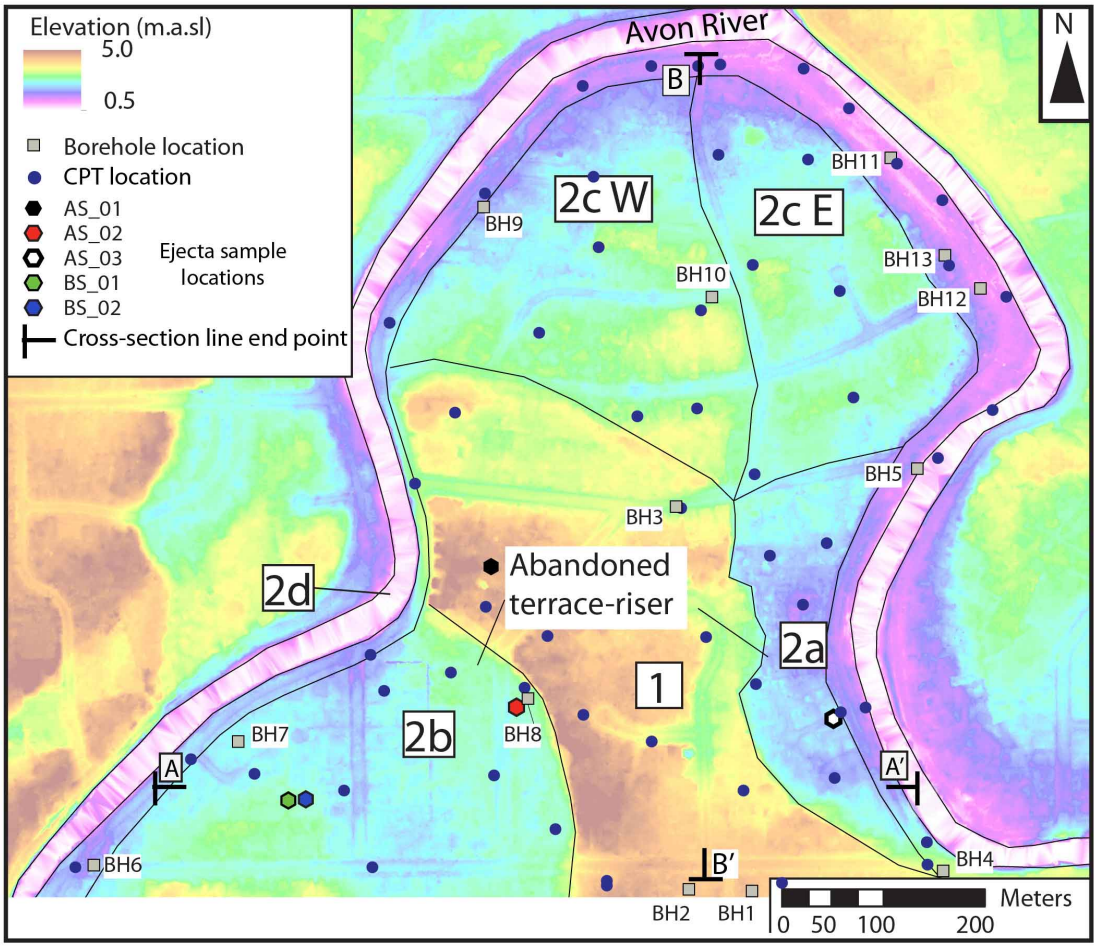

FIGURE 5.4: 0.5 m DEM of the Avonside study area with the location of the geomorphic areas (1. 2a-2d). The location of the cross-section lines (A-A', B-B'), CPTs, boreholes and grain-size samples are also indicated.

The predicted liquefaction profiles calculated for the CPTs using the Boulanger and Idriss (2014) methodology are also plotted for each geomorphic area for comparison of the depth and thickness of the liquefying units across the study area (Fig. 5.6). Green sections within the profile indicate sediment layers that are not predicted to liquefy (<15% probability), while the red sections indicate portions of the sediment profile that are predicted to liquefy (>85% probability). Orange sections represent >50% probability of liquefying, and yellow sections >15% probability.

The CPTs conducted in geomorphic area 1 indicate that the area is predominantly underlain by relatively low density inter-layered sands and silts to a depth of approximately 3 m which corresponds with silt underlain by sand intersected in the boreholes (Fig. 5.5). A sharp increase in relative density and reduction in

TABLE 5.2: Soil Behaviour Type Classification

I_c	Soil behaviour type
<1.31	Gravelly sand to dense sand
1.31 - 1.90	Sands: clean sand to silty sand
1.90 - 2.50	Sand mixtures: silty sand to sandy silt
2.50 - 3.20	Silt mixtures: clayey silt to silty clay
3.20 - 3.60	Clays: silty clay to clay
>3.60	Organics soils: peats.

I_c is observed beneath 3 m depth which likely corresponds with the gravels intersected in the borehole (Fig. 5.5). The boreholes indicate that the surficial silts thicken towards the northern extent of the area (BH1-3; Fig. 5.5). The CPTs conducted proximal to the river bank in area 1 (1-4) indicate that the subsurface sediment contain thin potentially liquefying layers for the September 2010 earthquake (>50% probability of liquefying), which may result from the increasing thickness of the silt cap towards the northern extent of the area (Fig. 5.5). The CPTs conducted within the central area (6-9) indicate that the subsurface sediment contains a comparably thicker liquefiable layer (>50% probability of liquefying) which thins towards the southern extent of the study area (CPTs 10-12) (Fig. 5.6A). For the February 2011 earthquake, the liquefying layer is comparably thicker in the central area of CPT 4-9 (>85% probability). The layer thins towards the river (CPT 1-3) and the southern extent of the study area (CPT 10-12) (Fig. 5.6B). The increased thicknesses of the liquefying layer results from the higher PGA triggering liquefaction in more of the subsurface sediments during the February 2011 earthquake.

The CPTs and boreholes conducted within geomorphic area 2a indicate that the area is underlain by low relative density silt from the surface to approximately 2 m depth at which point the sediment density becomes variable, most likely as a result of the interbedded sand to gravel layers intersected within the boreholes (BH4-5; Fig. 5.5). The boreholes indicate that the silt cap is thicker at the southern extent of the study area (BH4) (BH5; Fig. 5.5). Liquefaction analysis indicates that the area distal to the river (CPT 13 & 15) is underlain by a comparably thick layer of potentially liquefiable sediments (>50% probability) which may reflect sands within the paleo-channel formed adjacent to the paleo-cut bank (Fig. 5.6A). The central area contains a comparably thin layer potentially liquefiable sediment (CPT 14-16) for the September 2010 earthquake which may reflect lenses of sand within the over-bank silts (Fig. 5.6A). The CPT proximal to the

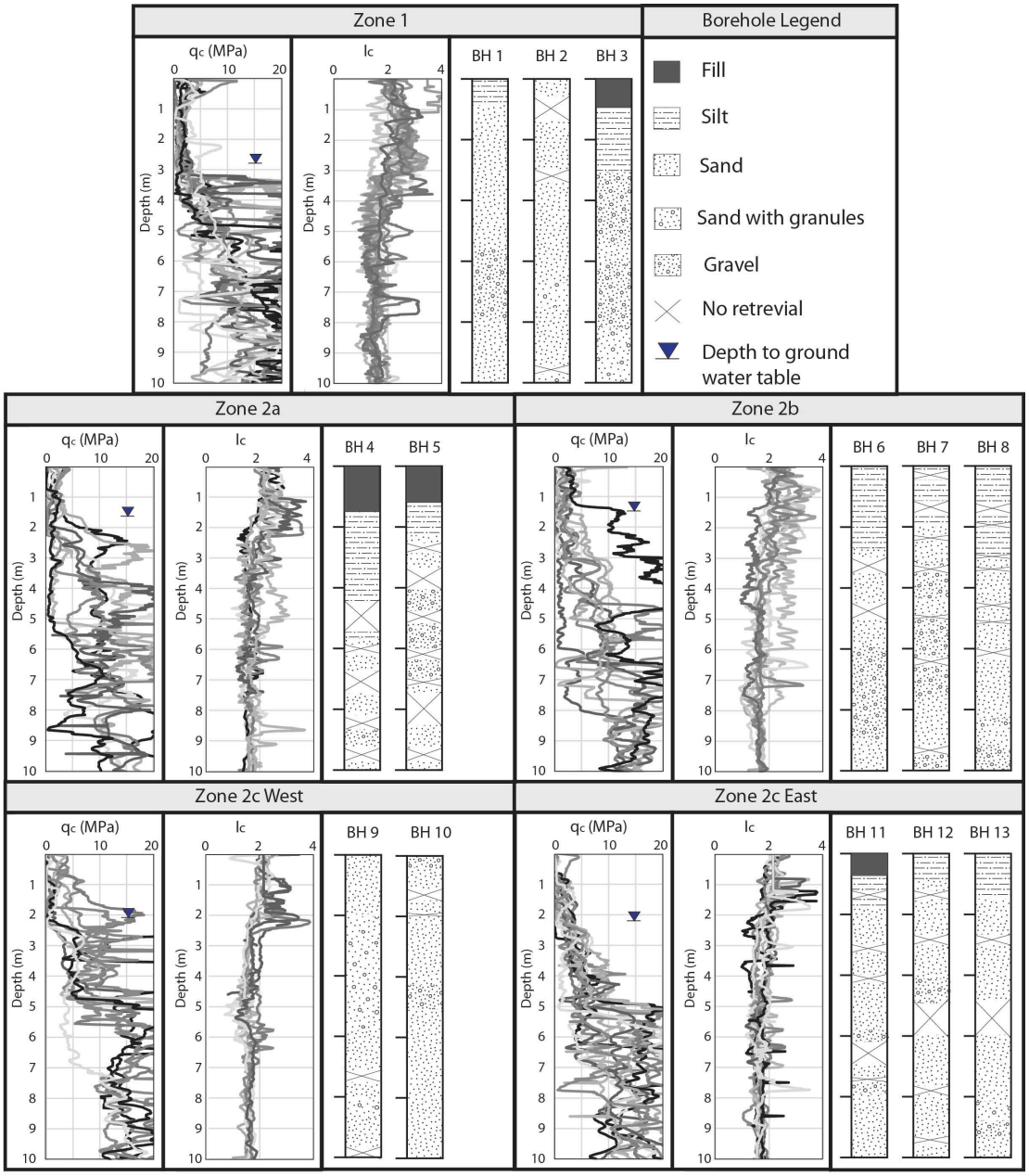

FIGURE 5.5: q_c and I_c traces of the CPT soundings conducted within each geomorphic area and simplified borehole logs taken from within each geomorphic area. Locations of the plotted boreholes are indicated in Figure 5.4.

river within geomorphic area 2d (CPT 56-58) indicate that the river bank is underlain by comparably thick liquefiable layers for the September 2010 earthquake, which may reflect sands deposited on the active-flood plain of the river (Fig. 5.6A). Similar trends are observed in the liquefaction profiles for the February 2011 earthquake, albeit the liquefying units are thicker (Fig. 5.6B). The liquefying units are encountered at varying depths across the geomorphic area suggesting that they exhibit spatial variability and may comprise localised lenses (Fig. 5.6B).

Geomorphic area 2b (Fig. 5.4) is uniformly underlain by low relative density silt to sand to approximately 3 m (Fig. 5.5). Beneath 3 m depth the relative density increases and becomes variable most likely as a result of the localized sand to gravel lenses intersected within the boreholes (BH6-8; Fig. 5.5). The CPTs indicate that the subsurface sediment in the area distal to the river contains comparably thick potentially liquefiable layers for the September 2010 earthquake (>50% probability; CPT 20, 23-25; Fig. 5.6A). It is possible that this reflects the loosely consolidated alluvial sands deposited within a paleo-channel formed adjacent to the abandoned terrace riser. The CPTs conducted proximal to the river in geomorphic area 2d (CPT 38-40) indicate that the thickness of the liquefying layer increases towards the southern extent of the geomorphic area (Fig. 5.6A). The CPT at the northern extent of the area indicates the subsurface sediment contains thin liquefying units which may reflect the interbedded sands and silts deposited in the active flood-plain. The profiles for the February 2011 earthquake indicate that the area is uniformly underlain by comparably thick and continuous liquefying layers (>85% probability) (Fig. 5.6B).

The CPTs and boreholes conducted in the western section of geomorphic area 2c indicate that the area is underlain by low relative density silt to sand from the surface to approximately 2 m depth (Fig. 5.5). The relative density increases and becomes variable from 2 to 5 m depth then increases below 5 m depth due to the localized sand to gravel lenses intersected within the boreholes (BH 9-10; Fig. 5.5). Liquefaction analysis of the CPTs indicate that no liquefaction was predicted to occur within the subsurface sediment across most of the area (CPT 26-29 and 31) for the September 2010 earthquake, with only a thin potentially liquefiable unit (>50% probability) is predicted within CPT 30 at the edge of the paleo-dunes comprising geomorphic area 1 (Fig. 5.6A). The CPT conducted proximal to the river in geomorphic area 2d (42-46) indicates that the potentially liquefying units

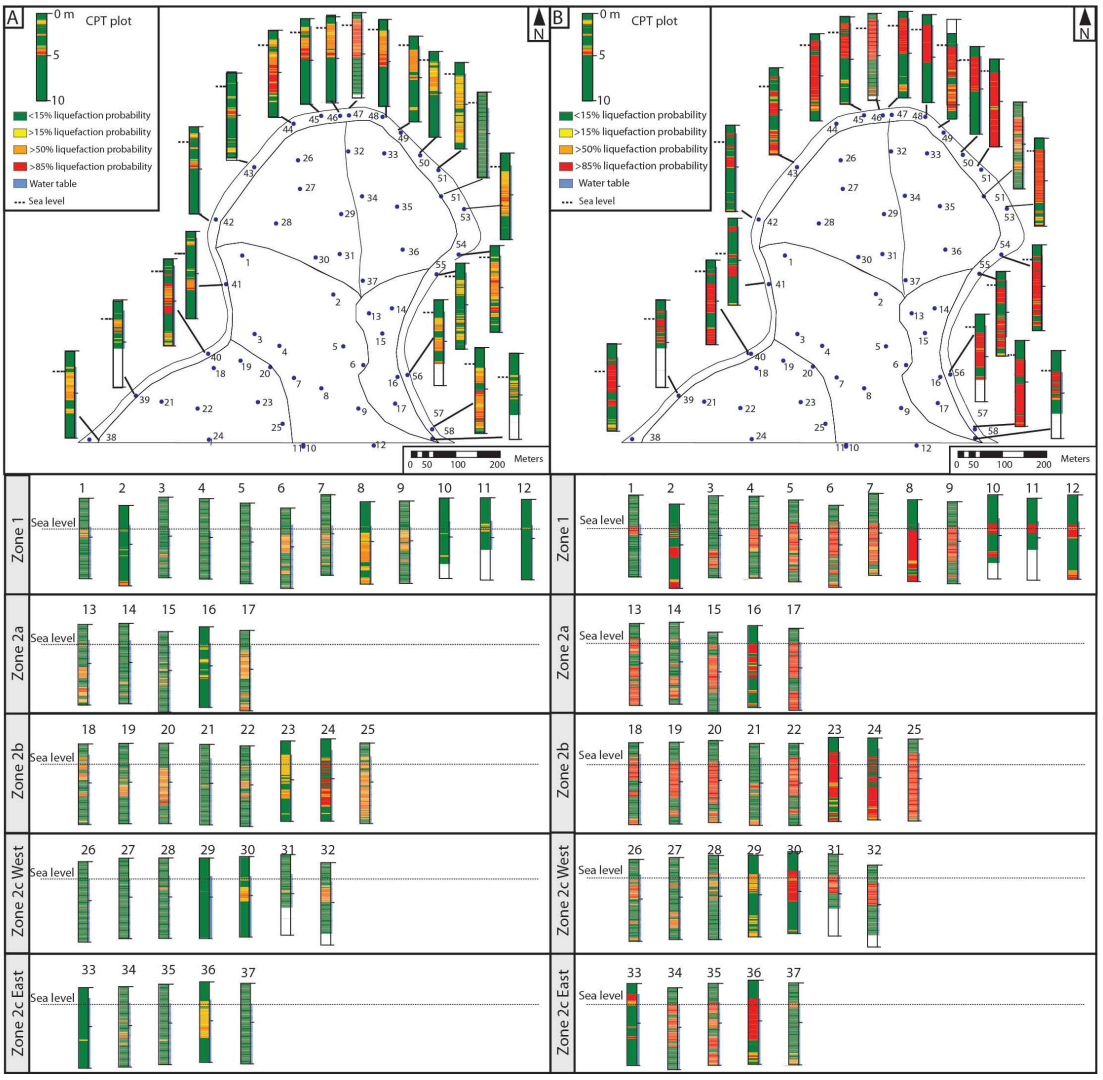

FIGURE 5.6: Predicted liquefaction profiles derived analysis of the CPTs conducted within each geomorphic area for the September 2010 and February 2011 earthquakes.

underlying the river bank increase in thickness towards the apex of the meander-bend for the September 2010 earthquake (Fig. 5.6A). The increasing thickness of the liquefying layer may represent increasing accumulation of point-bar towards the apex of the meander bend. For the February 2011 earthquake, the CPT proximal to the river indicate the subsurface sediment contained thicker liquefying units (Fig. 5.6). The CPT conducted centrally within the area (CPT 26-27) indicate that the subsurface sediments contains thin liquefying lenses interbedded with non-liquefying sediment which may result from interbedded sands and silts within the point-bar deposits (Fig. 5.6).

The eastern section of geomorphic area 2c is shown to be underlain by sands and silts with low relative densities to 5 m depth (Fig. 5.5). The boreholes indicate

the upper 5 m of the area comprises sands capped by silt (BH11-13; Fig. 5.5). Below 5 m the relative density becomes variable and increases, possibly as a result of the localized interbedded gravels (Fig. 5.5). Liquefaction analysis indicates that the central area is underlain by sediment that was not liquefiable during the September 2010 earthquake (CPT 33-35 and 37) (Fig. 5.6). The areas of CPT 32 and 36, and within geomorphic area 2d (47-54) contain thick liquefying units (>50% probability) for the September 2010 and February 2011 earthquakes. These thick units likely comprise recent over-bank or channel deposits composed of unconsolidated fine sand (Fig. 5.6). For the February 2011 earthquake, the areas distal to the river (CPT 33-35 and 37) contain thin liquefying units (>50% probability) which likely reflects the interbedded sands and silts intersected within the boreholes (Fig. 5.5).

Simplified north-south and east-west cross-sections are constructed across the study area from the raw CPT q_c traces, boreholes, and the predicted liquefaction profiles (Fig. 5.7). The cross-sections indicate that the surficial sediments within the upper 2-5 m vary between the geomorphic areas, however the study area is underlain by sand to silt with interbedded sand to gravel layers at depth (Fig. 5.7). The liquefaction profiles derived from the CPT indicate that the first liquefying unit is generally beneath 2-4 m depth for the September 2010 and February 2011 earthquakes, thus spatial variability in the surficial fluvial sediments between the geomorphic areas reflects variations in the composition of the non-liquefying cap (Fig. 5.6 & 5.7).

5.5 Distribution, grain-size, and geochemistry of surface liquefaction features

5.5.1 Distribution of linear liquefaction features

The surficial linear liquefaction features consist of aligned sand blows and lateral-spreading fissures. The lateral spreading fissures range from ~5 to >300 m in length for both the September 2010 and February 2011 earthquakes and were surrounded by localized areas of liquefaction ejecta (Fig. 5.8). The linear arrays of aligned sand blows consist of series of coalescing sand blows that often transition into lateral spreading fissures along their lengths.

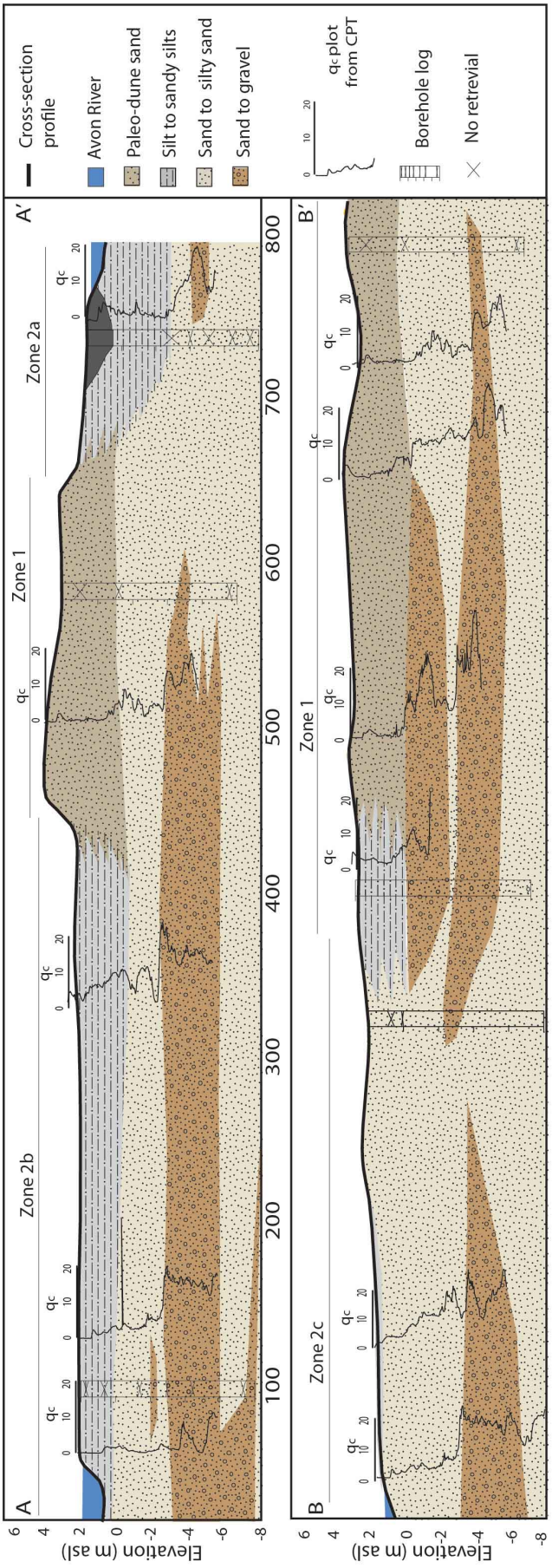

FIGURE 5.7: Simplified schematic cross-sections across the study area overlain with a_c traces from the proximal CPTs and borehole logs. Location of the geomorphic boundaries are also indicated. The position of the cross-section lines are indicated in Figure 5.4.

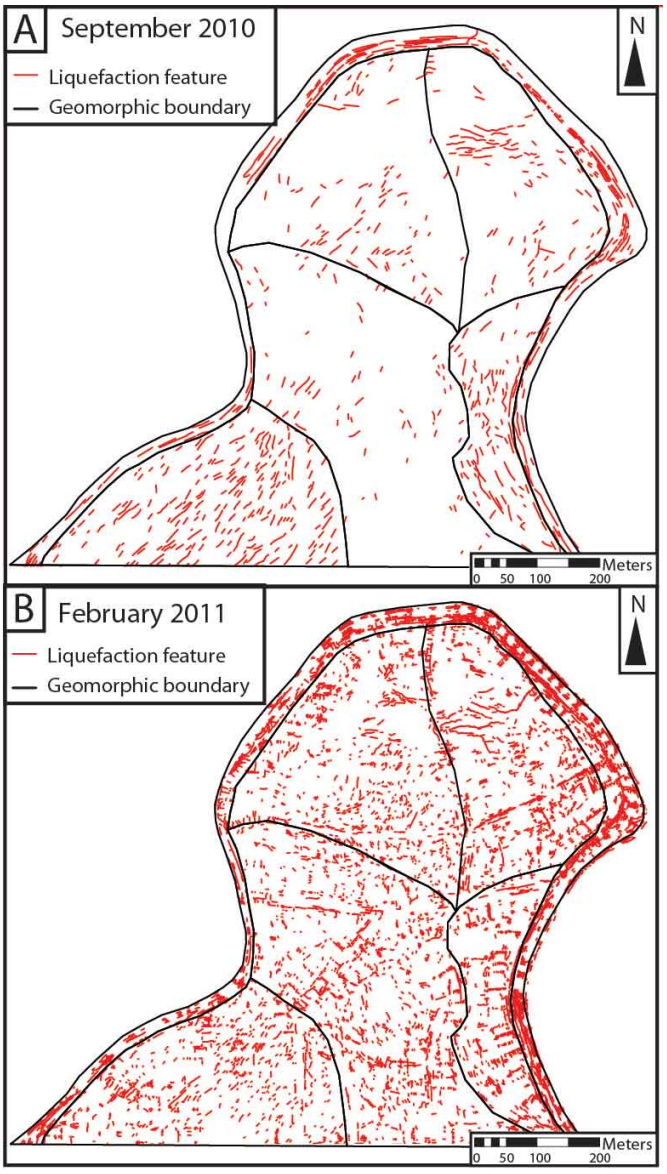

FIGURE 5.8: The distribution of the surface liquefaction features comprising aligned surface fissures and sand-blow vents as mapped within the study area following the September 2010 (A) and February 2011 (B) earthquakes from the aerial photographs.

Mapping indicates that highest ρ_L for the September 2010 earthquakes occurs in the low elevation areas proximal to the Avon River (geomorphic area 2d) and within the low elevation paleo-channels (geomorphic areas 2a and 2b) (Fig. 5.8A). Intermediate values of ρ_L occur within the geomorphic area 2c, while comparably low ρ_L is mapped within geomorphic area 1 for the September 2010 earthquake (Fig. 5.8A). Liquefaction features are more widespread across the study area for the February 2011 earthquake due to the higher PGA triggering liquefaction within more of the subsurface sediment (Fig. 5.6). High ρ_L is observed within

geomorphic areas 2a-c, while very high ρ_L is observed within geomorphic area 2d for the February 2011 earthquake (Fig. 5.8B).

The number and length of liquefaction features mapped following the February 2011 earthquake are binned into 10 m increments in distance from the free-face (Fig. 5.9A). The liquefaction features are shown to have formed in highest abundance and greatest length within 30 m of the down-slope free-faces (i.e. modern banks of the Avon River) (Fig. 5.9A) which corresponds with the location of area 2d. The liquefaction features are also shown to be predominantly orientated sub-parallel to the closest free-face, with 60% of the features orientated within 20° of the free-face (Fig. 5.9A).

Variations in ρ_L within the geomorphic areas are summarized as box and whisker plots constructed from the polygons within each geomorphic area (Fig. 5.10). The median ρ_L for the study area is 0.003 features per m_2 or 1 feature per 285.7 m^2 for the September 2010 earthquake, and 0.017 features per m_2 or 1 feature per 58.8 m^2 for the February 2011 earthquake.

Geomorphic area 1 exhibits a very low median ρ_L for the September 2010 earthquake compared to that derived for the study area (median = 0.001 features per m_2, or 1 feature per 1000 m^2). The area exhibits a slightly higher ρ_L for the February 2011 earthquake, albeit the median is still much lower than that derived for the study area (median = 0.009 features per m_2, or 1 feature per 107 m^2) (Fig. 5.10A).

Geomorphic area 2a exhibits a median ρ_L for the September 2010 earthquake of 0.007 features per m_2, or 1 feature per 142 m^2). The median ρ_L for the February 2011 earthquake is comparably higher than the rest of the study area median = 0.33 features per m_2, or 1 feature per 33.3 m^2) (Fig. 5.10A). Geomorphic area 2b exhibits a high median ρ_L for the September 2010 earthquake (median = 0.06 features per m_2 or 1 feature per 166 m^2) and a median of 0.012 features per m_2, or 1 feature per 83 m^2 for the February 2011 earthquake (Fig. 5.10A).

The eastern section geomorphic area 2c east exhibits a median ρ_L for the September 2010 earthquake of 0.002 features per m_2, or 1 feature per 500 m^2, and a median of 0.012 features per m_2, or 1 feature per 83 m^2 for February 2011 earthquake (Fig. 5.10A). The western section exhibits a median ρ_L of 0.003 features per m_2 or 1 feature per 333.3 m^2 for the September 2010 earthquake, and 0.02 features per m_2 or 1 feature per 50 m^2 for the February 2011 earthquake (Fig. 5.10A).

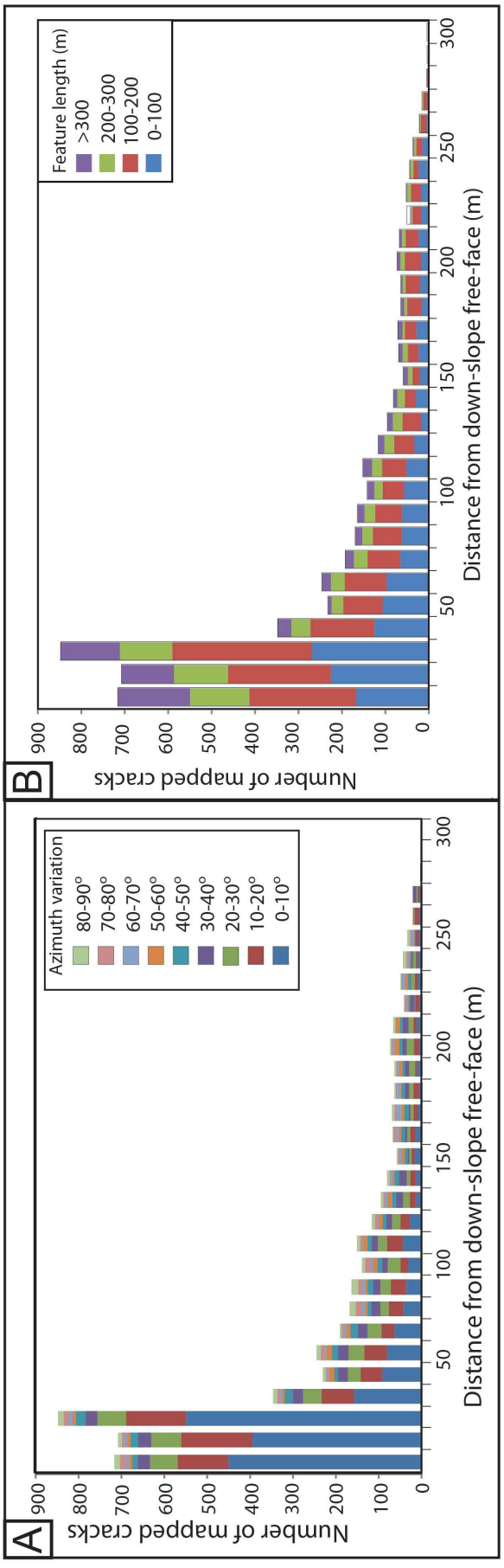

FIGURE 5.9: A) The mapped distribution of liquefaction features following the February 2011 earthquake are orientated sub-parallel with the closest free-face and decreased in abundance with increasing distance from the free-face. B) The number and length of the liquefaction features decreases with increasing distance from the free-faces.

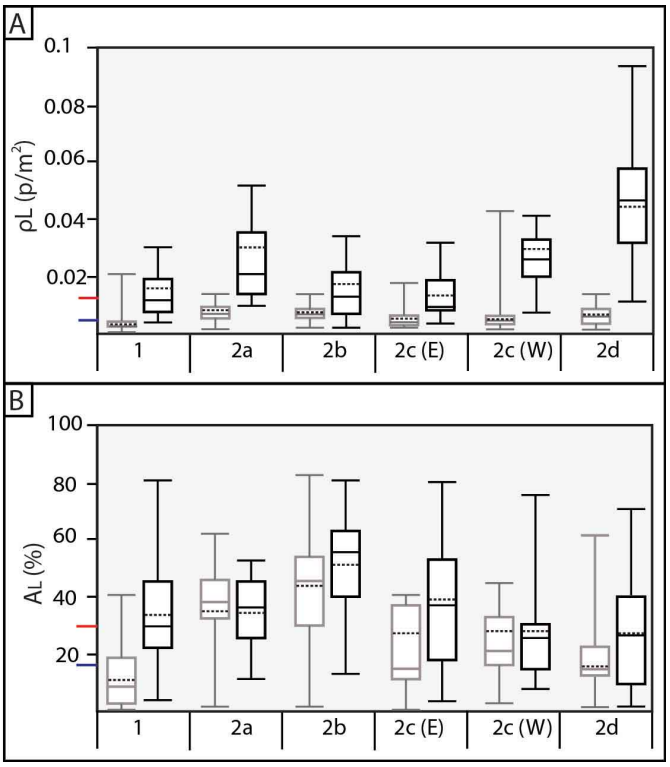

FIGURE 5.10: A) Comparison of the ρ_L across the five geomorphic areas for the September 2010 (outlined in grey) and February 2011 (outlined in black) earthquakes. B) Comparison of the A_L across the five geomorphic areas for the September 2010 (outlined in grey) and February 2011 (outlined in black) earthquakes. The box defines the 25th and 75th percentiles and the whiskers represent the data range, excluding outliers. Dotted lines are means and solid lines are the median. The blue-line indicates the median derived for the study area for the September 2010 earthquake, and the red line represents the median for the February 2011 earthquake.

Geomorphic area 2d exhibits a median ρ_L of 0.002 features per m_2 or 1 feature per 588 m^2 for the September 2010 earthquake, and a high median ρ_L for the February 2011 earthquake of 0.04 features per m_2 or1 feature per 25 m^2 (Fig. 5.10A). The high ρ_L is consistent with the high frequency of features that plot within 30 m of the free-face for the February 2011 earthquake (Fig. 5.9).

5.5.2 Distribution and extent of liquefaction ejecta

The liquefaction ejecta mapped within the study area comprises liquefaction ejecta surrounding localized and aligned sand-boil vents and surface flooding. Mapping indicates that areas distal to the river within geomorphic area 2b and 2c exhibited a higher A_L than areas proximal to the river during the September 2010 earthquake (Fig. 5.11). A_L mapped for the September 2010 earthquake appears to

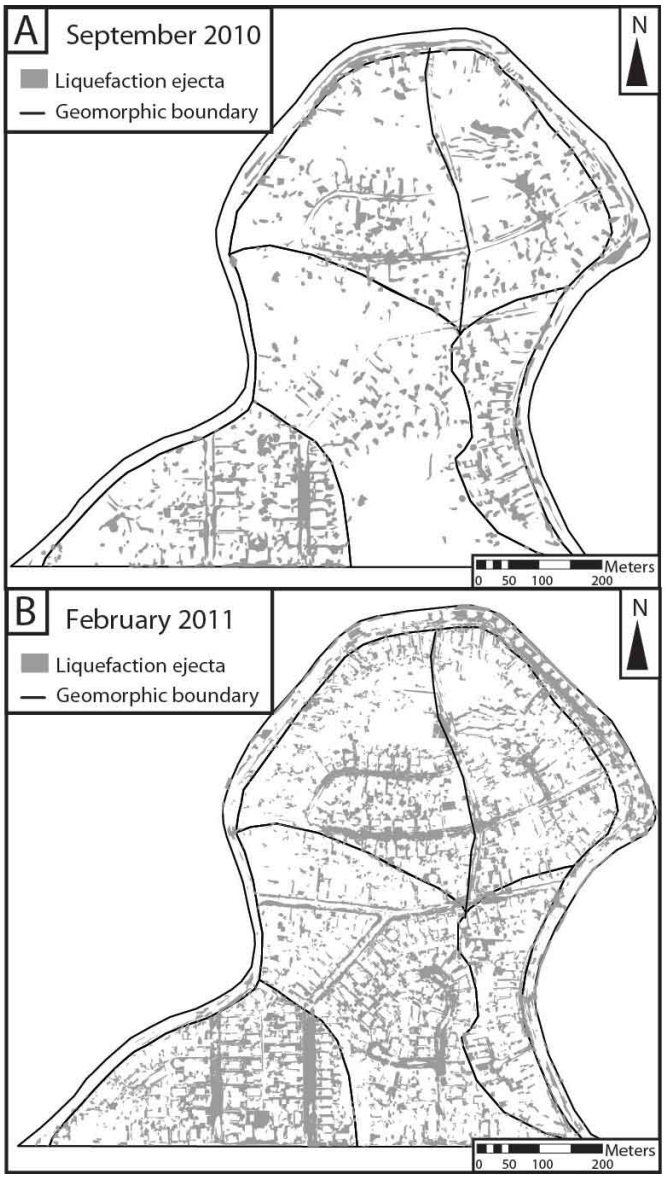

FIGURE 5.11: The aerial extent of the surface liquefaction features comprising the ejecta associated with localized and aligned sand-blow vents and surface flooding as mapped within the study area for the September 2010 (A) and February 2011 (B) earthquakes from the aerial photographs.

be comparably lower within geomorphic area 1 and geomorphic area 2d than the surrounding geomorphic areas (Fig. 5.11). For the February 2011 earthquake, A_L appears to be more wide-spread as a result of the higher PGA triggering liquefaction within more of the sediment profile (Fig. 5.11). Areas distal to the river within geomorphic areas 2b and 2c exhibit higher A_L than areas closer to the river. A_L within geomorphic area 1 is also comparably more widespread following the February 2011 earthquake (Fig. 5.11).

Variations in the A_L are summarized as box and whisker plots constructed from the

values assigned to the polygons within each geomorphic area (Fig. 5.10; Appendix G). The median A_L following the September 2010 earthquake is 18%, and 30% for the February 2011 earthquake (Fig. 5.10B).

Geomorphic area 1 exhibits low A_L for the September 2010 earthquake compared to the median of the study area (0.9% covered), while 27% of the area was covered following the February 2011 earthquake (Fig. 5.10B).

Geomorphic area 2a exhibits a median A_L of 32% for the September 2010 earthquake and 36% for the February 2011 earthquake (Fig. 5.10B. Geomorphic area 2b exhibits median A_L of 37% for the September 2010 earthquake, and 46% for the February 2011 earthquake (Fig. 5.10B). The eastern portion of geomorphic area 2c exhibits lower A_L than the western section for the September 2010 earthquake (east median = 24%; west median = 22%), and a higher A_L than the western section of geomorphic area 2c for the February 2011 earthquake (east median = 31%; west median = 28%) (Fig. 5.10B). Geomorphic area 2d exhibits a low median A_L for both the September 2010 and February 2011 earthquakes compared to the median of the study area (September 2010 median = 12%; February 2011 median = 26%) (Fig. 5.10B).

5.5.3 Grain-size and geochemistry of liquefaction ejecta

The grain-size and geochemical composition of the liquefaction ejecta was analysed to determine whether spatial variability exists in the liquefaction ejecta. The grain-size analysis indicates that the liquefaction ejecta is uniformly composed of well sorted and poorly graded fine to very fine sand with trace silt (predominately 100-150μm) (Fig. 5.12). The uniform grain-size indicates that a liquefiable source containing fine to very fine sand exists at depth beneath the study area.

The samples of liquefaction ejecta exhibit a uniform geochemistry that is consistent with that of the Torlesse Group that outcrops in the Southern Alps and is deposited on the Canterbury Plains by the braided rivers (i.e. Waimakariri) (Table 5.3 & 5.3; Roser & Korsch, 1999). The uniform geochemistry indicates that geochemical variability did not influence the spatial distribution or severity of liquefaction and associated ground displacements observed across the study area.

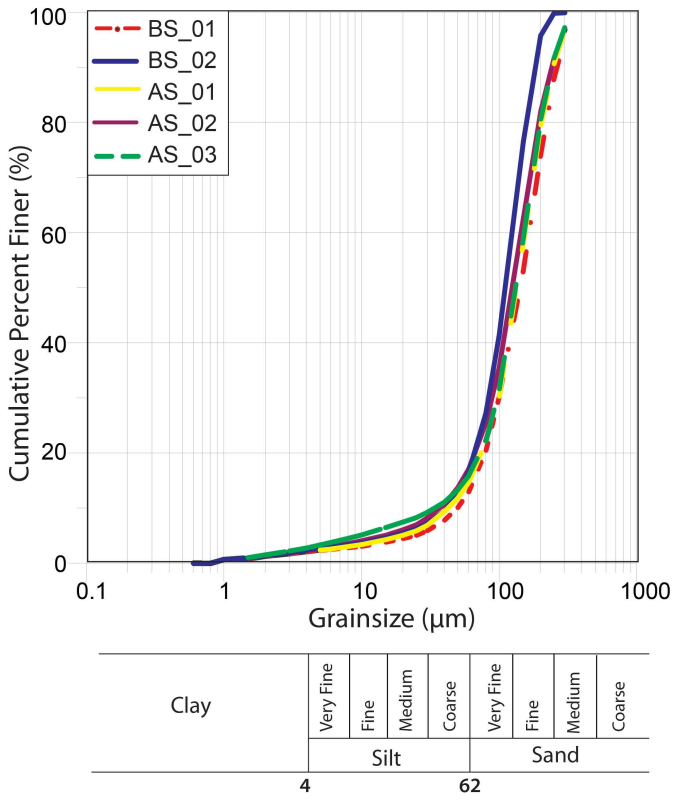

FIGURE 5.12: Cumulative percent grain-sizes for samples of surface liquefaction ejecta collected from within geomorphic areas 1, 2a, and 2b. The ejecta is uniformly composed of well sorted very fine to fine sand.

TABLE 5.3: Major elements of the liquefaction ejecta compared to Torlesse Supergroup

Sample Number	SiO_2 (%)	TiO_2 (%)	Al_2O_3 (%)	Fe_2O_3T (%)	MnO (%)	MgO (%)	CaO (%)	Na_2O (%)	K_2O (%)	P_2O_5 (%)	Lol (%)	Total (%)
AS_01	75.3	0.4	12.8	2.6	0.0	0.9	1.0	3.2	2.6	0.08	1.02	99.86
AS_02	75.4	0.4	12.6	2.5	0.0	0.9	1.0	3.2	2.5	0.08	1.17	99.84
AS_03	74.4	0.4	12.9	2.6	0.0	0.9	1.0	3.2	2.6	0.08	1.73	99.95
BS_01	75.5	0.4	12.5	2.6	0.0	0.9	1.0	3.2	2.5	0.08	1.29	99.92
BS_02	75.4	0.4	12.4	2.5	0.0	0.9	0.9	3.1	2.5	0.07	1.72	99.86
Torlesse*	70.7	0.5	14.5	4.4	0.1	1.4	2.1	3.8	2.4	0.11	1.3	99.91

TABLE 5.4: Minor elements of the liquefaction ejecta compared to Torlesse Supergroup

Sample Number	V (ppm)	Cr (ppm)	Ni (ppm)	Zn (ppm)	Zr (ppm)	Nb (ppm)	Ba (ppm (ppm)	La (ppm)	Ce (ppm)	Nd (ppm)	Ga (ppm)	Pb (ppm)	Rb (ppm)	Sr (ppm)	Th (ppm)	Y (ppm)
AS_01	61	34	12	42	200	8	596	31	58	24	14	12	104	287	11	19
AS_02	57	33	12	41	197	7	589	24	50	27	13	12	101	289	9	18
AS_)3	59	33	12	45	148	7	627	25	49	23	14	13	104	290	8	17
BS_01	57	30	13	41	172	7	626	26	36	32	13	12	100	290	9	17
BS_02	54	33	12	46	171	7	611	26	48	23	13	14	100	284	9	18
Torlesse	87	25	6	57	197	8	650	23	52	24	15	19	89	361	10	20

5.6 Liquefaction-induced ground horizontal displacements

5.6.1 Horizontal ground displacements

The magnitude and direction of D_H varies spatially across the study area for both the September 2010 and February 2011 earthquakes (Fig. 5.13). High D_H is observed within the eastern section of geomorphic area for the September 2010 earthquake, while intermediate values of D_H is observed within geomorphic areas 2a-2c west, and 2d (Fig. 5.13). For the February 2011 earthquake, high D_H is observed within geomorphic area 2b, while lower values of D_H are observed within geomorphic area 2c east than during the September 2010 earthquake (Fig. 5.13. Low D_H is observed within geomorphic area 1 for both earthquakes (Fig. 5.13).

Variations in the median D_H across the study area are derived from variations in the values assigned to the polygons and are summarized in Figure 5.14A. The median D_H in the study area for the September 2010 earthquake is 0.18 m and 0.36 m for the February 2011 earthquake (Fig. 5.14A).

Geomorphic area 1 exhibits a comparably low median D_H for the September 2010 and February 2011 earthquakes at 0.2 m and 0.25 m respectively (Fig. 5.14A).

Geomorphic area 2a exhibits a median D_H of 0.6 m for the September 2010 earthquake, and a median D_H of 0.5 m for the February 2011 earthquake (Fig. 5.14A). Geomorphic area 2b exhibits a median D_H of 0.4 m for the September 2010 earthquake, and a high median D_H of 0.7 m for the February 2011 earthquake compared to that derived for the rest of the study area (Fig. 5.14A).

The eastern section of geomorphic area 2c exhibits very high D_H during the September 2010 earthquake compared to the median of the study area (median = 1.0 m). The area exhibits a lower median D_H of 0.4 m for the February 2011 earthquake (Fig. 5.14A). The median D_H for the western section of geomorphic area 2c is 0.4 m for the September 2010 earthquake and 0.35 m for the February 2011 earthquake (Fig. 5.14A).

The median D_H of geomorphic area 2d is 0.4 m for the September 2010 earthquake. The area exhibits a comparably high median D_H for the February 2011 earthquake of 0.6 m (Fig. 5.14A).

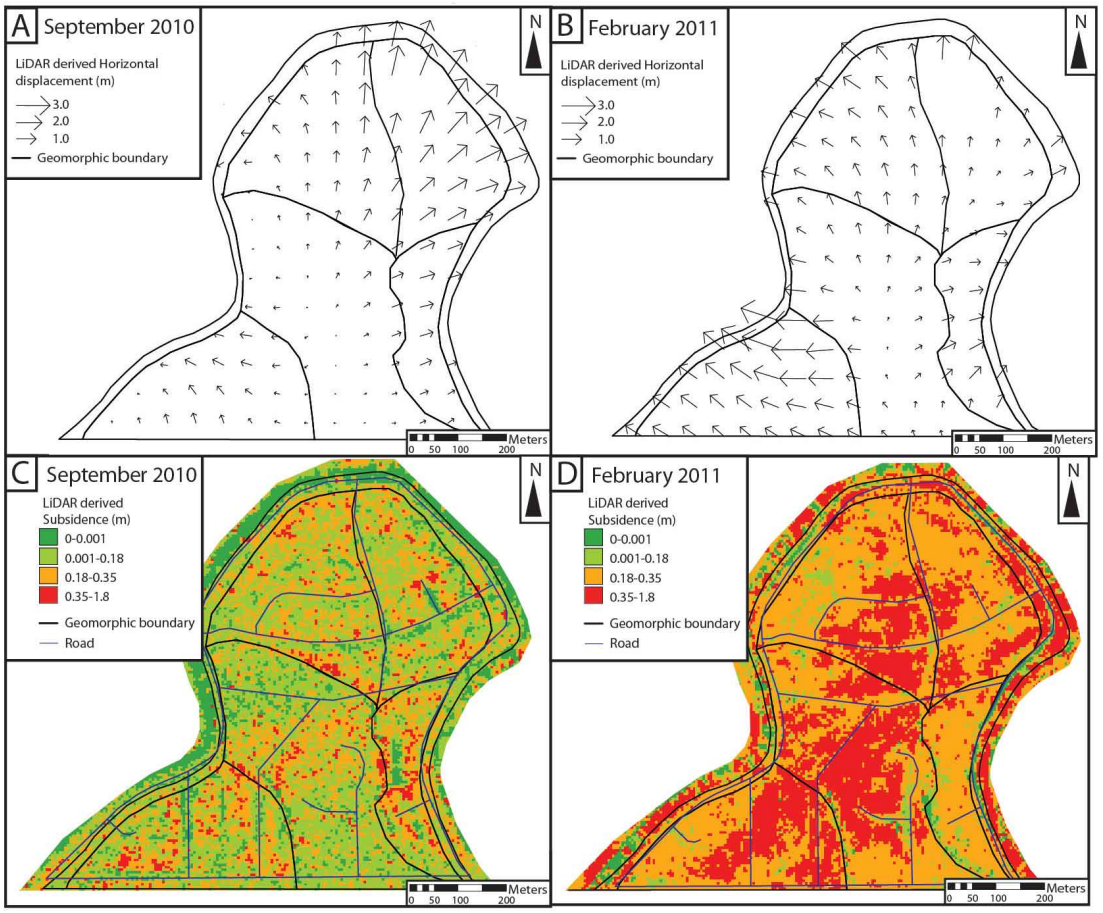

FIGURE 5.13: LiDAR derived D_H vectors for the September 2010 (A) and February 2011 (B) earthquakes. C) Liquefaction related D_S recorded within the study area following the September 2010 earthquake. D) D_S recorded following the February 2011 earthquake.

5.6.2 Vertical ground displacements

Liquefaction-induced D_S varies across the study area for both the September 2010 and February 2011 earthquakes. Comparably higher D_S occurred across all geomorphic areas during the February 2011 earthquake as a consequence of the higher PGA triggering liquefaction in more of the sediment profile (Fig. 5.13D). D_S does not appear to vary significantly between the geomorphic areas (Fig. 5.13). However, it appears that slightly higher D_S occurred on residential properties compared to that recorded on the surrounding roads during the September 2010 earthquake (Fig. 5.13D).

Variations in the D_S recorded across the geomorphic areas are summarized as box and whisker plots in Figure 5.14B. The median D_S recorded within the study area

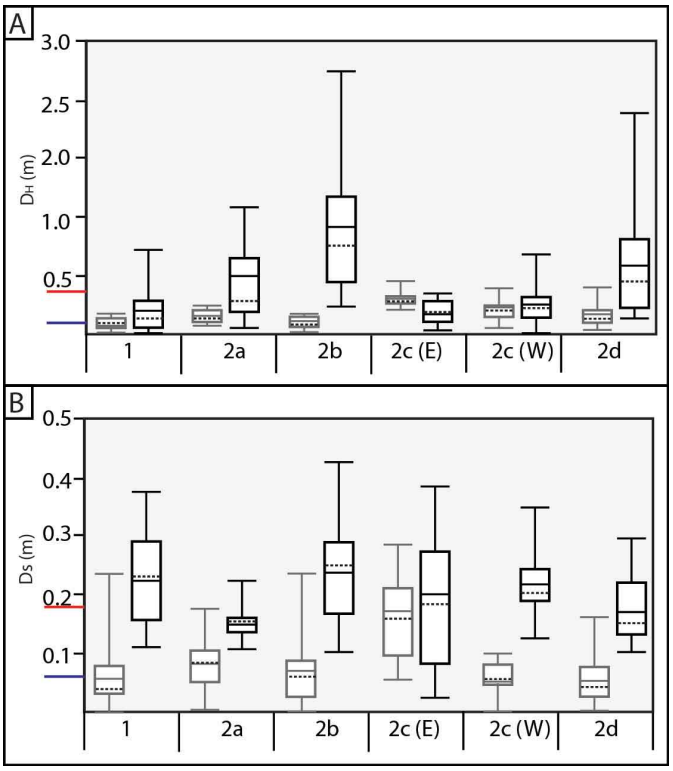

FIGURE 5.14: A) Comparison of the D_H across the five geomorphic areas for the September 2010 (outlined in grey) and February 2011 (outlined in black) earthquakes. B) Comparison of the D_S across the five geomorphic areas for the September 2010 (outlined in grey) and February 2011 (outlined in black) earthquakes. The box defines the 25th and 75th percentiles and the whiskers represent the data range. Dotted lines are means and solid lines are the median. The blue line represents the median for the September 2010 earthquake and the red line represents the median for the February 2011 earthquake.

is 0.06 m for the September 2010, and 0.19 m for the February 2011 earthquake (Fig. 5.14B).

Geomorphic area 1 exhibits median D_S of 0.06 m for the September 2010 earthquake, and a comparably high median D_S for the February 2011 earthquake compared to the study area of 0.22 (Fig. 5.14B).

Geomorphic area 2a exhibits a median D_S of 0.07 m for the September 2010 earthquake, and a median D_S of 0.15 m for the February 2011 earthquake (Fig. 5.14B). Geomorphic area 2b exhibits median D_S of 0.07 m for the September 2010 earthquake, and a high median D_S of 0.21 m for the February 2011 earthquake (Fig. 5.14B). The eastern section of geomorphic area 2c exhibits a higher median D_S than the western section for the September 2010 earthquake (east = 0.07 m; west = 0.05 m; Fig. 5.14B). The median D_s for the eastern section is 0.22 m following the September 2010 earthquake, while the median of western section is

0.18 m (Fig. 5.14B). Geomorphic area 2d exhibits a very low median D_S of 0.05 m for the September 2010 earthquake, and a median D_S of 0.27 m following the February 2011 earthquake (Fig. 5.14B).

5.7 Comparison of horizontal displacements and predicted liquefaction profiles

The vectors of D_H indicate that displacements vary spatially along the banks of the Avon River for both the September 2010 and February 2011 earthquakes (Fig. 5.13). The predicted liquefaction profiles derived for the CPTs conducted adjacent to the Avon River in geomorphic area 2d are plotted with D_H and A_L for both earthquakes (Fig. 5.15).

For the September 2010 earthquake, the D_H vectors indicate that the highest D_H occurred proximal to the river in the eastern section of geomorphic area 2c (Fig. 5.15). The high D_H correlates with a thick and continuous layer with a >50% probability of liquefying at approximately 1.5 m depth (Fig. 5.15A). The presence of this thick liquefying layer adjacent to the river bank suggests that this layer may comprise a continuous liquefiable unit at depth (Fig. 5.15). Liquefaction within this layer likely facilitated lateral spreading resulting in the high D_H (Fig. 5.15A). The exception to this is CPT 57 which indicates that the subsurface sediment was not liquefiable during the September 2010 earthquake (Fig. 5.15A). The high D_H recorded in the area of CPT 57 indicates that lateral spreading within this area was influenced by the overall properties of the area, and that small-scale variations in the liquefying sediment did not influence D_H (Fig. 5.15A). Additionally, the CPTs conducted centrally within geomorphic area 2c east (33-35 & 37) indicate that the subsurface sediment was not liquefiable for the September 2010 earthquake (Fig. 5.15A). The lack of liquefiable sediment suggests that the D_H recorded within this area was driven by lateral-spreading within the liquefying sediments proximal to the river (Fig. 5.6 & 5.15A).

Geomorphic area 1 exhibits low D_H proximal to the river bank and along the western margin of the abandoned terrace riser (Fig. 5.15). The CPTs indicate that these areas are underlain by sediment that was either not liquefiable for the September earthquake, or contained a comparably thin potentially (>50% probability) liquefiable layer (Fig. 5.15A). The lack of liquefiable sediment proximal

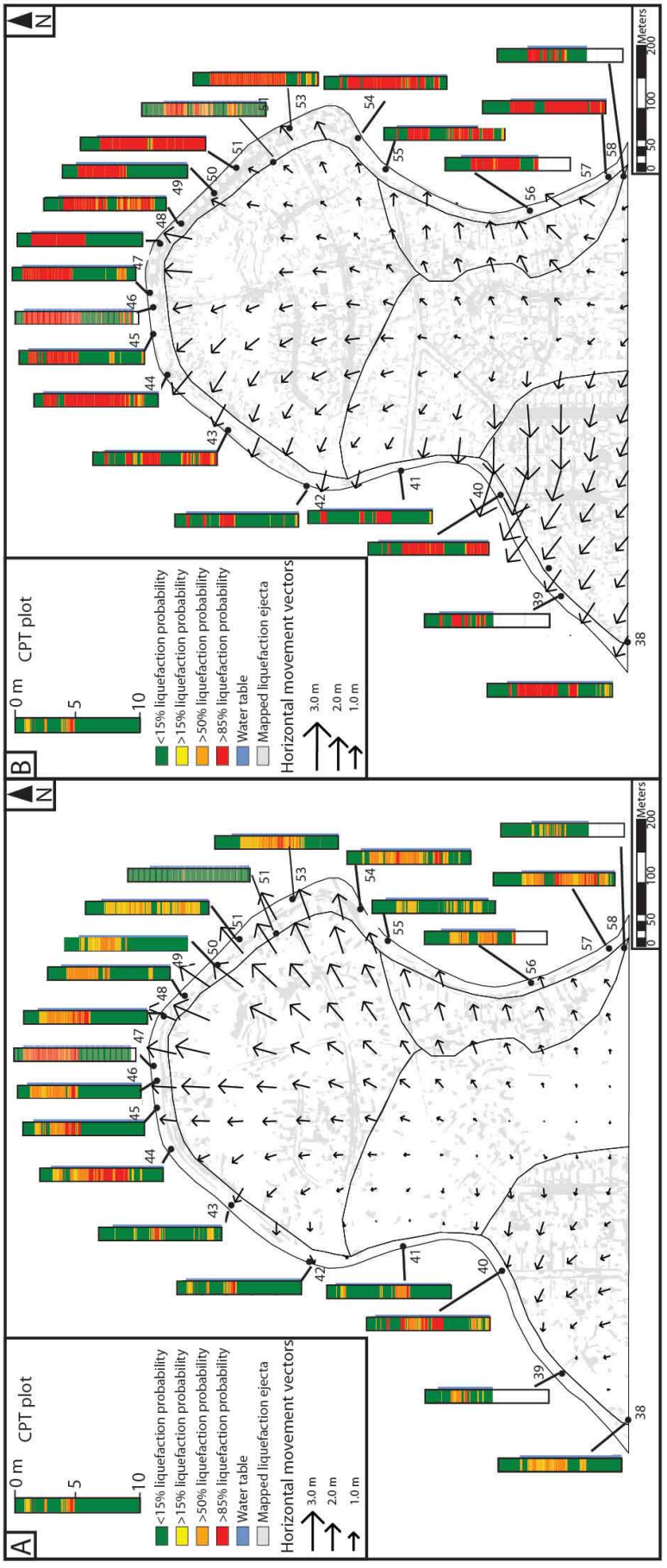

FIGURE 5.15: Lateral-spreading induced D_H derived for the study area following the September 2010 (A) and February 2011 (B) earthquakes plotted with the mapped A_L and the predicted liquefaction profiles as derived for the CPTs conducted proximal to the river using the Boulanger and Idriss (2014) methodology.

to the river bank likely limited lateral spreading and thus resulted in the low D_H (Fig. 5.15A & 5.6). Intermediate values of D_H recorded along the eastern margin of the abandoned terrace riser corresponds with a thicker layer of potentially (>50% probability) liquefiable sediment. The liquefiable sediment likely facilitated lateral spreading in this area, and may have been influenced by the proximity of this area to the river-bank (Fig. 5.6). A_L within the central area of the geomorphic area corresponds with a thicker layer of potentially liquefiable identified within the CPT profile (CPT 8) (Fig. 5.6). D_H along the western margin may have been limited by the distance from the river bank (Fig. 5.15A).

D_H in geomorphic area 2a is comparably higher at the northern extent of the area, which corresponds with a comparably thick unit of potentially (>50% probability) liquefiable sediment adjacent to the river (Fig. 5.15A). The CPTs conducted centrally within the area (CPT 13-15) indicate the subsurface sediment contains very thin potentially liquefiable layers (>50% probability; CPT 13-15) which suggests that D_H within this area was facilitated by the thick liquefying layer proximal to river bank (CPT 55) (Fig. 5.6 & 5.15). The presence of liquefiable sediment proximal to the abandoned terrace riser (CPT 13-17) does not appear to have influenced D_H (Fig. 5.15). It is unclear why lower D_H occurred at the southern extent of the area (Fig. 5.15).

Geomorphic area 2b also exhibits comparably higher D_H values at the northern extent of the area which corresponds with a thick unit of potentially (>50% probability) liquefiable sediment predicted in CPTs 18-20 and 40 (Fig. 5.15 & 5.6). Lower D_H recorded in the area where CPT 39 and 21 were conducted correlates with thinner liquefying units in the subsurface. The spatial variability in D_H indicates that the thickness of the potentially liquefiable units proximal to the river directly influences D_H (Fig. 5.6). It is possible that low D_H at the southern extent may be influenced by sediment properties outside of the study area. Low D_H is recorded adjacent to the abandoned terrace riser despite the presence of a thick potentially (>50% probability) liquefiable layer (CPT 20-23) likely results from the distance of the area from the river (Fig. 5.15 & 5.6).

D_H within the western section of geomorphic area 2c is comparably higher along the northern bank of the river which correlates with a comparably thick profile of liquefying sediment (CPT 44-46) (Fig. 5.15). Lower D_H is observed where the river bank is underlain by thin liquefying layers interbedded with non-liquefying layers (Fig. 5.15). The spatial variability in D_H across the area appears to result from

variations in the thickness of the liquefying layer proximal to the river bank (Fig. 5.15). The CPT conducted centrally within the area (29 and 31) indicate that the subsurface sediment was not liquefiable for the September 2010 earthquake, thus the D_H recorded at these sites most likely results from lateral-spreading within the liquefying layer proximal to the river (Fig. 5.15 & 5.6). The direction of D_H for the September 2010 earthquake appears to be directed towards the northern extent of the area, rather than the closest free-face, indicating that the lateral-spreading within the area was primarily influenced by the thick profile of liquefiable sediments along the northern river bank (CPT 44-47) (Fig. 5.15A).

For the February 2011 earthquake, the higher levels of shaking caused liquefaction in comparably thicker layers of sediment around the perimeter of the study area (Fig. 5.15). In geomorphic area 1, the thicker layers of liquefiable sediment predicted proximal to the river likely facilitated the higher D_H recorded during this event (Fig. 5.13B, 5.15B, & 5.6). The comparably higher A_L mapped corresponds with a comparably thicker profile of potentially (>85% probability) liquefiable sediments in the area of low D_H (Fig. 5.15 & 5.6).

D_H within geomorphic area 2a is similar to that recorded in the area for the September 2010 earthquake despite the area being underlain by thicker profiles of liquefying sediment (Fig. 5.15B). The thickness of liquefiable sediment predicted proximal to the river (CPT 55-58) is similar for both earthquakes, indicating that D_H may have been influenced by the thickness of liquefying sediment proximal to the river and that the thickness of liquefiable sediment distal to the river exerted minimal influence on D_H (Fig. 5.15 & 5.6).

Geomorphic area 2b exhibits very high D_H for the February 2011 earthquake compared to the other areas, and does not appear to decrease with increasing distance from the free-face (Fig. 5.15). The CPTs indicate that the sediment underlying the area contains a thicker liquefiable layer for this event that is encountered at similar depths within the profiles. The similar depths suggest that it may comprise a continuous layer and thus basal glide within this unit may have facilitated within the high D_H recorded within this area (Fig. 5.15 & 5.6).

D_H within the eastern section of geomorphic area 2c was comparably lower than that recorded following the September 2010 earthquake (Fig. 5.15B). The thickness of the liquefiable sediment proximal to the river bank is similar for both earthquakes, while the liquefiable layer observed centrally within the area (CPT

32-37) is comparably thicker for the February 2011 earthquake (Fig. 5.15 & 5.6). It is possible that the development of large surficial lateral-spreading fissures across the area during the September 2010 earthquake may have sufficiently cracked the non-liquefying crust, enabling more rapid dissipation of pore-water pressures in the liquefying sediment layers during the subsequent February 2011 earthquake and thus reducing liquefaction triggering, and resulting in the comparably lower D_H (Fig. 5.15B; see Chapter 4 for further discussion).

D_H within the western section of geomorphic area 2c is comparably higher than that recorded during the September 2010 earthquake (Fig. 5.15 & 5.6). The CPT indicate that the liquefying unit was thicker and more continuous beneath the area (CPT 26-31 & 42-46) which likely facilitated the higher D_H (Fig. 5.15 & 5.6).

5.8 Comparison of liquefying layer thicknesses between geomorphic areas

The thicknesses of H_1 and H_2, and the ratio of H_1 to H_2 are summarized for each geomorphic area to determine whether the liquefaction susceptibility of the sub-surface sediments varies between the geomorphic areas (Fig. 5.16). Liquefaction is predicted to manifest at the surface where H_1/H_2 is <1 (Ishihara, 1985). The L/H is also summarized for each geomorphic area (Fig. 5.16). Geomorphic area 2d is incorporated into the surrounding areas for further analysis.

Geomorphic area 1 exhibits a comparably high median H_1 of 4 m and a median H_2 of 0.75 for the September 2010 earthquake. The median H_1/H_2 ratio derived for the area from the CPTs is 4.9 (Fig. 5.16). The presence of mapped liquefaction in geomorphic area 1 highlights the influence of lateral spreading in facilitating the surface ejection of liquefied sediment where H_1/H_2 >1. The median H_1 is comparably thinner for the February 2011 earthquake (3.8 m), and the median H_2 comparably thicker (1.6 m) (Fig. 5.16). The median H_1/H_2 ratio is 2.25 (Fig. 5.16).

In geomorphic area 2a, the H_1 is 2.6 m and the H_2 is 2.4 m for the September 2010 earthquake (Fig. 5.16). The median H_1/H_2 is 0.9 (Fig. 5.16). The median H_1 is comparably thinner under the higher PGA of the February 2011 earthquakes (2.1 m), and the median H_2 is comparably thicker (3.9 m); the median H_1/H_2 is

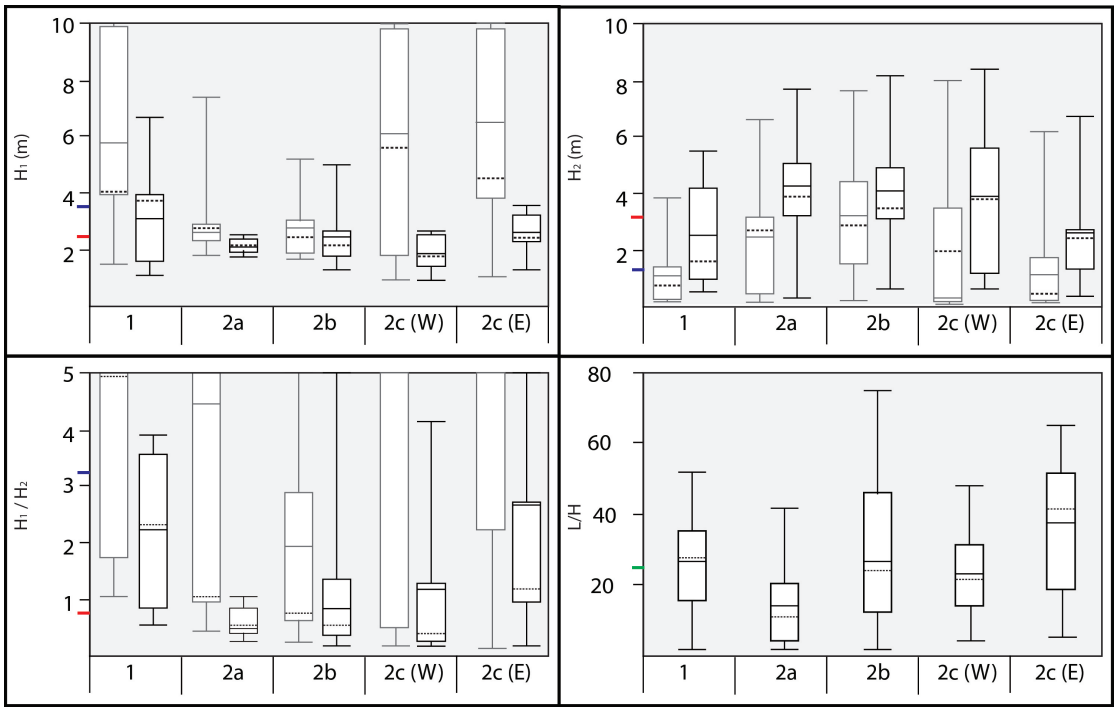

FIGURE 5.16: A) Comparison of the H_1 across the five geomorphic areas for the September 2010 (outlined in grey) and February 2011 (outlined in black) earthquakes. B) H_2 compared across the geomorphic areas, (C) H_1/H_2 for the geomorphic areas, D) L/H compared plotted for the give geomorphic areas. The box defines the 25th and 75th percentiles and the whiskers represent the data range, excluding outliers. Dotted lines are means and solid lines are the median. The blue line represents the median derived for the study area for the September 2010 earthquake, and the red line represents the median for the February 2011 earthquake. The green line in D) represents the median L/H for all geomorphic areas.

0.5 (Fig. 5.16). Geomorphic area 2b exhibits a median H_1 of 2.45 m and median H_2 of 2.8 m for the September 2010 earthquake. The median H_1/H_2 is 0.8 (Fig. 5.16D). For the February 2011 earthquake, the median H_1 and H_2 are 2.15 and 3.5 m respectively, and the median H_1/H_2 is 0.5 (Fig. 5.16).

The median H_1 for the eastern section of geomorphic area 2c is 4.5 m for the September 2010 earthquake, while the median H_2 is comparably thin at 0.3 m. The median H_1/H_2 is 15 (Fig. 5.16). The H_1 is comparably thinner for the February 2011 earthquake (median = 2.4 m), while the H_2 is comparably thicker (median = 2.0 m) (Fig. 5.16). The median H_1/H_2 ratio is comparably lower for the February 2011 earthquake at 1.2 (Fig. 5.16D). The western section of geomorphic area 2c, exhibits a comparably thick H_1 for the September 2010 earthquake (median = 7.8 m) and thin H_2 (median = 1.75 m). The median H_1/H_2 is 53.5 (Fig. 5.16). The median H_1 is comparably thinner during the February 2011 earthquake (7.75 m),

and the median H_2 comparably thicker (3.95 m). The median H_1/ H_2 is 0.38 (Fig. 5.16).

5.9 Comparison of mapped liquefaction severity and subsurface properties

The median H_1, H_2, H_1/H_2, and the L/H derived for each polygon are compared with the ρ_L, A_L, D_H, and D_S to determine whether trends exist between predicted liquefaction and that observed at the surface. Scatter plots are presented in Figures 5.17 5.18 5.19 5.20, and the trends observed within these plots are summarized in Table 5.5. The described trends are consistent for all geomorphic areas, with the exception of D_S and H_1/H_2 in geomorphic area 1. The consistency indicates that a strong correlation exists between the measurable parameters derived from the CPT, and the surface manifestation of liquefaction and total ground displacements within the study area.

A clear relationship is observed between H_1/H_2 and L/H and the ρ_L and D_H for the February earthquake (Fig. 5.19 & 5.20). An upper-bound curve between the occurrence of ρ_L and D_H is produced when L/H is multiplied by H_1/H_2 (Fig. 5.21). No clear relationship is observed between A_L or D_S and L/H x H_1/H_2 (Fig. 5.21).

5.10 Discussion of observed trends between the liquefaction severity and subsurface sediment properties between geomorphic areas

5.10.1 Distribution of liquefaction features and measured horizontal displacements

High ρ_L are observed proximal to the river as indicated in Figure 5.8 and 5.9. Areas exhibiting high ρ_L generally correspond with areas that experienced high D_H, indicating that the distribution of surface features was strongly influenced by lateral spreading. The range of ρ_L and D_H are shown to decrease with increasing L/H

TABLE 5.5: Trends observed from comparison of the liquefaction metrics, sub-surface properties, and L/H

Metric	Property	September 2010 earthquake	February 2011 earthquake
ρ_L	H_1	No clear relationship	Variable at low H_1, decreases with increasing H_1
	H_2	No relationship clear relationship	Increases with increasing H_2
	H_1/H_2	75% data plots at <1	Plots at <1 except area 1
	L/H	No clear relationship	Decreases with increasing L/H
A_L	H_1	Weakly increases with increasing H_1	Weakly increases with increasing H_1
	H_2	Weakly increases with increasing H_2	Weakly increases with increasing H_2
	H_1/H_2	No clear relationship	75% data plots at <1
	L/H	Weakly increases with increasing L/H	Increases with increasing L/H
D_H	H_1	No clear relationship	No clear relationship
	H_2	No relationship with H_2	Weakly increases with increasing H_2
	H_1/H_2	Range of values decreases with increasing H_1/H_2	Plots at <1 except area 1
	L/H	No clear relationship	Decreases with increasing L/H
D_S	H_1	No clear relationship	No clear relationship
	H_2	No clear relationship	Increases slightly with increasing H_2
	H_1/H_2	No clear relationship	Plots at <1 except area 1
	L/H	No clear relationship	Increases slightly with increasing L/H

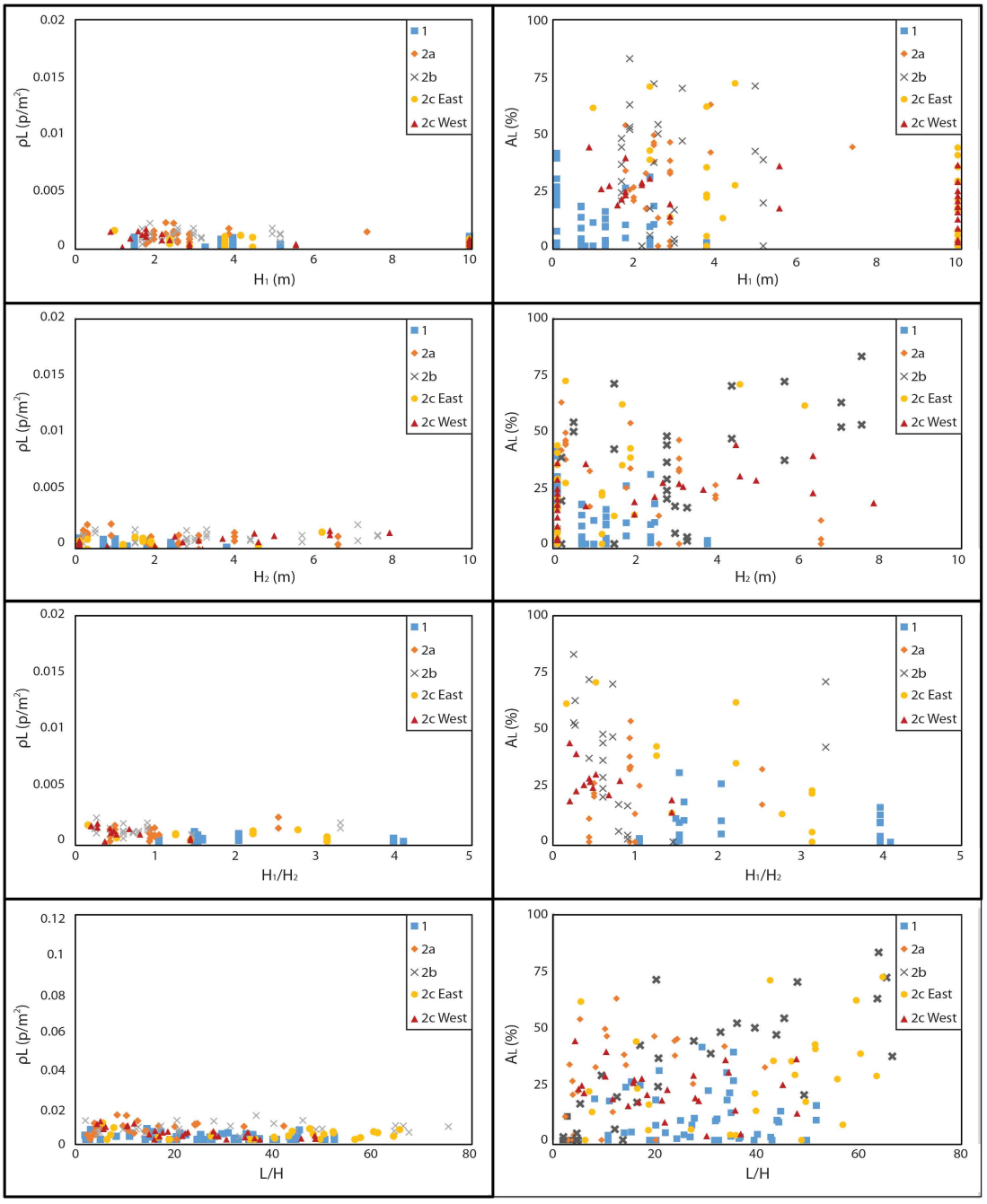

FIGURE 5.17: Plots comparing the ρ_L and A_L derived for each polygon following the September 2010 earthquake with the median H_1, H_2, H_1/H_2 derived from liquefaction analysis of the CPTs and the L/H.

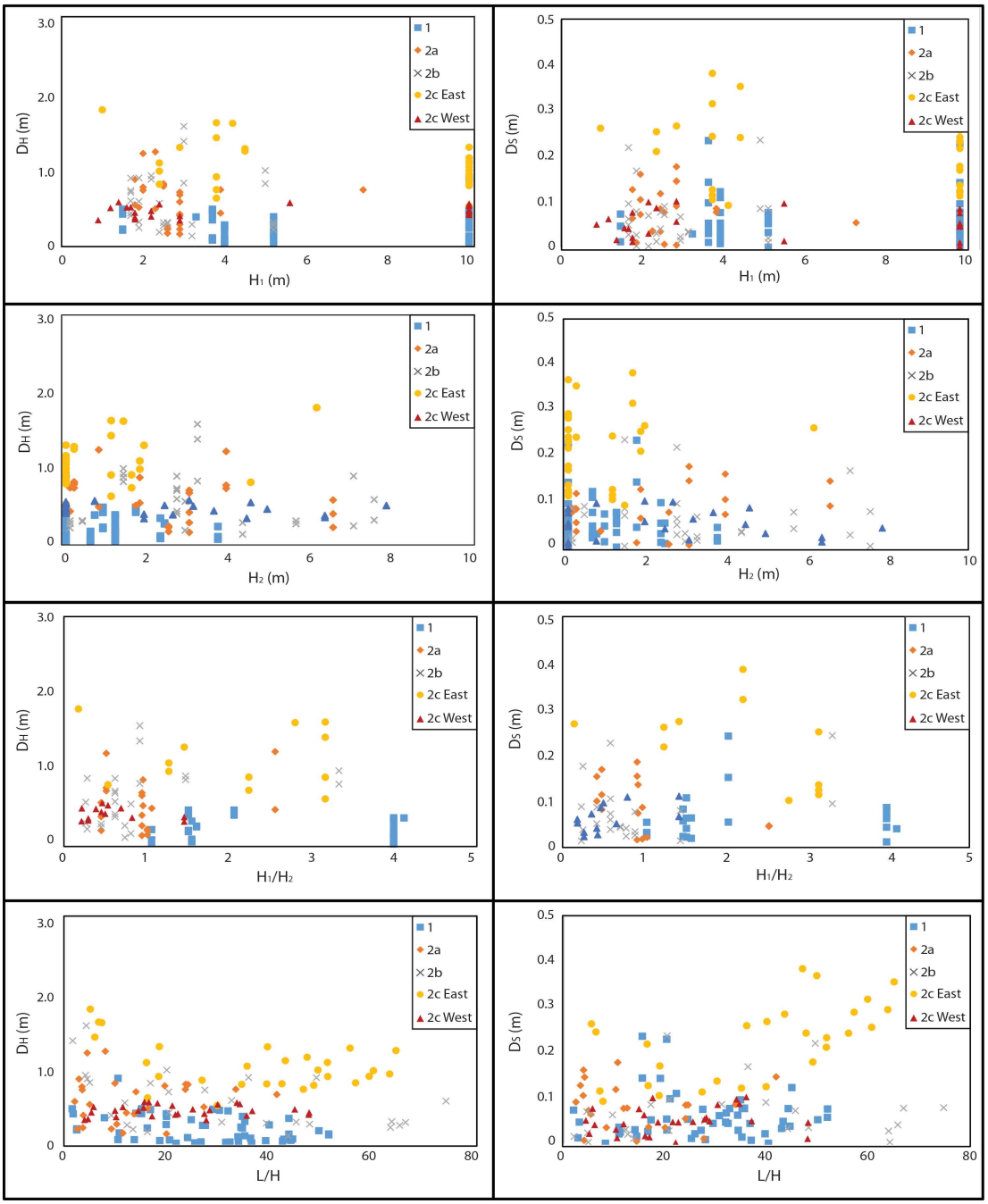

FIGURE 5.18: Plots comparing the median D_H and D_S derived for each polygon for the September 2010 earthquake with the median H_1, H_2, H_1/H_2 and L/H derived for each polygon.

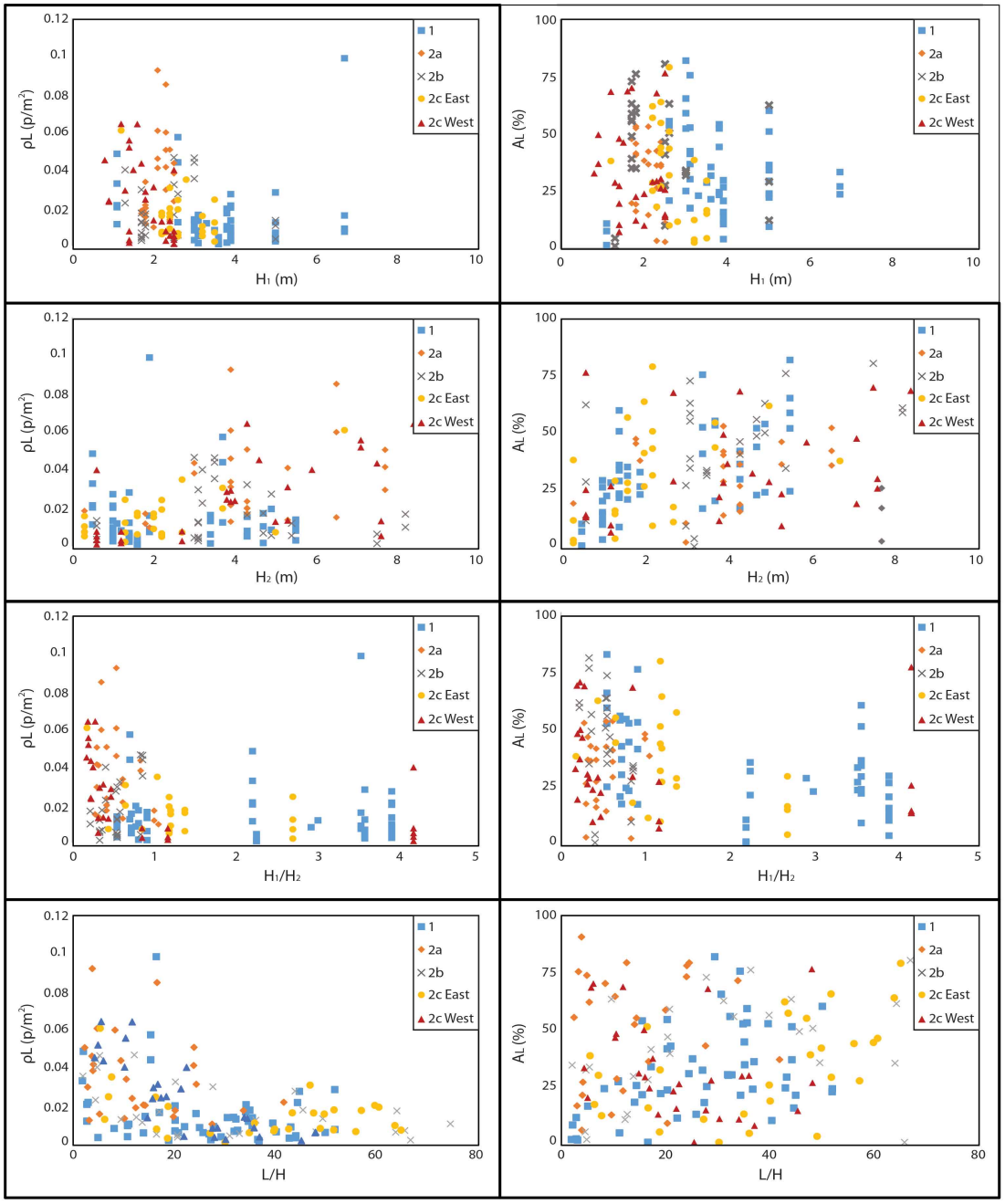

FIGURE 5.19: Plots comparing the ρ_L and A_L derived for each polygon following the February 2011 earthquake with the median H_1, H_2, H_1/H_2 derived from liquefaction analysis of the CPTs and the L/H.

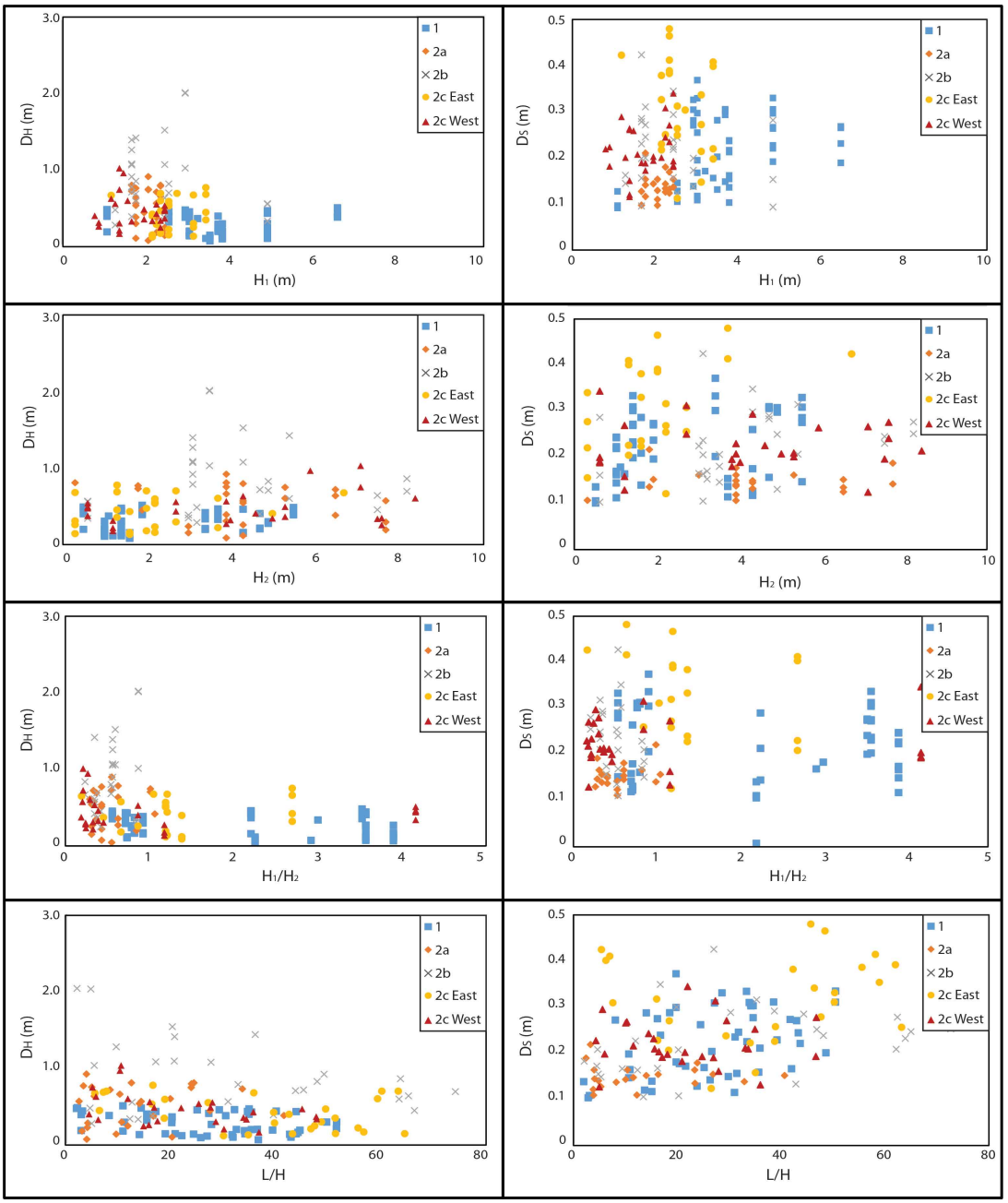

FIGURE 5.20: Plots comparing the median D_H and D_S derived for each polygon for the February 2011 earthquake with the median H_1, H_2, H_1/H_2 and L/H derived for each polygon.

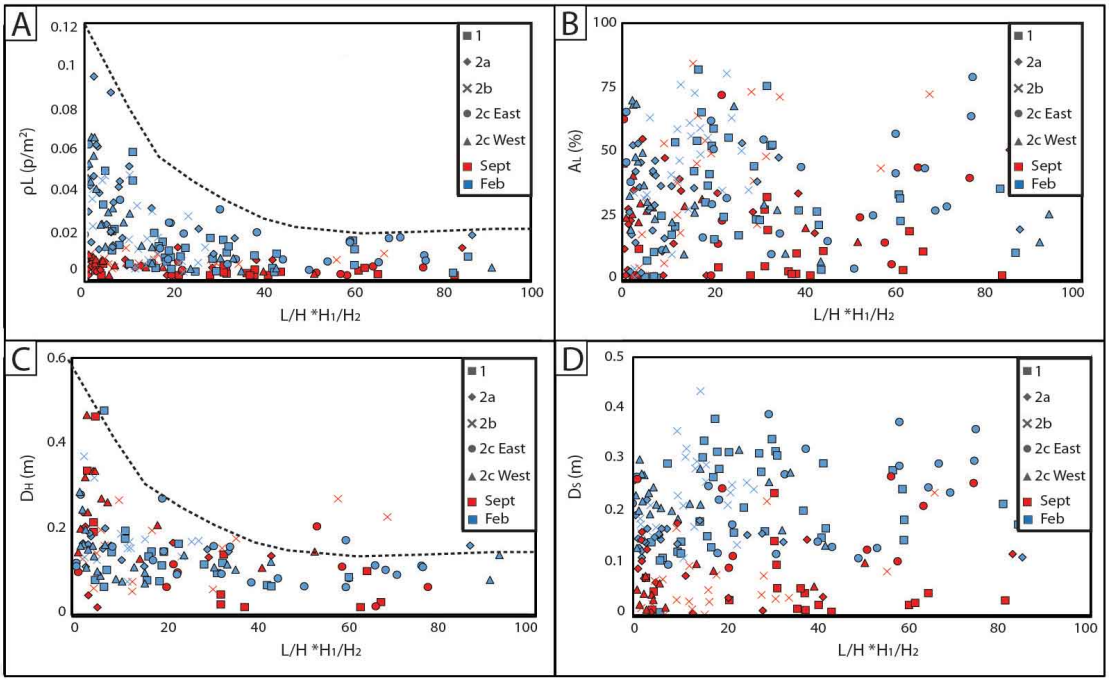

FIGURE 5.21: The ρ_L, A_L, and the D_H and D_S plotted against the H_1/H_2 multiplied by the L/H. A bounding curve between the occurrence and nonoccurrencee of ρ_L and D_H is indicated.

for the February 2011 earthquake (Fig. 5.19 & 5.20), indicating that the distance from the free-face and height of the free-face influences the surface manifestation of lateral spreading. The ρ_L and D_H generally plots at H_1/H_2 <1 indicating that lateral spreading is also strongly influenced by the liquefaction susceptibility of the subsurface sediment and the ratio of the non-liquefying cap to the underlying liquefying sediment.

High D_H recorded within geomorphic area 2c east and at the northern extent of geomorphic area 2c west during the September 2010 earthquake correlates with a thick profile of liquefiable sediment deposited at the apex of the meander bend (Fig. 5.15). The river morphology indicates that the liquefiable layer comprises loosely consolidated, sandy-point bar deposits of paleo-channel. The relatively high D_H recorded internally within geomorphic area 2c east despite the lack of liquefiable sediment predicted in the CPT profile indicates that the lateral-spreading proximal to the river influences the internal D_H (Fig. 5.15).

Comparably low ρ_L and D_H occurred within geomorphic area 1 following both the September 2010 and February 2011 earthquakes. The CPT liquefaction profiles indicate that the area proximal to the river is underlain by either no liquefiable

sediment or thin liquefiable layers that are comparably deeper than within geomorphic area 2 and are interbedded with non-liquefying sediment resulting in high H_1/H_2 values (Fig. 5.6 & 5.16). The increased depth to the liquefiable sediment results in the deeper depth to the water table as a result of the higher elevation of the area. The river morphology indicates that this area comprises the active flood-plain of the Avon River and thus it is likely to be underlain by silts with interbedded sand. The comparably lower ρ_L and D_H is consistent with the low ρ_L and D_H observed where H_1/H_2 >1. This supports that the surface manifestation of liquefaction is directly related to H_1/ H_2 and indicates that proximity to the river does not influence D_H where $H_1/_2$ >1.

Comparison of the D_H across the study area indicates that the thickness of the liquefying sediments proximal to the river directly influences the overall D_H recorded within the geographic area. Higher D_H occurs within areas underlain by thick liquefying layers comprising point-bar deposits, while D_H is lower within the flood-plain due to the thinner interbedded sand layers. The influence of the distance from the free-face and ratio of H_1 to H_2 on lateral-spreading and the surficial manifestation of liquefaction is outlined by the upper-bound curve produced when the L/H and H_1/H_2 are multiplied (Fig. 5.21).

5.10.2 Coverage of liquefaction ejecta

A_L is observed to increase with increasing distance from the free-face and decrease with increasing H_1/H_2 (Fig. 5.11). Comparably high A_L is observed within areas that experienced low to intermediate values of D_H, and low a H_1/H_2 ratio indicating that A_L predominantly occurs in areas susceptible to liquefaction with limited lateral spreading (Fig. 5.15). The limited A_L in areas of high D_H likely results from the fracturing of the non-liquefiable cap which dissipates pore-water pressures within the liquefiable stratum.

High A_L is observed adjacent to the abandoned terrace riser in geomorphic areas 2a and 2b which is shown to be underlain by thick and continuous liquefying layers possibly comprising paleo-channel deposits. The area between the paleo-channel and modern flood-plain (2d) comprises thin liquefying layers for the September 2010 earthquake which most likely reflects thin interbedded sand lenses within the over-bank silts. The spatial variability in the thickness of the liquefying layers across the area may have limited lateral spreading. For the February 2011

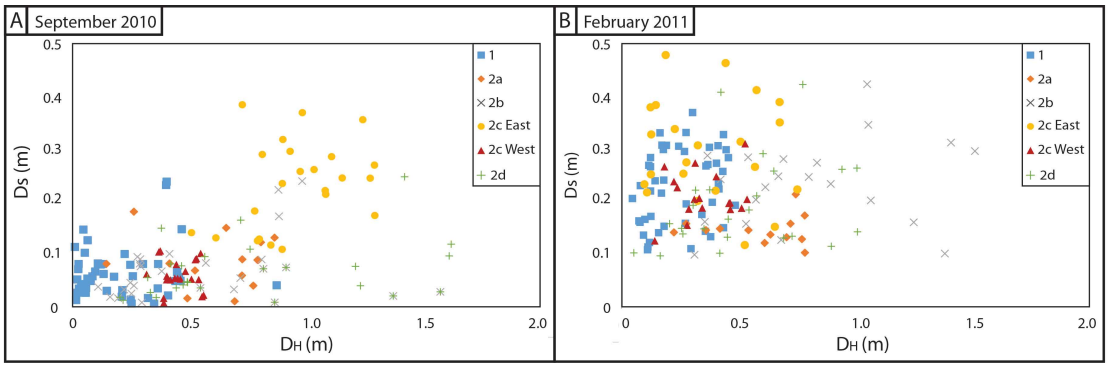

FIGURE 5.22: Comparison of the median D_S and median D_H derived for the polygons within each geomorphic area for the September 2010 (A) and February 2011 (B) earthquakes.

earthquake, the liquefiable layer is comparably thicker and continuous across geomorphic area 2b. It is possible that the thickness and continuity of this layer facilitated lateral spreading across the area resulting in the high D_H that did not decrease with increasing distance from the free-face. The high A_L for this event may result from the predominantly translational movement of the area (See Chapter 4 for further discussion).

5.10.3 Subsidence

D_S appears to be comparably higher in areas distal to the free-face which suggests that the ejection of liquefied sediment and subsequent clean-up resulted in higher subsidence.

D_S plots at H_1/H_2 <1 which is consistent with high D_S occurring in areas where liquefaction is predicted to manifest at the surface (Ishihara, 1985). The exception to this is geomorphic area 1 that plots at H_1/H_2 >1. Geomorphic area 1 exhibits a higher median D_S than geomorphic area 2. Additionally, D_S is observed to be comparably higher within the residential properties than on the surrounding roads (Fig. 5.13). The higher D_S within geomorphic area 1, and within the residential properties suggests that D_S predominantly occurs in areas of higher elevation that are surrounded by lower elevation areas and thus results in levelling of the ground surface.

D_S is plotted against D_H to determine whether a relationship exists between lateral spreading and D_S within the study area (Fig. 5.22). For the September 2010 earthquake D_S increases with increasing D_H for geomorphic area 2c east indicating

that areas with high D_H resulted in high D_S. No correlation is observed between D_S and D_H within the other geomorphic areas for the September 2010 nor February 2011 earthquake indicating that lateral spreading across the area during the CES did not unequivocally influence the recorded D_S (Fig. 5.22).

5.11 Modelled and measured horizontal ground displacements within the study area

The D_H measured within the study area are compared with those predicted from the Zhang et al. (2004) empiricial model to determine whether the predictive capacity of the model is influenced by the geomorphic, sedimetologic, and topographic variability across the study area.

5.11.1 Background on typical models employed for site selection

The New Zealand Transport Authority (NZTA) bridge manual is considered to be the industry standard in New Zealand for assessing slope and/or land stability during earthquakes (NZTA, 2013). The manual refers to the New Zealand Geotechnical Society (NZGS) liquefaction assessment guidelines to avoid repetition (NZGS, 2013). The NZGS guidelines require detailed site investigations to be undertaken at sites of future development to evaluate the potential for liquefaction triggering, and liquefaction-induced ground deformation (i.e. lateral spreading) (NZGS, 2013). At sites where lateral spreading is predicted, anticipated horizontal displacements must be determined for various earthquake scenarios (NZGS, 2013).

The Youd et al. (2001) model is considered to be the industry standard for simple analysis of lateral-spreading-induced horizontal ground displacements within New Zealand. This empirical method incorporates the distance of the site from the seismic energy source, earthquake magnitude, mean grain-size, and the thickness of sediment profile that is susceptible to liquefaction. The model utilises SPT parameters and thus requires conversions to incorporate CPT parameters which adds additional levels of uncertainty and potential sources of error. The method

assumes that lateral-spreading occurs co-seismically, that the entire profile of potentially liquefiable sediments liquefies, and that displacements are dependent on earthquake magnitude (Youd et al., 2001). The Zhang et al. (2004) method is not widely employed within industry, however it is recommended in the NZGS guidelines (NZGS, 2013). This semi-empirical model assumes that lateral-spreading is post-seismic, and incorporates liquefaction analysis from either the CPT or SPT with PGA, earthquake magnitude (M_w), and depth to ground water to derive the thickness of the potentially liquefiable sediments. The post-seismic assumption of this model is consistent with the observations of lateral-spreading fissures opening up in the minutes following the earthquake shaking in parts of eastern Christchurch (van Ballegooy pers. comms., 2010-2011).

The area of the Deterling (2015) study is located near the Avonside study area, within a similar geomorphic setting at similar elevations, suggesting that the conclusions from this study may be applicable to the Avonside study area (Fig. 5.2). The study concluded that the horizontal displacements predicted by the Youd et al. (2001) model were much smaller than those measured during the CES, while the Zhang et al. (2004) model predicted horizontal displacements those were more similar to that observed (Fig. 5.2).

5.11.2 Methodology for modelling the horizontal displacements

The Zhang et al. (2004) model is selected to model horizontal displacements based on the results from the Deterling (2015) study and the co-seismic observations of lateral spreading. Four profiles are constructed parallel to the direction of D_H within the study area (Fig. 5.23). A cross-section is not constructed adjacent to the river bank in geomorphic area 1 as the direction of D_H varied significantly and thus a cross-section perpendicular to the spreading direction could not be constructed (Fig. 5.23).

The Zhang et al. (2004) model requires the factor of safety against liquefaction to be computed from CPTs as a function of depth and integrated over the top 10 m to calculate the Lateral Displacement Index (LDI). The LDI for this study was calculated from the 50th percentile exceedance probability of the liquefaction potential as derived for each CPT using the Boulanger and Idriss (2014) method.

The Zhang et al. (2004) equation with the free-face condition was selected, which computes horizontal displacements as a function of the L/H and LDI.

The model was run five times using varied input parameters to determine whether the predictive capacity of the model was influenced by geomorphic variability across the study area. Two input L/H models were used in the analysis; a model that incorporates the abandoned terrace riser as a secondary free-face, and a model that excludes the abandoned terrace riser. The input parameters for the five models are outlined in Table 5.6. The LDI input for models 2-4 was varied where Lines 1 and 4 cross into geomorphic area 1 (Fig. 5.23). It is acknowledged that the use of median LDI would be considered more statistically robust, however the median produced horizontal displacements that poorly correlated with those measured.

TABLE 5.6: Horizontal displacement models used in analysis

Model	LDI input	L/H model
1	LDI from single CPT proximal to river	Incorporates paleo-cut bank
2	Mean LDI for each geomorphic area	Incorporates paleo-cut bank
3	Mean LDI for each geomorphic area	Excludes paleo-cut bank
4	LDI from proximal CPT	Excludes paleo-cut bank
5	Maximum LDI for geomorphic area	Excludes paleo-cut bank

5.11.3 Predicted and measured horizontal displacements

Line 1

Line 1 crosses geomorphic area 2b, the abandoned terrace riser and extends into geomorphic area 1 (Fig. 5.23).

For the September 2010 earthquake, the D_H predicted from models 1 and 2 exceed those measured within geomorphic areas 2b and 1, and are significantly higher than those measured across the abandoned terrace riser (Fig. 5.23). D_H predicted from model 3 exceed those measured within geomorphic area 2b and across the abandoned terrace riser, however are within a factor of two (i.e. ±50%) of those measured within geomorphic area 1 (Fig. 5.23). Models 4 and 5 approximate (i.e. ±50%) those measured (Fig. 5.23). For the February 2011 earthquake, the predicted D_H are significantly lower than those measured in geomorphic area 2b,

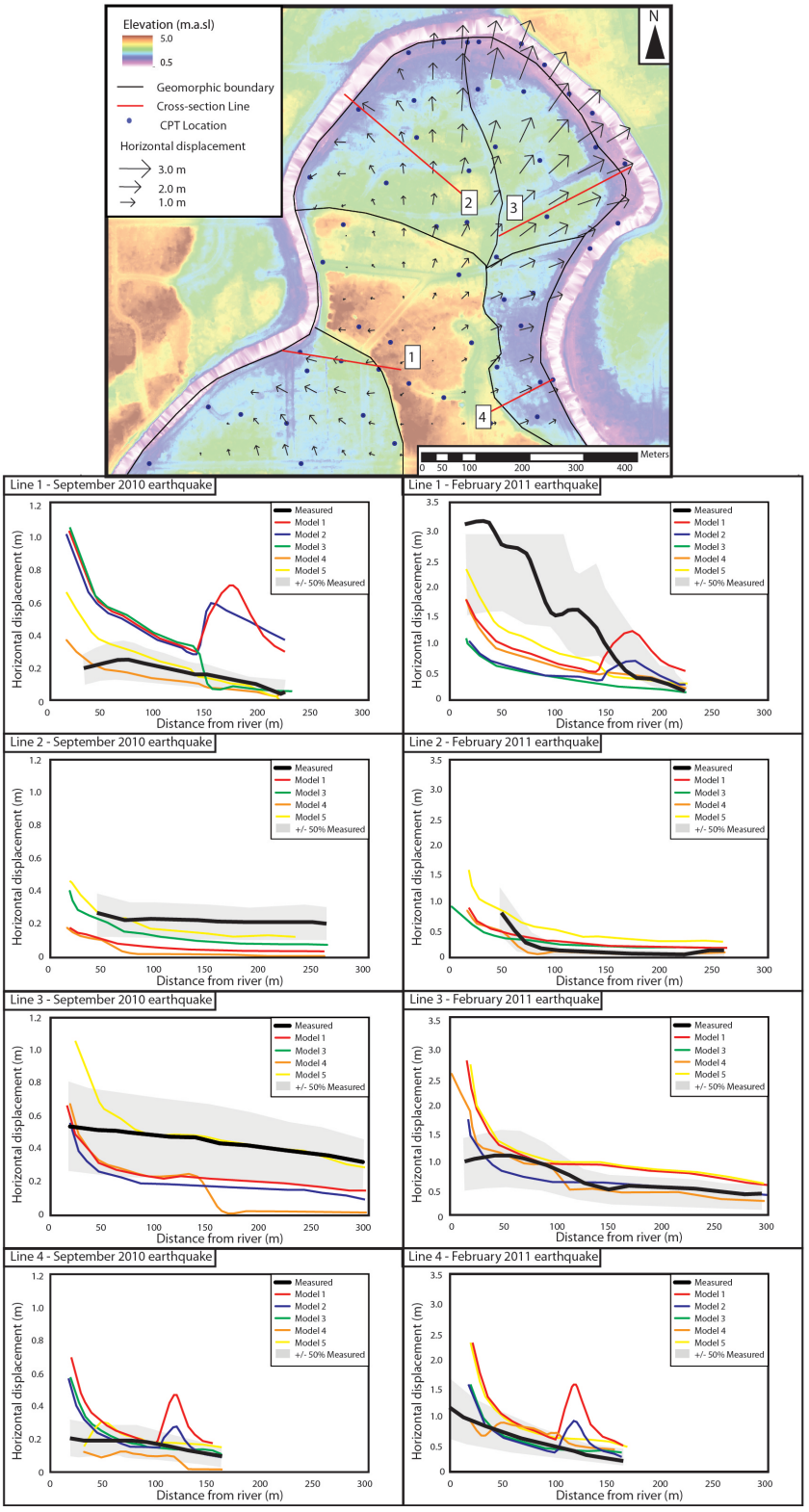

FIGURE 5.23: Location of the profile lines within the study area with the location of CPTs and horizontal displacements measured following the September 2010 earthquake indicated. Measured and predicted displacements from the models outlined in Table 5.6 are plotted for each profile line for the September 2010 and February 2011 earthquakes.

while the D_H predicted from models 4 and 5 closely approximate those measured at distances >180 m from the free-face (i.e. within geomorphic area 1) (Fig. 5.23).

Line 2

Line 2 is within the western section of geomorphic area 2c (Fig. 5.23).

For the September 2010 earthquake, the D_H predicted from model 5 are within a factor of two of those measured (i.e. ±50%) (Fig. 5.23). D_H predicted from models 1, 3, and 4 are significantly lower than those measured for the September 2010 earthquake (Fig. 5.23). For the February 2011 earthquake, the D_H predicted from models 1, 3, and 4 approximate the measured D_H at distances >50 m from the free-face (Fig. 5.23). Model 5 produces predicted D_H that exceeds those measured following the February earthquake by greater than a factor of two (Fig. 5.23).

Line 3

Line 3 is within the eastern section of geomorphic area 2c (Fig. 5.23).

For the September 2010 earthquake, the D_H predicted from model 5 closely approximate those measured at distances >75 m from the free-face (Fig. 5.23). The D_H predicted from models 1, 3, and 4 is much lower than those measured (Fig. 5.23). For the February 2011 earthquake, the D_H predicted from model 4 closely approximate those measured (Fig. 5.23). D_H predicted from the model 3 approximates the D_H at distances >100 m from the free-face however exceeds those measured at distances <100 m (Fig. 5.23). D_H predicted from the models 1 and 5 approximate the displacements measured at 50 to 100 m; at distances >100 m the predicted D_H exceeds those measured (Fig. 5.23).

Line 4

Line 4 crosses geomorphic area 2a, the abandoned terrace riser, and extends into geomorphic area 1 (Fig. 5.23).

For the September 2010 earthquake, the D_H predicted from models 3 and 5 closely approximate those measured along the cross-section at distances >75 m from the free-face (Fig. 5.23). D_H predicted from the model 1 are within a factor of two of those measured at distances >50 m from the free-face within geomorphic areas 1 and 2a, however significantly exceed those measured across the abandoned terrace riser (Fig. 5.23). Model 2 approximates the measured D_H within geomorphic areas 2a and 1, however also exceeds those measured across the abandoned terrace

riser following the September 2010 earthquake (Fig. 5.23). For the February 2011 earthquake, model 3 closely approximates those measured along the transect (Fig. 5.23). D_H predicted from model 2 also closely approximates the measured D_H within geomorphic areas 2a and 1, however exceeds those measured across the abandoned terrace riser (Fig. 5.23). D_H predicted from models 1, 4, and 5 are generally within a factor of two of those measured at distances >75 m from the free-face (Fig. 5.23).

5.11.4 Discussion of the applicability of the models

D_H predicted from model 1 generally vary significantly from those measured following the September 2010 and February 2011 earthquakes, with the exceptions of Line 1 for the September 2010 earthquake and Line 4 for the February 2011 earthquake (Fig. 5.23). The inconsistencies between the predicted and measured highlight the limitations of using single site-specific testing to approximate horizontal D_H with increasing distances from the free-face.

The D_H predicted from model 2 vary from those measured along Line 1 following the September 2010 and February 2011 earthquakes, and approximate those measured at distances >50 m from the river along line 4 (Fig. 5.23). However, the D_H predicted across the abandoned terrace riser significantly exceed those measured for both earthquakes indicating that the abandoned terrace riser did not influence lateral spreading within the study area (Fig. 5.23).

Model 3, which excludes the terrace riser, predicts D_H that approximates those measured across the terrace riser which further supports that the riser did not influence lateral spreading within the study area. D_H predicted along Line 1 from model 3 approximates those measured in geomorphic area 1 for both earthquakes, and approximates those measured at distances >150 m from the river along Line 3 for the February 2011 earthquake (Fig. 5.23). The model poorly correlates with those measured along Line 2 for both earthquakes (Fig. 5.23). The variations in the predictive capacity of the model at short distances and between earthquakes suggests that the mean LDI does not unequivocally improve the predictive capacity of the model and suggests factors in addition to the mean LDI influence D_H (Fig. 5.23). The thicknesses of the liquefying layers is shown to decrease with increasing distance from the free-face in the CPT profiles, thus the use of the mean LDI does

not account for the comparably thicker liquefying layers proximal to the free-face (Fig. 5.6).

Model 4 predicts D_H that are significantly lower than those measured along Lines 1-4 following the September 2010 earthquake, and higher than those measured along Line 4 following the February 2011 earthquake (Fig. 5.23). The CPTs conducted distal to the free-faces along Lines 1-4 indicate that subsurface sediments contain thin or no liquefying units for the September 2010 earthquake thus resulting in the prediction of low D_H distal to the free-face (Fig. 5.6 & 5.23). The variation between the measured and predicted D_H indicates that lateral spreading was not influenced by spatial variability in the liquefying layer with increasing distance from the free-face. The D_H predicted along Lines 2 and 3, and at distances >150 m along Line 1 following the February 2011 earthquake closely approximate those measured (Fig. 5.23). The CPT indicate that the liquefying layers distal to the free-face are comparably thicker for the February 2011 earthquake and approximate the thickness of the liquefying layer proximal to the river (Fig. 5.6). The consistency between the measured and predicted D_H for the February 2011 earthquake further indicates that the thickness of the liquefiable sediment proximal to the free-face influences D_H recorded within the geomorphic areas (Fig. 5.6).

D_H predicted along Lines 1-4 using model 5 closely approximate those measured following the September 2010 earthquake, and those measured at distances >150 m from the river along Line 1 following the February 2011 earthquake (Fig. 5.23). The maximum thickness of the liquefying layer occurs proximal to the free-face for the September 2010 earthquake and decreases with increasing distance. The correlation between the measured and predicted D_H supports that the measured D_H is influenced by the maximum thickness of the liquefying layer proximal to the river for the September 2010 earthquake. For the February 2011 earthquake the D_H predicted along Lines 2, 3, and 4 exceed those measured (Fig. 5.23). The CPT profiles indicate that much of the sediment profile proximal to the river was potentially liquefiable for the February 2011 earthquake, resulting in low H_1/H_2 values (Fig. 5.16). The use of the maximum LDI therefore assumes that much of the geomorphic area liquefied during the February 2011 earthquake. It is possible that the use of the mean or median LDI of the CPT proximal to the river may further improve the predictive capacity of these models.

The displacements predicted within geomorphic area 2b along Line 1 for the February 2011 earthquake are significantly lower than those measured (Fig. 5.23). The

measured D_H do not decrease with increasing distance from the free-face and thus do not fit the inherent assumption of D_H decreasing with increasing distance from the free-face (Zhang et al., 2004). Additionally, the displacements measured D_H along Line 2 for the September 2010 earthquake are more than a factor of two higher than those predicted from the models (Fig. 5.23). Although every effort was made to ensure that the cross-section was constructed parallel with the direction of spreading for both the September 2010 and February 2011 earthquakes, the direction of spreading varied between the two events (Fig. 5.15). The variation in the spreading direction likely accounts for some of the inconsistencies between the predicted and observed D_H for the September 2010 earthquake.

5.12 Discussion of factors influencing the severity of liquefaction and lateral spreading

Comparison the distribution of liquefaction and liquefaction-induced ground displacements across the Avonside study area indicates that the ratio of H_1 to H_2 and L/H exert a strong influence on the surface manifestation of liquefaction. The thickness, depth, and continuity of the liquefiable layers proximal to the river are shown to strongly influence D_H across the study area. High D_H in the thick liquefying layers proximal to the free-face at the apex of the meander bend which likely comprise loosely-consolidated sandy point-bar deposits. Lower D_H is observed proximal to the river in areas underlain by over-bank silts with thin interbedded sand layers which comprise thin liquefying layers interbedded with non-liquefiable sediment. The comparison of the predicted and measured D_H across the study area further indicates that D_H is influenced by area wide dimensional geometry and characteristics of the liquefying layers proximal to the river rather than small-scale site-specific variability.

The correlation derived between the characteristics of the liquefiable layers and distances to the free-face are consistent for all geomorphic areas, indicating that the geomorphic variability within these areas is adequately accounted for by these parameters. The ratio of H_1/H_2 corresponds with the depositional characteristics of the subsurface sediment (i.e. point-bar vs over-bank) suggesting that comparison of the liquefaction triggering assessments across geologically similar deposits

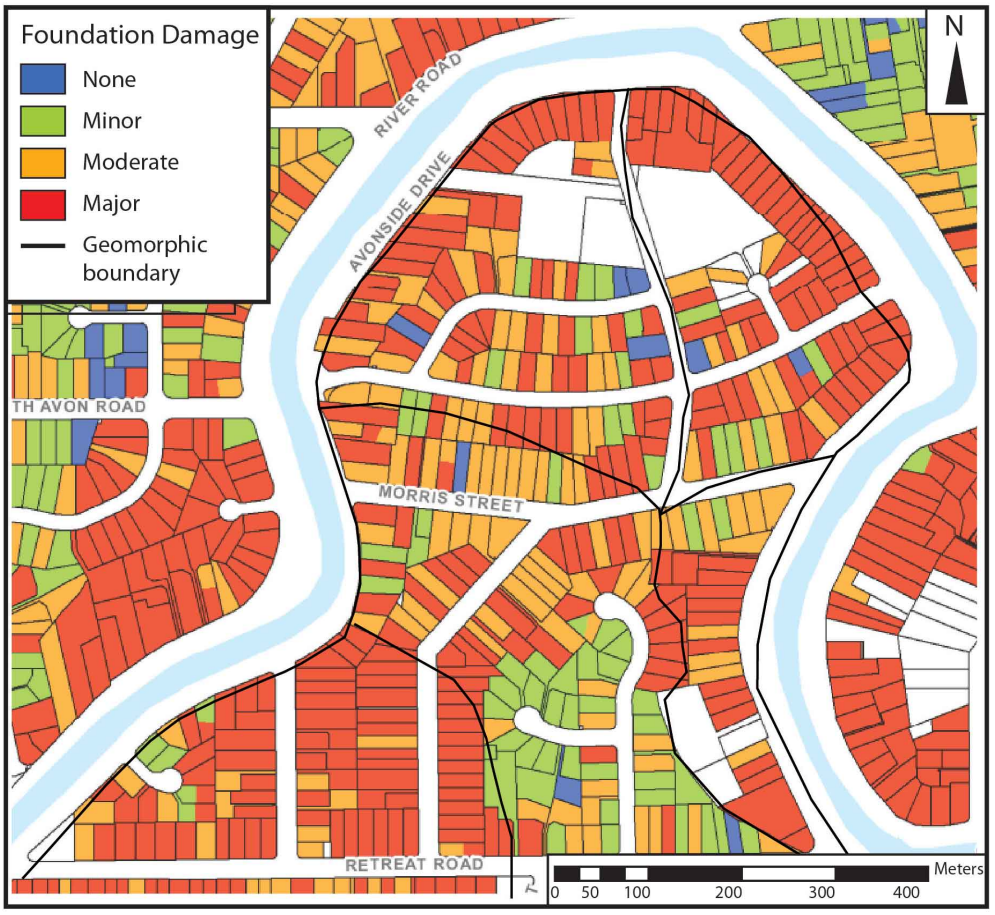

FIGURE 5.24: Foundation damage documented for the residential properties within the study area following the CES.

combined with mapping of free-faces may be employed to predict the surface manifestation of liquefaction during future events. A basic knowledge of meandering river processes may be employed to assess the distribution of sediments susceptible to liquefaction in addition to geotechnical testing. The incorporation of basic geomorphic mapping into standard geotechnical liquefaction hazard assessments may enable fewer tests to be conducted within an area, and may aid the interpretation of the liquefaction hazard of the overall area rather than the current site-specific methods which predict significant spatial variability in ground performance. The incorporation of geomorphology into these assessments, and the use of area-wide analysis rather than site-specific reporting may improve the correlation between predicted and observed liquefaction-triggering.

The physical damage to building foundations within the study area during the CES is also shown to spatially vary across the study area (Fig. 5.24). Areas distal to river with high H_1/H_2 values in geomorphic area 1 exhibit minor foundation

damage, whereas areas with low H_1/H_2 values and that exhibited high D_H and/or A_L generally exhibited major foundation damage (Fig. 5.24). Damage distal to the river in the point-bar deposits was generally classified as moderate which reflects the increasing elevation and intermediate-to-low H_1/H_2 values. The spatial variation in building damage highlights the influence of geomorphic variability on building performance across the geomorphic areas. The influence of geomorphic variability on liquefaction severity, D_H, and associated building damage indicates that the incorporation of geomorphic mapping may lead to improved loss modelling and management of lateral spreading hazard within existing built environments and for future land development.

5.13 Conclusions

Mapping of surficial liquefaction features and comparison of liquefaction-induced ground D_H within the study area indicates that the pattern of liquefaction ejecta, the density and length of liquefaction features, and the ground D_H are spatially variable within the study area.

The study area was divided into geomorphic areas based on variations in the river morphology and topography. The surface manifestation of liquefaction and ground displacements are shown to vary between the geomorphic areas. Comparison of the CPT traces, boreholes, and depth to the liquefying layer indicates that variations in the paleo-depositional setting across the study area influence variations in the depth and continuity of the liquefying layer. The spatial variability in the distribution of liquefaction and lateral-spreading across the study area cannot be correlated to a single parameter (i.e. L/H or H_1/H_2).

High densities of surface liquefaction features occur in areas exhibiting high horizontal ground displacements. The density of liquefaction features and horizontal displacements is found to be influenced by the thickness of liquefying sediments proximal to the river as outlined by the upper-bound curve constraining the occurrence of liquefaction features and horizontal displacements produced when the L/H is multiplied by the H_1/H_2. The thickness and continuity of the liquefying layer proximal to the river directly correlates with depositional setting and river

morphology, high D_H and low H_1/H_2 is observed within sandy point-bar to paleo-channel deposits that are actively accumulating, while lower D_H and higher H_1/H_2 is observed in areas underlain by over-bank silts interbedded with sands.

The aerial extent of liquefaction ejecta is higher in areas distal to the free-face that experienced low D_H however are underlain by sediments with low $_1/H_2$ (i.e. paleo-channel deposits). Low A_L proximal to the river likely results from D_H fracturing the non-liquefying cap which dissipates pore-water pressures in the liquefiable stratum.

Modelled horizontal displacements from single CPTs and from mean values derived for the geomorphic area poorly correlate with measured horizontal displacements in the study area following the September 2010 and February 2011 earthquake. The inconsistencies between predicted and observed displacements indicates that site-specific testing does not account for the variations in sediment properties within an area. Displacements appear to be influenced by the overall thickness of the liquefiable sediment proximal to the river.

The post-CES building damage data highlights the influence of geomorphic and topographic variability on the resultant building damage, and thus financial losses. This correlation supports that geomorphic mapping should be incorporated into liquefaction assessments to improve liquefaction hazard modelling, and that an area-wide approach to liquefaction triggering and horizontal displacement analyses should be taken.

Chapter 6

Conclusions

Trenching investigations conducted at five sites across eastern Christchurch and two sites in the northern township of Kaiapoi revealed subsurface CES liquefaction features including sub-vertical and planar dikes, lateral sills, and bulbous injection features. Dike width is shown to vary significantly between the study sites and does not unequivocally scale with the site-specific PGAs nor the distance from the epicentre of the main liquefaction triggering CES earthquakes. Extensional strains across the study sites exerts a first order influence on dike width, and is influenced by the amount of horizontal displacement at the site and the thickness and competency of the non-liquefying cap. Sites comprising alluvial sands exhibit high extensional strains and comparably wider dikes, while cohesion within the alluvial silts facilitate translational displacement with low extensional strain resulting in narrower dikes. The subsurface record of liquefaction is additionally shown to under-represent the number of liquefaction triggering earthquakes during the CES. Paleo-liquefaction studies therefore need to employ caution when inferring epicentral regions or earthquake magnitudes of pre-historic earthquakes from paleo-liquefaction features in areas underlain by sediments with heterogeneous resistances to liquefaction and/or where many potential fault sources are present.

The CES liquefaction dikes align with pre-Canterbury earthquake sequence liquefaction features including liquefaction dikes at Sites 1, 3 and 4, possible pre-CES injection features at Sites 2 and 5, a sill and compound sand-blow at Site 6, and a surface sand blister at Site 7. The presence of pre-CES liquefaction confirms that earthquake-induced strong ground motions exceeding the threshold

value for liquefaction have occurred within eastern Christchurch prior to the 2010 Darfield earthquake. Crosscutting relationships combined with ^{14}C dating at Site 1 indicate that this event most likely occurred between A.D. 1660-1803 and ca. 1905, while the event at Sites 3-5 most likely occurred between AD 1321 and pre 1901.ca. 1960. Pre-CES liquefaction in Kaiapoi likely formed during three separate episodes: post-1458 and possibly during the 1901 Cheviot earthquake, post-1297 and pre-1901, and pre 1458.

Combining the back-calculation approach with the PGA and $PGA_{7.5}$ derived from the Bradley (2013) GMPE proves effective in determining active faults capable of triggering liquefaction at the study sites, and are thus capable of triggering liquefaction in the future. Many active faults within 50 km of the study sites have the potential to trigger widespread liquefaction within eastern Canterbury and may have formed the pre-CES features. Additionally, many faults have the potential to trigger minor to moderate liquefaction in both Avondale and Kaiapoi. The GMPE also proves effective in evaluating the liquefaction potential of historic earthquakes. The 1869 Christchurch earthquake is the only well documented historical event to produce modelled ground motions in excess of the local and global liquefaction triggering thresholds indicating that liquefaction may have been triggered during this event. The 1717 Alpine Fault rupture falls within the age ranges constrained for the pre-CES features in Avonside and Avondale, and for the pre-CES sand-blister in Kaiapoi and therefore provides an additional potential seismic source for the pre-CES features exposed in eastern Canterbury.

The distribution of surficial liquefaction features and liquefaction-induced ground displacements within Avonside were influenced by geomorphic, sedimentologic, and topographic variability during the September 2010 and February 2011 earthquakes. Horizontal displacements are also shown to be strongly influenced by the thickness and continuity of the liquefiable layer proximal to the river rather than site-specific variability. High densities of liquefaction features and horizontal ground displacements occurred where the river bank is underlain by point-bar deposits, while lower horizontal displacements occurred where the river-bank comprises over-bank silts with interbedded sands. Liquefaction ejecta predominantly occurred in paleo-channels distal to the river. Sedimentologic and geomorphic variability is not currently incorporated into engineering-based assessments of liquefaction and lateral spreading hazards and may improve the predictive capacity of these models. This variability is also shown to directly correlate with building

foundation damage within the study area and thus highlights the importance of incorporating geomorphic mapping into liquefaction hazard assessments and loss modelling.

6.1 Implications for future work and potential applications

The work presented in this thesis includes the results of the some of the first paleo-liquefaction studies to be conducted within eastern Canterbury and New Zealand and is limited to seven study sites across eastern Canterbury. As a result there is a lot of scope for future work to expand and build upon the initial conclusions presented within this thesis. The paleo-liquefaction features presented in this thesis are not temporally constrained to the resolution required to discriminate between possible causative earthquakes. Additional paleo-liquefaction studies across the Christchurch region are required to further constrain the timing of the pre-historic earthquakes forming the paleo-liquefaction features, and the size of the associated liquefaction field. This would require trenching at many additional sites across the Canterbury region and is beyond the scope of this thesis.

The preservation of the CES and pre-CES liquefaction features within the subsurface indicates that liquefaction features may be used to approximate return times of strong-ground motions triggering liquefaction within the Christchurch area. The widespread liquefaction across eastern Canterbury during the CES is likely to be preserved within the subsurface sediments. It is anticipated that the paleo-liquefaction studies presented in Chapters 2 and 3 may highlight the potential applications of paleo-liquefaction studies as an alternative tool for assessing seismic hazards within New Zealand. Paleo-liquefaction studies may also provide a method to ground-truth the results of geotechnical testing to determine whether pre-historic evidence of liquefaction is present in areas where standard geotechnical methods may over or under-predict liquefaction hazards.

The research presented in Chapters 2 and 3 has gained widespread interest from civil engineers and local councils who recognise the limitations of geotechnical testing however want to best understand the hazard posed to local communities and determine whether land-use is unnecessarily restricted in some areas. This work has been presented at many local and international conferences, including

the NZGS conference where it won best paper/ talk by a young geotechnical professional. The award reflected that this work presents a new idea to the problem of assessing liquefaction triggering and seismic hazards, and has subsequently resulted in many national and international collaborations.

The work presented in Chapter 5 presents a pilot study on the geomorphic influences on the surface manifestation of liquefaction and associated ground displacements and is confined to the Avonside study area. The suburb of Avonside provided an excellent study area due to the geomorphic and topographic variability across the area and the abundance of observational data throughout the CES. Further work is required to expand this study across the wider Canterbury region to determine whether these strong correlations exist across wider geomorphic areas.

This work highlights the need for improved links between engineering and geology. Current engineering based liquefaction assessments utilise site-specific techniques that do not account for geomorphic variability. The content presented in Chapter 2 was presented at the 6ICEGE conference where it gained a lot of interest from engineers who have started to realise importance of geomorphology and depositional setting to the liquefaction susceptibility of the subsurface deposits and resultant ground deformation patterns. It is anticipated that this work will lead to future collaborative research projects to further constrain the geomorphic influences on liquefaction.

Bibliography

Aitken, M. (1998). *Introduction to Optical Dating*. Oxford University Press, United Kingdom.

Ambraseys, N. (1988). Engineering Seismology Part 1. *Earthquake Engineering and Structural Dynamics*, 17(1):1–50.

Barnes, P., Castellazzi, C., Gorman, A., and Wilcox, S. (2011). *Submarine Faulting Beneath Pegasus Bay, Offshore Christchurch*. National Institute of Water and Atmospheric Research Ltd (NIWA), Report WLG2011-28, p. 46., Wellington, New Zealand.

Bartlett, S. and Youd, T. (1995). Empirical prediction of liquefaction induced lateral spread. *Journal of Geotechnical Engineering*, 121(4):316–329.

Bastin, S., Bassett, K., Quigley, M., B, M., Green, R., Bradley, B., and Jacobson, D. (2016). Late Holocene liquefaction at sites of contemporary liquefaction during the 2010-2011 Canterbury earthquake sequence, New Zealand.

Bastin, S., Quigley, M., and Bassett, K. (2015a). *Comparison of liquefaction-induced land damage and geomorphic variability in Avonside, New Zealand*. Proceedings 6th International Conference of Earthquake Geotechnical Engineering, Christchurch, New Zealand.

Bastin, S., Quigley, M., and Bassett, K. (2015b). Paleo-liquefaction in Christchurch, New Zealand. *GSA Bulletin*, 127(9-10):1348–1365.

Bastin, S. H., Quigley, M., Bassett, K., and Green, R. (2013a). Characterisation of modern and paleo-liquefaction features in eastern Christchurch, NZ, following the 2010-2011 Canterbury earthquake sequence. *NZ Geomechanics News*, 26:38–46.

Bastin, S. H., Quigley, M., Bassett, K., and Green, R. (2013b). *Characterisation of modern and paleo-liquefaction features in eastern Christchurch, NZ, following the 2010-2011 Canterbury earthquake sequence.* Proceedings 19th NZGS Geotechnical Symposium, Queenstown, New Zealand.

Beavan, J., Motagh, M., Fielding, E., Donnelly, N., and Collett, D. (2012). Fault slip models of the 2010-2011 Canterbury, New Zealand, earthquakes from geodetic data and observations of post-seismic ground deformation. *New Zealand Journal of Geology and Geophysics*, 55(3):207–221.

Beca (2000). *Liquefaction Study, Report prepared for Waimakariri District Council and Environment Canterbury.* Beca Carter Hollings & Ferner Ltd, Christchurch, New Zealand.

Berrill, J., Mulqueen, P., and Ooi, E. (1994). Liquefaction at Kaiapoi in the 1901 Cheviot, New Zealand, Earthquake. *Bulletin of the New Zealand National Society for Earthquake Engineering*, 24(3):178–189.

Boulanger, R. and Idriss, I. (2014). *CPT and SPT based liquefaction triggering procedures, Report No. UCD/CGM-14/01.* Center for Geotechnical Modeling, Department of Civil and Environmental Engineering, University of California Davis, California.

Bowen, H., Jacka, M., van Ballegooy, S., and Sinclair, T. (2012). *Lateral spreading in the Canterbury earthquake - observations and empirical prediction methods.* Proceedings, 15th World Conferences on Earthquake Engineering (WCEE), Lisboa, Portugal.

Bradley, B. (2013). A New Zealand-specific pseudospectral acceleration ground-motion prediction equation for active shallow crustal earthquakes based on foreign models. *Bulletin of the Seismological Society of America*, 103(3):1801–1822.

Bradley, B., Quigley, M., van Dissen, R., and Litchfield, N. (2014). Ground motion and seismic source aspects of the Canterbury earthquake sequence. *Earthquake Spectra*, 30(1):1–15.

Bremer, J. (1985). *Wool Scours of New Zealand Tales of the Early Industry: Christchurch, New Zealand.* New Zealand Woolscours Association Inc, New Zealand.

Brown, L. and Weeber, J. (1992). *Geology of the Christchurch Urban Area. Scale 1:25 000.* Institute of Geological and Nuclear Sciences geological map 1. 1 sheet + 105 p, Lower Hutt, New Zealand.

Castilla, R. and Audemard, R. (2007). Sand blows as a potential tool for magnitude estimation of pre-instrumental earthquakes. *Journal of Seismology*, 11:473–387.

Chiou, B. and Youngs, R. R. (2008). An NGA model for the average horizontal component of peak ground motion and response spectra. *Earthquake Spectra*, 24:173–215.

Christchurch Engineering Lifelines Group (1997). *Risks and Realities: A multi-disciplinary approach to the vulnerability of lifelines to natural hazards.* Report of the Christchurch Engineering Lifelines Group. Centre for Advanced Engineering, Christchurch, New Zealand.

Christensen, S. A. (1994). *Liquefaction of cohesionless soils in the March 2, 1987 Edgecombe Earthquake, Bay of Plenty, New Zealand and other earthquakes.* Unpublished MSc thesis. University of Canterbury, Christchurch, New Zealand.

Clough, B. (2005). *Christchurch Liquefaction Study Stage IV.* Environment Canterbury report U04/25/2, Beca, Carter, Hollings and Ferner Ltd, Christchurch, New Zealand.

Counts, R. and Obermeier, S. (2012). Subtle seismic signatures: Using small-scale features and ground fractures as indicators of paleoseismicity in Cox, R.T., Tuttle, M.P., Boyd, O., Locat, J., (eds)., Recent advances in North American paleoseismology and neotectonics east of the Rockies. *Geological Society of America Special Paper*, 493:203–219.

Cowan, H. (1991). The North Canterbury earthquake of September 1, 1888. *Journal of the Royal Society of New Zealand*, 21:1–12.

Cowie, C. A. (1957). *Floods in New Zealand 1920-1953, with notes on some earlier floods.* The Soil Conservation and Rivers Control Council, Wellington, New Zealand.

Cox, R., Hill, A., Larsen, D., Holzer, T., Forman, S., Noce, T., Gardner, C., and Morat, J. (2007). Seismotectonic implications of sand blows in the southern Mississippi embayment. *Engineering Geolology*, 89(3-4):278–299.

Cox, S., Rutter, H., Sims, A., Manga, M., Weir, J., Ezzy, T., White, P., Horton, T., and Scott, D. (2012). Hydrological effects of the Mw 7.1 Darfield (Canterbury) earthquake, 4 September 2010. *New Zealand Journal of Geology and Geophysics*, 55(3):231–247.

Cubrinovski, M., Bray, J., M., T., Giorgini, S., Bradley, B., Wotherspoon, L., and Zupan, J. (2011). Soil liquefaction effects in the central business district during the February 2011 Christchurch Earthquake. *Seismological Research Letters*, 82(6):893–904.

Cubrinovski, M. and Green, R. (2010). Geotechnical reconnaissance of the 2010 Darfield (Canterbury) earthquake (contributing authors: Allen, J., Ashford, S., Bowman, E., Bradley, B., Cox, B., Cubrinovski, M., Green, R., Hutchinson, T., Kavazanjian, E., Orense, R., Pender, M., Quigley, M., Wotherspoon, L. *Bulletin of the New Zealand Society for Earthquake Engineering*, 43(4):243–320.

Cubrinovski, M. and Robinson, K. (2015). *Lateral spreading: observations and interpretation from the 2010- 2011 Christchurch earthquakes*. Proceedings 6th International Conference of Earthquake Geotechnical Engineering, Christchurch, New Zealand.

Cubrinovski, M., Robinson, K., Taylor, M., Hughes, M., and Orense, R. (2012). Lateral spreading and its impacts in urban areas in the 2010-2011 Christchurch earthquakes. *New Zealand Journal of Geology and Geophysics*, 55(4):255–269.

Deterling, O. (2015). *Factors influencing the lateral spread displacements from the 2011 Christchurch, New Zealand earthquake*. M.Sc. in Engineering Thesis, University of Texas at Austin, United States of America.

Doser, D., Webb, T., and Mauder, D. (1999). Source parameters of large historical (1918-1962) earthquakes, South Island, New Zealand. *Geophysical Journal International*, 139(3):769–794.

Downes, G. and Yetton, M. (2012). Pre-2010 historical seismicity near Christchurch, New Zealand: The 1869 Mw 4.7-4.9 Christchurch and 1870 Mw 5.6-5.8 Lake Ellesmere earthquakes. *New Zealand Journal of Geology and Geophysics*, 55(3):199–205.

Duffy, B., Quigley, M., Barrell, D., Dissen, R. V., Stahl, T., Leprince, S., McInnes, C., and Bilderback, E. (2013). Fault kinematics and surface deformation across

a releasing bend during the 2010 MW 7.1 Darfield, New Zealand, earthquake revealed by differential LiDAR and cadastral surveying. *Geological Society of America Bulletin*, 125(3-4):420–431.

Elder, D., McCahon, I., and Yetton, M. (1991). *The earthquake hazard in Christchurch: a detailed evaluation*. Christchurch, New Zealand, Research report to the EQC: Soils and Foundations Ltd.

Fairless, J. and Berrill, J. (1984). Liquefaction during historic earthquakes in New Zealand. *Bulletin of the New Zealand Society for Earthquake Engineering*, 17(4):280–291.

Forsyth, P., Barrell, D., and Jongens, R. (2008). *Geology of the Christchurch area: scale 1:250,000*. Institute of Geological and Nuclear Sciences, 1:250,000 geological map 16. 67 p. + 1 folded map, Lower Hutt, New Zealand.

Fryirs, K. and Brierley, G. (2012). *Geomorphic analysis of river systems: an approach to reading the landscape*. John Wiley & Sons, United Kingdom.

Galli, P. (2000). New empirical relationships between magnitude and distance for liquefaction. *Tectonophysics*, 324:169–187.

Ghinassi, M., Billi, P., Libsekal, Y., and Rook, M. P. L. (2013). Inferring fluvial morphodynamics and overbank flow control from 3D outcrop sections of a Pleistocene point bar, Dandiero Basin, Eritrea. *Journal of Sedimentary Research*, 83(12):1066–1084.

Green, R., Obermeier, S., and Olsond, S. (2005). Engineering geologic and geotechnical analysis of paleoseismic shaking using liquefaction effects: field examples. *Engineering Geology*, 76:263–293.

Griffiths, G. (1979). Recent sedimentation history of the Waimakariri river, New Zealand. *Journal of Hydrology*, 18:6–28.

Hawkins, D. (1957). *Beyond the Waimakariri: A regional history*. Whitcombe and Tombs, Christchurch, New Zealand.

Hayati, H. and Andrus, R. (2009). Updated liquefaction resistance correction factors of aged sands. *Journal of Geotechnical and Geoenvironmental Engineering*, 135(11):1683–1692.

Hjulstrm, F. (1939). Transportation of detritus by moving water: Part 1. Transportation. *Special Volume 10: Recent Marine Sediments*, 4:5–31.

Hooke, J. (2004). Cutoffs galore!: occurrence and causes of multiple cutoffs on a meandering river. *Geomorphology*, 61(3):225–238.

Hornblow, S., Quigley, M., Nicol, A., van Dissen, R., and Wang, N. (2014). Paleoseismology of the 2010 Mw 7.1 Darfield (Canterbury) earthquake source, Greendale Fault, New Zealand. *Tectonophysics*, 637:178–190.

Howard, M., Nicol, A., Campbell, J., and Pettinga, J. (2005). Holocene paleoearthquakes on the strike-slip Porters Pass fault, Canterbury, New Zealand. *Journal of Geology and Geophysics*, 48(1):59–74.

Hughes, M., Quigley, M., van Ballegooy, S., Deam, B., Bradley, B., and Hart, D. (2015). The sinking city: Earthquakes increase flood hazard in Christchurch, New Zealand. *GSA Today*, 25(3):4–10.

Idriss, I. and Boulanger, R. (2008). *Soil Liquefaction during Earthquakes*. Monograph Series: Earthquake Engineering Research Institute, Oakland, California.

Ishihara, K. (1985). Stability of natural deposits during earthquakes. *Proceedings 11th International Conference on soil mechanics and foundation engineering, San Francisco*, 1:321–376.

Iwasaki, T., Tatsuoka, F., Tokida, K., and Yasuda, S. (1978). *A practical method for assessing soil liquefaction potential based on case studies at various sites in Japan*. Proc., 2nd Int. Conf. on Microzonation, National Science Foundation, Washington, D.C.

Lees, J., van Ballegooy, S., and Wentz, F. (2015). *Liquefaction Susceptibility and Fines Content Correlations of the Christchurch Soils*. 6th International Conference on Earthquake Geotechnical Engineering, Christchurch.

Leprince, S., Barbot, S., Ayoub, F., and Avouac, J. (2007). Automatic and precise ortho-rectification, co-registration, and subpixel correlation of satellite images, application to ground deformation measurements. *IEEE Transactions on Geoscience and Remote Sensing*, 45(6):1529–1558.

Litchfield, N., Dissen, R. V., Sutherland, R., Barnes, P., Cox, S., Norris, R., Beavan, R., Langridge, R., Villamor, P., Stirling, K. B. M., Nicol, A., Nodder,

S., Lamarche, G., Barrell, D., Pettinga, J., Little, T., Pondard, N., Mountjoy, J., and Clark, K. (2014). A model of active faulting in New Zealand. *New Zealand Journal of Geology and Geophysics*, 57(1):32–56.

Loope, D., Elder, J., Zlotnik, V., Kettler, R., and Pederson, D. (2013). Jurassic earthquake sequence recorded by multiple generations of sand blows, Zion National Park, Utah. *Geology*, 41(10):1127–1134.

Lunina, O. and Gladkov, A. (2015). Seismically induced clastic dikes as a potential approach for the estimation of the lower-bound magnitude/ intensity of paleoearthquakes. *Engineering Geology*, 195:206–213.

Lunne, T., Robertson, P. K., and Powell, J. (2014). *Cone Penetration Testing in Geotechnical Practice*. Taylor & Francis Group, United States.

Madabhushi, S., Saito, K., and Booth, E. (2013). EEFIT mission to Haiti following the 12th January 2010 earthquake. *Bulletin Earthquake Engineering*, 11:35–68.

Martin, J. and Rathje, E. (2014). *Lateral spread deformations from the 2011 Christchurch, New Zealand earthquake measured from Satellite images and optical image correlation*. Proceedings, Tenth U.S. National Conference on Earthquake Engineering Frontiers of Earthquake Engineering, Anchorage, Alaska.

Maurer, B., Green, R., Cubrinovski, M., and Bradley, B. (2014). Evaluation of the Liquefaction Potential index for assessing liquefaction hazard in Christchurch, New Zealand. *Journal of Geotechnical and Geoenvironmental Engineering*, 140(7):04014032–1–11.

Maurer, B., Green, R., Quigley, M., and Bastin, S. (2015). Development of magnitude-bound relations for paleoliquefaction analyses: New Zealand Case Study. *Engineering Geology*, 197:253–266.

McCormac, F., Hogg, A., Blackwell, P., Buck, C., Higham, T., and Reimer, P. (2004). SHCAL04 Southern Hemisphere Calibration, 0-11.0 Cal kyr BP. *Radiocarbon*, 46(3):1087–1092.

Ministry of Health (2011). *Liquefaction dust risk rated low*. Ministry of Health, New Zealand.

Montenat, C., Barrier, P., dEstevou, P., and Hibsch, C. (2007). Seismites: An attempt at critical analysis and classification. *Sedimentary Geology*, 196:5–30.

Moss, R., Seed, R., Kayen, R., Stewart, J., Der-Kiureghian, A., and Cetin, K. (2006). CPT-Based probabilistic and deterministic assessment of in situ seismic soil liquefaction potential. *Journal of Geotechnical and Geoenvironmental Engineering*, 132(8):1032–1051.

Norrish, K. and Hutton, J. (1969). An accurate X-ray spectrographic method for the analysis of a wide range of geological samples. *Geochimica et Cosmochimica Acta*, 33.

NZGS (2013). *Geotechnical earthquake engineering practice Module 1 Guideline for the identification, assessment and mitigation of liquefaction hazards*. New Zealand Geotechnical Society, Wellington, New Zealand.

NZS.1170.5 (2004). *Structural Design Actions Part 5: Earthquake Actions*. Standard New Zealand, Wellington, New Zealand.

NZTA (2013). *Bridge manual (SP/M/022) third edition*. New Zealand Transport Authority, Wellington, New Zealand.

Obermeier, S. (1996). Use of liquefaction-induced features for paleoseismic analysis - an overview of how seismic liquefaction features can be distinguished from other features and how their regional distribution and properties of source sediment can be used to infer the location and strength of Holocene paleo-earthquakes. *Engineering Geology*, 44:1–76.

Obermeier, S. (1998). Liquefaction evidence for strong earthquakes of Holocene and latest Pleistocene ages in the states of Indiana and Illinois, USA. *Engineering Geolology*, 50:227–254.

Obermeier, S., Bleuer, N., Munson, C., Munson, P., Martin, W., McWilliams, K., Tabaczynski, D., Odum, J., Rubin, M., and Eggart, D. (1991). Evidence of strong earthquake shaking in the lower Wabash Valley from prehistoric liquefaction features. *Science*, 251:1061–1063.

Obermeier, S., Olson, S., and Green, R. (2005). Field occurrences of liquefaction-induced features: A primer for engineering geologic analysis of paleoseismic shaking. *Engineering Geology*, 76:209–234.

Obermeier, S. F., Pond, E. C., Olson, S. M., Green, R. A., Stark, T. D., and Mitchell, J. K. (2001). *Paleoliquefaction Studies in Continential Settings: Geologic and Geotechnical Factors in Interpretations and Back-Analysis*. US Geological Survey Open-File Report 01-29, United States of America.

Olson, S., Green, R., and Obermeier, S. (2005). Revised magnitude bound relation for the Wabash Valley Seismic Zone of the central United States. *Seismological Research Letters*, 76(6):756–771.

Orense, R. (2011). *Soil liquefaction during the 2010 Darfield and 1990 Luzon Earthquakes: A comparative study*. Proceedings of the Ninth Pacific Conference on Earthquake Engineering Building an Earthquake-Resilient Society 14-16 April, 2011, Auckland, New Zealand.

Owen, G., Moretti, M., and Alfaro, P. (2011). Recognising triggers for soft-sediment deformation: Current understanding and future directions. *Sedimentary Geology*, 235:133–140.

Papathanassiou, G., Pavlides, S., Christaras, B., and Pitilakis, K. (2005). Liquefaction case histories and empirical relations of earthquake magnitude versus distance from the broader Aegean region. *Journal of Geodynamics*, 40(2-3):257–278.

Parker, M. and Steenkamp, D. (2012). The economic impact of the Canterbury earthquakes. *Reserve Bank of New Zealand Bulletin*, 75(3):13–25.

Pettinga, J., Yetton, M., Dissen, R. V., and Downes, G. (2001). Earthquake source identification and characteristics for the Canterbury region, South Island, New Zealand. *Bulletin of the New Zealand Society for Earthquake Engineering*, 34(4):282–317.

Pirrotta, C., Barbano, M., Guarnieri, P., and Gerardi, F. (2007). A new dataset and empirical relationships between magnitude/intensity and epicentral distance for liquefaction in central-eastern Sicily. *Annals of Geophysics*, 50(6):763–774.

Quigley, M., Bastin, S., and Bradley, B. (2013). Recurrent liquefaction in Christchurch, New Zealand, during the Canterbury earthquake sequence. *Geology*, 41(4):419–422.

Quigley, M., Hughes, M., Bradley, B., van Ballegooy, S., Reid, C., Morgenroth, J., Horton, T., Duffy, B., and Pettinga, J. (2016). The 2010-2011 Canterbury

earthquake sequence: Environmental effects, seismic triggering thresholds and geologic legacy.

Reid, C., Thompson, N., Irvine, J., and Laird, T. (2012). Sand volcanoes in the Avon-Heathcote estuary produced by the 2010-2011 Christchurch earthquakes: Implications for geological preservation and expression. *New Zealand Journal of Geology and Geophysics*, 55(3):249–254.

Ristau, J. (2009). Comparison of magnitude estimates for New Zealand earthquakes: Moment magnitude, local magnitude, and teleseismic body-wave magnitude. *Bulletin of the Seismological Society of America*, 99(3):1841–1852.

Robertson, P. and Wride, C. (1998). Evaluating cyclic liquefaction potential using the cone penetration test. *Canadian Geotechnical Journal, Ottawa*, 35(3):442–459.

Robinson, K., Cubrinovski, M., and Bradley, B. (2013). *Sensitivity of predicted liquefaction-induced lateral spreading displacements from the 2010 Darfield and 2011 Christchurch earthquakes.* Proceedings 19th NZGS Geotechnical Symposium, Queenstown, New Zealand.

Rogers, N., van Ballegooy, S., Williams, K., and Johnson, L. (2015). *Considering Post-Disaster Damage to Residential Building Construction - Is Our Modern Building Construction Resilient?* Proceedings 6th International Conference of Earthquake Geotechnical Engineering, Christchurch, New Zealand.

Russell, J., van Ballegooy, S., Torvelainen, E., and Gulley, R. (2015). *Consideration of ground variability over an area of geological similarity as part of liquefaction assessment for foundation design.* Proceedings 6th International Conference of Earthquake Geotechnical Engineering, Christchurch, New Zealand.

Santucci de Magistris, F., Lanzano, G., Forte, G., and Fabbrocino, G. (2013). A database for PGA threshold in liquefaction occurrence. *Soil Dynamics and Earthquake Engineering*, 54:17–19.

Scherbaum, F., Schmedes, J., and Cotton, F. (2004). On the conversion of source-to-site distance measures for extended earthquake source models. *Bulletin of the Seismological Society of America*, 94(3):1053–1069.

Seed, H. and Idriss, I. (1982). *Ground Motions and Soil Liquefaction during Earthquakes*. Monograph Series: Earthquake Engineering Research Institute, Berkeley, California, United States of America.

Silby, K. (1856). *Christchurch area showing waterways swamps and vegetation*. Christchurch Drainage board, Christchurch, New Zealand.

Sims, J. (1975). Determining earthquake recurrence intervals from deformational structures in young lacustrine sediment. *Tectonophysics*, 29:141–152.

Sims, J. and Garvin, C. (1995). Recurrent liquefaction induced by the 1989 Loma Prieta earthquake and 1990 and 1991 aftershocks: Implications for paleoseismicity studies. *Bulletin of the Seismological Society of America*, 85(I):51–65.

Sonmez, B., Ulusay, R., and Sonmez, H. (2008). A study on the identification of liquefaction-induced failures on ground surface based on the data from the 1999 Kocaeli and Chi-Chi earthquakes. *Engineering Geology*, 97:112–125.

Stirling, M., Gerstenberger, M., Litchfield, N., McVerry, G., Smith, W., Pettinga, J., and Barnes, P. (2008). Seismic hazard of the Canterbury region, New Zealand: New earthquake source model and methodology. *Bulletin of the New Zealand Society for Earthquake Engineering*, 41(2):51–67.

Stirling, M., McVerry, G., Gerstenberger, M., Litchfield, N., Dissen, R. V., Berryman, K., Barnes, P., Wallace, L., Villamor, P., Langridge, R., Lamarche, G., Nodder, S., Reyners, M., Bradley, B., Rhoades, D., Smith, W., Nicol, A., Pettinga, J., Clark, K., and Jacobs, K. (2012). National seismic hazard model for New Zealand: 2010 update. *Bulletin of the Seismological Society of America*, 102(4):1514–1542.

Stirling, M., Yetton, M., Pettinga, J., Berryman, K., and Downes, G. (1999). *Probabilistic Seismic Hazard Assessment and Earthquake Scenarios for the Canterbury Region, and Historic Earthquakes in Christchurch. Stage 1 (Part B) of Canterbury Regional Councils Earthquake Hazard and Risk Assessment Study*. Institute of Geological and Nuclear Sciences Client Report 1999/53, GNS Science, 14 p., Lower Hutt, New Zealand.

Storti, F. and Balsamo, F. (2010). Particle size distributions by laser diffraction: sensitivity of granular matter strength to analytical operating procedures. *Solid Earth*, 1:25–48.

Stringer, M., Beyzaei, C., Cubrinovski, M., Bray, J., Riemer, M., Jacka, M., and Wentz, F. (2015). *Liquefaction Characteristics of Christchurch Silty Soils: Gainsborough Reserve*. Proceedings 6th International Conference of Earthquake Geotechnical Engineering, Christchurch, New Zealand.

Sutherland, R., Eberhart-Phillips, D., Harris, R., Stern, T., Beavan, R., Ellis, S., Henrys, S., Cox, S., Norris, R., Berryman, K., Townend, J., Bannister, S., Pettinga, J., Leitner, B., Wallace, L., Little, T., Cooper, A., Yetton, M., and Stirling, M. (2007). Do great earthquakes occur on the Alpine fault in central South Island, New Zealand?, in Okaya, D.A., Stern, T.A., and Davey, F.J., eds., A Continental Plate Boundary: Tectonics at South Island, New Zealand. *American Geophysical Union Geophysical Monograph*, 175:235–251.

Tonkin and Taylor (2011). *Christchurch Earthquake Recovery Geotechnical Factual Report*. Report prepared for Earthquake Commission, New Zealand.

Tonkin and Taylor (2013a). *Liquefaction Evaluation of CPT Investigations (Technical specification 01)*. Canterbury Geotechnical Database, Christchurch, New Zealand.

Tonkin and Taylor (2013b). *Liquefaction Vulnerability Study*. Report prepared for Earthquake Commission, New Zealand.

Tonkin and Taylor (2015). *Canterbury Earthquake Sequence: Increased Liquefaction Vulnerability Assessment Methodology*. Report to Chapman Tripp on behalf of the Earthquake Commission, New Zealand.

Toonen, W., Kleinhans, M., and Cohen, K. (2012). Sedimentary architecture of abandoned channel fills. *Earth surface processes and landforms*, 37(4):459–472.

Tuttle, M. (2001). The use of liquefaction features in paleoseismology: lessons learnt in the New Madrid Seismic Zone, Central United States. *Journal of Seismology*, 5:361–380.

Tuttle, M., Al-Shukri, H., and Mahdi, H. (2006). Very large earthquakes centered southwest of the New Madrid seismic zone 5,000-7,000 years ago. *Seismological Research Letters*, 77(6):755–770.

Tuttle, M. and Atkinson, G. (2010). Localization of large earthquakes in the Charlevoix seismic zone, Quebec, Canada, during the past 10,000 years. *Seismological Research Letters*, 81(1):140–147.

Tuttle, M. and Barstow, N. (1996). Liquefaction-related ground failure: A case study in the New Madrid Seismic Zone, Central United States. *Bulletin of the Seismological Society of America*, 86(3):636–645.

Tuttle, M. and Hartleb, R. (2012). *CEUS Paleo-liquefaction Database, Uncertainties Associated with Paleo-liquefaction Data, and Guidance for Seismic Source Characterization: Central and Eastern United States Seismic Source Characterization for Nuclear Facilities, Appendix E. NUREG-2115, Volume 5: Appendices C to F.* U.S. Department of Energy (DOE), U.S. Nuclear Regulatory Commission (NRC), and Electric Power Research Institute (EPRI), Palo Alto, California. Accession No. ML12048A859, United States of America.

Tuttle, M., Schweig, E., Sims, J., Lafferty, R., Wolf, L., and Haynes, M. (2002). The earthquake potential of the New Madrid Seismic Zone. *Bulletin of the Seismological Society of America*, 92(6):2080–2089.

van Ballegooy, S., Berryman, K., Deam, B., and Jacka, M. (2014a). Repeated major episodes of tectonic deformation, lateral spread and liquefaction in Christchurch during the Canterbury earthquake sequence of 2010-2011. *Engineering Geology for Society and Territory*, 5:1043–1049.

van Ballegooy, S., Malan, P., Lacrosse, V., Jacka, M., Cubrinovski, M., Bray, J., O'Rourke, T., Crawford, S., and Cowan, H. (2014b). Assessment of liquefaction-induced land damage for residential Christchurch. *Earthquake Spectra*, 30:31–55.

van Breemen, N. and Buurman, P. (2002). *Soil Formation, Second Edition.* Kluwer Academic Publishers, The Netherlands.

van Dissen, R., McSaveney, M., Townsend, D., Hancox, G., Little, T., Ries, W., Perrin, N., Archibald, G., Dellow, G., Massey, C., and Misra, S. (2013). Landslides and liquefaction generated by the Cook Strait and Lake Grassmere earthquakes: A reconnaissance report. *Bulletin of the New Zealand Society for Earthquake Engineering*, 46(4):196–200.

Villamor, P., Almond, P., Tuttle, M., Giona-Bucci, M., Langridge, R., Clark, K., Ries, W., Bastin, S., Eger, A., Vandergoes, M., Quigley, M., Barker, P., Martin, F., and Howarth, J. (2016). Liquefaction features produced by the 2010-2011 Canterbury earthquake sequence in southwest Christchurch, New Zealand and preliminary assessment of paleoliquefaction features. In review at Bulletin of the Seismological Society of America.

Villemure, M. (2013). *Fine grained sediment clean-up in a modern urban environment*. M.Sc thesis, University of Canterbury, Christchurch, New Zealand.

Willis, B. and Tang, H. (2010). Three-dimensional connectivity of point-bar deposits. *Journal of Sedimentary Research*, 80(5):440–454.

Wilson, J. (1989). *Christchurch swamp to city: a short history of the Christchurch Drainage Board 1875-1989*. Christchurch Drainage Board, Christchurch, New Zealand.

Wood, P. (1993). *Kaiapoi: A Search for Identity*. Waimakariri District Council, Rangiora, New Zealand.

Wotherspoon, L., Pender, M., and Orense, R. (2011). Relationship between observed at Kaiapoi following the 2010 Darfield earthquake and former channels of the Waimakariri river. *Engineering Geology*, 125(27):45–55.

Yenier, E., Erdoan, O., and Akkar, S. (2008). *Empirical relationships for magnitude and source-to-ite distance conversions using recently compiled Turkish strong-ground motion database*. The 14_{th} World Conference on Earthquake Engineering October 12-17, 2008, Beijing, China.

Youd, T., Hansen, C., and Bartlett, S. (2002). Revised multilinear regression equations for prediction of lateral spread displacement. 128(12):1007–1017.

Youd, T. and Hoose, S. (1977). *Liquefaction Susceptibility and Geological Setting*. Proc., 6th World Conference on Earthquake Engineering, Vol. 3, Prentice-Hall, Englewood Cliffs, N.J., 2189-2194, United States of America.

Youd, T., Idriss, I., Andrus, R., Arango, I., Castro, G., Christian, J., Dobry, R., Finn, W. L., Jr., L. H., Hynes, M., Ishihara, K., Koester, J., Liao, S., III, W. M., Martin, P., Mitchell, J., Moriwaki, Y., Power, M., Roberston, P., Seed, R., and II, K. S. (2001). Liquefaction Resistance of Soils: Summary Report from the 1996 NCEER and 1998 NCEER/NSF Workshops on Evaluation of Liquefaction Resistance of soils. *Journal of Geotechnical and Geoenvironmental Engineering*, 127:817–833.

Zhang, G., Robertson, P., and Brachman, R. (2004). Estimating liquefaction-induced lateral displacements using the standard penetration test or cone penetration test. *Journal of Geotechnical and Geoenvironmental Engineering*, 130:861–871.

Appendix A

Detailed Sediment Descriptions

TABLE A.1: Sedimentological descriptions of sediment units described in Chapter 2

Site	Unit	Thickness (cm)	Description
1	I	20-40	Dark brown, carbonaceous, bioturbated silt loam containing a discontinuous unit of pebbles, and fragments of brick and pottery at 20 cm depth.
1	IIa-e	100	Repeating normally graded beds, 20-40 cm thick, comprised of tan, moderately sorted, medium to very fine sand grading into silt with gradational contacts, and localised vertical bioturbation. Unit IIc contains localised lenses of tan, moderately sorted very fine sand to silt (Unit IIc').
1	III	2-5	Blue-grey, mottled, massive, plastic sandy silt
1	IV	40	Grey, moderately sorted, mottled, medium sand.
1	V	20	Tan, moderately sorted, mottled and oxidised fine to medium sand.
1	VI	60	Grey, moderately sorted, medium sand with granules that coarsen downward to pebbles
1	PF	20-100	Dark brown, massive, mottled silt loam. Contains irregular lenses 2-25 cm thick of massive, carbonaceous (5-10%) silt; oxidised whole and fragmented lamb fetlock bone; fern mats; and white, coarse sand to pebble sized fragments of spongy and compact bone.
2	VII	20-25	Dark brown, carbonaceous, bioturbated, silt to very fine sand containing discontinuous unit of pottery, glass and pebbles. Appears to be re-worked.
2	VIII	20-30	Dark brown, massive, carbonaceous, bioturbated, silt loam
2	IXa	20-60	Blue-grey, moderately sorted, bioturbated, mottled, and oxidised sandy silt
2	IXb	10-15	Tan, moderately sorted, mottled and oxidised silt to very fine sand with gradational and bioturbated contacts with IXa

TABLE A.2: Sediment descriptions of units described in Chapter 3

Site	Unit	Thickness (cm)	Description
3	A1	20-70	Poorly sorted, sub-rounded pebbles to granules in a fine sand to silt matrix with fragments of pipes and clasts of blue-grey fine to very fine sand.
4		5-22	Poorly sorted, sub-rounded grey pebbles to granules in silt matrix.
6		20-35	Poorly sorted, sub-rounded grey pebbles in silt to very fine sand matrix.
3	A2	25-50	Well sorted, dark brown, 5% carbonaceous, silt to very fine sand with interbedded grey, well sorted fine sand with 2% mottled.
3	A3	15-35	Poorly sorted, brown, silt to fine sand with granules and rare organics.
3	I	20-30	Well sorted, dark brown 5% carbonaceous, silt to very fine sand with modern rootlets and a bioturbated lower contact (Buried soil).
3	II	30-40	Moderately sorted, light brown silt to very fine sand with interbedded well sorted fine sand, 5- 10 % mottled, contains modern rootlets.
3	III	15-40	Moderately sorted, brown 2% carbonaceous fine to very fine sand 10% mottled with modern rootlets.
4	IV	25-40	Moderately sorted, brown, 20% carbonaceous, very fine sand to silt with silt clasts and bioturbated contacts (topsoil).
4	V	2-7	Well sorted, tan, bioturbated fine to very fine sand, with rare silt and carbonaceous silt clasts, 2% mottled.
4	VI	40-60	Moderately sorted, blue-grey silt with interbedded very fine sand, 5% mottled.
5	VII	15-25	Moderately sorted, 20% carbonaceous, dark brown very fine sand to silt with clasts of grey & carbonaceous silt, rare charcoal fragments, and modern rootlets.
5	VIII	55-75	Moderately sorted, light brown, 2% carbonaceous, very fine sand with rare silt clasts.
5	IX	2-5	Moderately sorted, 5% carbonaceous, tan fine to very fine sand with rare charcoal fragments.
5	X	10-15	Moderately sorted, blue grey, fine to very fine sand, 2% mottled, contains rare charcoal fragments.
5	XI	5-20	Well sorted, blue-grey, carbonaceous, very fine sand to silt, 5% mottled.
6	XII	45-50	Dark grey, well sorted silt to very fine sand, 5% mottled, with 10-15% charcoal.
6	XIII	35-65	Tan, well sorted, silt to very fine sand with interbedded fine sand, 10% mottled, with rare charcoal.
6	XIV	5-10	Tan-light grey, well sorted, silt to very fine sand with cross-laminations, 20% mottled.
6	XV	5-10	Tan, moderately sorted fine to very fine sand, 5% mottled.
6	XVI	2-5	Tan- light grey, well sorted fine to very fine sand with silt laminations, 10% mottled.
7	XVII	15-25	Grey, moderately sorted silt with rare granules, silt clasts, and brick fragments.
7	XVIII	15-35	Tan, moderately sorted, fine to very fine sand with rare silt and carbonaceous silt clasts, and granules, with interbedded fine sand with cross-laminations lined with siltstone clasts.
7	XVIII'	5-10	Grey, moderately sorted, sub-rounded granules to pebbles in fine sand matrix.
7	XIX	5-15	Tan, oxidised and mottled, moderately sorted fine to very fine sand grading to silt with cross-laminations and sub-rounded granule lag deposit along basal contact.
7	XX	5-10	Grey, mottled, moderately sorted fine to very fine sand with rare granules and silt and carbonaceous silt clasts.
7	XXI	5-20	Grey, oxidised and mottled, moderately sorted fine sand with cross-laminations and rare granules and silt clasts.
7	XXII	5-15	Buried soil - Grey, mottled, moderately sorted, silt to very fine sand with rare granules.
7	XXIII	30-40	Poorly sorted, mottled, fine to very fine sand with granules and silt clasts
7	XXVI	5-25	Well sorted silt to very fine sand with carbonaceous laminations

Appendix B

Modelled PGA of active faults in the wider Canterbury region

TABLE B.1: Modelled PGA and $PGA_{7.5}$ of known active faults within the wider Canterbury area

Fault ID	Fault Name	Mw Max	Avondale			Kaiapoi		
			R_{rup} (km)	PGA (g)	$PGA_{7.5}$	R_{rup} (km)	PGA (g)	$PGA_{7.5}$
1	Ashley	7.4	33	0.15	0.14	18	0.23	0.22
2	Ashley mouth	5.4	27	0.05	0.03	10	0.14	0.08
3	Ashley part	6.1	32	0.07	0.05	18	0.14	0.09
4	Cust	7.2	35	0.12	0.11	22	0.18	0.17
5	Offshore Fault III	6.3	49	0.05	0.04	35	0.08	0.06
6	Offshore Fault V	6.3	58	0.04	0.03	45	0.06	0.04
7	Offshore Fault V2	6.3	62	0.04	0.03	47	0.06	0.04
8	Offshore Fault VIII	6.1	69	0.03	0.02	58	0.04	0.02
9	Offshore Fault VII	6.3	69	0.03	0.03	57	0.04	0.03
10	Offshore Fault VI	6.4	62	0.04	0.03	50	0.06	0.04
11	Offshore Fault IV	6.9	43	0.10	0.08	32	0.13	0.11
12	Hororata	7.4	54	0.09	0.09	50	0.10	0.10
13	Kaiapoi offshore	6.4	13	0.21	0.16	5	0.34	0.26
14	Kaiapoi offshore2	6.3	49	0.05	0.04	22	0.13	0.09
15	Kaipoi total	6.8	13	0.24	0.20	5	0.37	0.31
16	Kaipoi total+Peg 4+4km	7	13	0.26	0.23	5	0.39	0.34
17	Kaiwara (North)	7	89	0.04	0.04	77	0.05	0.05
18	Kaiwara (South)	7.3	62	0.08	0.07	46	0.10	0.10
19	Leithfield	6.8	42	0.09	0.08	25	0.15	0.12
20	Lyt heads 1	5.1	15	0.07	0.04	27	0.03	0.02
21	Lyt heads 2	5	20	0.04	0.02	35	0.02	0.01
22	Lyt heads 3	5	19	0.05	0.02	35	0.02	0.01
23	Lyt heads 4	4.6	13	0.05	0.02	25	0.02	0.01
24	Lyt heads 5	4.9	13	0.07	0.03	25	0.03	0.01
25	Motunaua	5.9	21	0.10	0.07	35	0.06	0.04
26	North Canterbury1	7	35	0.11	0.10	22	0.17	0.15
27	North Canterbury2	6.9	70	0.05	0.04	60	0.06	0.05
28	North Canterbury4	6.6	109	0.02	0.02	99	0.02	0.02
29	North Canterbury11	6.7	52	0.06	0.05	44	0.07	0.06
30	North Canterbury8	7.3	107	0.04	0.04	97	0.04	0.04
31	North Canterbury10	7	35	0.11	0.10	29	0.13	0.12
32	North Canterbury13	7.1	65	0.06	0.06	56	0.07	0.07
33	Omihi	6.7	51	0.06	0.05	36	0.09	0.08

34	Pegasus	7.2	22	0.18	0.17	9	0.32	0.29
35	Pegasus small	5.9	49	0.04	0.02	24	0.09	0.06
36	Pegasus pup	5.6	18	0.09	0.06	12	0.14	0.08
37	Pegasus 3	6.2	31	0.08	0.06	22	0.12	0.08
38	Pegasus 4	6.1	28	0.09	0.06	22	0.11	0.08
39	Pegasus 5	6.5	29	0.13	0.10	15	0.22	0.17
40	Pegasus 6b	6.4	21	0.14	0.11	15	0.19	0.14
41	Port hills	6.5	7	0.31	0.24	17	0.18	0.14
42	Porters to Grey	7.7	45	0.13	0.14	29	0.19	0.20
43	Springbank	7.2	32	0.13	0.12	18	0.21	0.20
44	Springfield	7.1	55	0.08	0.07	45	0.10	0.09
45	Waikuku	6.8	29	0.11	0.09	25	0.13	0.11
46	Awatere (SW)	7.6	170	0.03	0.03	224	0.02	0.02
47	Barefell Pass	7	146	0.02	0.02	131	0.02	0.02
48	Browning Pass	7	124	0.03	0.02	112	0.03	0.03
49	Brunner Anticline	7.4	156	0.03	0.03	146	0.03	0.03
50	Cheesman	7	87	0.04	0.04	81	0.04	0.04
51	Clarence (Central)	7.3	118	0.04	0.04	110	0.04	0.04
52	Clarence (SW)	7.5	125	0.04	0.04	97	0.06	0.06
53	Esk	7.1	72	0.06	0.05	55	0.08	0.07
54	Fidget	7	161	0.02	0.02	148	0.02	0.02
55	Fowlers	7.3	131	0.03	0.03	115	0.04	0.04
56	Fox (Peak	7.4	150	0.03	0.03	151	0.03	0.03
57	Hope (1888 Rupture)	7.2	106	0.04	0.04	88	0.05	0.05
58	Hope (Conway)	7.6	113	0.05	0.05	99	0.06	0.06
59	Hope (Central-west)	7.1	105	0.04	0.03	90	0.05	0.04
60	Hope (Taramakau)	7	106	0.03	0.03	91	0.04	0.04
61	Hundalee	7.4	103	0.05	0.05	91	0.06	0.06
62	Inangahua	7.3	184	0.02	0.02	168	0.02	0.02
63	Kakapo	7.2	104	0.04	0.04	84	0.05	0.05
64	Kelly	6.9	113	0.04	0.04	99	0.05	0.05
65	Lake Heron-Forest Ck	7.4	130	0.03	0.03	124	0.04	0.03
66	Lowry	7.3	69	0.07	0.07	53	0.10	0.09
67	Lyell	7.2	186	0.02	0.01	171	0.02	0.02
68	Maimai	7.3	172	0.02	0.02	158	0.02	0.02
69	Poulter	7.2	100	0.04	0.04	85	0.05	0.05
70	Torlesse	7.3	76	0.07	0.06	63	0.08	0.08
71	Waimea South	7.5	193	0.01	0.01	178	0.02	0.02
72	Waimea North	7.1	231	0.01	0.01	215	0.02	0.01

73	Waitohi	7.2	69	0.07	0.06	53	0.09	0.08
74	White Creek	8	174	0.03	0.04	158	0.04	0.05
75	Jordan-BKeke-Chancet	7.8	157	0.03	0.04	144	0.04	0.04
76	Jordan-Keke-Chancet	7.8	157	0.03	0.04	144	0.04	0.04
77	Paparoa Range front	7.6	183	0.02	0.02	169	0.03	0.03
78	Quartz Creek	6.5	133	0.01	0.01	135	0.01	0.01
79	Hutt-Peel	7.3	96	0.05	0.04	96	0.05	0.04
80	Ostler	7.6	215	0.02	0.02	217	0.02	0.02
81	Ahuriri	7.4	256	0.01	0.01	259	0.01	0.01
82	Irishman Creek	7.3	178	0.02	0.02	180	0.02	0.02
83	Hanmer	6.8	111	0.02	0.02	96	0.03	0.03
84	Otaraia	7.2	298	0.00	0.00	289	0.01	0.00
85	North Mernoo B0	7.3	158	0.02	0.02	156	0.02	0.02
86	North Mernoo B1	6.8	127	0.02	0.02	121	0.03	0.02
87	North Mernoo B2	7.3	127	0.04	0.04	121	0.04	0.04
88	North Mernoo 4646	7.2	140	0.03	0.03	137	0.03	0.03
89	North Mernoo E1	7.2	159	0.02	0.02	156	0.02	0.02
90	North Mernoo E2	7.1	153	0.02	0.02	148	0.02	0.02
91	North Mernoo F1	7	174	0.02	0.01	171	0.02	0.02
92	North Mernoo F2	7.1	183	0.02	0.01	179	0.02	0.02
93	North Mernoo 1818	7.2	117	0.04	0.03	109	0.04	0.04
94	North Mernoo K1	7.5	190	0.02	0.02	185	0.02	0.02
95	North Mernoo K2	7	241	0.01	0.01	238	0.01	0.01
96	North Mernoo M	7.3	195	0.02	0.02	190	0.02	0.02
97	Marlborough Slope 9	6.7	144	0.01	0.01	134	0.02	0.01
98	Marlborough Slope 4	7.5	142	0.03	0.03	133	0.04	0.04
99	Marlborough Slope 2	6.7	174	0.01	0.01	165	0.01	0.01
100	Marlborough Slope 1	7.2	139	0.02	0.02	131	0.03	0.03
101	UpperSlope offhsore	7.4	185	0.02	0.02	176	0.02	0.02
102	Albury	6.8	169	0.01	0.01	173	0.01	0.01
103	Brothers	7.1	164	0.02	0.02	168	0.02	0.02
104	Dalgety	6.9	180	0.01	0.01	185	0.01	0.01
105	Hunter	7.3	173	0.02	0.02	178	0.02	0.02
106	Kirkliston	7.5	192	0.02	0.02	198	0.02	0.02
107	Opawa	7	178	0.01	0.01	183	0.01	0.01
108	Wairau	7.6	214	0.02	0.02	199	0.03	0.03
109	Awatere (NE)	7.7	136	0.05	0.05	120	0.06	0.06
110	Clarence (NE)	7.8	131	0.05	0.05	117	0.06	0.06
111	Kekerengu-Campbell	7.6	183	0.03	0.03	171	0.03	0.03

112	Kekerengu-Chancet	7.3	213	0.02	0.02	190	0.02	0.02
113	Hope (Conway Offshore)	7.8	156	0.04	0.04	144	0.04	0.05
114	Kekerengu Bank	7.8	168	0.03	0.03	159	0.03	0.04
115	Te Rapa segment 1-2	7.2	228	0.01	0.01	218	0.01	0.01
116	Needles	7.3	213	0.02	0.01	202	0.02	0.02
117	Wairarapa-Nicholson	8.3	243	0.02	0.03	232	0.03	0.03
118	Wellington	7.6	272	0.01	0.01	261	0.01	0.01
119	Dry River-Huangarua	7.4	293	0.01	0.01	283	0.01	0.01
120	Boo Boo	7.7	248	0.01	0.01	237	0.01	0.02
121	Alpine (Fiord-Kelly)	8.3	144	0.06	0.07	130	0.07	0.09
122	Alpine (Kelly-Tophouse)	7.9	327	0.01	0.01	340	0.01	0.01
123	Hikurangi Wellington	9	244	0.05	0.07	233	0.05	0.08
124	Pisa	7.4	289	0.01	0.01	295	0.01	0.01
125	Nevis	7.7	345	0.00	0.00	351	0.00	0.00
126	Old Man	7.5	336	0.00	0.00	343	0.00	0.00
127	Lindis Peak	7.2	262	0.01	0.01	267	0.01	0.01
128	Grandview	7.2	296	0.00	0.00	300	0.00	0.00
129	Cardrona South	7.1	296	0.00	0.00	331	0.00	0.00
130	Cardrona North	7.2	326	0.00	0.00	301	0.00	0.00
131	Blue Lake	7.2	266	0.01	0.01	272	0.01	0.01
132	Dunstan	7.5	275	0.01	0.01	282	0.01	0.01
133	Raggedy	7.2	273	0.01	0.01	281	0.01	0.01
134	Ranfurly	6.7	265	0.00	0.00	274	0.00	0.00
135	Gimmerburn	7.4	265	0.01	0.01	273	0.01	0.01
136	Hyde	7.4	274	0.01	0.01	284	0.01	0.01
137	Billys Ridge	7.3	266	0.01	0.01	277	0.01	0.01
138	Taieri Ridge	7.3	263	0.01	0.01	274	0.01	0.01
139	Waipiata	7.6	265	0.01	0.01	274	0.01	0.01
140	Long Valley	6.9	305	0.00	0.00	314	0.00	0.00
141	Spylaw	7.4	361	0.00	0.00	371	0.00	0.00
142	Blue Mountain	7.4	344	0.00	0.00	354	0.00	0.00
143	Moonlight South	7.7	399	0.00	0.00	405	0.00	0.00
144	Moonlight North	7.7	332	0.01	0.01	336	0.01	0.01
145	Whitemans	7.1	299	0.00	0.00	289	0.00	0.00
146	Moonshine	7.2	309	0.00	0.00	296	0.00	0.00
147	Dryburgh	7	220	0.01	0.01	228	0.01	0.01
148	Otematata	6.7	241	0.01	0.00	248	0.00	0.00
149	Fern Gully	7.3	227	0.01	0.01	235	0.01	0.01
150	Waitangi	7	224	0.01	0.00	230	0.01	0.00

151	Wairau (Offshore)	7.5	266	0.01	0.01	254	0.01	0.01
152	Pukerua-Shepherds	7.4	292	0.01	0.01	288	0.01	0.01
153	Ohariu South	7.5	280	0.01	0.01	267	0.01	0.01
154	Akatarawa-Otaki Forks	7.6	329	0.01	0.01	318	0.01	0.01

Appendix C

Radiocarbon Results

TABLE C.1: Radiocarbon sample identification codes and ages

Laboratory code	Field code	Site	Sample number	Radiocarbon Age
NZA 51908	SP_T5_O3	Site 1	S5	$111_{\pm 14}$
NZA 51893	SP_T5_O4	Site 1	N/A	$1176_{\pm 17}$
NZA 51900	SP_T5_C10	Site 1	S4	$1364_{\pm 15}$
NZA 51903	SP_T5_S8	Site 1	S7	$2683_{\pm 16}$
NZA 52118	SP_T6_Ewall_S1	Site 1	S3	$813_{\pm 38}$
NZA 50573	BS_T4_S1	Site 2	S8	$545_{\pm 18}$
NZA 50575	BS_T4_S9	Site 1	S9	$606_{\pm 18}$
NZA 56669	KSR_S22	Site 7	R5	$777_{\pm 22}$
NZA 56524	SP_AP_S3	Site 1	S2	$220_{\pm 19}$
NZA 56503	SP_AP_S2	Site 1	S1	$4126_{\pm 25}$
NZA 56504	SP_AP_S1	Site 1	S6	$815_{\pm 20}$
NZA 56525	SP_T6_S1	Site 1	N/A	$950_{\pm 21}$
NZA 56505	SP_T4_S5	Site 1	N/A	$674_{\pm 20}$
NZA 56676	AD_T1_S2	Site 3	R1	$563_{\pm 45}$
NZA 56780	AD_T2_S1	Site 5	R2	$195_{\pm 20}$
NZA 56779	SP_AP_S2	Site 1	N/A	$4187_{\pm 22}$
NZA 53811	SB_SWS_N1	Site 6	N/A	$16452_{\pm 72}$
NZA 53812	SB_SWS_S30	Site 6	N/A	$14807_{\pm 60}$
NZA 53733	SB_KSR_S20	Site 7	R7	$703_{\pm 16}$
NZA 53715	SB_SWs_N2	Site 6	R4	$420_{\pm 16}$

RAFTER RADIOCARBON LABORATORY

R40131/1

INSTITUTE OF GEOLOGICAL AND NUCLEAR SCIENCES LTD.
PO Box 31312, Lower Hutt, New Zealand
Phone (+64 4) 570 4671, Fax (+64 4) 570 4657

RADIOCARBON CALIBRATION REPORT

NZA 51908 CONVENTIONAL RADIOCARBON AGE 111 ± 14 years BP

Southern Hemisphere Atmospheric data from McCormac et al (2004);
FG McCormac, AG Hogg, PG Blackwell, CE Buck, TFG Higham, and PJ Reimer (2004)
Radiocarbon 46, 1087-1092

CALIBRATED AGE in terms of confidence intervals (Smoothing parameter: 0, Offset: 0)

68% confidence interval is 1817 AD to 1828 AD	133 BP to 122 BP (21.2% of area)
plus 1894 AD to 1919 AD	56 BP to 31 BP (46.3% of area)
95% confidence interval is 1708 AD to 1722 AD	242 BP to 228 BP (5.6% of area)
plus 1810 AD to 1838 AD	140 BP to 112 BP (30.3% of area)
plus 1847 AD to 1857 AD	103 BP to 93 BP (1.9% of area)
plus 1862 AD to 1867 AD	88 BP to 83 BP (0.8% of area)
plus 1879 AD to 1926 AD	71 BP to 24 BP (56.8% of area)

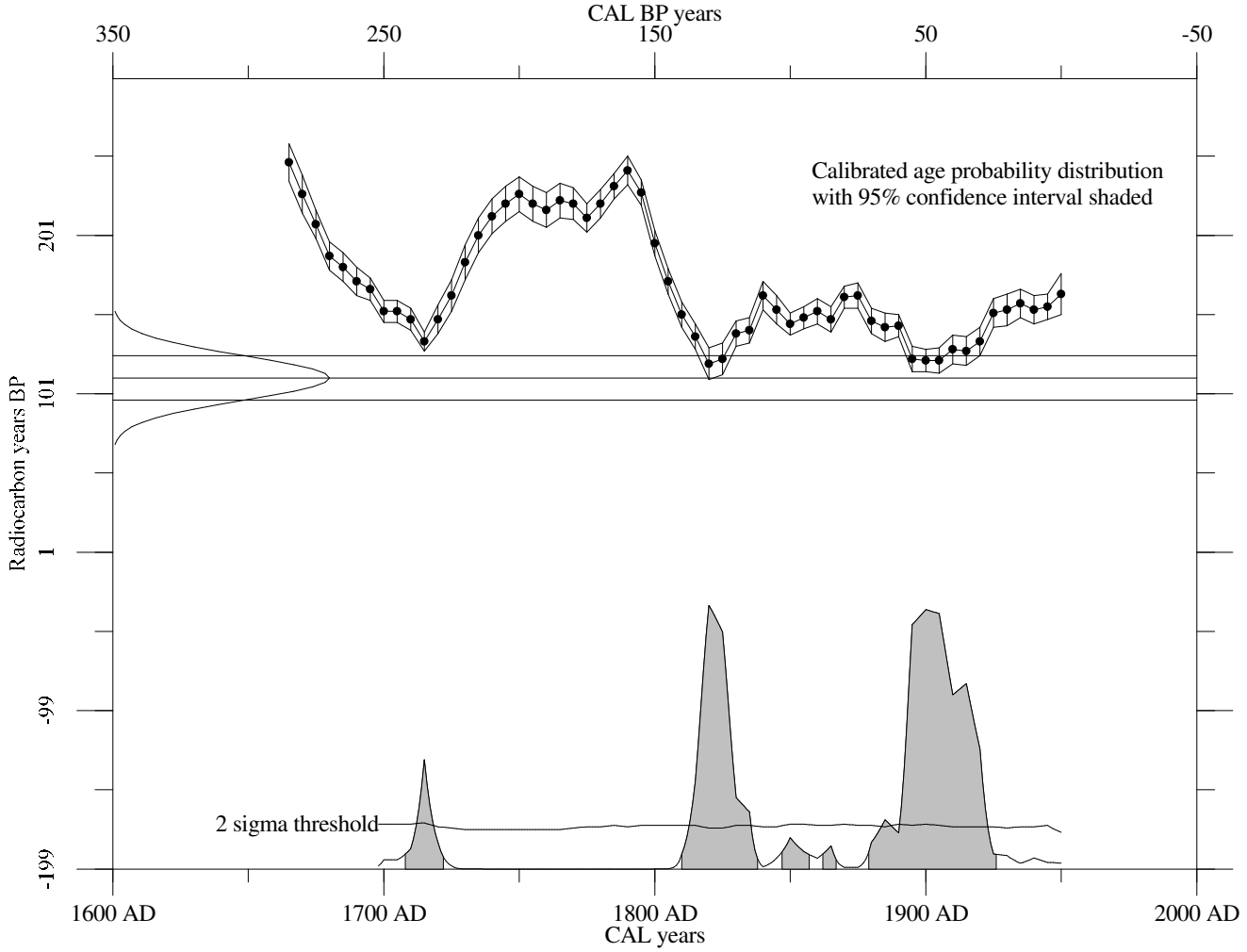

RAFTER RADIOCARBON LABORATORY

R40131/2

INSTITUTE OF GEOLOGICAL AND NUCLEAR SCIENCES LTD.
PO Box 31312, Lower Hutt, New Zealand
Phone (+64 4) 570 4671, Fax (+64 4) 570 4657

RADIOCARBON CALIBRATION REPORT

NZA 51893 CONVENTIONAL RADIOCARBON AGE 1176 ± 17 years BP

Southern Hemisphere Atmospheric data from McCormac et al (2004);
FG McCormac, AG Hogg, PG Blackwell, CE Buck, TFG Higham, and PJ Reimer (2004)
Radiocarbon 46, 1087-1092

CALIBRATED AGE in terms of confidence intervals (Smoothing parameter: 0, Offset: 0)

68% confidence interval is 895 AD to 904 AD	1055 BP to 1046 BP (10.1% of area)
plus 915 AD to 928 AD	1035 BP to 1022 BP (14.5% of area)
plus 934 AD to 970 AD	1016 BP to 980 BP (44.4% of area)
95% confidence interval is 890 AD to 980 AD	1060 BP to 970 BP (95.3% of area)

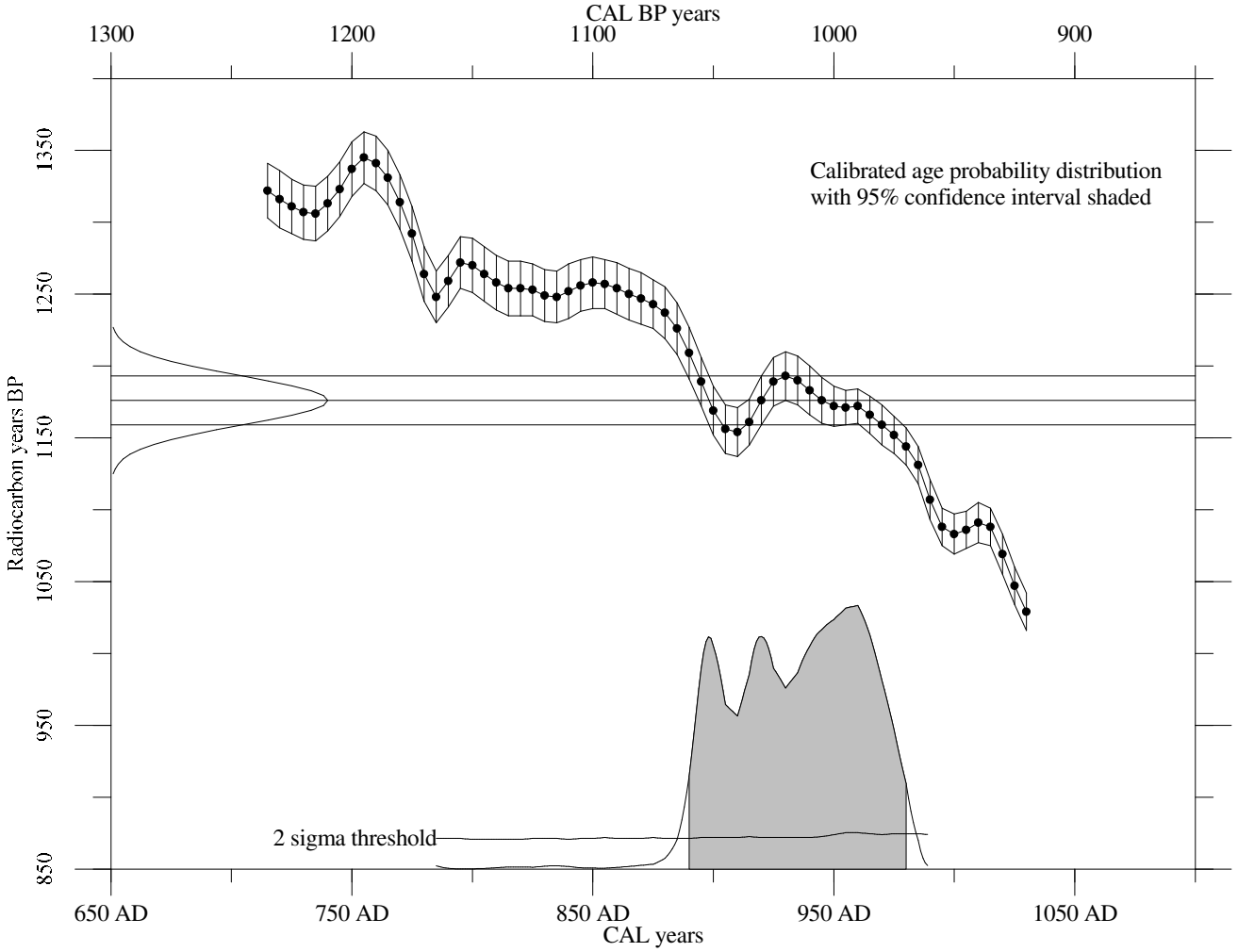

RAFTER RADIOCARBON LABORATORY

R40131/3

INSTITUTE OF GEOLOGICAL AND NUCLEAR SCIENCES LTD.
PO Box 31312, Lower Hutt, New Zealand
Phone (+64 4) 570 4671, Fax (+64 4) 570 4657

RADIOCARBON CALIBRATION REPORT

NZA 51900 CONVENTIONAL RADIOCARBON AGE 1364 ± 15 years BP

Southern Hemisphere Atmospheric data from McCormac et al (2004);
FG McCormac, AG Hogg, PG Blackwell, CE Buck, TFG Higham, and PJ Reimer (2004)
Radiocarbon 46, 1087-1092

CALIBRATED AGE in terms of confidence intervals (Smoothing parameter: 0, Offset: 0)

68% confidence interval is 665 AD to 694 AD	1285 BP to 1256 BP (46.6% of area)
plus 705 AD to 706 AD	1245 BP to 1244 BP (0.9% of area)
plus 749 AD to 765 AD	1201 BP to 1185 BP (20.2% of area)
95% confidence interval is 660 AD to 721 AD	1290 BP to 1229 BP (68.1% of area)
plus 742 AD to 770 AD	1208 BP to 1180 BP (26.7% of area)

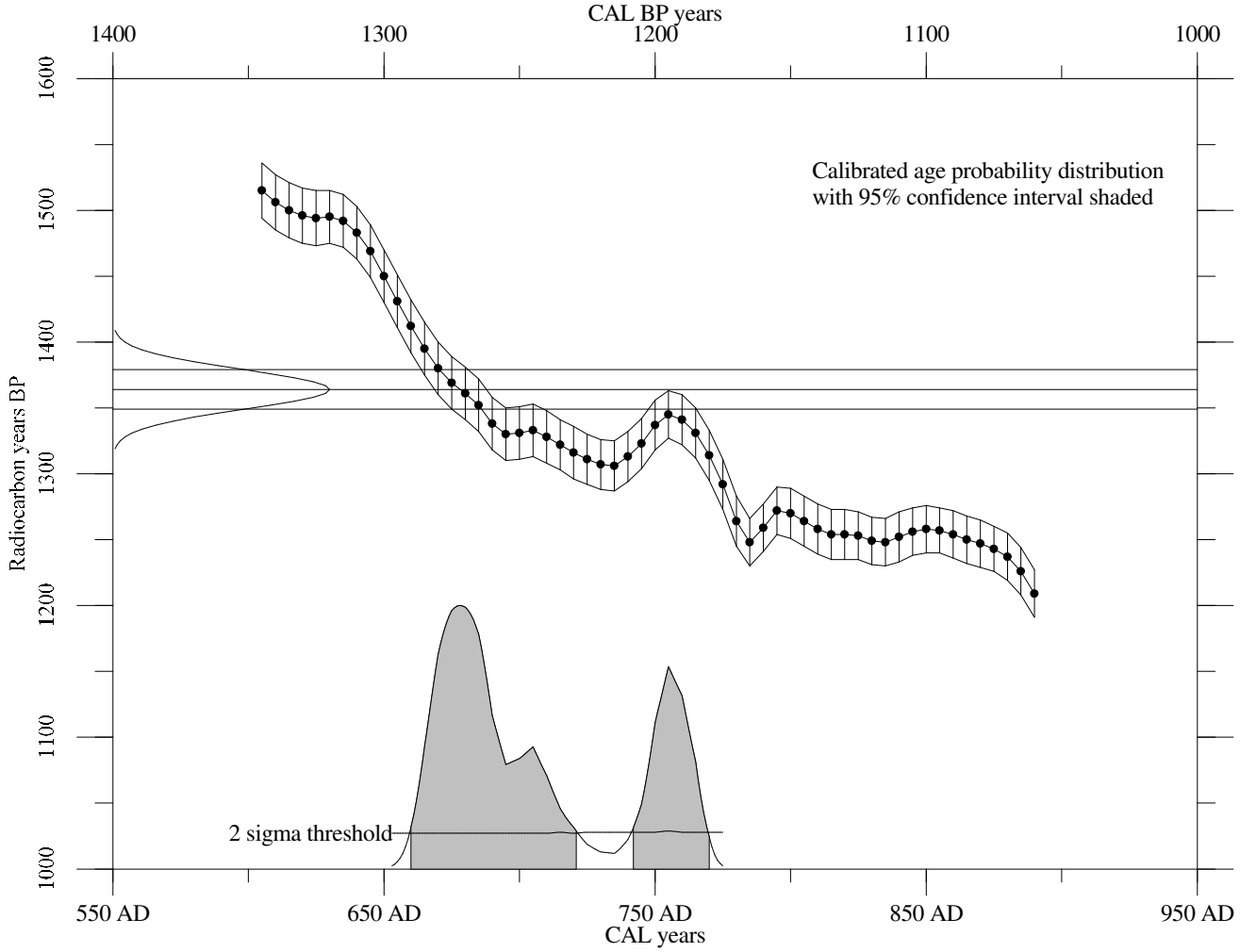

RAFTER RADIOCARBON LABORATORY

R40131/4

INSTITUTE OF GEOLOGICAL AND NUCLEAR SCIENCES LTD.
PO Box 31312, Lower Hutt, New Zealand
Phone (+64 4) 570 4671, Fax (+64 4) 570 4657

RADIOCARBON CALIBRATION REPORT

NZA 51903 CONVENTIONAL RADIOCARBON AGE 2683 ± 16 years BP

Southern Hemisphere Atmospheric data from McCormac et al (2004);
FG McCormac, AG Hogg, PG Blackwell, CE Buck, TFG Higham, and PJ Reimer (2004)
Radiocarbon 46, 1087-1092

CALIBRATED AGE in terms of confidence intervals (Smoothing parameter: 0, Offset: 0)

68% confidence interval is 810 BC to 792 BC	2759 BP to 2741 BP (66.8% of area)
95% confidence interval is 828 BC to 779 BC	2777 BP to 2728 BP (94.9% of area)

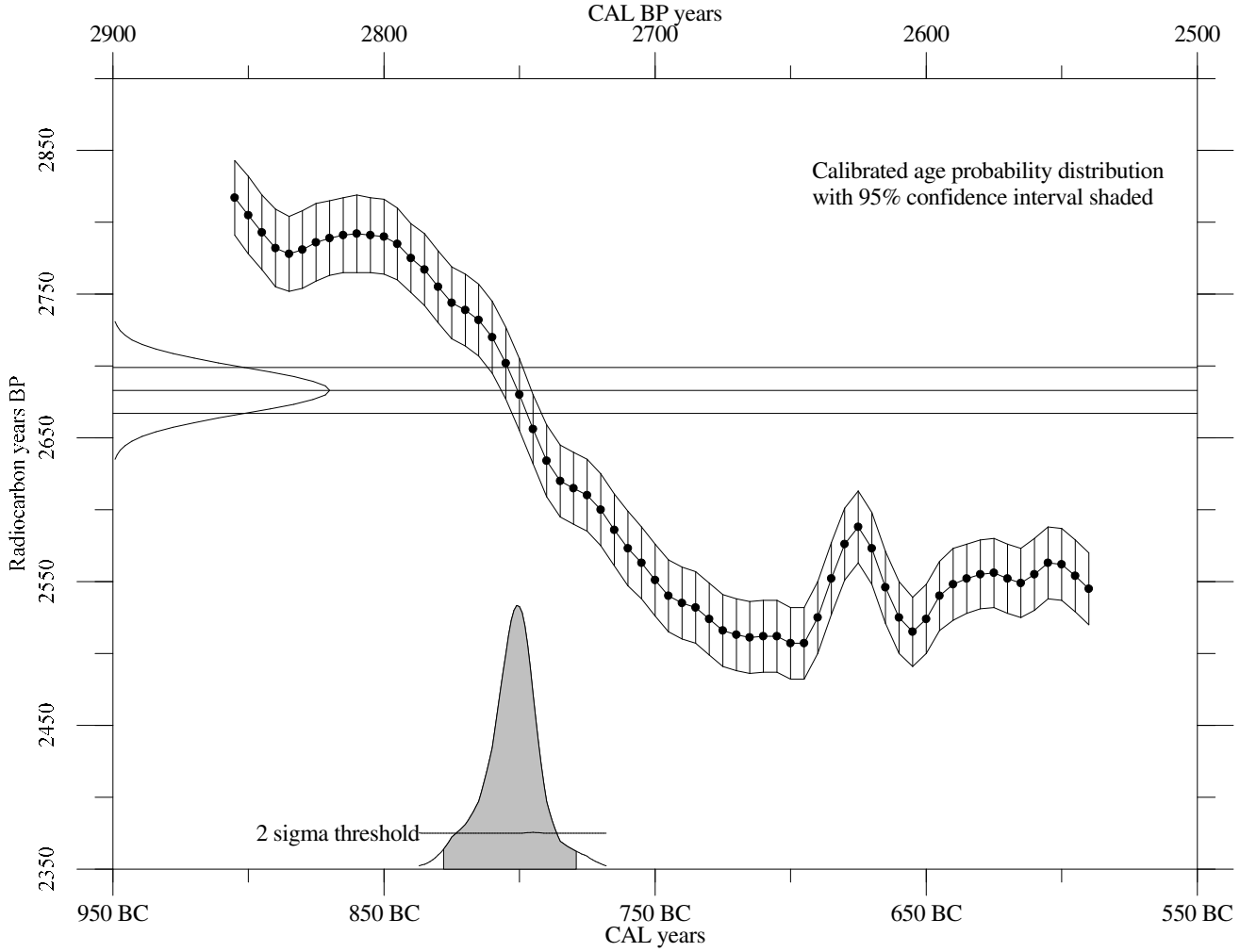

RAFTER RADIOCARBON LABORATORY

R40131/5

INSTITUTE OF GEOLOGICAL AND NUCLEAR SCIENCES LTD.
PO Box 31312, Lower Hutt, New Zealand
Phone (+64 4) 570 4671, Fax (+64 4) 570 4657

RADIOCARBON CALIBRATION REPORT

NZA 52118 CONVENTIONAL RADIOCARBON AGE 813 ± 38 years BP

Southern Hemisphere Atmospheric data from McCormac et al (2004);
FG McCormac, AG Hogg, PG Blackwell, CE Buck, TFG Higham, and PJ Reimer (2004)
Radiocarbon 46, 1087-1092

CALIBRATED AGE in terms of confidence intervals (Smoothing parameter: 0, Offset: 0)

68% confidence interval is 1229 AD to 1276 AD	721 BP to 674 BP (66.8% of area)
95% confidence interval is 1203 AD to 1295 AD	747 BP to 655 BP (94.8% of area)

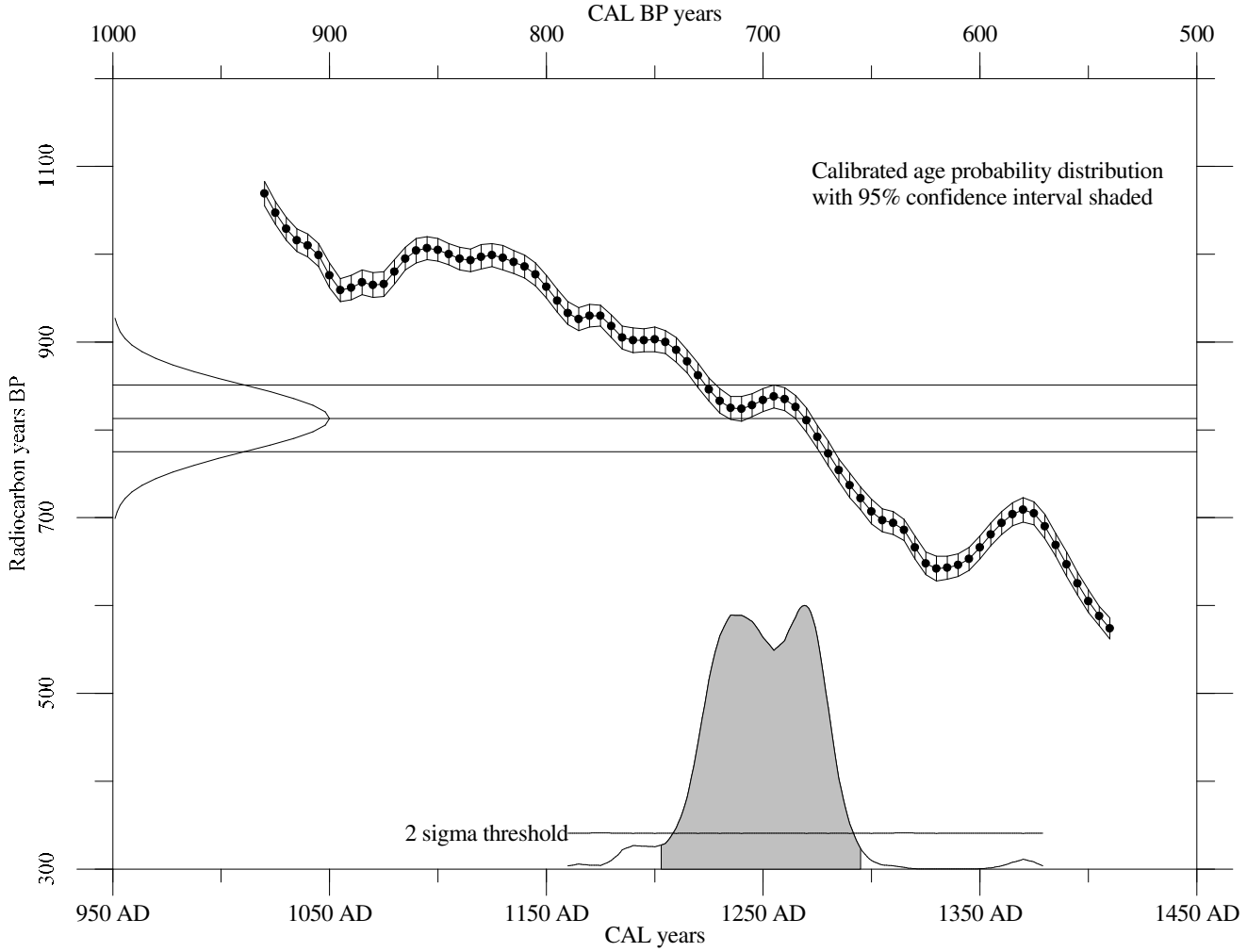

RAFTER RADIOCARBON LABORATORY

R40012/1

INSTITUTE OF GEOLOGICAL AND NUCLEAR SCIENCES LTD.
PO Box 31312, Lower Hutt, New Zealand
Phone (+64 4) 570 4671, Fax (+64 4) 570 4657

RADIOCARBON CALIBRATION REPORT

NZA 50573 CONVENTIONAL RADIOCARBON AGE 545 ± 18 years BP

Southern Hemisphere Atmospheric data from McCormac et al (2004);
FG McCormac, AG Hogg, PG Blackwell, CE Buck, TFG Higham, and PJ Reimer (2004)
Radiocarbon 46, 1087-1092

CALIBRATED AGE in terms of confidence intervals (Smoothing parameter: 0, Offset: 0)

68% confidence interval is 1415 AD to 1435 AD	535 BP to 515 BP (70.4% of area)
95% confidence interval is 1408 AD to 1442 AD	542 BP to 508 BP (94.5% of area)

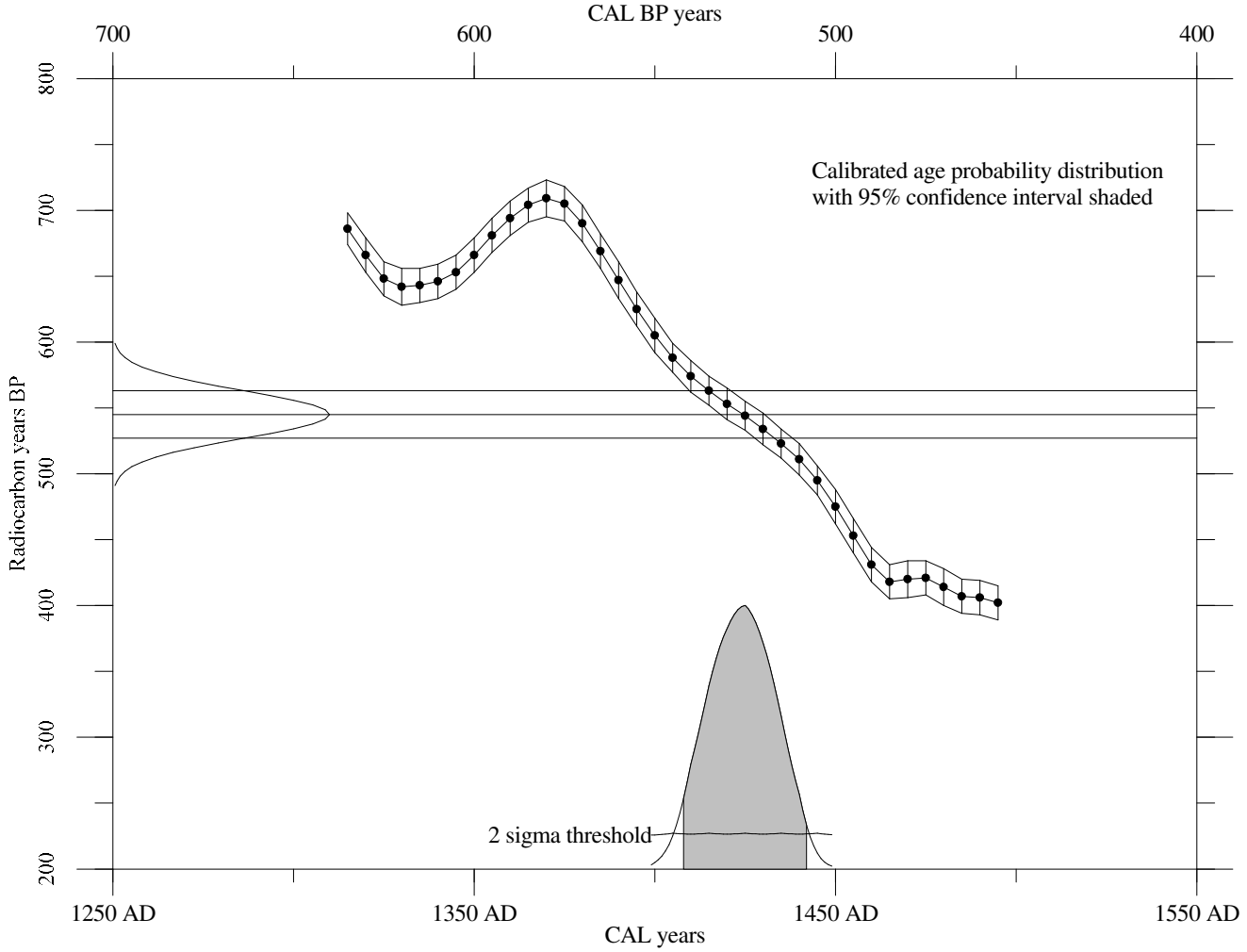

RAFTER RADIOCARBON LABORATORY

R40012/3

INSTITUTE OF GEOLOGICAL AND NUCLEAR SCIENCES LTD.
PO Box 31312, Lower Hutt, New Zealand
Phone (+64 4) 570 4671, Fax (+64 4) 570 4657

RADIOCARBON CALIBRATION REPORT

NZA 50575 CONVENTIONAL RADIOCARBON AGE 606 ± 18 years BP

Southern Hemisphere Atmospheric data from McCormac et al (2004);
FG McCormac, AG Hogg, PG Blackwell, CE Buck, TFG Higham, and PJ Reimer (2004)
Radiocarbon 46, 1087-1092

CALIBRATED AGE in terms of confidence intervals (Smoothing parameter: 0, Offset: 0)

68% confidence interval is 1330 AD to 1331 AD	620 BP to 619 BP (1.3% of area)
plus 1392 AD to 1412 AD	558 BP to 538 BP (65.8% of area)
95% confidence interval is 1324 AD to 1346 AD	626 BP to 604 BP (21.6% of area)
plus 1389 AD to 1418 AD	561 BP to 532 BP (73.1% of area)

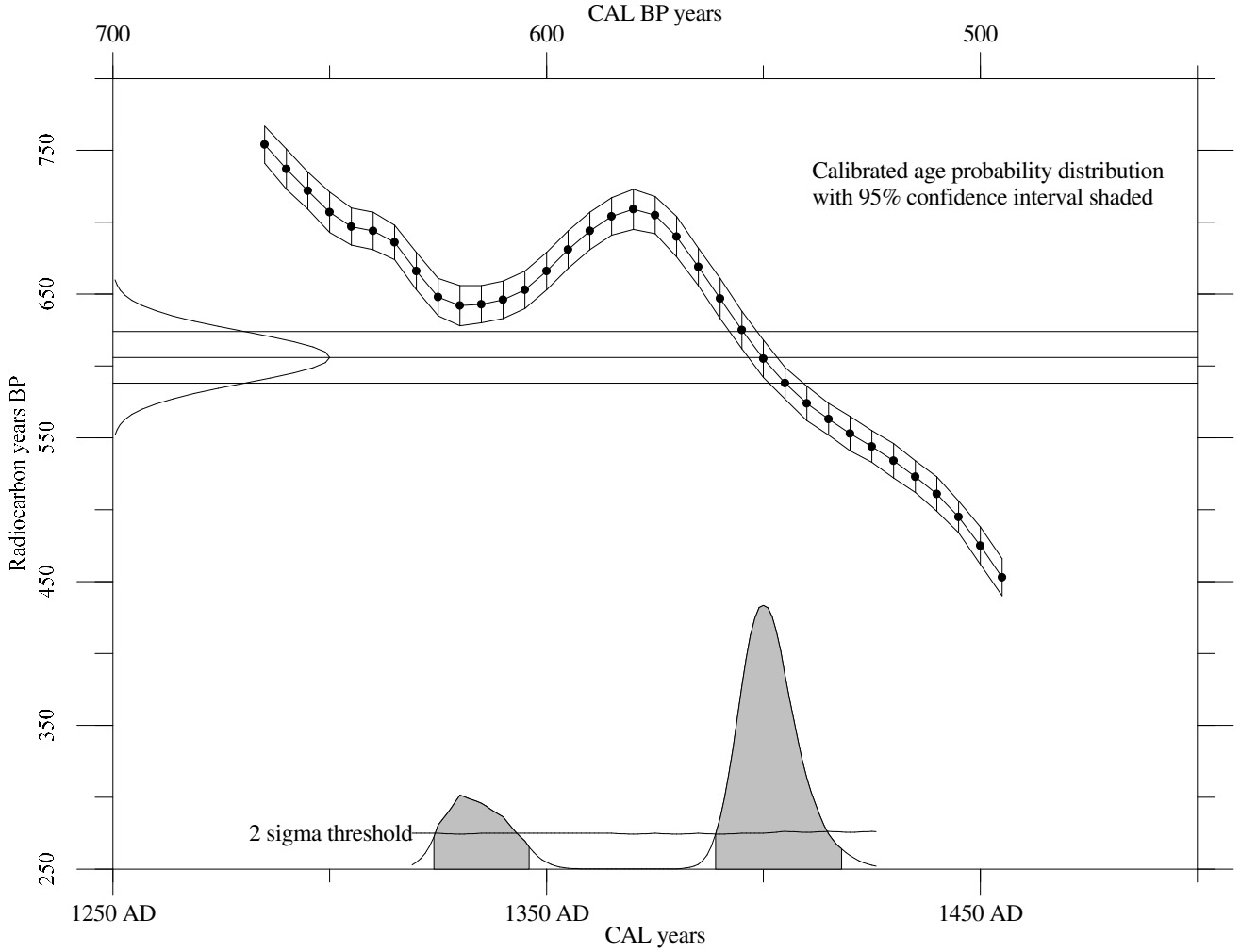

Rafter Radiocarbon
Calibration Report

NZA 56669

R 40511/1

Report issued: 20 Jun 2014

CONVENTIONAL RADIOCARBON AGE 777 ± 22 years BP

Calibrated with Marine13 (Reimer et al., Radiocarbon 55(4):1869-1887, 2013).
ΔR -7 ± 45

CALIBRATED AGE in terms of confidence intervals

1 sigma interval is 1468 AD to 1576 AD 482 BP to 374 BP (67.7% of area)

2 sigma interval is 1452 AD to 1644 AD 498 BP to 306 BP (95.3% of area)

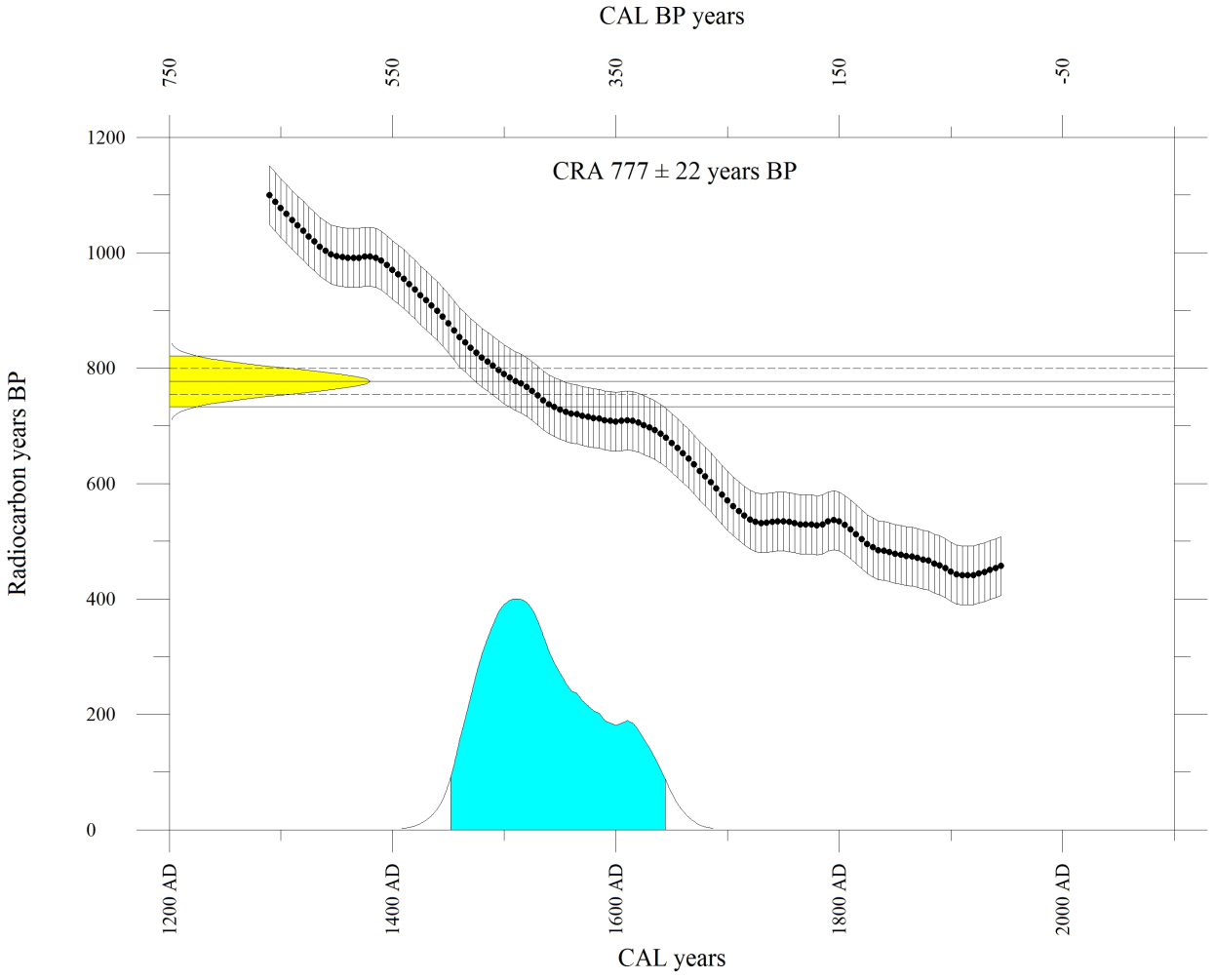

Calibration performed using Winscal v. 6.0 adapted from: Stuiver and Reimer (*Radiocarbon 35*(1): 215-230, 1993).

National Isotope Centre, GNS Science
PO Box 31-312 Lower Hutt, New Zealand Phone +64 4 570 4644
Email radiocarbon@gns.cri.nz Website www.RafterRadiocarbon.co.nz

Rafter Radiocarbon
Calibration Report

NZA 56524

R 40511/2

Report issued: 20 Jun 2014

CONVENTIONAL RADIOCARBON AGE 220 ± 19 years BP

Calibrated with SHCal13 (Hogg et al., Radiocarbon 55(4):1889-1902, 2013).

CALIBRATED AGE in terms of confidence intervals

1 sigma interval is	1669 AD to 1675 AD	281 BP to 275 BP (6.9% of area)
	1739 AD to 1787 AD	211 BP to 163 BP (56.2% of area)
	1793 AD to 1798 AD	157 BP to 152 BP (5.9% of area)
2 sigma interval is	1660 AD to 1684 AD	290 BP to 266 BP (17.3% of area)
	1730 AD to 1803 AD	220 BP to 147 BP (77.4% of area)

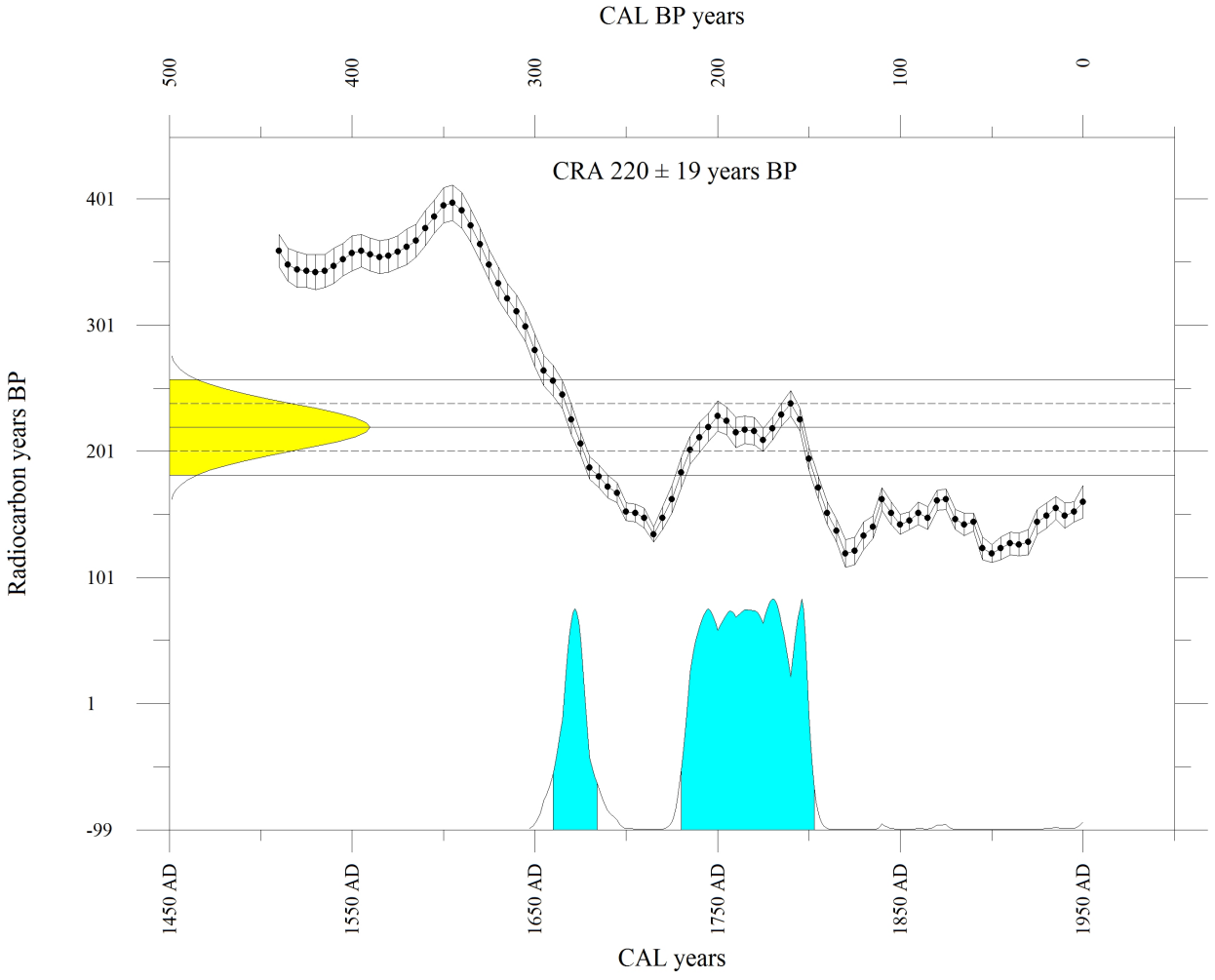

Calibration performed using Winscal v. 6.0 adapted from: Stuiver and Reimer (*Radiocarbon 35*(1): 215-230, 1993).

National Isotope Centre, GNS Science
PO Box 31-312 Lower Hutt, New Zealand Phone +64 4 570 4644
Email radiocarbon@gns.cri.nz Website www.RafterRadiocarbon.co.nz

Rafter Radiocarbon
Calibration Report

NZA 56503

R 40511/3

Report issued: 20 Jun 2014

CONVENTIONAL RADIOCARBON AGE 4126 ± 25 years BP

Calibrated with SHCal13 (Hogg et al., Radiocarbon 55(4):1889-1902, 2013).

CALIBRATED AGE in terms of confidence intervals

1 sigma interval is	2834 BC to 2814 BC	4783 BP to 4763 BP (10.6% of area)
	2670 BC to 2571 BC	4619 BP to 4520 BP (55.7% of area)
	2509 BC to 2504 BC	4458 BP to 4453 BP (1.7% of area)
2 sigma interval is	2858 BC to 2807 BC	4807 BP to 4756 BP (17.1% of area)
	2752 BC to 2719 BC	4701 BP to 4668 BP (5.8% of area)
	2701 BC to 2562 BC	4650 BP to 4511 BP (64.1% of area)
	2531 BC to 2493 BC	4480 BP to 4442 BP (7.8% of area)

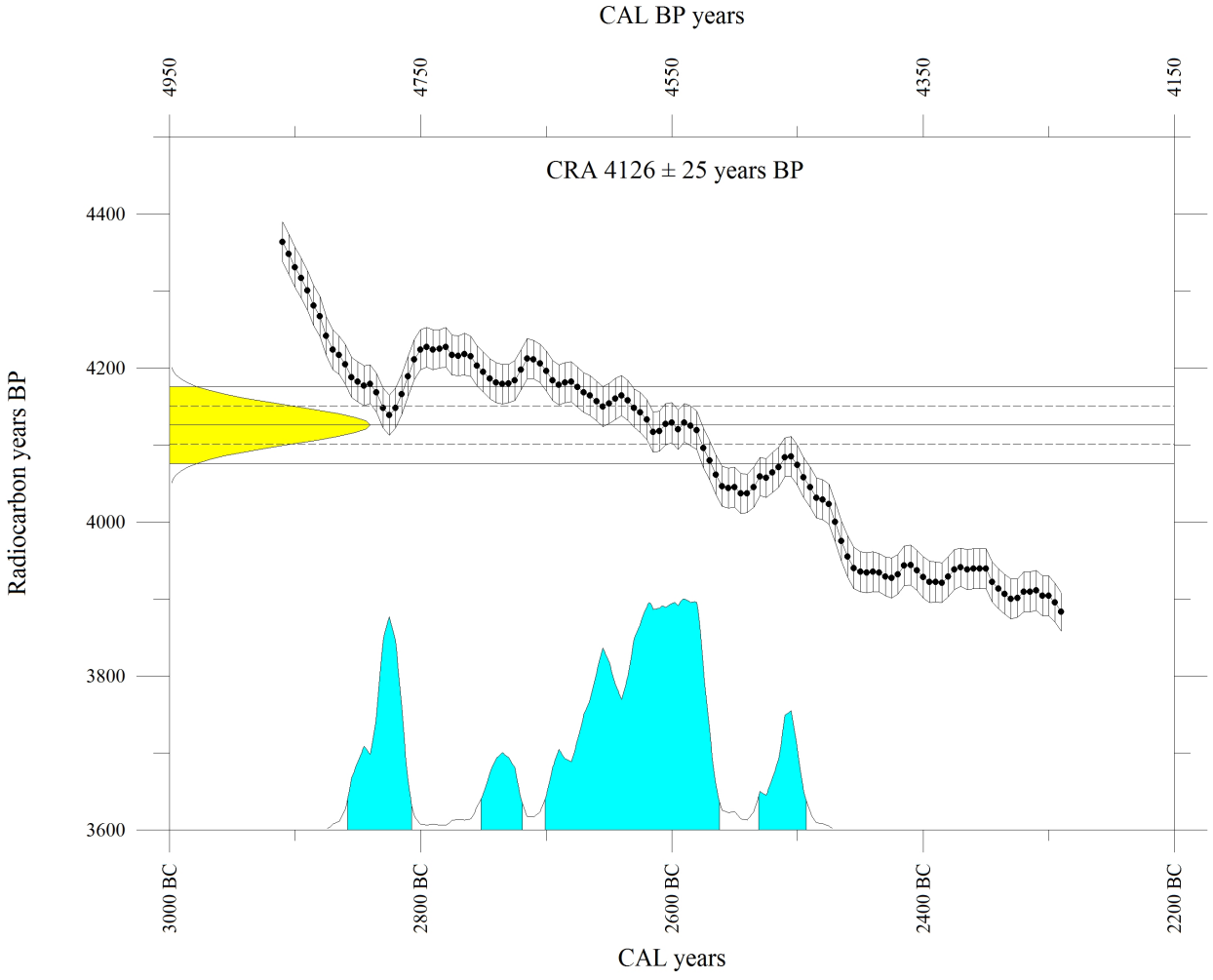

Calibration performed using Winscal v. 6.0 adapted from: Stuiver and Reimer (*Radiocarbon 35*(1): 215-230, 1993).

National Isotope Centre, GNS Science
PO Box 31-312 Lower Hutt, New Zealand Phone +64 4 570 4644
Email radiocarbon@gns.cri.nz Website www.RafterRadiocarbon.co.nz

Rafter Radiocarbon
Calibration Report

NZA 56504

R 40511/4

Report issued: 20 Jun 2014

CONVENTIONAL RADIOCARBON AGE 815 ± 20 years BP

Calibrated with SHCal13 (Hogg et al., Radiocarbon 55(4):1889-1902, 2013).

CALIBRATED AGE in terms of confidence intervals

1 sigma interval is 1230 AD to 1252 AD	720 BP to 698 BP	(41.9% of area)
1261 AD to 1275 AD	689 BP to 675 BP	(27.7% of area)
2 sigma interval is 1223 AD to 1279 AD	727 BP to 671 BP	(95.3% of area)

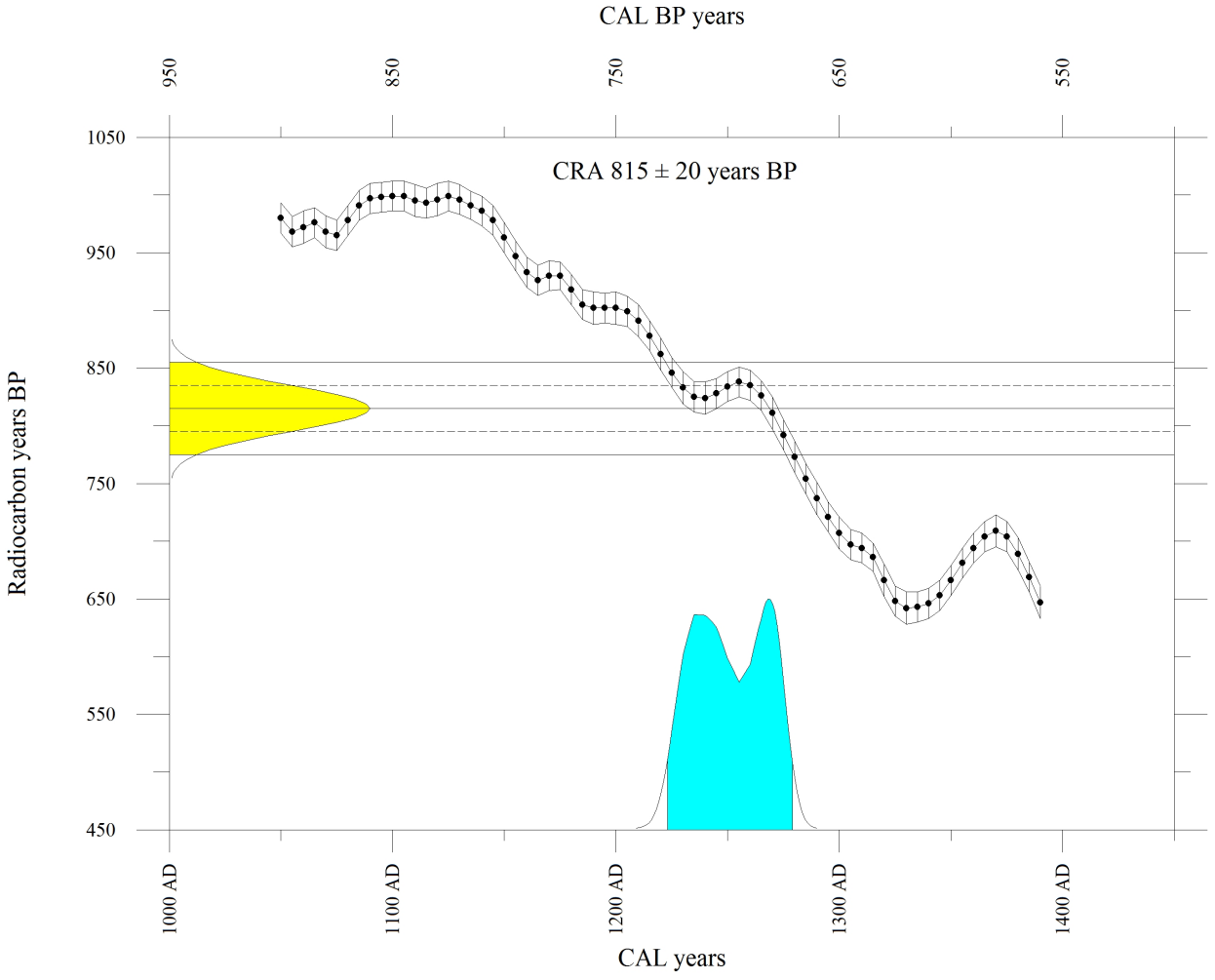

Calibration performed using Winscal v. 6.0 adapted from: Stuiver and Reimer (*Radiocarbon 35*(1): 215-230, 1993).

National Isotope Centre, GNS Science
PO Box 31-312 Lower Hutt, New Zealand Phone +64 4 570 4644
Email radiocarbon@gns.cri.nz Website www.RafterRadiocarbon.co.nz

Rafter Radiocarbon
Calibration Report

NZA 56525

R 40511/5

Report issued: 20 Jun 2014

CONVENTIONAL RADIOCARBON AGE 950 ± 21 years BP

Calibrated with SHCal13 (Hogg et al., Radiocarbon 55(4):1889-1902, 2013).

CALIBRATED AGE in terms of confidence intervals

1 sigma interval is	1051 AD to 1081 AD	899 BP to 869 BP (29.8% of area)
	1145 AD to 1179 AD	805 BP to 771 BP (37.5% of area)
2 sigma interval is	1046 AD to 1099 AD	904 BP to 851 BP (38.0% of area)
	1106 AD to 1202 AD	844 BP to 748 BP (57.2% of area)

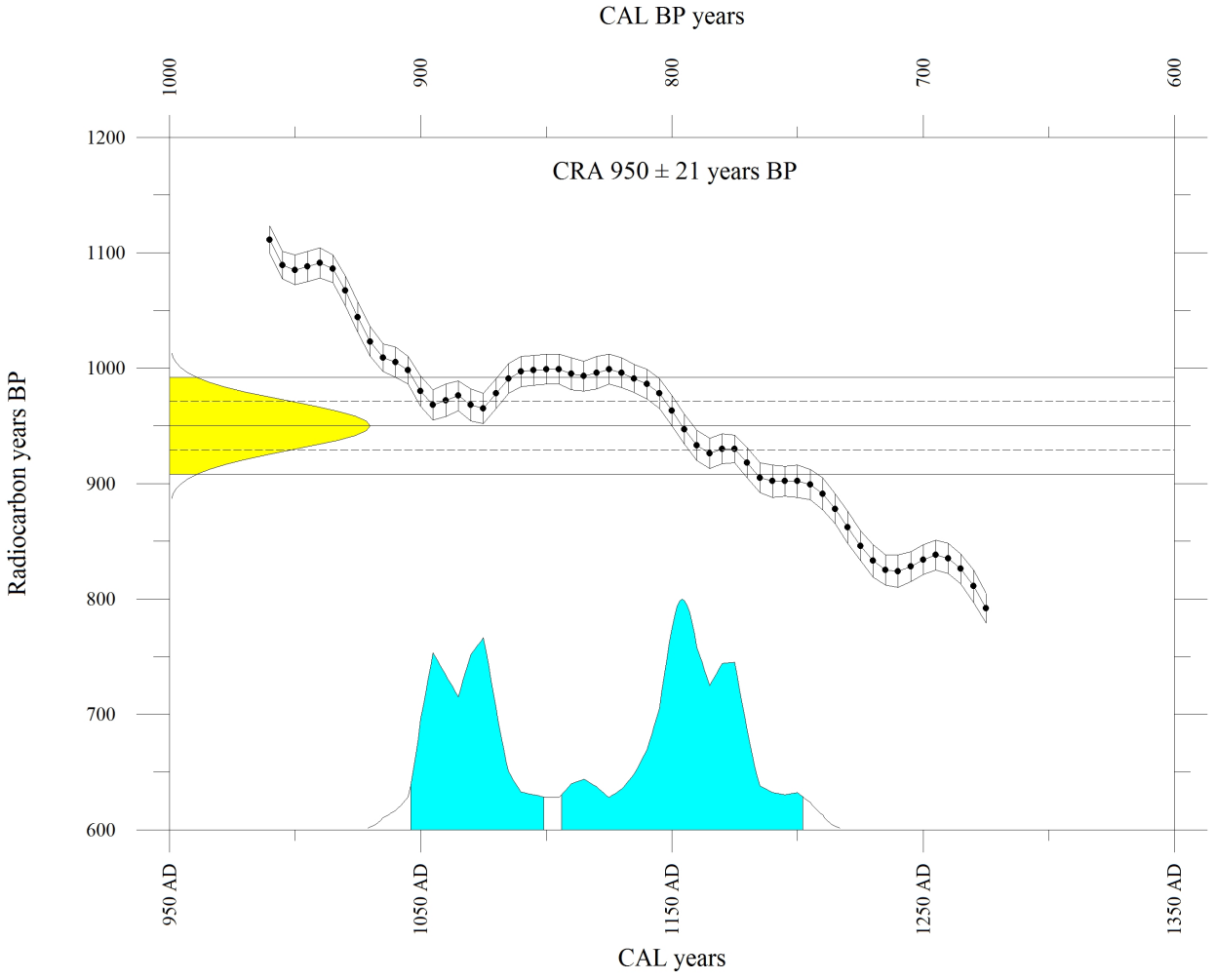

Calibration performed using Winscal v. 6.0 adapted from: Stuiver and Reimer (*Radiocarbon 35*(1): 215-230, 1993).

National Isotope Centre, GNS Science
PO Box 31-312 Lower Hutt, New Zealand Phone +64 4 570 4644
Email radiocarbon@gns.cri.nz Website www.RafterRadiocarbon.co.nz

Rafter Radiocarbon
Calibration Report

NZA 56505

R 40511/6

Report issued: 20 Jun 2014

CONVENTIONAL RADIOCARBON AGE 674 ± 20 years BP

Calibrated with SHCal13 (Hogg et al., Radiocarbon 55(4):1889-1902, 2013).

CALIBRATED AGE in terms of confidence intervals

1 sigma interval is 1305 AD to 1325 AD	645 BP to 625 BP	(25.1% of area)
1343 AD to 1363 AD	607 BP to 587 BP	(25.8% of area)
1377 AD to 1390 AD	573 BP to 560 BP	(16.9% of area)
2 sigma interval is 1300 AD to 1392 AD	650 BP to 558 BP	(94.1% of area)

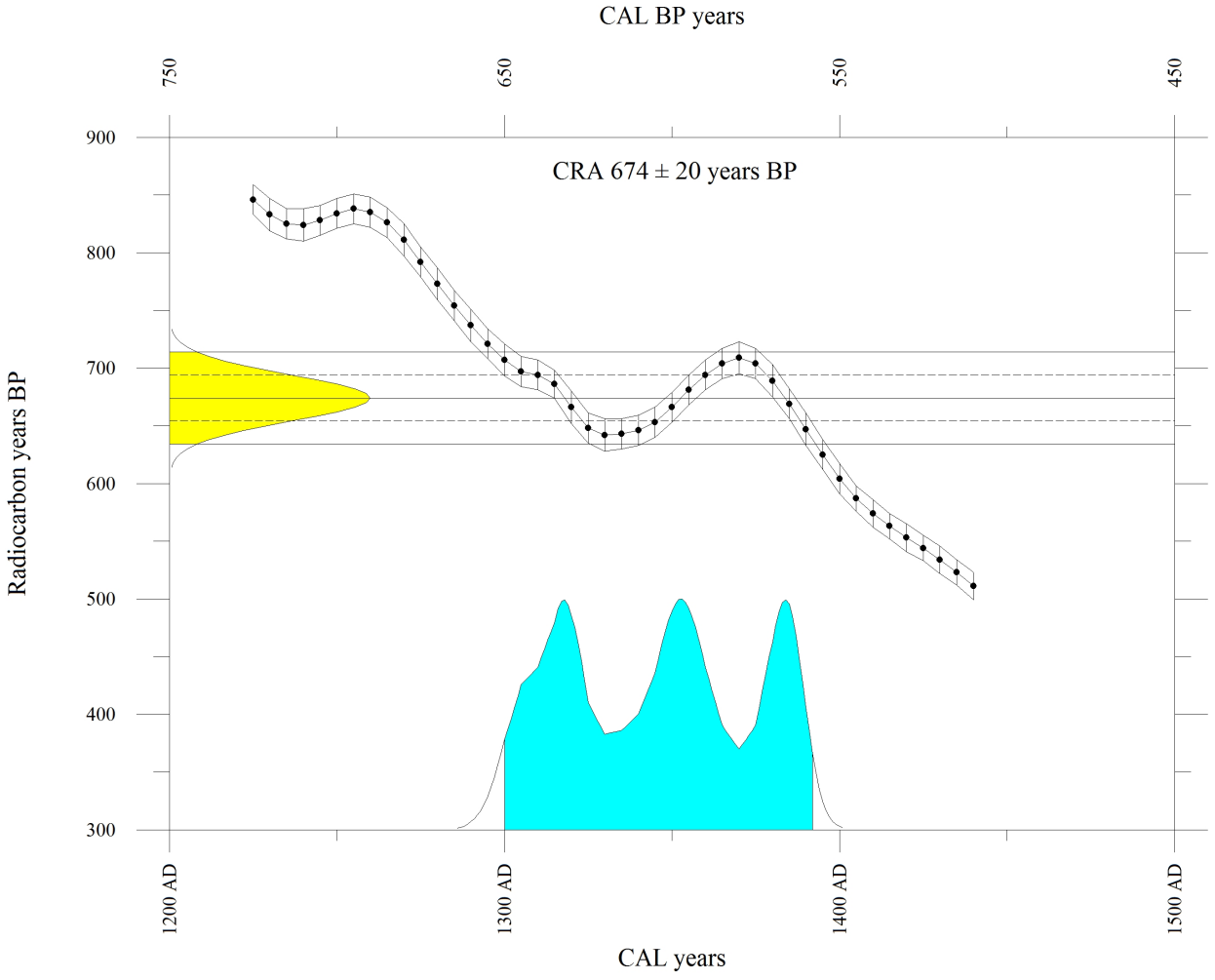

Calibration performed using Winscal v. 6.0 adapted from: Stuiver and Reimer (*Radiocarbon 35*(1): 215-230, 1993).

National Isotope Centre, GNS Science
PO Box 31-312 Lower Hutt, New Zealand Phone +64 4 570 4644
Email radiocarbon@gns.cri.nz Website www.RafterRadiocarbon.co.nz

Rafter Radiocarbon
Calibration Report

NZA 56676

R 40511/7

Report issued: 20 Jun 2014

CONVENTIONAL RADIOCARBON AGE 563 ± 45 years BP

Calibrated with SHCal13 (Hogg et al., Radiocarbon 55(4):1889-1902, 2013).

CALIBRATED AGE in terms of confidence intervals

1 sigma interval is 1398 AD to 1439 AD 552 BP to 511 BP (69.0% of area)

2 sigma interval is 1321 AD to 1350 AD 629 BP to 600 BP (10.7% of area)
1387 AD to 1453 AD 563 BP to 497 BP (84.4% of area)

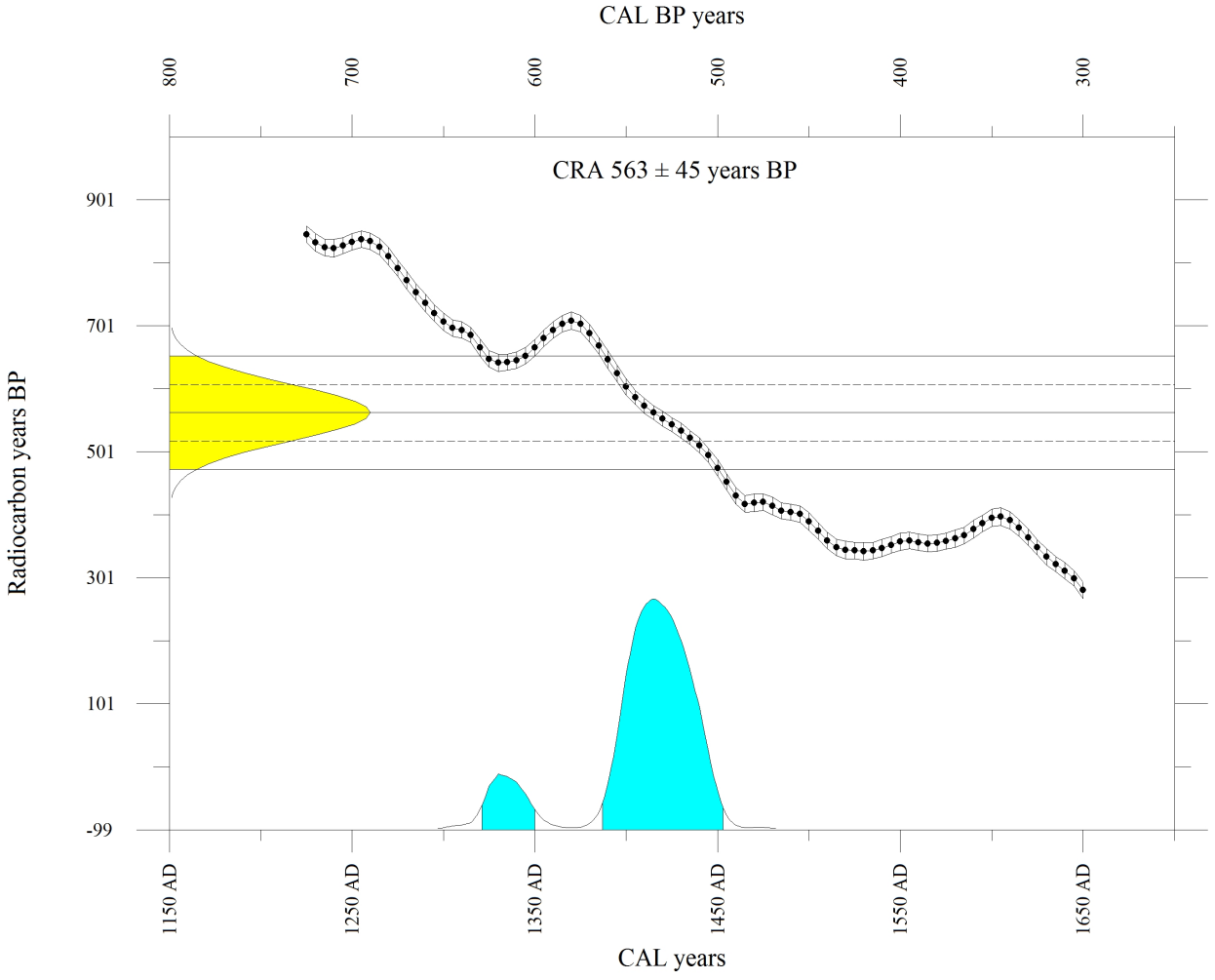

Calibration performed using Winscal v. 6.0 adapted from: Stuiver and Reimer (*Radiocarbon 35*(1): 215-230, 1993).

National Isotope Centre, GNS Science
PO Box 31-312 Lower Hutt, New Zealand Phone +64 4 570 4644
Email radiocarbon@gns.cri.nz Website www.RafterRadiocarbon.co.nz

Rafter Radiocarbon
Calibration Report

NZA 56780

R 40511/9

Report issued: 20 Jun 2014

CONVENTIONAL RADIOCARBON AGE 195 ± 20 years BP

Calibrated with SHCal13 (Hogg et al., Radiocarbon 55(4):1889-1902, 2013).

CALIBRATED AGE in terms of confidence intervals

1 sigma interval is	1671 AD to 1696 AD	279 BP to 254 BP (21.6% of area)
	1726 AD to 1747 AD	224 BP to 203 BP (18.0% of area)
	1756 AD to 1782 AD	194 BP to 168 BP (18.5% of area)
	1796 AD to 1807 AD	154 BP to 143 BP (9.9% of area)
2 sigma interval is	1666 AD to 1709 AD	284 BP to 241 BP (25.7% of area)
	1721 AD to 1812 AD	229 BP to 138 BP (57.4% of area)
	1837 AD to 1847 AD	113 BP to 103 BP (2.4% of area)
	1858 AD to 1880 AD	92 BP to 70 BP (5.0% of area)
	1929 AD to 1950 AD	21 BP to 0 BP (4.5% of area)

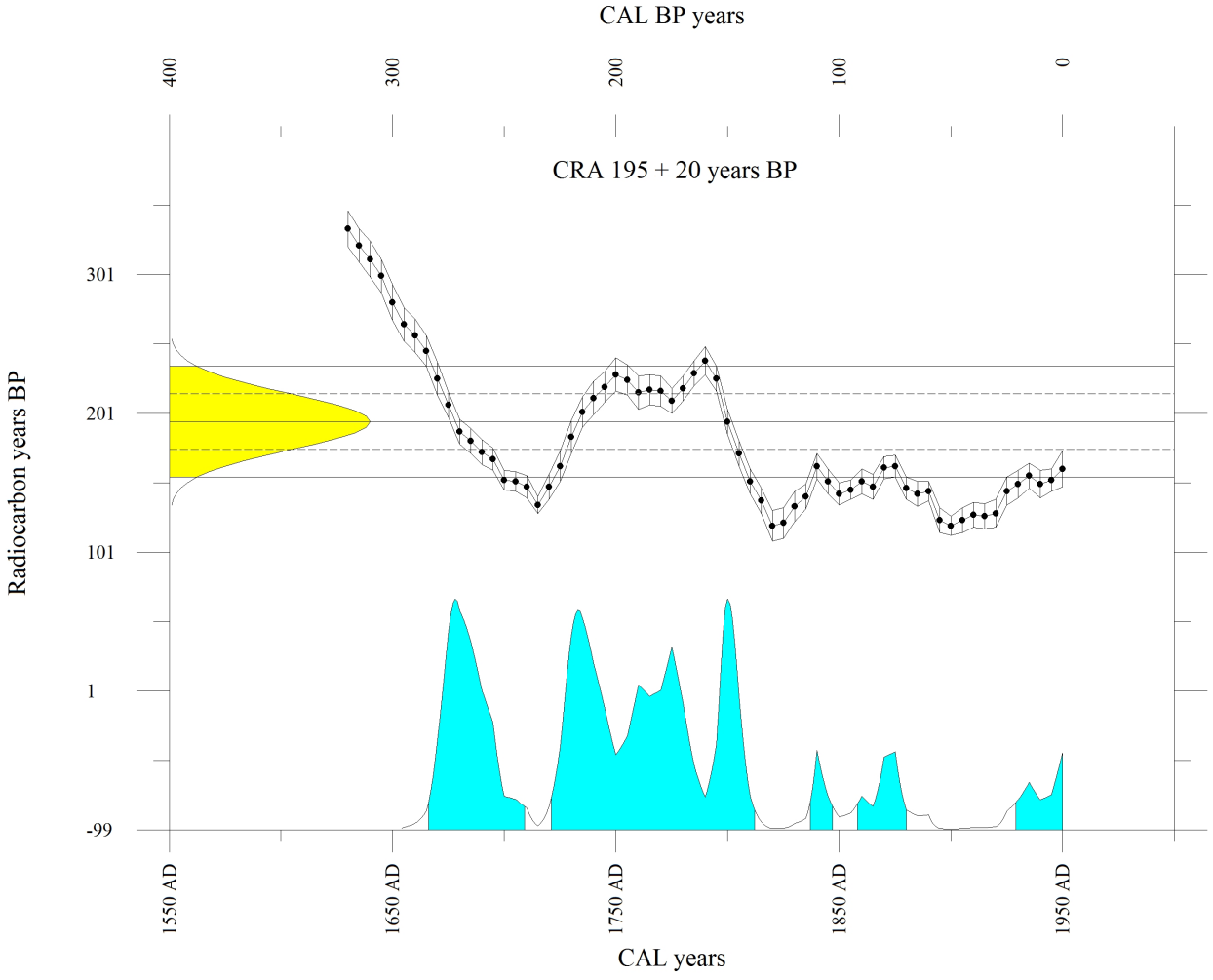

Calibration performed using Winscal v. 6.0 adapted from: Stuiver and Reimer (*Radiocarbon 35*(1): 215-230, 1993).

National Isotope Centre, GNS Science
PO Box 31-312 Lower Hutt, New Zealand Phone +64 4 570 4644
Email radiocarbon@gns.cri.nz Website www.RafterRadiocarbon.co.nz

Rafter Radiocarbon
Calibration Report

NZA 56779

R 40511/3

Report issued: 20 Jun 2014

CONVENTIONAL RADIOCARBON AGE 4187 ± 22 years BP

Calibrated with SHCal13 (Hogg et al., Radiocarbon 55(4):1889-1902, 2013).

CALIBRATED AGE in terms of confidence intervals

1 sigma interval is	2864 BC to 2832 BC	4813 BP to 4781 BP (14.4% of area)
	2816 BC to 2803 BC	4765 BP to 4752 BP (5.6% of area)
	2759 BC to 2661 BC	4708 BP to 4610 BP (44.1% of area)
	2645 BC to 2635 BC	4594 BP to 4584 BP (3.7% of area)
2 sigma interval is	2873 BC to 2623 BC	4822 BP to 4572 BP (94.9% of area)

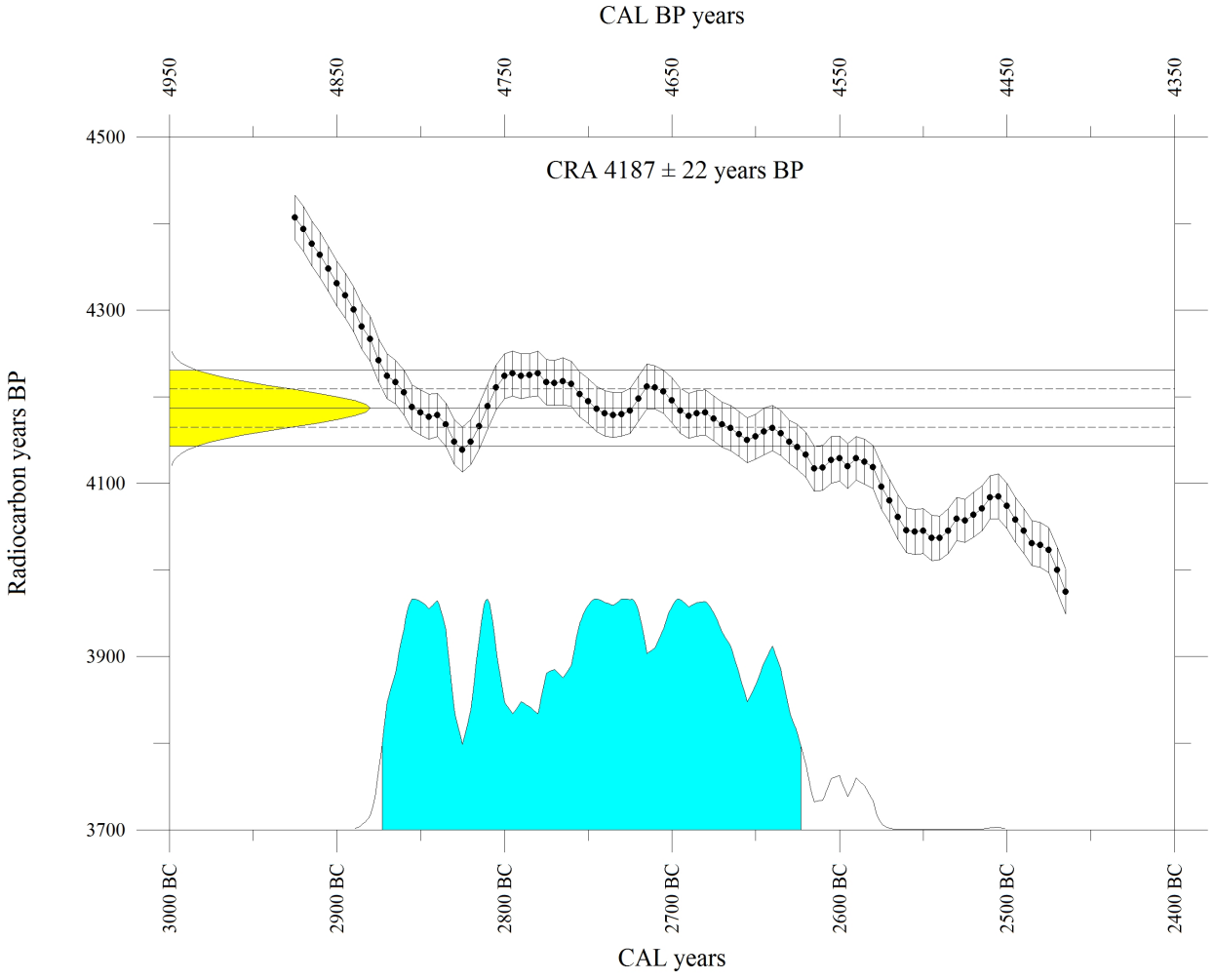

Calibration performed using Winscal v. 6.0 adapted from: Stuiver and Reimer (*Radiocarbon 35*(1): 215-230, 1993).

National Isotope Centre, GNS Science
PO Box 31-312 Lower Hutt, New Zealand Phone +64 4 570 4644
Email radiocarbon@gns.cri.nz Website www.RafterRadiocarbon.co.nz

RAFTER RADIOCARBON LABORATORY

R40277/5

INSTITUTE OF GEOLOGICAL AND NUCLEAR SCIENCES LTD.
PO Box 31312, Lower Hutt, New Zealand
Phone (+64 4) 570 4671, Fax (+64 4) 570 4657

RADIOCARBON CALIBRATION REPORT

NZA 53811 CONVENTIONAL RADIOCARBON AGE 16452 ± 72 years BP

Atmospheric data from Reimer et al (2009);
PJ Reimer, MGL Baillie, E Bard, A Bayliss, JW Beck, PG Blackwell,
C Bronk Ramsey, CE Buck, GS Burr, RL Edwards, M Friedrich, PM Grootes,
TP Guilderson, I Hajdas, TJ Heaton, AG Hogg, KA Hughen, KF Kaiser, B Kromer,
FG McCormac, SW Manning, RW Reimer, DA Richards, JR Southon, S Talamo,
CSM Turney, J van der Plicht, CE Weyhenmeyer (2009) Radiocarbon 51:1111-1150.

CALIBRATED AGE in terms of confidence intervals (Smoothing parameter: 0, Offset: 0)

68% confidence interval is 17825 BC to 17774 BC	19774 BP to 19723 BP (12.9% of area)
plus 17631 BC to 17491 BC	19580 BP to 19440 BP (54.9% of area)
95% confidence interval is 17922 BC to 17722 BC	19871 BP to 19671 BP (32.9% of area)
plus 17664 BC to 17466 BC	19613 BP to 19415 BP (62.2% of area)

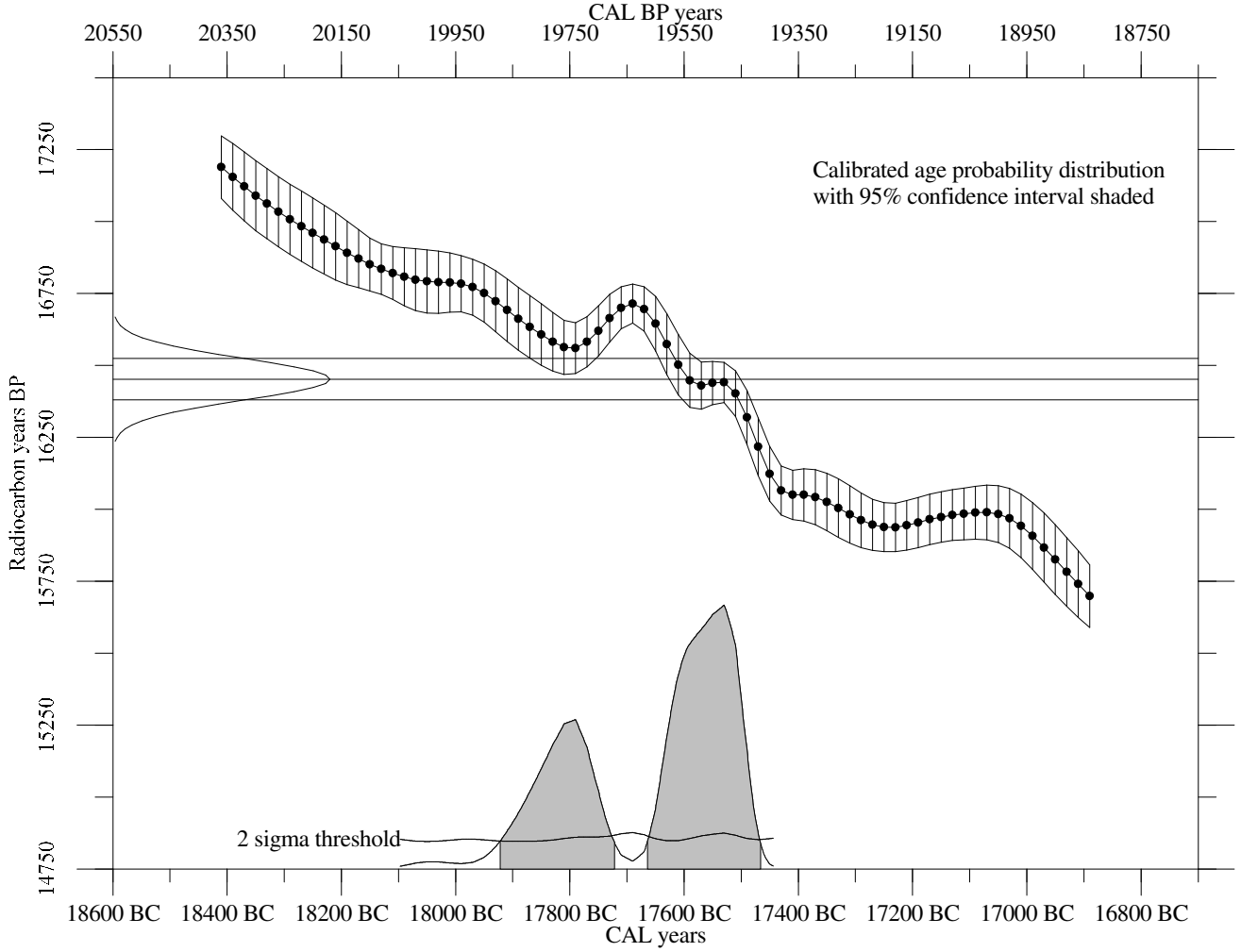

RAFTER RADIOCARBON LABORATORY

R40277/7

INSTITUTE OF GEOLOGICAL AND NUCLEAR SCIENCES LTD.
PO Box 31312, Lower Hutt, New Zealand
Phone (+64 4) 570 4671, Fax (+64 4) 570 4657

RADIOCARBON CALIBRATION REPORT

NZA 53812 CONVENTIONAL RADIOCARBON AGE 14807 ± 60 years BP

Atmospheric data from Reimer et al (2009);
PJ Reimer, MGL Baillie, E Bard, A Bayliss, JW Beck, PG Blackwell,
C Bronk Ramsey, CE Buck, GS Burr, RL Edwards, M Friedrich, PM Grootes,
TP Guilderson, I Hajdas, TJ Heaton, AG Hogg, KA Hughen, KF Kaiser, B Kromer,
FG McCormac, SW Manning, RW Reimer, DA Richards, JR Southon, S Talamo,
CSM Turney, J van der Plicht, CE Weyhenmeyer (2009) Radiocarbon 51:1111-1150.

CALIBRATED AGE in terms of confidence intervals (Smoothing parameter: 0, Offset: 0)

68% confidence interval is 16496 BC to 16376 BC	18445 BP to 18325 BP (22.4% of area)
plus 16114 BC to 15919 BC	18063 BP to 17868 BP (45.5% of area)
95% confidence interval is 16548 BC to 16306 BC	18497 BP to 18255 BP (32.6% of area)
plus 16160 BC to 15747 BC	18109 BP to 17696 BP (62.5% of area)

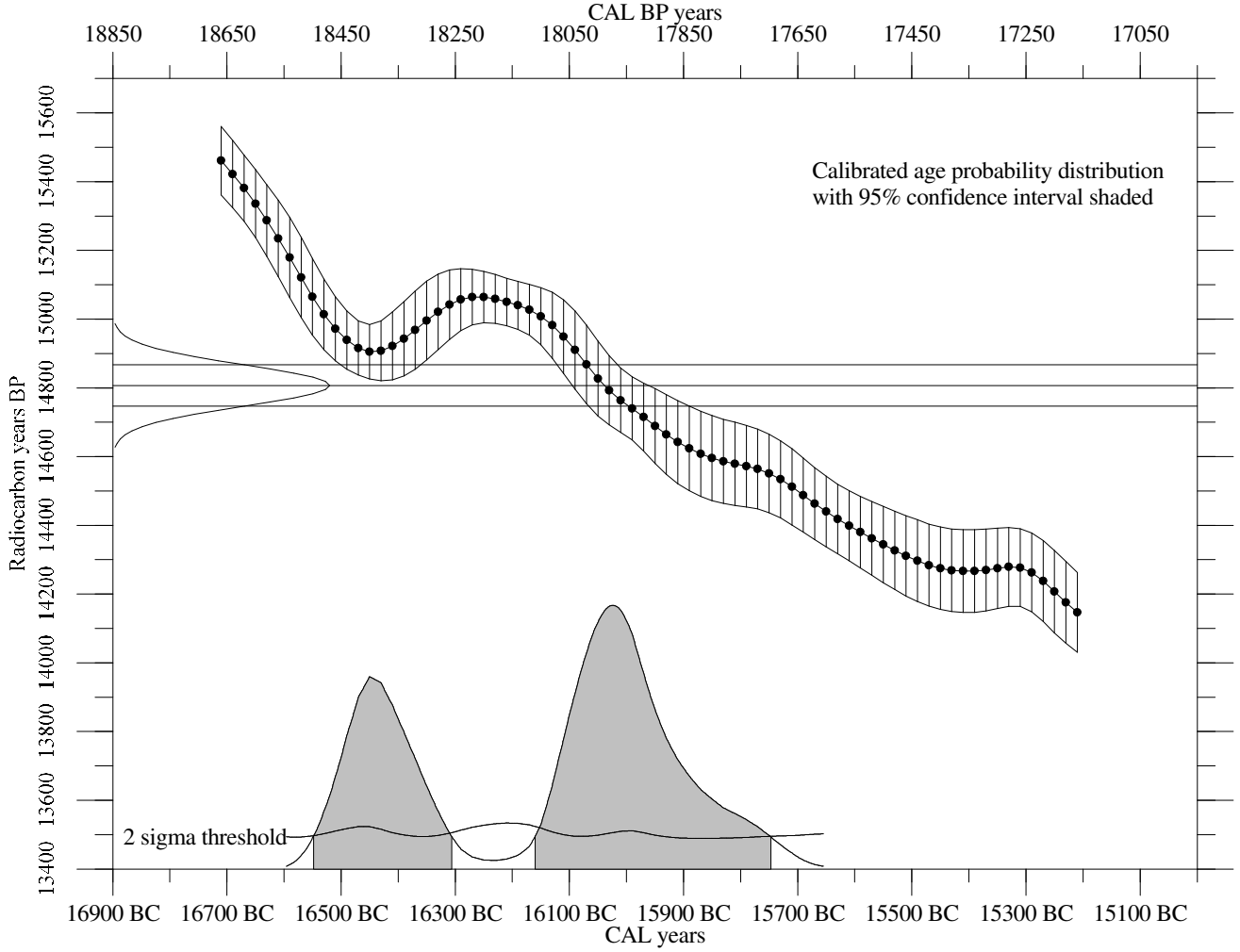

RAFTER RADIOCARBON LABORATORY

R40277/3

INSTITUTE OF GEOLOGICAL AND NUCLEAR SCIENCES LTD.
PO Box 31312, Lower Hutt, New Zealand
Phone (+64 4) 570 4671, Fax (+64 4) 570 4657

RADIOCARBON CALIBRATION REPORT

NZA 53733 CONVENTIONAL RADIOCARBON AGE 703 ± 16 years BP

Southern Hemisphere Atmospheric data from McCormac et al (2004);
FG McCormac, AG Hogg, PG Blackwell, CE Buck, TFG Higham, and PJ Reimer (2004)
Radiocarbon 46, 1087-1092

CALIBRATED AGE in terms of confidence intervals (Smoothing parameter: 0, Offset: 0)

68% confidence interval is 1297 AD to 1314 AD	653 BP to 636 BP (29.7% of area)
plus 1359 AD to 1381 AD	591 BP to 569 BP (39.8% of area)
95% confidence interval is 1289 AD to 1321 AD	661 BP to 629 BP (43.1% of area)
plus 1350 AD to 1386 AD	600 BP to 564 BP (52.6% of area)

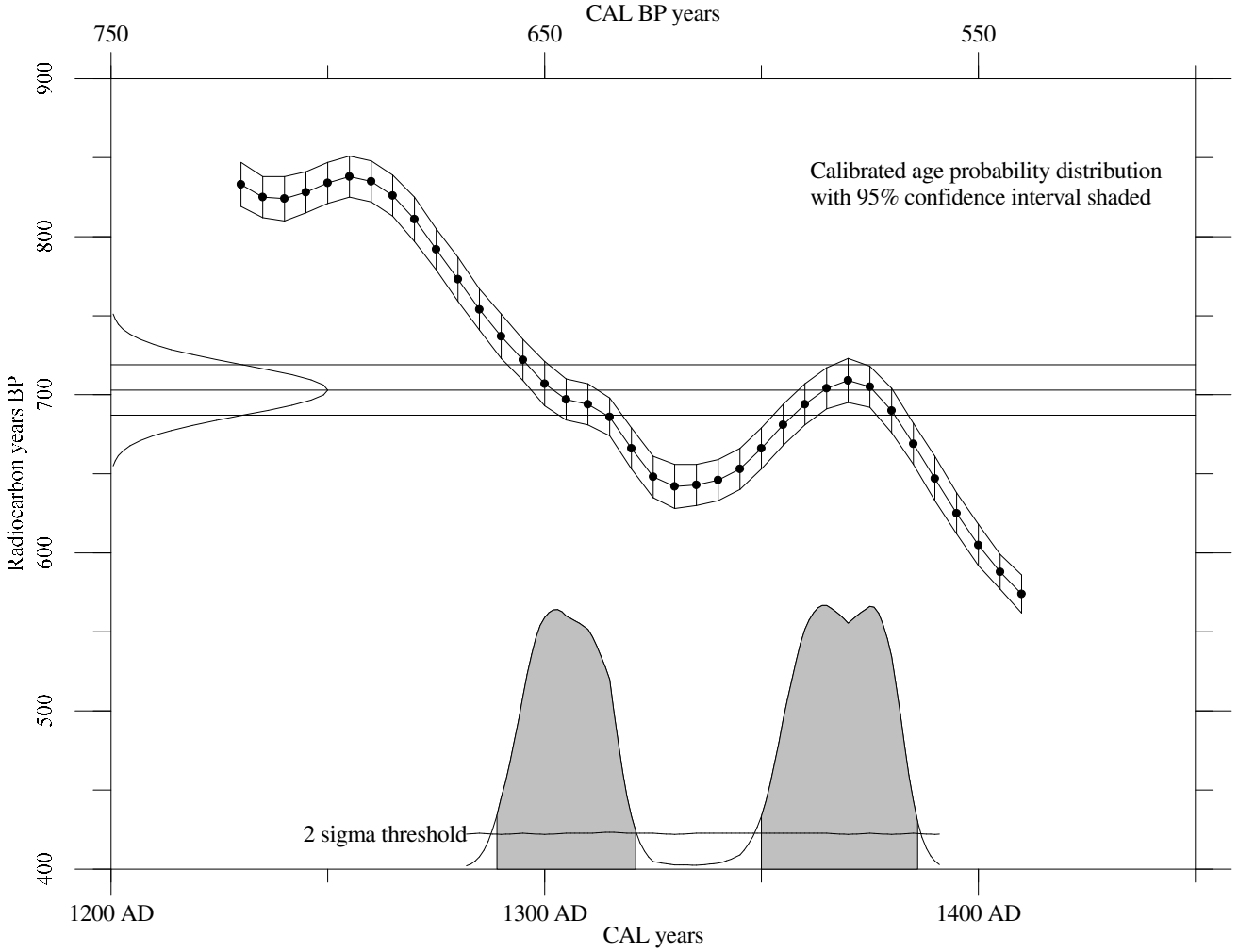

RAFTER RADIOCARBON LABORATORY

R40277/6

INSTITUTE OF GEOLOGICAL AND NUCLEAR SCIENCES LTD.
PO Box 31312, Lower Hutt, New Zealand
Phone (+64 4) 570 4671, Fax (+64 4) 570 4657

RADIOCARBON CALIBRATION REPORT

NZA 53715 CONVENTIONAL RADIOCARBON AGE 420 ± 16 years BP

Southern Hemisphere Atmospheric data from McCormac et al (2004);
FG McCormac, AG Hogg, PG Blackwell, CE Buck, TFG Higham, and PJ Reimer (2004)
Radiocarbon 46, 1087-1092

CALIBRATED AGE in terms of confidence intervals (Smoothing parameter: 0, Offset: 0)

68% confidence interval is 1458 AD to 1497 AD	492 BP to 453 BP (69.2% of area)
95% confidence interval is 1454 AD to 1504 AD	496 BP to 446 BP (76.9% of area)
plus 1591 AD to 1615 AD	359 BP to 335 BP (18.4% of area)

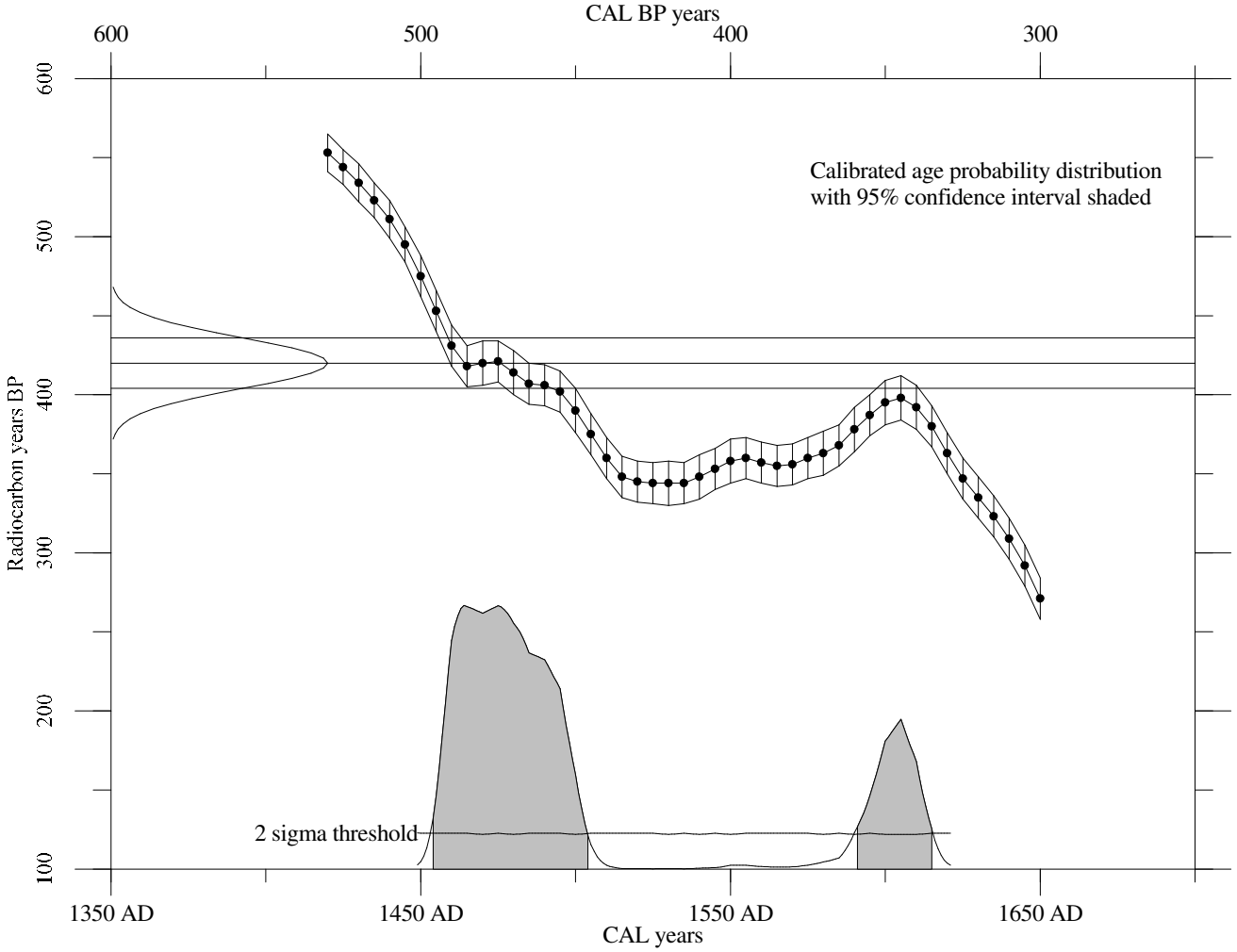

Appendix D

OSL Technical Report

Report No.9/13

Luminescence Dating Technical Report

Luminescence Dating Laboratory
School of Geography, Environment and Earth Sciences
Victoria University of Wellington
Wellington
New Zealand

Reported by: Ms. Ningsheng Wang
Date of Issue: 10-07-2013
Contact: Room 414
Cotton Building
Victoria University of Wellington
Ph: (04) 463 6127

CONTENTS

1. SUMMARY

Two samples (Field code: SP_T5_01 and SP_T5_02) were submitted for luminescence dating by Sarah Bastin and Dr. Mark Quigley, University of Canterbury. The laboratory codes of the samples are WLL1075 and WLL1076 respectively.

The fine grain (4-11μm) preparation technique was used. The paleodose (the equivalent dose) of all samples was evaluated using the Multiple Aliquot Additive Dose method (MAAD) based on measurements of blue luminescence from the fine grain feldspar produced during infrared stimulation. The dose rate was determined on the basis of gamma spectrometry measurements.

2. EXPERIMENTAL WORK

A) Sample Preparation

Samples had their outer surfaces removed. "Fresh" sample material, that had outer surfaces removed earlier (unexposed light sample material), was treated in 10% HCl. This was carried out overnight until all carbonate was removed by the reaction. Following this treatment the sample was further reacted overnight with 10% H_2O_2 in order to remove organic matter. The next step involved 200ml CBD* solution being added to the sample for 12 hours to remove iron oxide coatings. Note, after every chemical treatment procedure distilled water was used to wash the sample several times. After chemical treatment, calgon solution (1g sodium hexametaphosphate per litre distilled water) was added to make thick slurry. This slurry was placed into an ultrasonic bath and mechanically agitated for an hour. The sample was then placed into a 1L measuring cylinder, filled with a certain amount of distilled water to separate out the 4-11μm grains according to Stokes' Law.

The 4-11μm grains were then rinsed with ethanol and acetone and a suspension of these grains were then deposited evenly onto 70 aluminium disks (diameter 9.8mm).

This removed outer scraping was then dried in an oven, milled, weighed and sealed in air tight perspex containers, then stored for at least four weeks before the gamma spectrometer analysis. The storage time minimizes the loss of the short lived noble gas ^{222} Rn and allows ^{226}Ra to reach equilibrium with its daughters ^{214} Pb and ^{214} Bi.

A plastic cube was then filled with remaining scrapings in preparation for water content measuring.

*CBD solution: 71g sodium citrate, 8.5 g sodium bicarbonate, and 2g sodium dithionate per litre of distilled water

B) Measurements

Luminescence age was determined by two factors: the equivalent dose (De) and the dose rate. It involves measurements of luminescence for determination of De and concentrations of ^{238}U, ^{232}Th, ^{40} K and water contents (used to determine of dose rate).

Equivalent dose: obtained from the lab equivalents to the paleodose absorbed by samples during the burial time in the natural environment since their last exposure to the light.
Dose rate: amount dose received by the sample each year.

B1. Determination of Equivalent Dose (D_e)

D_e for all of these samples were obtained by using the *Multiple Aliquot Additive Dose Method (MAAD*).

The test dose obtained from an initial test measurement was used for the MAAD. As luminescence vary between disks, all disks for MAAD need to be normalised before β irradiation. 0.1 second infrared measurements were taken before irradiation of all aliquots. Six groups (30 disks divided by five) were β irradiated up to five times of the test dose. Beta irradiation were done on the Riso TL-DA-15 ^{90}Sr/Y β irradiator, calibrated against ^{60}Co gamma source, SFU, Vancouver, Canada with about 3% uncertainty. Three groups (three disks per group) were α irradiated up to three times of the test dose. The α irradiation was carried out on a ^{241} Am irradiator,

supplied and calibrated by ELSEC Littlemore, UK. The next step was that these 39 disks together with nine non-irradiated disks (total of 48 disks) were stored for four weeks to relax the crystal lattice after irradiation.

After storage, the 48 disks were preheated for five minutes at 230^{o}C, then were measured using a Riso TL-DA-15 reader with infrared diodes at 880nm used to deliver a stimulated beam (30mW/cm^{2})at the room temperature for 100s. Blue luminescence centred about 410nm emission from feldspar was then detected by an EMI 9235QA photomultiplier fixed behind two filters consisting of a Schott BG-39 and Kopp 5-58.

Luminescence growth curve (β induced luminescence intensity versus added dose) was constructed by using the initial the 4 seconds of the shine down curves and subtracting the average of the last 20 seconds, along with the so called late light which was thought to be a mixture of background and hardly bleachable components. Extrapolation of this growth curve to the dose axis was obtained the equivalent dose De which was used as a paleodose.

Measurement of a-value

A similar plot for the alpha irradiated disks allows for an estimation of α efficiency, a-value (a-value is measured by comparing the luminescence induced by alpha irradiation with that induced by beta or gamma irradiation). The a-value was for dose rate calculation.

B2: Determination of Dose Rate

Dose rate consisted of two parts.

(i) Dose rate from sample's burial environment

(ii) Dose rate from cosmic rays.

(i) ***Dose rate from burial environment***

Dose rate from sample's burial environment was determined by radionuclide contents of ^{238}U, ^{232}Th and ^{40}K, a-value and water content.

Determination of Contents of U, Th and K by Gamma spectrometry

Gamma rays produced from sample material was counted for a minimum time of 24 hours by a high resolution and broad energy gamma spectrometer. The spectra were then analysed using GENIE2000 software. The contents of U, Th and K were obtained by comparison with standard samples. The dose rate calculation was based on the activity concentration of the nuclides ^{40} K, ^{208}TL, ^{212}Pb, ^{228} Ac, ^{214} Bi, ^{214}Pb, ^{226} Ra, using dose rate conversion factors published by Guérin, G., Mercier, N., Adamiec, G. 2011.

Measurement of Water Contents

Water content was measured as weight of water divided by dry weight of the sample taking into account a 25% uncertainty.

(ii) *Dose rate from cosmic rays*

Dose rate from cosmic rays were determined by the depth of sample below the surface along with its longitude, latitude and altitude, convention formula and factors published by Prescott, J.R. & Hutton, J.T. (1994).

3. RESULTS

Table 1 Cosmic dose rates

Table 2 Water contents, radionuclide contents

Table 3 a- Values, dose rates, equivalent doses and luminescence ages.

Table 1: Cosmic Dose Rates

Laboratory Code	Depth Below the Surface(m)	Cosmic Dose Rate (Gy/ka)	Field Code
WLL1075	1.05	0.1797±0.0090	SP_T5_01
WLL1076	0.86	0.1845±0.0092	SP_T5_02

Table 2: Water Contents, Radionuclide Contents

Laboratory Code	Water Content (%)	U(ppm) from ^{234}Th	U(ppm) from ^{226}Ra, ^{214}Pb, ^{214} Bi	U(ppm) from ^{210}Pb	Th(ppm) From ^{208}Tl ^{212} Pb ^{228} Ac	K(%)	Field Code
WLL1075	21.2*	3.00±0.37	3.02±0.22	3.66±0.32	10.88±0.18	2.22±0.05	SP_T5_01
WLL1076	21.2	3.42±0.26	2.99±0.15	3.32±0.23	10.54±0.14	2.24±0.05	SP_T5_02

* The water content of WLL1075 was used the same value of WLL1076

Table 3: a-Values, Dose Rates, Equivalent Doses and Luminescence Ages

Laboratory Code	a-value	D_e(Gy)	Dose Rate(Gy/ka)	**Luminescence Age(a)#**	Field Code
WLL1075	0.13±0.01	13.21±0.57	4.64±0.28	**2850±210**	SP_T5_01
WLL1076	0.09±0.01	11.95±0.62	4.24±0.23	**2820±210**	SP_T5_02

Age is expressed in years and rounded to nearest 10 years (or 10a)

Comments:

The D_e plateaus of the two samples are not flat from data observation which implies that the samples had partial bleaching before redisposition. Therefore, the OSL ages in the report are the maximum ages. Their true ages are very likely younger than the reported ages.

4. REFERENCES

Guérin, G., Mercier, N., Adamiec, G. 2011: Dose- rate conversion factors: update. Ancient TL, Vol.29, No.1, 5-8.

Murry, A.S. & Wintle, A.G. 2000: Luminescence dating of quartz using an improved single aliquot regenerative dose protocol. Radiation Measurements 32, 57-73.

Prescott, J.R. & Hutton, J.T. 1994: Cosmic ray contributions to dose rates for luminescence and ESR dating: Large depths and long-term time variations. Radiation Measurements. Vol.23,Nos.2/3, 497-500.

Appendix E

Publications arising from thesis

Paleoliquefaction in Christchurch, New Zealand
Sarah H. Bastin†, Mark C. Quigley, and Kari Bassett
Geological Society of America Bulletin, B31174.1, first published on April 14, 2015,
Department of Geological Sciences, University of Canterbury, Christchurch 8014, New Zealand
doi: 10.1130/B31174.1

Characterisation of modern and paleoliquefaction features in eastern Christchurch, NZ following the 2010-2011 Canterbury earthquake Sequence
Bastin, S.H., Quigley, M.C., Bassett, K., Green, R.A., (2013)
Proceedings of the 19th NZGS Symposium – Lifelines, Infrastructure and Natural Disasters, Queenstown, New Zealand, 20-23 November.

Comparison of liquefaction-induced land damage and geomorphic variability in Avonside, New Zealand
S.H. Bastin, M.C. Quigley, K. Bassett
6th International Conference on Earthquake Geotechnical Engineering
1-4 November 2015
Christchurch, New Zealand